Study of J/ψ-hadron azimuthal correlations in pp collisions at 13 TeV with ALICE and commissioning of the muon spectrometer

Sébastien Perrin

université
PARIS-SACLAY

Study of J/ψ-hadron azimuthal correlations in pp collisions at 13 TeV with ALICE and commissioning of the muon spectrometer

Étude des corrélations azimutales J/ψ-hadron dans les collisions pp à 13 TeV avec ALICE et commissioning du spectromètre à muons

Thèse de doctorat de l'université Paris-Saclay

École doctorale n° 576, Particules Hadrons Énergie et Noyau : Instrumentation, Image, Cosmos et Simulation (PHENIICS)
Spécialité de doctorat: Physique hadronique
Graduate School: Physique, Référent: Faculté des sciences d'Orsay

Thèse préparée dans le **Département de Physique Nucléaire - DPhN (Université Paris-Saclay, CEA)**, sous la direction de **Andrea FERRERO**, Cadre scientifique CEA, et la co-direction de **Javier Ernesto CASTILLO CASTELLANOS**, Directeur de recherche CEA

Thèse soutenue à Paris-Saclay, le 21 octobre 2022, par

Sébastien PERRIN

Composition du Jury

Membres du jury avec voix délibérative

Jean-Yves OLLITRAULT Directeur de recherche CNRS, IPhT (Université Paris-Saclay, CNRS/CEA)	Président
Anton ANDRONIC Professeur, Institüt fur Kernphysik (Université de Münster)	Rapporteur & Examinateur
Elena FERREIRO Professeure, Department of Particle Physics (Université de Saint-Jacques de Compostelle)	Rapporteure & Examinatrice
Cvetan CHESHKOV Directeur de recherche, IN2P3 Lyon (Université Claude Bernard Lyon 1)	Examinateur
Pasquale DI NEZZA Professeur, Laboratori Nazionali di Frascati (INFN)	Examinateur

THÈSE DE DOCTORAT
NNT : 2022UPASP114

université PARIS-SACLAY

ÉCOLE DOCTORALE
Particules, hadrons, énergie et noyau : instrumentation, imagerie, cosmos et simulation (PHENIICS)

Titre: Étude des corrélations azimutales J/ψ-hadron dans les collisions pp à 13 TeV avec ALICE et commissioning du spectromètre à muons
Mots clés: Quarkonium, Quarks lourds, ALICE, QCD, LHC, QGP

Résumé:

Le plasma de quarks et de gluons (QGP) est un état de la matière déconfiné où les quarks et les gluons évoluent librement. Il peut être produit lors de collisions d'ions lourds au LHC. L'etude du QGP grâce aux détecteurs d'ALICE passe en partie par l'étude des quarkonia, états liés d'un quark lourd et de son antiquark comme le J/ψ ($c\bar{c}$) par exemple. Les quarkonia sont des sondes privilégiées puisqu'ils se forment aux premiers instants de la collision et sont influencés par le milieu coloré. Une signature du QGP, le flot elliptique, témoigne des effets collectifs entre les particules et a été observée pour les particules légères dans les collisions Pb–Pb et, étonnemment dans les collisions p–Pb et pp, quand bien même aucune formation de plasma n'y était attendue. En ce qui concerne le J/ψ, un flot positif a été mesuré en Pb–Pb et p–Pb bien qu'aucune explication robuste n'ait été apportée. Par conséquent, cette thèse présente la mesure du flot elliptique du J/ψ par corrélation de paires J/ψ-hadron dans les collisions pp à $\sqrt{s} = 13$ TeV mesurées pendant le Run 2 du LHC (de 2016 à 2018). Aucun flot n'est observé ce qui confirme les attentes des modèles de transport ainsi que certaines propriétés observées dans d'autres systèmes.

L'amélioration de l'electronique de mesure et l'ajout de nouveaux détecteurs va permettre à ALICE d'acquérir plus de données dès le Run 3. Au niveau des détecteurs, cette thèse met en avant le commissioning du spectromètre à muons et le développement d'outils de contrôle qualité (QC) permettant aux shifters et aux experts de surveiller l'état des détecteurs en temps réel à partir d'observables choisies. Cette thèse traite également du comportement de la nouvelle électronique de mesure en ce qu'elle affecte la reconstruction des impacts des partiules (le clustering) et par conséquent la résolution de nos mesures.

Title: Study of J/ψ-hadron azimuthal correlations in pp collisions at 13 TeV with ALICE and commissioning of the muon spectrometer
Keywords: Quarkonium, Heavy quarks, ALICE, QCD, LHC, QGP

Abstract: The quark-gluon plasma (QGP) is a deconfined state of matter in which quarks and gluons move freely, which can be produced in heavy-ion collisions at the LHC. The study of the QGP using the ALICE apparatus relies partly on quarkonia, bound states of a heavy quark and antiquark of which the J/ψ ($c\bar{c}$) is an example. They are probes of choice as they are formed at the early stages of the collision and are influenced by the color-charged medium. A signature of QGP formation, the elliptic flow, provides an assessment of collective effects between the produced particles and was observed for light particles in Pb–Pb collisions and, surprisingly, in p–Pb and p–p systems although no QGP formation was expected. For the J/ψ, flow has been observed in both Pb–Pb and p–Pb systems, however without a clear theoretical explanation. Consequently, this thesis focuses on the measurement of the elliptic flow of the J/ψ in pp collisions at $\sqrt{s} = 13$ TeV acquired during LHC Run 2 (2016 to 2018), through correlations of J/ψ-hadron pairs. No significant elliptic flow is found which is compatible with transport model expectations and properties observed in larger systems.

Improvements to the electronics and the addition of new detectors will allow for more data to be acquired from Run 3 onwards. On the detector side, this thesis discusses the commissioning of the muon spectrometer and the development of Quality Control (QC) software allowing shifters and experts to monitor the status of the detector using dedicated observables. We also study the behaviour of the electronics and how it affects particle hit reconstruction (clustering) and ultimately the resolution of our measurements.

À ma famille et mes amis

Acknowledgements

Alors voilà. On dirait que c'est le moment d'écrire les remerciements. Et il y en a tellememt et je suis si peu doué pour ça, alors je vais faire comme je peux. Un immense merci à tout les membres du LQGP pour leur gentillesse, leur bonne humeur et pour l'enviromment bienveillant qu'ils ont permis de créer durant ces trois ans. En particulier, merci à Andrea et Javier, vous qui avez su supporter mes bêtises allant de casser O2 à faire les plots moches qu'on n'ait jamais vus (certains ont peut-être même survécu et se sont insérés dans la thèse qui suit). Merci pour votre soutien et votre écoute, pour m'avoir aiguillé et apporté votre expertise scientifique au long de ces trois ans, surtout durant les périodes plus difficiles. Mention spéciale à Andrea pour m'avoir en plus appris à conduire une boîte auto sans devenir le danger public de Saint-Genis.

Merci Aude pour avoir été la meilleure co-bureau, pas sûr que blaster Djadja nous ait rendus plus efficaces, mais au moins ça nous aura mis de bonne humeur. Merci Maurice, pour ces dabs dans les couloirs et ce Quark Matter, marqué à jamais par les zupy et les pierogis. Merci Batul, pour la gentillesse et la haine partagée du 91.06. Merci Lucrecia, pour le soutien moral et les gifs sur Mattermost depuis Étretat. Merci Robin et Florian, pour les discussions, les conseils et la bonne humeur durant nos premières années. Merci Michael pour ton expertise, ta capacité à motiver et à expliquer, même si je n'ai jamais rien compris de ce que tu nous disais en allemand. Merci Stefano pour la bonne humeur, l'expertise et les taquineries (toujours bienveillantes — j'espère !), pour m'avoir fait visiter ALICE pour la première fois, un mélange d'émerveillement et de panique quand tu as commencé à me faire une interro surprise. Merci Andry, pour ta gentillesse, ta bienveillance, et le soutien moral pendant la rédaction ou le développement logiciel. Enfin merci à Alberto et Hervé pour leur disponibilité, leur expertise et leurs discussions. Merci aux autres doctorants du DPhN pour les cafés en présentiel comme en Zoom, les discussions à la cantine ou au détour d'une navette. Paul, Rudolphe, Andrea, Aurore, Hervé, Benjamin, Zoé, et tous les autres, merci. Au plaisir de tous vous revoir par la suite !

Merci à mon jury de thèse pour avoir pris le temps de lire et d'évaluer mon travail et dont les retours m'ont fait pleinement gagner en confiance. En particulier, merci à mes rapporteurs, Anton et Elena, Cvetan pour son accompagnement et expertise sur l'analyse, Jean-Yves pour son expertise sur le flow et nos discussions ainsi que Pasquale, Andrea, et Javier pour leurs commentaires constructifs sur la thèse et sur l'avenir. Merci aux membres meeting groups d'ALICE, MCH, les PAG, pour les conseils et les feedbacks toujours pertinents.

Merci à Franck pour m'avoir donné l'opportunité de travailler au DPhN et m'avoir suivi pendant ces trois ans, merci à Danielle pour sa gentillesse et son accompagnement bienveillant des doctorants facilement impressionés, merci Isabelle pour les discussions au détour d'un couloir, ta disponibilité et tes conseils pour sauver mes pauvres fleurs, même si je maintiens que les narcisses étaient voués à l'échec, pourtant j'ai tout donné.

Merci aux enseignants passionnés qui au cours de ma scolarité m'ont partagé leur passion de la physique et des sciences en général. Dominique, Catherine, Nathalie, Philippe et tant d'autres, un grand merci.

Merci à ma famille, Maman, Max, et puis Jelly le bébou chat d'amour, qui m'avez soutenu pendant ces années. Et merci à mes amis qui avez toujours été là pour m'accompagner à chaque instant depuis longtemps, pour toutes les rigolades et pour tout les memes. La coloc, le M7, l'Auberge, CentRUle, les HX4, les Parigots, les Ch'tis, les Limougeauds, et tous les autres. Je vous dois tant.

Contents

General introduction

Particle physics is the study of the fundamental bricks of matter and their interactions. How does matter work, what it is made of? Where does matter come from, and how was our Universe born? These are some of the many questions particle physicists try to answer. Because no microscope can observe the finest structures of matter and nobody can travel back to the birth of the Universe, experimentalists devised more ingenious ways to study matter and its birth. Particle accelerators and colliders, like the LHC at CERN, allow physicists to reproduce the Big Bang in a controlled environment. Particles are accelerated to speeds close to the speed of light, and when they collide, they release so much energy that the matter they are made of becomes so hot that it melts. And here we are, with droplets of hot and dense "cosmic soup". In this soup, the most fundamental bricks of matter, quarks and gluons, are moving freely, hence its name: the quark-gluon plasma.

The plasma, believed to have been the state of all matter in the Universe some microseconds after the Big Bang, only has a very short lifetime, which means it cannot be directly observed by scientists in a lab as if it were stable. In order to study the quark-gluon plasma, the only solution, for now, is to examine the clues and hints it left before disappearing. Dedicated experiments like ALICE at the LHC, composed of many large-scale detectors arranged around the collision point, act as investigators and measure particles left by the plasma after it cooled down and became ordinary matter again.

In this investigation, a key witness is a particle called the J/ψ. It is composed of a heavy quark bound to its anti-quark. The J/ψ is a heavy particle compared to the vast majority of particles produced in the collision. It has been there since the beginning of the collision and saw the whole formation, evolution and destruction of the plasma. As the J/ψ and the plasma evolved together, the behaviour of the J/ψ remains influenced by its interaction with the plasma. For example, as the J/ψ bathes in the soup, if the medium is too energetic and dense, the J/ψ can melt. So if we know the initial population of J/ψ and measure less J/ψ in the detectors, it indicates that the plasma may have melted them.

In this thesis, we focus on another characteristic of the J/ψ in the plasma: the flow. The quark and gluon soup behaves like a fluid. Therefore, particles within tend to be dragged along as it expands and cools down. In heavy-ion collisions, light particles tend to be easily swept by the current, and heavier particles too but to a lesser extent because they are harder to move. Measuring the flow of a particle provides a comparison to theory trying to predict why the flow develops and to what extent. However, in smaller collision systems like p–Pb, where it was thought no plasma was formed, J/ψ and lighter particles were seen flowing to extents comparable with Pb–Pb collisions. Does this mean that plasma is formed even in p–Pb collisions? In this thesis, we go even further and investigate the smallest hadronic collisions: proton-proton (pp) collisions. In this system, light particles have been seen flowing. Does the J/ψ flow too? What can this measurement tell us about the plasma and the properties of matter?

To answer these questions the best, the ALICE Collaboration spent three years between 2018 and 2021 upgrading the experiment's detectors and even adding brand new detectors. In further data taking, these upgrades will allow for more precise measurements and more events seen, allowing us to study the quark-gluon plasma with a renewed accuracy. In this context, this thesis also focuses on the experiment's detectors and their upgrade, namely their commissioning, which covers their installation and the monitoring of their proper functioning through Quality Control (QC).

In the first chapter, we will introduce the quark-gluon plasma and its study using heavy-flavour probes. In the second chapter, we will focus specifically on the flow to better understand what this observable is and discuss the current status of the results. In the third chapter, we will present the experimental setup of ALICE in the context of the LHC as well as the latest and future upgrades. In the fourth chapter, we will cover the quality control of the upgraded detectors of the muon spectrometer as well as event simulation, which allowed us to study the impact of new electronics on particle tracking.

After discussing the detector side of this work, we will present, in the fifth chapter, the analysis procedure of the J/ψ elliptic flow in pp collisions, before, finally, in the sixth chapter, presenting and discussing the results of said analysis and their meaning within the context of the study of the quark-gluon plasma.

Chapter 1

Introduction to the Quark-Gluon Plasma

Au matin de ta vie sur la planète, ébloui par le dieu Soleil / À l'infini, tu t'éveilles aux merveilles de la Terre, qui t'attend et t'appelle / Tu auras tant de choses à voir, pour franchir la frontière du savoir / Recueillir l'héritage, qui vient du fond des âges, dans l'harmonie d'une chaîne d'amour / C'est l'histoire de la vie, le cycle éternel.

– Debbie Davis (Le Roi Lion), *L'histoire de la vie*

This chapter presents a brief overview of particle physics and the quark-gluon plasma.

1.1 The Standard Model of particle physics

1.1.1 A catalog of equations and particles

Words make up our language and allow us to communicate. We can list common words in dictionaries, and such catalogues would be enough for everyday use. It would be functional but would gloss over many subtleties of the language, like the internal structure of words. In that sense, one could argue that letters are the most fundamental brick of language. They interact and arrange themselves to form words, and we can list them in an alphabet. A linguist can study letters and their interactions to gain knowledge about the formation of a language, its pronunciation and its use [1]. Similarly, chemical elements are what people use on a daily basis when they talk about matter. As a dictionary, the periodic table of elements by Mendeleev was a significant step in the understanding of matter by classifying it. However, its properties indicated a deeper level of understanding that needed to be reached at the subatomic level to make progress. During the twentieth century, with the development of quantum physics and relativity, the field of particle physics was born, and with it, a new comprehensive model to explain matter and forces: the Standard Model. The Standard Model (SM) can be seen as the alphabet of subatomic physics. It lists the fundamental particles and their interactions, encoded in fundamental equations.

A representation of the Standard Model is shown in Figure 1.1. Elementary particles are divided between "matter particles", the spin-half fermions, and "force carriers", the integer spin bosons. The fermions are further divided into quarks and leptons. Quarks are electrically charged ($+2/3$ or $-1/3$) and colour charged. Colour charge is similar to electric charge, but instead of having a $+$ and a $-$ charge, there are three colours (red, green, and blue) and their anti-colours. There are six quark flavours: up, down, charm, strange, top and bottom (also called beauty). The lepton family contains the electron and its more massive counterparts, the muon and the tau, which are negatively charged, and their respective neutrinos, which are massive particles. However, the mass ordering is still to be clarified. The fermions are grouped into three generations, each containing a pair of quarks (one positively, one negatively charged), a lepton and its neutrino. Each generation is heavier and more unstable than the previous one. Consequently, protons and neutrons, making up everyday matter, are themselves made of light-flavour (up and down) stable quarks and not higher generations. We can also add the

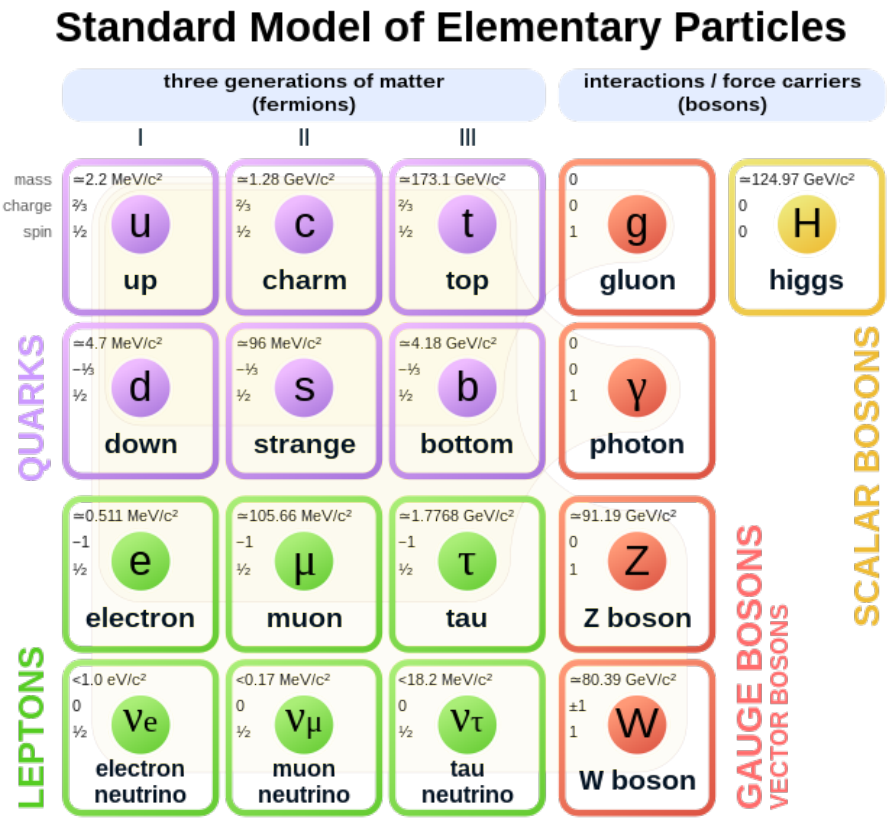

Figure 1.1: Representation of the Standard Model of particle physics [2].

antimatter particles to these matter particles, negative energy states propagating backwards in time that are predicted by the Dirac equation. Compared to their ordinary matter counterparts, they have opposite quantum numbers.

In the Standard Model, forces are mediated by bosons. The massless photon mediates the electromagnetic force, as described by Quantum Electro-Dynamics (QED). The $W^{\pm}$ and Z^0 bosons mediate the weak nuclear force, which is, for example, responsible for beta decay. The gluon mediates the strong nuclear force, binding the quarks together and thus ensuring cohesion within the nucleus. As we will see in the section dedicated to Quantum Chromo-Dynamics (QCD), the gluon itself is colour charged, which makes it able to interact with itself, making QCD differ from QED. Finally, the spin-0 Higgs boson, jointly observed in 2012 by ATLAS [3] and CMS [4], explains how particles can acquire their mass by interacting with its field [5].

1.1.2 Limitations and shortcomings

Even though the Standard Model proved its highly predictive power through thorough experimental testing, it suffers from the high number of free parameters tuned to make it work. We can count the masses of the twelve fermions, the three coupling constants for gauge interactions, the two parameters of the Higgs potential (vacuum expectation value and mass) and eight mixing angles in CKM and PMNS matrices. This sums up to 25 free parameters, which is too much to pretend that the Standard Model is the true fundamental theory of particle physics. To further develop this argument, the Standard Model resembles Mendeleev's table, in which species belonging to the same period tend to possess similar properties, which indicate a deeper structure. The repetition between the three fermion families in the Standard Model may indicate a more refined structure that we are yet to unveil.

The Standard Model presents some other issues or incompleteness. For example, it only accounts for ordinary matter, which makes up about 5% of matter in the Universe. According to the ΛCDM

"Standard Model" of cosmology [6], 25% of matter is dark matter and the rest is dark energy. Dark matter is an invisible form of matter which does not interact through QED or QCD processes. It was experimentally identified by looking at the velocity profiles of galaxies, which were not in agreement with what gravity imposes [7]. Maybe new particles that would interact weakly with ordinary matter (WIMPs) could complete the Standard Model [8]. Dark energy accounts for the accelerating expansion of the Universe. Also, the great absentee of the Standard Model is gravity, which is not accounted for contrary to all the other fundamental forces we know of and which would gradually become more crucial as higher experimental energies are reached.

Another form of incompleteness found in the Standard Model concerns the Higgs mass. Loop corrections from bosons and fermions to the Higgs propagator contribute positively and negatively to the Higgs squared mass. Suppose the Standard Model is valid up to a given energy scale Λ (typically the Planck scale 10^{19} GeV), the contributions to the Higgs squared mass scale as Λ^2. The Higgs mass is of order 10^2 GeV. Considering it comes from a sum of terms way higher in magnitude, this value seems unbelievably finely tuned. One theory beyond the SM which aims at explaining this "Hierarchy problem" is Supersymmetry (SUSY) [9]. To summarize, every particle has a supersymmetric double. Every fermion is paired with a boson (like squarks, sleptons) and vice versa (gauginos). If SUSY particles have masses close to their SM counterparts (typically of order 1 TeV), the Hierarchy problem could be solved. Moreover, conservation laws in SUSY would imply the existence of the lightest stable particle, the neutralino, which could be a viable candidate for dark matter, and SUSY calculations tend to show a running of the coupling constants towards the same value at a Grand Unified Theory scale. SUSY could solve various SM shortcomings at once. However, none of these particles have been discovered despite the energies probed at the LHC, which continue to put more and more stringent limits on the validity of SUSY [10, 11].

Beyond the Standard Model, theories with new interactions and particles are prompted by measurements that start to put tension on the Standard Model itself. For instance, LHCb has been investigating lepton universality, which is the fact that electrons, muons, and tau exhibit the same couplings (if not for their different masses). For example, $B^+ \longrightarrow K^+\mu^+\mu^-$ should be as frequent as $B^+ \longrightarrow K^+e^+e^-$. The flavour change from beauty to strange is highly suppressed as it can only be done through loop diagrams, also called penguin diagrams, due to their apparent resemblance as seen in Figure 1.2. They are very sensitive to unknown particles, which could contribute to the loop. A test of lepton universality using $B^+ \longrightarrow K^+l^+l^-$ decay by LHCb [12] shows tensions of order 3.1σ with the Standard Model. Such deviation is not enough to claim discovery which would prompt the detailed search for a new particle like, for example, leptoquarks [13], but it hints at SM weaknesses, and such measurements will be further studied. A full introduction to particle physics, the Standard Model and its limits can be found in Refs. [14] and [15] (with a more computational aspect).

1.2 Quantum Chromo-Dynamics (QCD)

As we have mentioned, QCD is the theory of the strong interaction which binds the nucleus. Reviews on QCD can be found in Refs. [16] and [17]. The following equation gives the Lagrangian of QCD:

$$\mathcal{L} = \sum_{flavour\ q} \overline{\psi_{q,\alpha}}(i\gamma^\mu\partial_\mu\delta^{\alpha\beta} - \frac{g_S}{2}\gamma^\mu\lambda_k A^k_\mu - m_q\delta^{\alpha\beta})\psi_{q,\beta} \ - \ \frac{1}{4}F^{i\mu\nu}F^i_{\mu\nu}. \tag{1.1}$$

In Equation 1.1, $\psi_{q,\alpha}$ denotes a quark field of flavour q and colour α, γ^μ are the Pauli matrices, $\delta^{\alpha\beta}$ is the Kronecker symbol, g_S the strong force coupling factor, λ_k the Gell-Mann matrices, m_q the quark mass and A^k_μ the gluon fields. The commutation laws of Gell-Mann matrices are:

$$[\lambda_i, \lambda_j] = 2if_{ijk}\lambda_k,$$

and writing

$$F^i_{\mu\nu} = \partial_\mu A^i_\nu + \partial_\nu A^i_\mu - g_S f_{ijk} A^j_\mu A^k_\nu,$$

the Lagrangian satisfies the requirements of gauge and local phase transformation invariance, similarly to QED. However, the representation group of QCD is not U(1); it is SU(3). This difference prompts the emergence of new degrees of freedom, colours (red, green or blue), a 3D space in which rotations are a linear combination of the SU(3) symmetry group generators, the Gell-Mann 3×3 matrices. Contrary

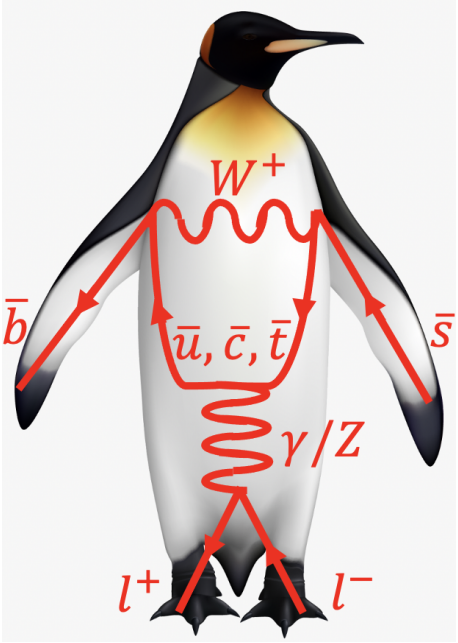

Figure 1.2: Representation of a flavour-changing neutral current (FCNC) penguin diagram, contributing to $B^+ \longrightarrow K^+ l^+ l^-$.

to QED, where only one gauge field was necessary, in QCD, eight fields are needed. They are the eight gluon fields. They carry colour charges, which is where QCD mainly differs from QED: gluons can self-interact. This effect makes QCD non-Abelian, as shown by the self-interaction terms in its Lagrangian proportional to A^3 or A^4 for three and four-gluon vertices, respectively.

So, while in QED, photon pair fluctuations would screen charge and weaken the coupling at large distances, in QCD, there is a competition between screening from quark-antiquark pair fluctuations and anti-screening from colour-charged gluon pairs fluctuations. This competition is won by the gluons which make the α_S $(= \frac{g_S^2}{4\pi})$ coupling constant run as expressed by the following equation from Ref. [16]:

$$\alpha_S(Q^2) = \frac{12\pi}{(33 - 2n_f) log(\frac{Q^2}{\Lambda^2_{QCD}})}, \tag{1.2}$$

with n_f the number of quark flavours, Q^2 the amount of exchanged momentum, and Λ_{QCD} (≈ 200 MeV) the cutoff scale of QCD. We see that the strength of the coupling depends on the energy Q^2 at which we probe QCD: the coupling constant runs as represented in Figure 1.3.

In practice, the running of the coupling constant means that, at low energy (so low resolution power and large distances), α_S is large and the quarks appear confined due to the intensity of the strong force. This necessity to appear as colourless bound states is responsible for jets. As the quark and antiquark forming a pair become more and more distant, the coupling increases due to gluon pairs forming in the flux tube linking the quarks. When the coupling is too strong, a quark-antiquark pair is created from the vacuum and the broken flux tube reforms as two quark-antiquark pairs. At high energy (small distances), the coupling constant is small, and the quarks appear free, not needing to be bound in colourless states. In the confinement regime, quarks only appear grouped with other colour charges to form colourless hadrons, of which mesons (quark-antiquark states) and baryons (three-quark states) are an example. QCD also predicts the existence of more exotic states like the pentaquark (four quarks and one antiquark) presumably observed by LHCb [18]. The coupling is too large to apply perturbation theory in the confinement regime as higher-order terms are not negligible. Lattice QCD is then used: space is discretized, and QCD calculations are carried out on the mesh. The finer the mesh, the better the result, but this is very computer-intensive. On the contrary, at high energies in the asymptotic freedom regime, perturbative calculations (pQCD) are possible as higher-order terms

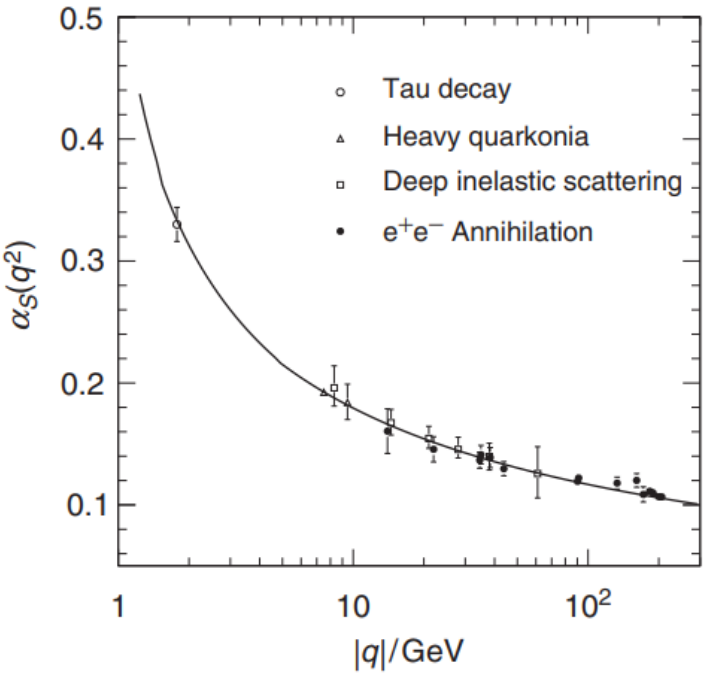

Figure 1.3: Measurements of the coupling constant $\alpha_S(Q^2)$, taken from Ref. [15].

are negligible. Λ_{QCD} makes the separation between the two regimes.

Another property of QCD is chiral symmetry breaking [19]. In QCD theory, axial flavour transformations are a type of unitary transformation of the fermion fields that changes parity. If the quarks are massless, the Lagrangian is invariant under such transformations. In practice, it means that left-handed and right-handed quarks do not interact. Nevertheless, as the quarks have mass, this chiral symmetry is spontaneously broken. However, if the energy increases sufficiently due to the running coupling constant, the measured quark masses decrease towards their low naked masses, restoring chiral symmetry. Such restoration would constitute a phase transition from hadronic matter to a new deconfined state of matter, the Quark-Gluon Plasma (QGP).

1.3 Heavy-ion collisions and the Quark-Gluon Plasma (QGP)

1.3.1 The QCD phase diagram

In Figure 1.4, we can see a sketch of the QCD phase diagram. In particular, it shows that when the temperature increases and surpasses a critical value, the quarks confined into colourless hadrons are freed. This deconfined state of matter is the QGP. As we discussed previously, the transition to the QGP phase is characterised by chiral symmetry restoration and thermodynamical changes to the medium. At vanishing baryonic chemical potential μ_B (which is the amount of energy needed to be given to the system to increase the baryon number by one), the critical temperature is $T_c \approx 154$ MeV [21] and the equivalent critical energy density is of the order 1 GeV/fm^3 [22]. Above these values, hadronic matter deconfines and the QGP is formed.

Because we cannot go back to the early Universe or study the insides of neutron stars, where QGP is believed to exist, we need ways to create an energetic system that is so hot and dense that QGP could be formed. This can be done through heavy-ion collisions (HIC). In colliders like the LHC, heavy-ion collisions allow producing highly energetic systems (currently up to centre-of-mass energies of $\sqrt{s} = 5.02$ TeV in Pb–Pb collisions), which can create droplets of QGP in a controlled environment. However, many factors like the number of colliding nucleons or the centrality of the collision (how head-on the collision is, described by the Glauber model [23]) play a role in the formation of QGP. A

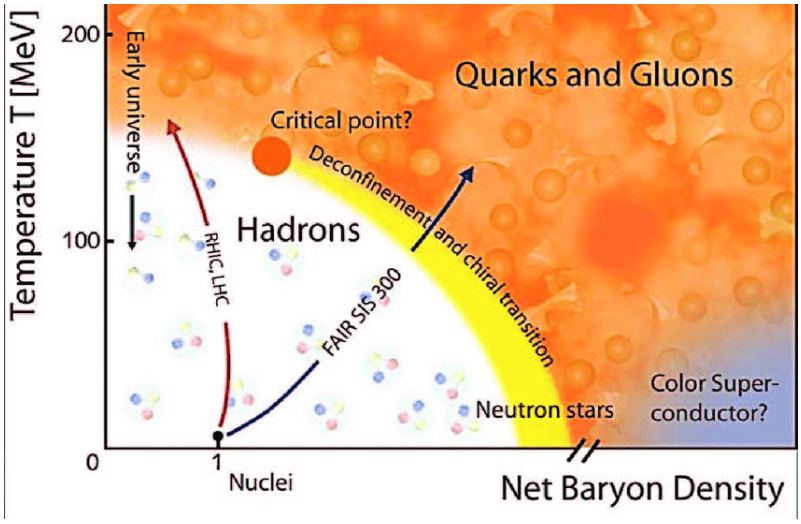

Figure 1.4: Illustration of the phase diagram of QCD matter, from Ref. [20].

peripheral Pb–Pb collision with barely any participant parton will not form a QGP. Smaller systems are also investigated (like p–A or pp) as they can give an insight into effects that are present without QGP formation (like Cold Nuclear Matter effects) and act as a baseline in the study of the QGP.

1.3.2 Evolution of the medium

The Bjorken model [24] is, in a way, the "Standard Model" of heavy-ion collisions. It explains the different stages of the collision and the evolution of the colliding system, as represented in Figure 1.5.

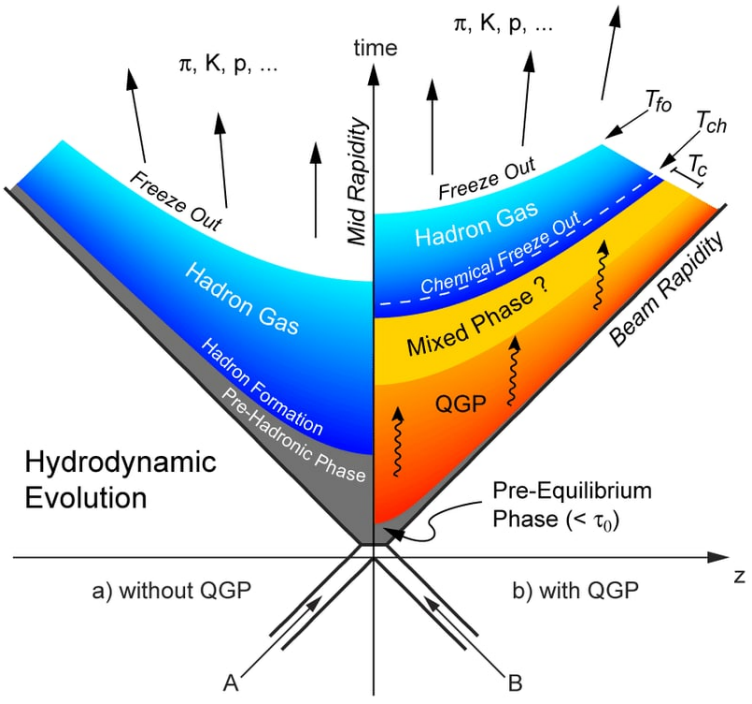

Figure 1.5: Illustration of the Bjorken scenario of heavy-ion collisions, with or without QGP formation, taken from Ref. [25].

Before the collision Due to the ultra-relativistic speeds of the heavy nuclei, lengths contract in the direction of the boosted beams. The nuclei appear like flattened disks, contracted by the Lorentz gamma factor. For Pb–Pb collisions at a centre-of-mass energy $\sqrt{s_{NN}} = 5.02$ TeV per nucleon pair, each Pb beam has an energy of 2.5 TeV per nucleon, equal to $m_N c^2(\gamma - 1)$ which gives $\gamma \approx 2500$. The nuclei crossing time is given by $2R/\gamma$ which, with $R \approx 7$ fm, yields 6 am$/c$.

Collision - Time 0 As the nuclei cross each other, some of their nucleons will interact. The crossing time of order 1 am$/c$ is negligible compared to the timescale of QCD $1/\Lambda_{QCD} = 1$ fm$/c$. Therefore, only once the nuclei have crossed one another will the participant nucleons form a strongly interacting medium.

Pre-equilibrium state - From 0 to 1 fm$/c$ As nuclei have just crossed, initial state effects occur which affect particle production. For example, the Color Glass Condensate model [26] predicts strong colour flux tubes in the interaction region and, in this medium, strong inelastic interactions occur between the partons until they thermalize. A more detailed description of the onset of heavy-ion collisions in accordance with the CGC is given in Ref. [27].

QGP phase and hydrodynamical expansion - From 1 to $\approx$ 10 fm$/c$ If the temperature and energy density surpass the critical values, the hadronic matter transitions and deconfines: QGP is formed and partons reach thermal equilibrium. It has been shown from measurements by ALICE [28] that the QGP would behave like a (nearly-)perfect fluid [29], and as such, it will hydrodynamically expand in all directions as it cools down.

Hadronization and hadron gas phase As the medium cools down, its temperature and energy density pass below the critical value and the QGP starts to hadronize. There is a mixed phase of QGP and hadrons until the hadronization is complete. Once all QGP has hadronized, all that is left is a hadron gas. Inelastic scatterings of hadrons continue to happen and change the abundances of hadronic species until the chemical freeze-out (happening at a temperature of $T_{chem} = 156.5$ MeV [21] which is around T_c), and elastic scatterings changing the kinematics of the hadrons occur until the kinetic freeze-out. Then, the hadrons stop interacting, and they continue their trajectory until they leave signals in the surrounding detectors.

If the system is not energetic enough to form a QGP, then the out-of-equilibrium phase thermalizes and directly hadronizes into a hadron gas without going through the QGP phase or hydrodynamical expansion.

In the Bjorken scenario for heavy-ion collisions lie two assumptions:

- The crossing time is negligible compared to the QCD interaction time so that strong interactions can occur in the medium of participants left after the collision
- The distribution of final state particles should plateau at mid-rapidity. It is a symmetry of the system implying that the particle distribution typically seen in the centre-of-mass frame at mid-rapidity is independent of the chosen reference frame. This has for instance been verified at LHC [30], as shown in Figure 1.6.

In these Bjorken assumptions, we use the concept of rapidity. The rapidity y is a boost-invariant quantity used as an alternative to the polar coordinate θ or the z coordinate to define the trajectory of a particle.

$$y = \frac{1}{2} ln(\frac{E + p_z}{E - p_z}).$$

Often, pseudo-rapidity η is also used

$$\eta = \frac{1}{2} ln(\frac{p + p_z}{p - p_z}) = -ln(tan(\frac{\theta}{2})).$$

For massless particles or ultra-relativistic particles, pseudo-rapidity or rapidity can be used interchangeably. The second assumption we have highlighted then states that if we take our final state and cut slices along the longitudinal z-axis, slices around the interaction point (mid-rapidity) are equivalent.

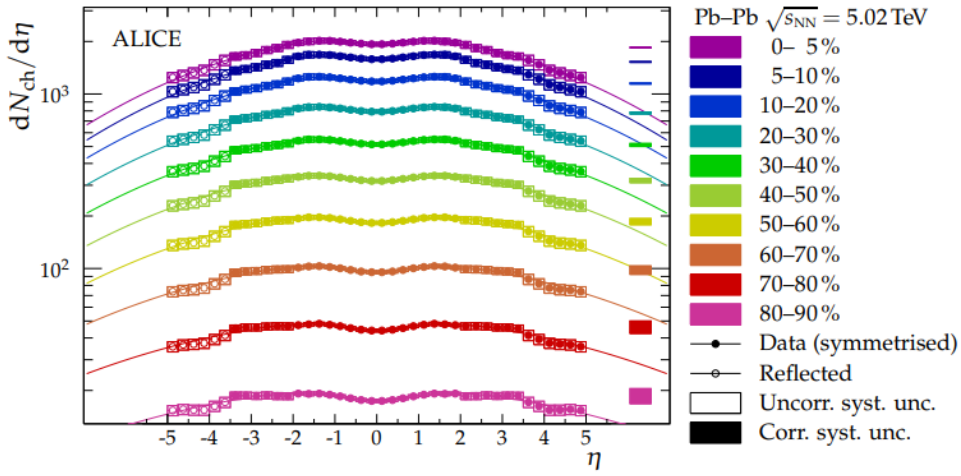

Figure 1.6: From Ref. [30], charged particle multiplicity density as a function of pseudo-rapidity in Pb–Pb collisions at 5.02 TeV, showing a stable plateau over a large pseudo-rapidity range for a variety of centrality classes.

1.3.3 Studying QGP properties

The QGP is short-lived, so we cannot hope to detect it directly. We can only detect particles produced during the collisions, like decay products. They are the remnants of the QGP phase or even earlier stages of the collision. Studying these probes is the key to understanding QGP formation and its evolution aspects. Many probes are used to study heavy-ion collisions, some directly linked to the study of the QGP. Different probes can provide insight into different steps of the collision as they are sensitive to different processes or produced at different times.

Global collision probes are dedicated to the search for general information concerning the collision. By studying the charged-particle multiplicity or the energy of the spectators, information concerning the initial energy density or the geometry of the collision (like the centrality and the impact parameter obtained by a Glauber fit as we have mentionned) can be accessed.

Soft probes are low-momentum probes that give us access to the hadronic phase and the freeze-out. They are typically light-flavour hadrons that are directly identified by ALICE detectors. As they are light, they constitute the bulk of the fireball. Hence, they can show collective behaviour and inform us about the thermodynamic evolution of the hadronic gas. For example, correlating hadrons gives us information regarding the spatial distribution of the light particles, and whether they exhibit collective effects like flow, which will be detailed in the following sections. Studying the yield (amount) of hadrons in Pb–Pb collisions compared to reference collisions in smaller systems (using the nuclear modification factor that we will also cover) allows us to detect effects on hadronic production due to, for example, QGP formation. QGP formation would also come with a restoration of chiral symmetry. It would allow strange and anti-strange quarks to be produced abundantly (as $T_c \approx m_s$), which would then lead to an over-production of strange hadrons, and in particular multi-strange hadrons, known as the strangeness enhancement [31, 32, 33]. Given that the abundances of hadrons are fixed at the chemical freeze-out, their measurement can give information concerning when the freeze-out happens as well as the corresponding baryonic chemical potential or temperature of the medium. Models like the statistical hadronization model allow to link the measured abundances to thermodynamic properties of the medium

[21]. Thermal photons and dileptons, emitted by the QGP, can also be studied as they are sensitive to the QGP thermodynamical properties as well.

Initial state probes are produced in initial hard collisions but do not have a colour charge, so they are not influenced by the strongly interacting medium. These probes like the Z^0, the $W^{\pm}$ or direct photons give an insight into the early times of the collision, before an eventual QGP formation. As such, they are a powerful tool to study the structure of the colliding nuclei and help constrain the parton distribution functions (PDF) that give information regarding the dynamics of individual partons within a hadron.

Hard probes are also produced in initial hard scatterings, but they are sensitive to the strongly interacting medium. They can be affected by the QGP, and the consequences on their production/dynamics can be studied and used to understand QGP better. For example, jets can lose energy in the medium and be "quenched". In heavy-ion collisions, heavy quarks are produced in pairs in early stage hard scatterings. They can hadronize as open heavy-flavour hadrons or as closed heavy-flavour mesons called quarkonia ($Q\bar{Q}$). They are particularly interesting because they probe the system from the early stages of the collision. In the same way as for soft probes, nuclear modification factors can be computed, and correlations made to see the influence of QGP on heavy-flavour production and interpret it using theory.

A complete description of the hadronic probes to study the QGP phase specifically can be found in Ref. [34] and a review on all probes of the QGP phase can be found in Ref. [35].

1.4 Quarkonium

In this thesis, we focus on quarkonia to study the QGP. The interest of quarkonia states is that they are only produced at the early stages of the collision, before the QGP is formed, due to the hard scale involved. They are colour neutral, however, their constituents are colour charged, meaning they can interact with the strongly interacting deconfined medium and be influenced by it, especially as it takes time from pair creation to colour neutralization. Moreover, their lifetimes are long enough to let them decay after the freeze-out. These reasons make them a probe of choice in the study of the QGP. In this section, we will go through the whole zoology of quarkonia. We will then focus on the charmonia to expose the main principles of quarkonium formation and their evolution in the QGP or nuclear matter in general.

1.4.1 Zoology

A quarkonium state is created when a $Q\bar{Q}$ pair, from either charm ($m_c = 1.27$ GeV/c^2), bottom ($m_b = 4.2$ GeV/c^2) or top ($m_t \approx 170$ GeV/c^2) [36] families, is formed and evolves into a bound state. The pair formation time is typically given by $1/2m_Q$, which is of the order of 0.1 fm/c for charm and bottom quarks, and the bound state formation time is of order 1 fm/c [37]. Given that the $c\bar{c}$ and $b\bar{b}$ formation times are much shorter than the lifetimes of the corresponding bound states, charm and bottom quarks can form quarkonia states. On the other hand, the lifetime of the top quark is of order 10^{-25} s, and therefore it will decay before it could have formed a $t\bar{t}$ pair, let alone a bound state.
The Cornell potential [38, 39, 40] describes the potential of the quarkonia state:

$$V(r) = -\frac{\alpha}{r} + \sigma r. \tag{1.3}$$

In Equation 1.3, r is the distance between the heavy quarks, and we see that the potential is made of two parts:

- The Coulombian part ($-\frac{\alpha}{r}$) describes the potential at low radius, analogous to electromagnetism.
- The confinement part (σr) describes the potential at large r as coming from a rope of tension σ. It describes the confinement process. If we try to extend the pair, more energy is stored within the gluon flux tubes, and when there is enough energy, the pair can break, forming a new pair along the way, as seen in Figure 1.7.

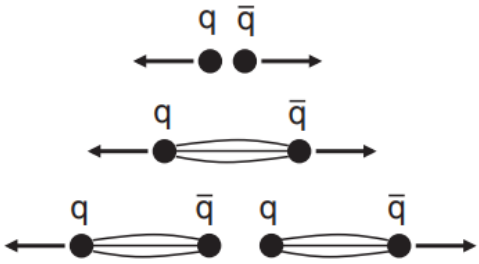

Figure 1.7: From Ref. [15], representation of the stretching of a $q\bar{q}$ pair and the consequence of confinement.

However, from this simple potential of a $Q\bar{Q}$ state, many bound states can emerge. We can see the whole charmonium and bottomonium families in Figures 1.8 and 1.9, respectively.

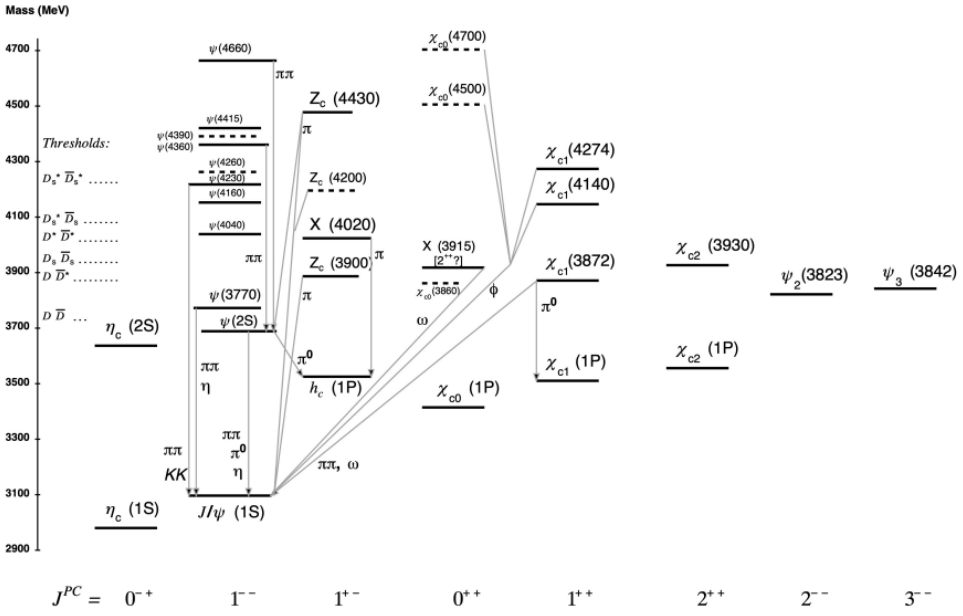

Figure 1.8: From Ref. [36], representation of the current picture of the charmonium family, states are arranged by their quantum numbers.

We see that, in order to be stable, the charmonium mass must be below a $2m_D$ threshold. Moreover, many bound states decay into the stable J/ψ, making it a probe of choice for our studies. These types of decay from charmonium excited states constitute (with the "direct" J/ψ itself) the prompt J/ψ production. However, long-lived beauty hadrons can also decay into a J/ψ. Given their long lifetimes, they live through the QGP phase, such that the properties of the final charmonia are influenced only indirectly. In addition, their decay vertex is displaced with respect to the interaction point, and can thus be detected if the vertex position can be experimentally measured with enough accuracy. Decay from beauty hadrons constitutes the non-prompt J/ψ production, which usually constitutes a background when studying the effects of QGP on the charm. As of Run 2, as we will discuss in Chapter 3, ALICE cannot distinguish prompt from non-prompt at forward rapidity. We then speak of inclusive production.

Experimentally, quarkonia are reconstructed from their decay products. For instance, the excited $\psi(2S)$ state can decay into a lepton pair but will mostly decay into other hadrons, namely the J/ψ, which in turn can decay into dileptons (electrons or muons) with a probability of around 6% each, producing a clean signal in the detectors. Going further than the experimental signal properties, let us

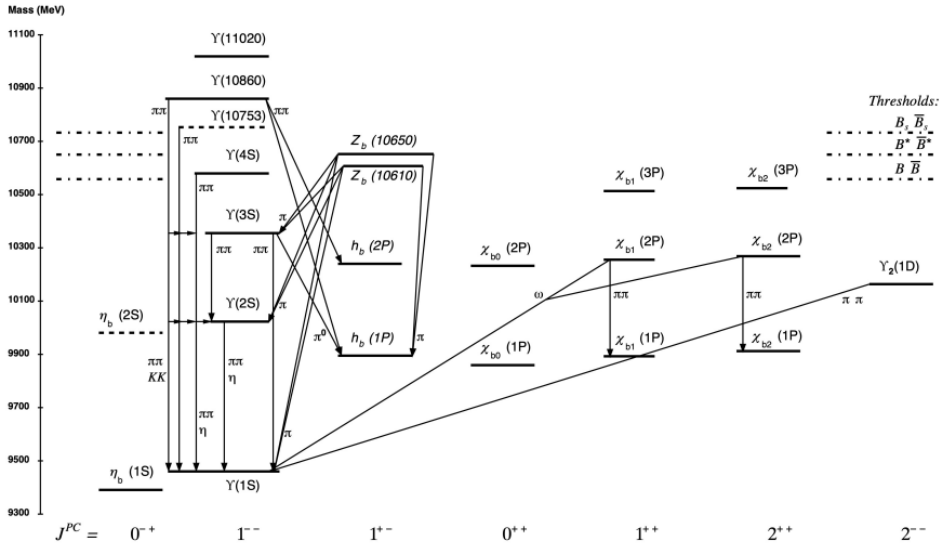

Figure 1.9: From Ref. [36], representation of the current picture of the bottomonium family, states are arranged by their quantum numbers.

justify the study of the QGP using the J/ψ and $\psi(2S)$ by computing their respective lifetimes. Ref. [36] gives the widths Γ of the J/ψ and $\psi(2S)$ at 92.6 keV and 294 keV respectively. As the lifetime of a particle is equal to $1/\Gamma$, we can compute $\tau_{life,J/\psi} \approx 2000$ fm/c and $\tau_{life,\psi(2S)} \approx 600$ fm/c. The lifetimes of the quarkonia are much longer than the lifetime of the QGP (of order 10 fm/c), which justifies the use of quarkonia as QGP probes, as quarkonia can live through the whole evolution of the QGP before decaying.

As we see from the charmonium and bottomonium families diagrams, from a given $Q\bar{Q}$ pair, many bound states are accessible. A distinction must be made between quark-pair formation and quarkonium state formation. We will now discuss the production mechanisms of both by focusing on the case of the charmonium.

1.4.2 Formation mechanisms

The creation of a $Q\bar{Q}$ pair requires an amount of energy above $2m_Q$. For charm quarks, $2m_c \gg \Lambda_{QCD}$ so this process can be treated using perturbative QCD techniques. As an approximation, quark pairs are created through Leading Order (LO) processes of quark or gluon fusion, shown in Figure 1.10.

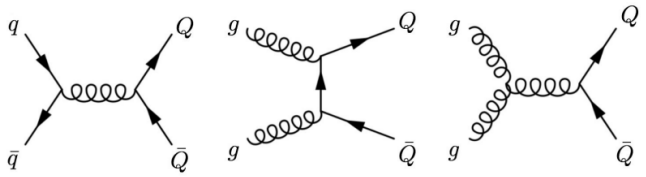

Figure 1.10: Leading Order (LO) Feynman diagrams of heavy quark-antiquark pair production.

However, the formation of a charmonium bound state from this pair is more complex. The reason is that the energy scale involved for the bonding is of order $m_Q \times v$. However, because of the high mass of the heavy quarks, their velocity v in the rest frame of the pair is small, which is why we are allowed to use a non-relativistic treatment of the quarkonium potential, for example. The perturbative theory cannot be applied here, and lattice QCD is needed to estimate the production of such bound states.

When a pair is created, it has a colour state that is either coloured (there are eight states, an octet) or colour-neutral (only one state, a singlet). Charmonia are colour-neutral, so the coloured states need

to lose their colour. There are various theories to model this process, and all are exposed with the experimental viewpoint in the extensive review in Ref. [41].

Colour Evaporation Model (CEM)

The idea of this model [42, 43, 44] is that many soft gluons can be emitted from the $Q\bar{Q}$ pair to make the octet states lose their colour and completely decorrelate the colour quantum state of the initial pair and the final bound state. The quarkonium state production cross section is directly linked to the heavy-quark pair production cross section in the invariant mass region from $2m_Q$, the low limit for pair production, to $2m_H$, with H being the lightest open heavy-flavour hadron. Formally,

$$\sigma_{\mathscr{Q}} = \mathscr{P}_{\mathscr{Q}} \int_{2m_Q}^{2m_H} \frac{d\sigma_{Q\bar{Q}}}{dm_{Q\bar{Q}}} dm_{Q\bar{Q}},$$

where $\mathscr{P}_{\mathscr{Q}}$ is the probability that a quark pair binds into the state $\mathscr{Q}$. As the quantum state is randomly chosen because of the radiated soft gluons, $\mathscr{P}_{\mathscr{Q}}$ has a factor $\frac{2J_{\mathscr{Q}}+1}{\sum_{i\ states} 2J_{i+1}}$, which is the probability to randomly select a quantum state associated to $\mathscr{Q}$ over all the accessible ones (the states between $2m_Q$ and $2m_H$). There is also a factor $\frac{1}{9}$ because the randomly chosen colour state must be the colour singlet which is colour-neutral.

Finally, we obtain

$$\sigma_{\mathscr{Q}} = \frac{1}{9} \frac{2J_{\mathscr{Q}}+1}{\sum_{i\ states} 2J_{i+1}} \int_{2m_Q}^{2m_H} \frac{d\sigma_{Q\bar{Q}}}{dm_{Q\bar{Q}}} dm_{Q\bar{Q}}.$$

Color Singlet Model (CSM)

The CSM [45] can be seen as the opposite of the CEM. In this model, the quantum state of the pair is fixed until it hadronizes [46]. Gluon emissions are suppressed by a factor α_S. So, the production cross section of a bound state $\mathscr{Q}$ is the production of a pair with no relative velocity between its components, in a colour-neutral state, with the same spin and angular momentum as the final $\mathscr{Q}$, times the probability of hadronization (the squared Schrodinger wave function estimated in position 0, noted $R(0)$). As we produce the heavy quarks in heavy-ion collisions, we must also consider the parton densities from PDFs f_i and f_j. This yields,

$$\sigma_{\mathscr{Q}} = \sum_{i,j} \int f_i(x_i, \mu_a) dx_i f_j(x_j, \mu_b) dx_j d\sigma_{i,j\to Q\bar{Q}}(\mu_a, \mu_b) |R(0)|^2.$$

Color Octet (CO) based on Non-relativistic QCD (NRQCD)

In NRQCD [47], the relative velocity of the paired quarks is taken into account. In addition to the usual expansion in powers of α_S, there is also an expansion in powers of v [48]. In this framework, the hadronization process is expressed through Long Distance Matrix Elements (LMDEs), which link quantum states together and allow transitions between them. In practice, it means that through soft gluon emissions, a color octet can transition into a color singlet and that a direct transition from a coloured state to $\mathscr{Q}$ is possible. This approach is an extension of the CSM, as CO to leading order in v is the CSM itself. Hence, $\sigma_{\mathscr{Q}}$ has a similar expression,

$$\sigma_{\mathscr{Q}} = \sum_{i,j,n} \int f_i(x_i, \mu_a) dx_i f_j(x_j, \mu_b) dx_j d\sigma_{i,j\to Q\bar{Q}}(\mu_a, \mu_b) \langle \mathscr{O}^n_{\mathscr{Q}} \rangle,$$

where $\langle \mathscr{O}^n_{\mathscr{Q}} \rangle$ comes from the LMDEs and models the probability that a $Q\bar{Q}$ pair with quantum numbers n hadronizes into $\mathscr{Q}$.

1.4.3 Evolution in the QGP

We have repeatedly stated that quarkonia are powerful probes of the QGP because the strongly interacting medium influences them. We will now discuss how quarkonia evolve following the collision.

Colour screening and sequential suppression

When other charges surround electric charges, the true charge is screened. When $q\bar{q}$ pairs fluctuate, they screen the true colour charge in QCD, leading to the running of α_S. Similarly, one should expect that in the QGP phase, the freely-moving colour charges in the medium screen the $Q\bar{Q}$ pair, as represented in Figure 1.11. If we go back to the Cornell potential of a quarkonium in Equation 1.3, assume that $\sigma = 0$ as colour charges are deconfined, and add a screening effect analogous to Debye screening in electromagnetism, we have

$$V(r) = -\frac{\alpha}{r} e^{-\frac{r}{r_D}}, \tag{1.4}$$

with r_D the Debye screening radius [49], equal to the average distance between colour charges in the QGP, which is inversely proportional to the temperature of the medium. Indeed, as detailled in Ref. [22], in plasma physics, $r_D \propto \sqrt{\frac{T}{\rho}}$. In the QGP, ρ is proportional to T^3 which leads to $r_D \propto \frac{1}{T}$.

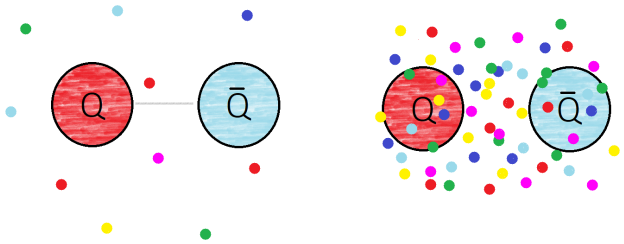

Figure 1.11: Schematic representation of a $Q\bar{Q}$ pair surrounded by light coloured quarks. On the left, the colour density is low, the pair is not screened. On the right, the colour density is high, the pair melts.

This screening effect means that a given critical melting temperature exists at which, without any additional external energy, the heavy quark pair cannot be considered a pair anymore. There is no hadronization into a bound state possible, the heavy quarks are separated, and the pair melts. This process was the first impulsion towards the study of the J/ψ [50]. A direct consequence of the screening effect is sequential melting [51, 52]. It is the idea that, considering that different bound states have different radii (from Ref. [53], J/ψ has a radius of 0.5 fm and $\psi(2S)$ has a radius of 0.9 fm), every bound state has its own melting point ($2.10\ T_c$ for J/ψ and $1.12\ T_c$ for $\psi(2S)$). When we gradually increase the temperature, more loosely bound states will melt first, as represented in Figure 1.12. By studying the multiplicity of different bound states in the final state of a collision, we can determine which quarkonium states have melted and which have "survived" the QGP. This is a powerful signature of QGP formation and an indicator of the temperature of the QGP using this "quarkonia thermometer". This is a static interpretation of the thermometer, and it is not the most accurate picture as heavy-ion collisions are dynamic systems. Hence, dynamic interpretations of the suppression have been developed [54, 55], where the melting of bound states depends on both interactions with the medium and the time spent in the medium.

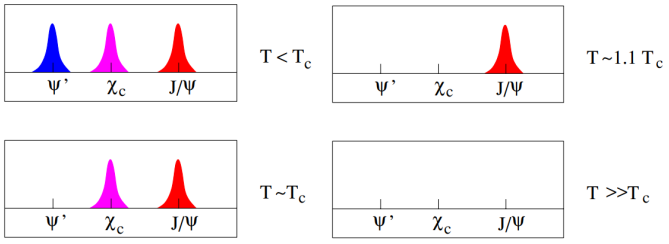

Figure 1.12: From Ref. [56], schematic representation of the gradual melting of charmonia states as the temperature of the medium increases.

Regeneration

Regeneration (also called recombination) is the opposite effect of screening. Although heavy flavours are created at the early stage of the collision, as they evolve in the QGP, a $Q\bar{Q}$ pair can still form if two heavy quarks from different initial hard scatterings (re)bind together. This recombination process can happen at the phase boundary, as assumed in statistical models [57] (see Figure 1.13), or it can be in dynamical interplay with dissociation during the QGP evolution [58]. For the J/ψ, the number of initial $c\bar{c}$ pairs $N_{c\bar{c}}$ scales as the number of binary collisions N_{coll}, while the number of produced light hadrons N_h scales as the number of participant partons N_{part}. The number of regenerated J/ψ scales as $\frac{N_{c\bar{c}}^2}{N_h}$, so, as the energy of the collision increases, the amount of regenerated J/ψ is predicted to increase as well. In practice, regeneration of the J/ψ is expected at LHC energies, which was not the case at RHIC where $N_{c\bar{c}}$ is small due to the lower energies, as we will discuss in the next section concerning observables. In addition, regeneration will be prevalent at low transverse momentum p_{T} (below 3 GeV/c). It can be seen as a consequence of the need for the heavy quarks to travel close to one another to be able to form a bound state. Finally, as $\sigma_{c\bar{c}}$ is expected to diminish with increasing rapidity, we expect the amount of regenerated J/ψ to follow the same trend. The verification of these statements by experiment will be presented in the next section.

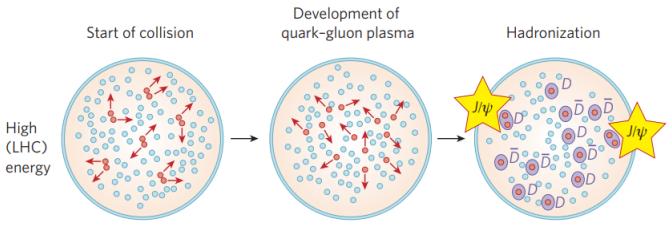

Figure 1.13: From Ref. [59], schematic representation of the evolution of hot matter and heavy quarks in energetic heavy-ion collisions and the regeneration of charmonia.

Cold Nuclear Matter (CNM) effects

The initial nucleus can affect the quarkonia via Cold Nuclear Matter (CNM) effects, even without QGP formation. The review in Ref. [60] covers them in detail, as well as QGP effects, theories and their experimental testing.

Modification of nuclear parton distribution functions

In a free proton, parton distribution functions (PDFs) $f_i(x, Q^2)$ describe the fraction of longitudinal momentum x carried by a parton of flavour i in a process with momentum transfer Q^2. For example, in a photon-hadron scattering where a incoming photon interacts with a parton, x is defined as $\frac{Q^2}{2pq}$, where p and q are the quadrivectors of the incoming hadron and photon respectively.

However, this description is different for partons within nuclei with $A > 1$. Nuclear parton distribution functions (nPDFs) $f_i^A(x, Q^2)$ are then used, as the behaviour of a given parton is impacted by the higher partonic density from within surrounding nucleons [61].

Typically, for x below 0.01, the nuclear overlap incites partons to rearrange, and the nPDFs are suppressed compared to PDFs. This effect is called "nuclear shadowing". Unlike a screening effect, here the main physical process behind the shadowing effect is multiple scatterings [62] on the vast number of partons. As shown on Figure 1.14, this number diverges at very low x and leads to gluon saturation, which can also be explained within the CGC framework and studied through quarkonium production [63]. For other ranges of x, the effects on nPDFs change. For example, between 0.01 and 0.1, there is an enhancement of the nPDFs called anti-shadowing, and above 0.1 there is a new suppression region due to the EMC effect [64].

Multiple scatterings of partons

As $Q\bar{Q}$ pairs evolve in cold nuclear matter, they will scatter on the surrounding partons. There are multiple proposals of effects that could occur due to these scatterings. The rescattering of the colour

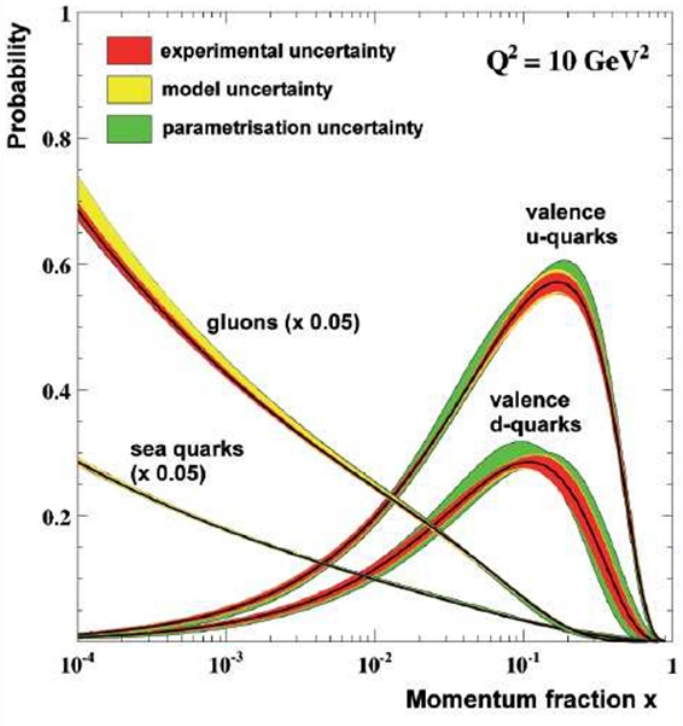

Figure 1.14: From Ref. [65], probability distribution of quarks and gluons in the proton as a function of x. Sea gluons dominate the proton content at low x.

dipole could be a source of quarkonia suppression [66], as coherent energy loss could occur, for example, via the radiation of soft gluons by interaction with the medium [67]. As the partons scatter, their transverse momentum is modified, and one could expect a broadening of the quarkonia $\langle p_{\mathrm{T}} \rangle$ spectra known as the Cronin effect [68].

Final state nuclear interaction

When scattering on nuclei, quark pairs can dissociate. They are said to be absorbed. The absorption cross section σ_{abs} is based on an effective theory [66] following which the probability for a pair not to be absorbed after crossing a length L of a medium of nuclear density ρ is $P_{survival} \propto e^{-\rho\sigma_{abs}L}$. This process can also occur with the particles travelling around the quark pair, the comovers [69, 70].

Coherent J/ψ photoproduction

In p–Pb collisions (as well as in Pb–Pb collisions), the electrically charged Pb nuclei can spontaneously emit photons which can scatter off the proton. The inverse is also true but, due to the higher charge of the Pb nuclei, 95% of the photon production is assured by the Pb. As a photon is emitted, it can fluctuate into a quark-antiquark pair which can produce a J/ψ via gluon exchange with the proton, as seen in Figure 1.15.
This mechanism is particularly relevant in ultra-peripheral collisions [72] where there is no hard scatterings of the nuclei, but also in collisions with a non-negligible but small nuclear overlap [73].

These cold nuclear matter effects are typically studied using p–Pb collisions, where no QGP formation is expected.

1.5 Powerful quarkonium observables

As we have discussed, quarkonia are impacted by both cold and hot nuclear matter in a variety of ways. Each effect is described by models which must be put to the test by comparing them to data. This

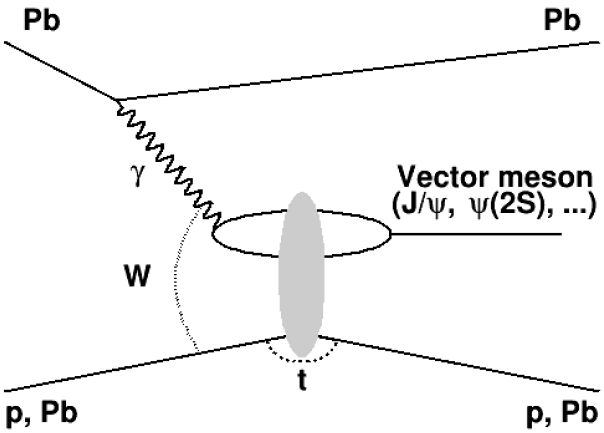

Figure 1.15: From Ref. [71], Feynman diagram of the vector meson photoproduction in Pb–p and Pb–Pb collisions.

section presents essential observables that concern quarkonia in heavy-ion collisions, some experimental results, and how they relate to the existing models.

1.5.1 Nuclear modification factor

The nuclear modification factor is an observable dedicated to assessing the effects of cold and hot nuclear matter on particle production. Formally it is defined as:

$$R_{AA} = \frac{\frac{d^2 N_{AA}}{dy dp_{\mathrm{T}}}}{\langle T_{AA} \rangle \frac{d^2 \sigma_{pp}}{dy dp_{\mathrm{T}}}} \tag{1.5}$$

where $\langle T_{AA} \rangle$ is the nuclear overlap function which is proportional to $\langle N_{coll} \rangle$. Essentially, R_{AA} is the ratio between the yield of a particle in A–A collisions over the expected yield from pp collisions scaled to account for the higher number of binary collisions. If it is above unity, it indicates an overall production enhancement from cold or hot nuclear matter effects. If it is below unity, it indicates a suppression. In order to assess cold nuclear matter (CNM) effects specifically, R_{pA} can also be computed from p–A collisions.

Hints of regeneration In Figure 1.16, we can see the nuclear modification factor for inclusive J/ψ as a function of the average number of participants in Au–Au collisions from PHENIX at RHIC and more energetic Pb–Pb collisions from ALICE at the LHC. For PHENIX data, we observe that with increasing number of participants (N_{part}) (so as collisions get more central), the J/ψ is more suppressed, which is expected from screening effects. However, in more energetic collisions with ALICE, the suppression is less prevalent even if this same suppression trend is seen. This is in line with the regeneration scenario as more energetic collisions produce more $c\bar{c}$ pairs which will favour charmonium regeneration and compensate for the in-medium melting. Indeed, if there was no regeneration and only suppression mechanisms were involved, one would expect a lower nuclear modification factor at LHC than at RHIC due to the larger temperature of the QGP.

If we focus on the more energetic Pb–Pb collisions at 5.02 TeV from ALICE, we see in Figures 1.17 and 1.18 the behaviour of the nuclear modification factor of inclusive J/ψ as a function of $\langle N_{part} \rangle$ and p_{T} at mid-rapidity, in the dielectron decay channel, and forward-rapidity, in the dimuon decay channel. This allows a thorough comparison with models. Concerning the multiplicity dependence, it is well described by all models implementing recombination, be it at the phase boundary for the statistical hadronization model [75] or during the expansion of the QGP as described in transport [76, 77, 78] and comovers [70, 79] models, and on both rapidity ranges. Concerning the p_{T} dependence, we observe less suppression at low-p_{T}, below 3 GeV/c, than at high-p_{T} as it is where regeneration is expected to be prevalent. These observations on both rapidity ranges agree with the transport model and the statistical

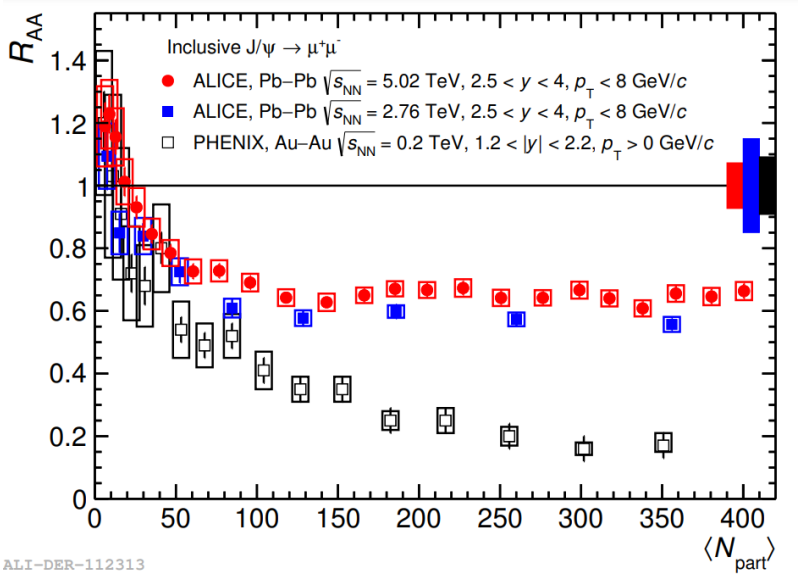

Figure 1.16: From Ref. [74], nuclear modification factor for inclusive J/ψ from ALICE and PHENIX measurements in A–A collisions.

hadronization model (although at p_T higher than 3 GeV/c the latter predicts more suppression than is actually measured).

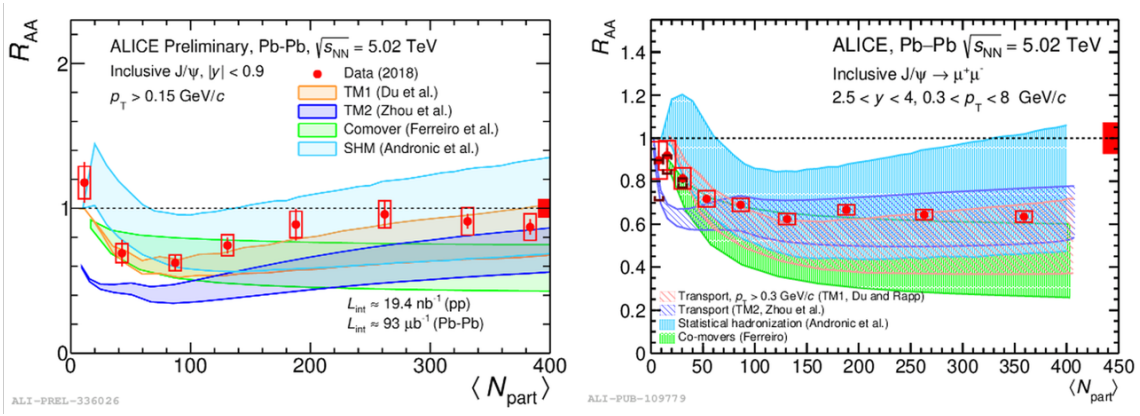

Figure 1.17: Nuclear modification factor for inclusive J/ψ from ALICE as a function of the number of participants, at mid and forward-rapidity in Pb–Pb collisions at $\sqrt{s_{\rm NN}} = 5.02$ TeV.

At mid-rapidity, vertexing abilities allow distinguishing J/ψ contribution from prompt (direct or excited state feed-down) and non-prompt (beauty feed-down). In Figure 1.19 the nuclear modification factor of prompt J/ψ at mid-rapidity in Pb–Pb collisions at 5.02 TeV for different centralities is another smoking gun of regeneration. The more the collision is central, the more regeneration is expected. At low-p_T, we do see an enhancement of the prompt J/ψ yield with collisions becoming more central, in line with the regeneration scenario.

Sequential melting By studying the suppression of different quarkonium states, one can see if excited states that are more loosely bound than ground states would be more suppressed. In Figure 1.20, the R_{AA} of inclusive J/ψ and $\psi(2S)$ measured by ALICE and CMS is presented as a function of p_T at forward rapidity in Pb–Pb collisions at 5.02 TeV.

In addition to the agreement between ALICE and CMS results, one can see that the $\psi(2S)$ is more suppressed than the J/ψ and even shows hints of regeneration. Recently, both ATLAS [82] and CMS [83] looked into the sequential suppression of the bottomonia $\Upsilon(nS)$ states, where the impact of

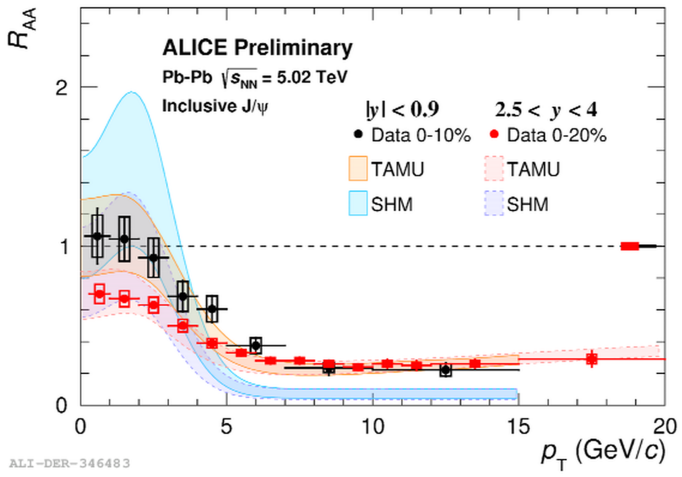

Figure 1.18: Nuclear modification factor for inclusive J/ψ from ALICE as a function of transverse momentum, at mid and forward-rapidity in Pb–Pb collisions at $\sqrt{s_{\rm NN}} = 5.02$ TeV.

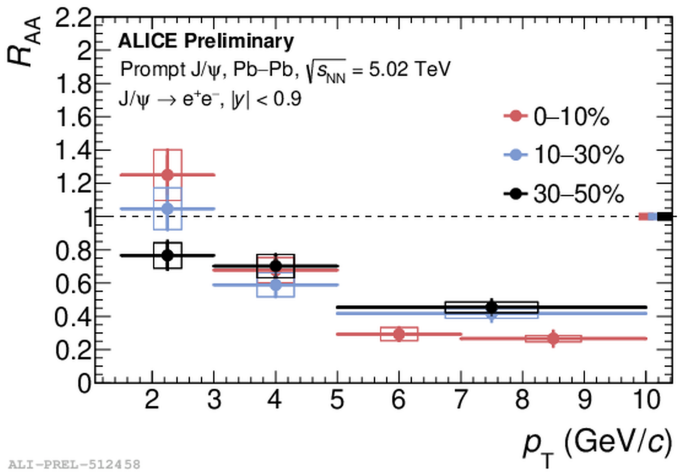

Figure 1.19: Nuclear modification factor for prompt J/ψ from ALICE as a function of transverse momentum, at mid-rapidity for various centrality classes in Pb–Pb collisions at $\sqrt{s_{\rm NN}} = 5.02$ TeV.

recombination is weaker as less $b\bar{b}$ are produced compared to $c\bar{c}$. The results concerining the nuclear modification factor of bottomonia are presented in Figure 1.21.

We observe a clear hierarchy of the nuclear modification factors of the $\Upsilon(nS)$ states which is expected from the sequential melting process. Similar effects are seen at forward rapidity by ALICE [84].

J/ψ photoproduction ALICE [73] has measured the J/ψ nuclear modification factor in peripheral Pb–Pb collisions at very low $p_{\rm T}$. As seen in Figure 1.22, the J/ψ is enhanced, especially in very low $p_{\rm T}$ and very peripheral collisions, by up to a factor 10. The explanation currently lies in the photoproduction of the J/ψ which would become the prevalent formation mechanism at this very-low $p_{\rm T}$. This is validated by the fact that photoproduction models using photon and pomeron fluxes adapted from ultra-peripheral collisions [85, 86, 87, 88] are in good agreement with the observations, at least until the collisions become less peripheral [73].

1.5.2 Polarization

Polarization is the observable linked to the alignment between the spin of a particle and a given axis. For quarkonia, it has been shown [89] that the angular distribution of the decay dileptons in the quarkonia

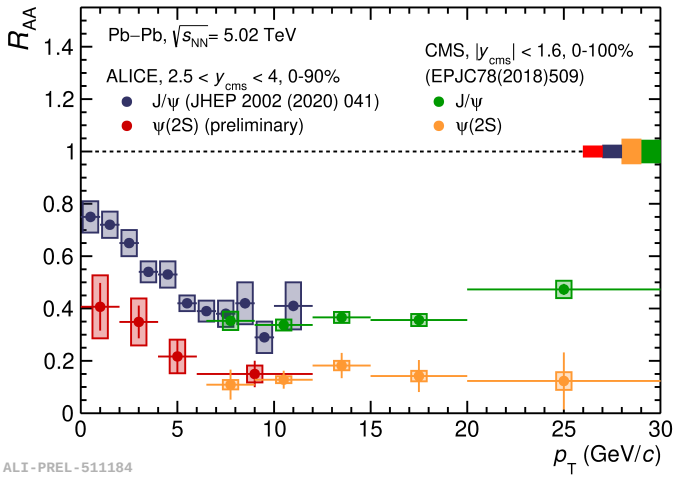

Figure 1.20: Nuclear modification factor for J/ψ and $\psi(2S)$ from ALICE [80] (inclusive) and CMS [81] (prompt) as a function of transverse momentum in Pb–Pb collisions at $\sqrt{s_{\mathrm{NN}}} = 5.02$ TeV.

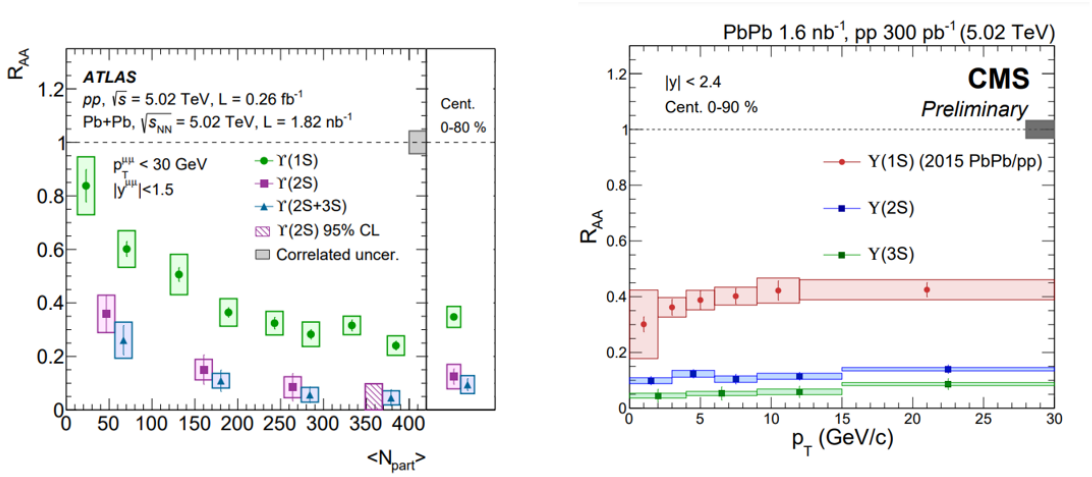

Figure 1.21: Nuclear modification factor for $\Upsilon(nS)$ states measured by ATLAS [82] and CMS [83] in Pb–Pb collisions at $\sqrt{s_{\mathrm{NN}}} = 5.02$ TeV.

rest frame, and relative to the production plane, can be expressed as in the following equation:

$$W(cos\theta, \phi) \propto \frac{1}{3+\lambda_\theta}(1 + \lambda_\theta cos^2\theta + \lambda_\phi sin^2\theta cos2\phi + \lambda_{\theta\phi} sin2\theta cos\phi). \tag{1.6}$$

In the above expression, $(\lambda_\theta, \lambda_\phi, \lambda_{\theta\phi})$ is a triplet of polarization parameters, with the angles θ and ϕ defined in Figure 1.23. At $(0,0,0)$ the quarkonium is unpolarized, at $(+1,0,0)$ it is purely transversely polarized, and at $(-1,0,0)$ it is purely longitudinally polarized.

Studying the quarkonium polarization in pp allows us to test predictions from production models. In the helicity frame (where we look at the spin alignment with the quarkonium trajectory), NRQCD predicts transverse polarization, while CSM predicts longitudinal polarization [90]. Measurement of quarkonia at different energies have been made by the LHC experiments [91, 92, 93, 94, 95, 96]. All find results compatible with no polarization for the quarkonia in pp, which leaves open the question of the production mechanism, as shown in Figure 1.24.

The pp measurements are crucial as they serve as a baseline for Pb–Pb collisions, where feed-down to J/ψ is expected to change due to suppression in the QGP. Regeneration will also play a role, and the large magnetic field and initial angular momentum in semi-central collisions will impact quarkonium polarization. A measurement of the J/ψ polarization in Pb–Pb has been carried out by ALICE [97]

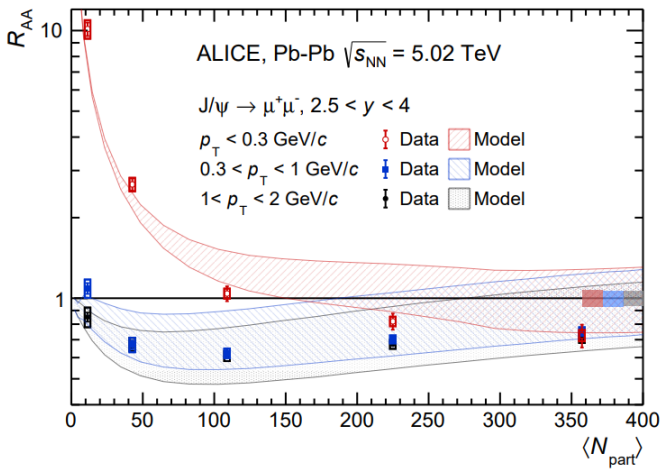

Figure 1.22: From Ref. [73], nuclear modification factor for inclusive J/ψ in peripheral Pb–Pb collisions at $\sqrt{s_{\mathrm{NN}}} = 5.02$ TeV.

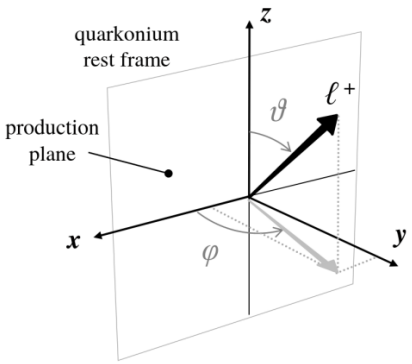

Figure 1.23: Definition of the θ and ϕ angles used in polarization parameters definition.

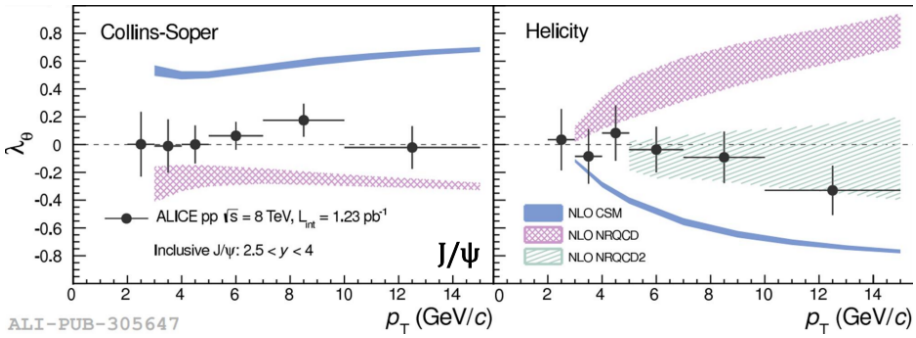

Figure 1.24: From Ref. [92], measurement of the λ_θ parameter for the polarization on inclusive J/ψ as a function of transverse momentum in different frames in pp collisions at $\sqrt{s} = 8$ TeV.

showing a small but significant transverse polarization in semi-central collisions at low-p_{T}. Although light hadrons were also measured [98] to be polarized in semi-central Pb–Pb collisions, their polarization was stronger and longitudinal, indicating potential differences in production mechanisms that could be flavour-dependent.

1.5.3 Elliptic flow

Elliptic flow is an observable related to collective effects. We will thoroughly review related results in the next chapter. However, we will now give a short introduction to its usefulness. When heavy nuclei collide, the collision is not necessarily head-on: there is a non-zero impact parameter b (which is linked to centrality). By using Bjorken's assumptions, we can disregard the longitudinal dimension (along the beam pipe). If, in the transverse plane, we imagine the colliding nuclei as disks, the collision region is almond-shaped. It is anisotropic, as represented in Figure 1.25. However, if QGP is formed, it will hydrodynamically expand in all directions and, like a perfect fluid, will try to form a circle. To go from this initial anisotropic geometry to a circular shape, strong pressure gradients will generate strong forces on particles within the event plane, defined as the plane generated by the impact parameter and the beam line. In contrast, small forces will apply to particles perpendicular to the event plane. This angular anisotropy of forces will translate into an angular anisotropy of the momenta of the particles and their decay products.

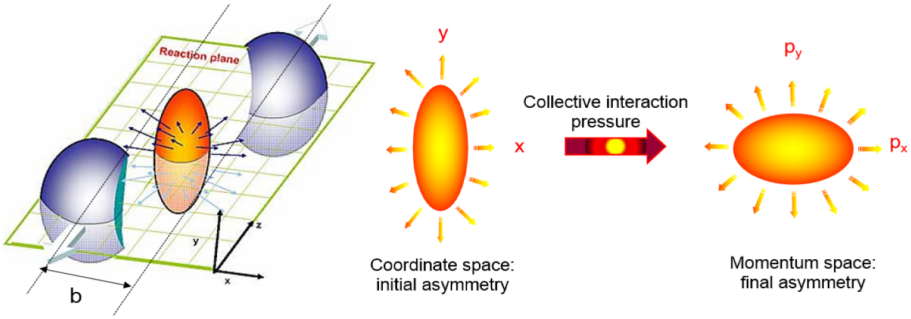

Figure 1.25: From Ref. [99], representation of a heavy-ion collision illustrating geometrical origins of flow.

If there is enough particle multiplicity to define an event plane and its angle Ψ_n, one can write the angular distribution of final state particles as:

$$\frac{dN}{d\phi} = \langle\frac{dN}{d\phi}\rangle(1 + \sum_n 2v_n cos(n(\phi - \Psi_n))). \tag{1.7}$$

If however, as is the case in smaller systems like p–Pb or pp, the particle multiplicity does not allow to precisely define an event plane, particle correlations can be measured by pairing particles together and studying the angular distribution of the pairs, which writes:

$$\frac{dN_{pairs}}{d\Delta\phi} = \langle\frac{dN_{pairs}}{d\Delta\phi}\rangle(1 + \sum_n 2v_n^2 cos(n\Delta\phi)). \tag{1.8}$$

By measuring the angular distribution of particles or pairs of particles, one can obtain the flow coefficients v_n. v_2 is the elliptic flow and the more the distribution is elliptic, the greater the v_2, which is linked to the anisotropic geometry of the collision. v_3 is the triangular flow and is linked to the initial state energy fluctuation between events. Non-zero flow coefficients are a signature of QGP formation as they prove that the final-state particle distribution is anisotropic. Such anisotropies could be caused by the anisotropic expansion of the QGP fireball. The values of the flow coefficients help constrain theoretical models that try to predict them.

QGP has a strong influence on the flow of quarkonia. Hot nuclear matter effects like the recombination of thermalized heavy quarks into a bound state allows them to pass their flow to the quarkonium as they coalesce. Depending on when this recombination happens, the amount of transferred flow will be different, which could distinguish transport models and comovers, where recombination and suppression are competing as the medium expands, and the statistical hadronization model where the recombination happens at the phase boundary, which would increase the flow. As recombination is prevalent at low p_{T} under 3 GeV/c, this is where an increase of the flow is expected. At higher p_{T} as recombination becomes less prevalent, flow is expected to decrease although remaining non-zero, thanks to primordial quarkonium contribution. Primordial quarkonium is a bound state that has not melted in the QGP,

which happens at high-p_{T} as the bound state can escape the expanding QGP quicker. In this case, the flow is explained by the path-length angular dependence. Quarkonia going along the reaction plane will cross less QGP than quarkonia produced out-of-plane and will be less suppressed, leading to flow-like angular dependency.

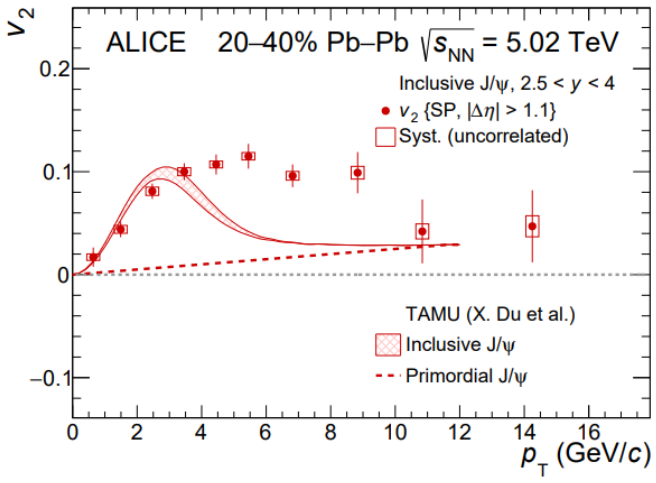

Figure 1.26: From Ref. [100], elliptic flow of inclusive J/ψ produced at forward-rapidity in Pb–Pb collisions at $\sqrt{s_{\mathrm{NN}}} = 5.02$ TeV, measured as a function of transverse momentum.

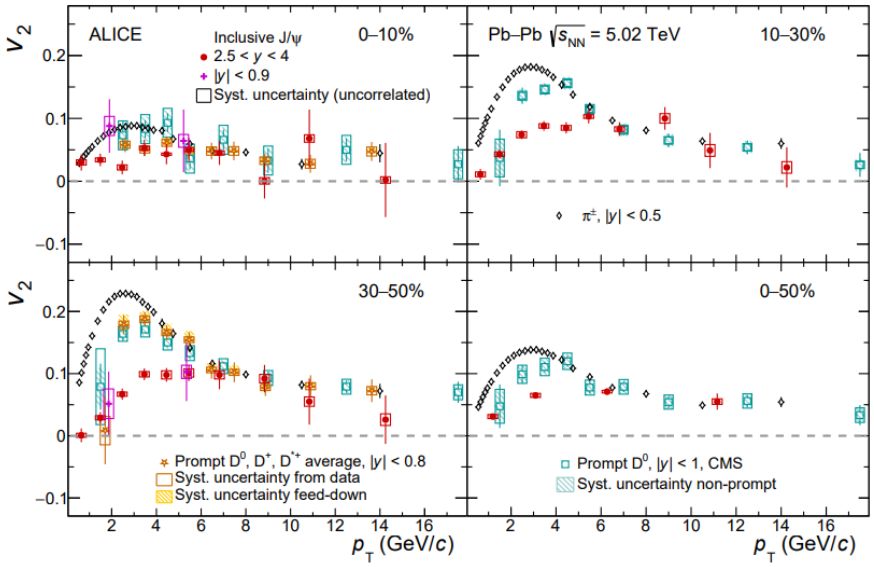

Figure 1.27: From Ref. [100], elliptic flow of various hadrons as a function of transverse momentum for different centrality classes in Pb–Pb collisions at $\sqrt{s_{\mathrm{NN}}} = 5.02$ TeV.

Measurement of the J/ψ flow by ALICE [100] as shown in Figure 1.26 displays a non-zero elliptic flow over a large p_{T} range. Its behaviour is compatible with expectations from recombination effects. Moreover, a different parametrization of the transport model, discussed in Ref. [101], allows for a far better agreement between data and theory. As we can already notice and will further develop in the following chapter, comparisons with other species like light hadrons and open-charm, presented in Figure 1.27, show a mass hierarchy which is compatible with hydrodynamics. Their common asymptote at high p_{T} could suggest a common origin of the flow. The similar overall magnitude of the flow across the different species is compatible with charm quark thermalization in the QGP. In that same contribution, higher harmonics like the triangular flow were studied, as presented in Figure 1.28, and they display

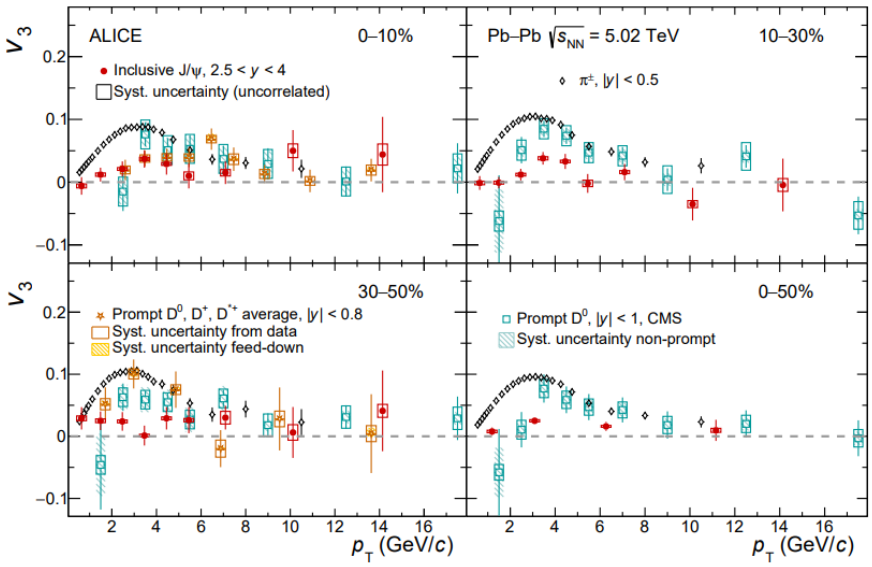

Figure 1.28: From Ref. [100], triangular flow of various hadrons as a function of transverse momentum for different centrality classes in Pb–Pb collisions at $\sqrt{s_{\rm NN}} = 5.02$ TeV.

a positive v_3 at mid-$p_{\rm T}$ which is significant and is compatible with the idea that charm quarks are sensitive to the initial fluctuations probed by v_3.

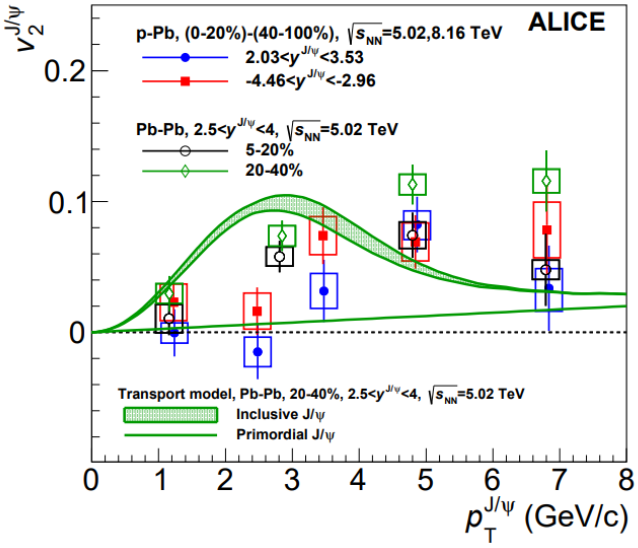

Figure 1.29: From Ref. [102], elliptic flow of inclusive J/ψ as a function of transverse momentum at forward-rapidity in Pb–Pb collisions at $\sqrt{s_{\rm NN}} = 5.02$ TeV and p–Pb collisions at $\sqrt{s_{\rm NN}} = 5.02$ and 8.16 TeV.

However, prompted by flow measurements in smaller systems like p-Pb and pp that displayed a positive flow for light particles [103, 104, 105, 106, 107] and charmed hadrons [108], the elliptic flow of the J/ψ was measured by ALICE in p-Pb [102] and was observed to be significantly positive for $p_{\rm T}$ between 3 and 6 GeV/c, as shown in Figure 1.29. The magnitude of the flow, similar to what was observed in Pb-Pb, could indicate a similar origin regardless of system size, even though the transport model has not been able to reproduce this result correctly [109]. The study of the J/ψ flow in pp is the natural consequence of such measurements, as we try to answer the question: Does the J/ψ flow in the smallest hadronic collision system?

In the next chapter, we will review the current results on flow measurement from large systems down to pp.

1.5.4 Existing models

We have discussed some of the observables used in studying quarkonium production by focusing on the case of the charmonium. The results from the studies mentioned above are compared to theoretical models trying to predict them. When discussing the existing results we mentioned three main models.

The transport model [78] describes the evolution of the QGP phase through the Boltzmann equation. It incorporates dynamical components of dissociation and regeneration of quarkonia that compete during the whole evolution of the medium as well as cold nuclear matter effects.

The comovers model [69, 70] resembles the transport model in the sense that dynamical components of dissociation and regeneration of quarkonia, as well as cold nuclear matter effects, are included, and the equations that hold the model are similar. However, the main difference with the transport model is that the theory is an effective theory where interactions between the quarkonia and the medium are additionally described through partonic or hadronic interactions with the comover particles surrounding the moving quarkonia.

The statistical hadronization model [57] does not implement this dynamical competition between dissociation and regeneration. In this model, the dynamics of the medium are not what matters, as everything melts in the medium and is in thermal equilibrium. Everything is generated and hadronized at the phase boundary. Thermodynamics fully describes the abundances of hadronic species using a grand canonical ensemble model where all is dictated solely by the freeze-out temperature and the baryonic chemical potential.

Chapter 2

Anisotropic flow for the study of the QGP

Emportés par la foule, qui nous traîne, nous entraîne, écrasés l'un contre l'autre nous ne formons qu'un seul corps / Et le flot sans effort nous pousse enchaînés l'un et l'autre, et nous laisse tout deux épanouis, enivrés et heureux.

– Edith Piaf, *La foule*

In this chapter, we provide a deeper description of the flow with a review of measurements for various collision systems. Refs. [110, 111] offer extensive reviews on the theory of flow and existing measurements in the pre-LHC era.

As stated in Chapter 1, the flow is a favoured observable in the study of the QGP. As the expansion of the QGP is three-dimensional, flow can develop in multiple directions, so multiple subtypes of flow can be defined [112]. Radial flow is the flow created uniformly as particles are pushed away from the interaction point, and longitudinal flow is the flow developed from particles travelling along the beamline. We focus on the azimuthal anisotropic flow, which is developed non-uniformly in the transverse plane. It was first proposed as a sign of collectivity by Ollitrault [113] in 1992.

Anisotropic flow stems from the initial anisotropic geometry of the collision region in semi-central collisions and it results from collective phenomena from within the strongly interacting medium. As such, it is a powerful indicator of thermalization [113]. Measuring the flow allows one to access information regarding the QGP like its viscosity [114, 115], and many models try to predict the origin and extent of the flow in different collision systems, which can then be compared to experimental data. For instance, the expansion of the QGP as modelled by hydrodynamics [116, 117, 118] has direct consequences on the development of the flow for different species, leading to a mass-ordering at low-p_{T}, which will be addressed further in this chapter. The transport models [78, 119, 109, 120], including recombination of quarkonia in the QGP, predict flow at low-p_{T} coming from the flowing charm quarks pairing up. Initial state effects [26, 121] suggest flow development is influenced by the strong initial colour fields' impact on the quarks. Measuring flow coefficients and studying their evolution as a function of various variables should allow one to discriminate between the existing models.

2.1 Measuring the flow

2.1.1 Flow coefficients

Anisotropic flow is extracted from the distribution of the particles in an event. Since particles are emitted independently in every event, one gets the following equation:

$$\frac{dN}{dyd\phi} = \frac{1}{2\pi}\sum_{-\infty}^{+\infty} v_n e^{-in\phi}. \tag{2.1}$$

In Equation 2.1 the flow coefficients v_n represent the coefficients of the Fourier expansion of the particle distribution. v_1 is the direct flow, v_2 is the elliptic flow, sensitive to the initial anisotropic geometry,

and v_3 is the triangular flow, sensitive to event-by-event fluctuations like all odd-order coefficients. The azimuthal distribution of particles is the sum of Fourier harmonics [122], whose shapes are represented in Figure 2.1, weighted by the flow coefficients.

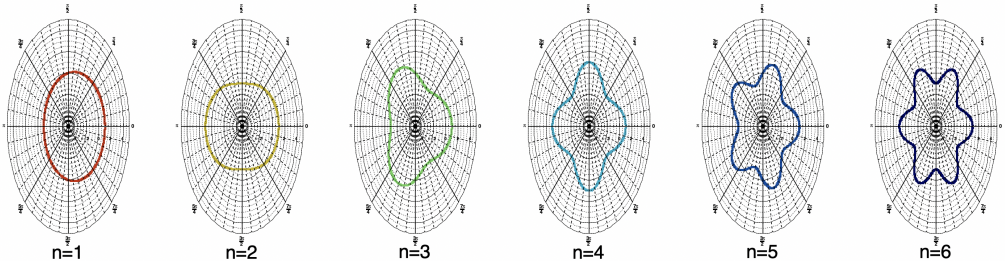

Figure 2.1: Representation of the Fourier harmonics $cos(n\Delta\phi)$ for the first six orders.

From Equation 2.1, it is tempting to try and measure v_n on an event-by-event basis using an event's N particles as shown in the following equation.

$$v_n \approx \frac{1}{N}|\sum_{j=1}^{N} e^{in\phi_j}| \tag{2.2}$$

However, this "flow of an event" observable is biased [113] as the expectation value of v_n is $\frac{1}{\sqrt{N}}$, which is coming from self-correlation terms. Because it is not zero, this observable is unreliable, and the flow is not measurable on an event-by-event basis by looking at individual particles.

On the other hand, quantities defined from multiple events provide meaningful insight into the flow, which can be extracted following two main approaches [123]. The first approach is based on correlating particles with an event plane [124].

$$Q_n = \sum_{j=1}^{N} cos(n\phi_j) + isin(n\phi_j) = Q_{n,x} + iQ_{n,y} = |Q_n|e^{in\Psi_n} \tag{2.3}$$

$$\Psi_n = \frac{1}{n}tan^{-1}(\frac{Q_{n,y}}{Q_{n,x}}) \tag{2.4}$$

For every order n, the flow vector Q_n is defined following Equation 2.3 using particles of an event. It is then used to define the Ψ_n angle of the event plane (EP), as in Equation 2.4. This event plane is correlated to the event particles, and these correlations are averaged over all studied events. This method can provide a first estimate of the flow coefficients:

$$v_n^{raw} = \langle\langle cos(n(\phi - \Psi_n))\rangle_{particles}\rangle_{events}. \tag{2.5}$$

The final v_n coefficient is then defined as the ratio of v_n^{raw} and the resolution of the event plane r_n:

$$v_n = \frac{v_n^{raw}}{r_n}. \tag{2.6}$$

Such resolution r_n can be determined by correlating two event planes computed from two subevents of the same event.

This method is used in large systems like A–A where there is enough multiplicity to define an event plane with precision. Too few particles in an event would make the event plane ill-defined and the corresponding resolution too low to be usable. Consequently, another method is preferably used in small systems where multiplicities are lower, which relies on particle-pair correlations. From Equation 2.1, we can deduce the pair distribution as follows:

$$\frac{dN_{pair}}{dy_1 dy_2 \Delta\phi} = \frac{1}{2\pi}(v_0^2 + 2\sum_{n=1}^{+\infty} v_n\{2\}^2 cos(n\Delta\phi)). \tag{2.7}$$

In this case, instead of correlating particles with an event plane, particles are associated two by two [125]. One can measure the pair distribution over events and extract its Fourier coefficients to obtain the flow coefficients without having to compute an event plane. $v_n\{2\}$, which is the v_n obtained from pair correlations, is the r.m.s. of v_n over the events [111]. This method is not limited to 2-particle correlations and can be applied to any number of particle-pairs, called cumulants [126, 127, 128, 129]. They can even give access to correlations between the flow coefficients themselves. However, the number of candidates, especially considering heavy flavours, can limit the ability to compute higher-order cumulants [127].

2.1.2 Non-flow contributions

The flow coefficients quantify anisotropies in particle distribution. Although anisotropies can partly be attributed to collective effects, some are due to effects that have nothing to do with collectivity. Such effects that produce flow-like contributions are called non-flow. There are many sources of non-flow, detailed in Ref. [130], and they affect more strongly small systems, as the non-flow contribution scales as $\frac{1}{N_{part}}$ [123, 130], with N_{part} the particle multiplicity. It is necessary to understand those sources to suppress them reliably.

Jets are probably the most straightforward source of non-flow. They are a consequence of the confinement of QCD, which causes the production of highly-collimated groups of particles. In pair correlations, jets will introduce an excess of correlations at $\Delta\phi = 0$ as we correlate particles from the same jet cone, as well as an excess at $\Delta\phi = \pi$ as we correlate particles from back-to-back jets (see Figure 2.2).

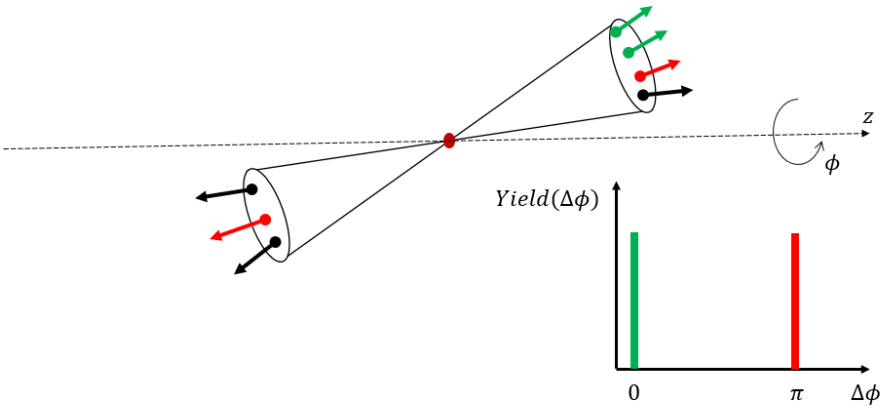

Figure 2.2: Representation of a dijet event where the highly collimated streams of particles result in pair correlation yields around 0 and π.

Short-range correlations like the Hanbury Brown and Twiss (HBT) effect [131, 132] (called Bose-Einstein correlations for bosons) can lead to an excess of correlations of particles that are close in phase space. As bosons are not subject to the Fermi exclusion principle, pions tend to correlate at very short distances, leading to an excess of pairs around $\Delta\eta \approx 0$ and $\Delta\phi \approx 0$.

Momentum conservation is also a source of non-flow, especially for the direct flow v_1. Indeed, due to momentum conservation in a collision, if we randomly select a pair of particles, there is a stronger chance that these particles are back-to-back. This effect results in an intrinsic amount of non-flow [130], following Equation 2.8, which needs to be taken into account [133] if one wants to reliably measure direct flow.

$$E(cos\Delta\phi) = \frac{-p_{\mathrm{T},j}p_{\mathrm{T},k}}{\sum_{l=1}^{N} p_{\mathrm{T},l}^2} \tag{2.8}$$

There exist other sources of non-flow, like resonance decays or path-length dependent suppression. The latter is detailed in Chapter 1 and stems from the uneven suppression of quarkonia depending on the

length of QGP they crossed. Flow studies aim to compute flow coefficients that are as free from non-flow effects as possible to ensure that collective effects are adequately assessed, which is particularly critical in small systems where non-flow is dominant.

2.1.3 Removing the non-flow

Some non-flow sources impact short-range correlations, like jets and Bose-Einstein correlations. Cuts on $\Delta\eta$ can be applied to suppress non-flow in pair-correlation methods. Such "η-gap" of order two units in ATLAS and CMS and one unit in ALICE reduces the non-flow peak coming from short-range correlations. However, for dijets which also generate a non-flow peak around $\Delta\phi = \pi$, a short-range cut is not enough. Different collaborations have employed various methods to suppress this contribution, as detailed in Ref. [134]. These methods rely on the definition of per-trigger yields $Y(\Delta\phi)$. They are the average number of pairs with a given azimuthal separation $\Delta\phi$ over studied events. We will define this quantity properly in Chapter 5, but for now, we can see it as an indicator of how particles tend to arrange spatially around the reference particle of a pair.

Yield subtraction

As in Ref. [102], the ALICE Collaboration separates high-multiplicity and low-multiplicity events. In high-multiplicity (central) events, collective effects are expected. On the contrary, no collectivity is expected in low-multiplicity events (especially in small systems). So much so that the only contribution that should be visible in low-multiplicity events is from non-flow effects, which are mostly dominated by (di)jets. By considering that jet contribution is independent of multiplicity, the non-flow contribution can be suppressed by subtracting the low-multiplicity yields from the high-multiplicity yields:

$$Y^{sub}(\Delta\phi) = Y^{Central}(\Delta\phi) - Y^{Peripheral}(\Delta\phi) = a_0 + \sum_{n=1}^{+\infty} 2a_n cos(n\Delta\phi). \tag{2.9}$$

The flow coefficients are then extracted from the $Y^{sub}(\Delta\phi)$ distribution, which is defined in the following equation. $v_n\{2\}^2 = \frac{a_n}{a_0 + Y^{Peripheral}(0)}$, as will be detailed in Chapter 5. The $Y^{Peripheral}(0)$ is the minimum of the yields in the low-multiplicity class. It is assumed that no collective effects are present in low-multiplicity yields, so the distribution's baseline is an offset.

The CMS method used in Ref. [135] is similar, except that both the central and peripheral yields baselines are subtracted, and there is an additional scaling of the non-flow. While flow correlations are estimated on the away-side with an η-gap of 2 units, the non-flow contribution is evaluated in both low-multiplicity and high-multiplicity events by assessing short-range correlations. The ratio between the non-flow contributions in the two classes provides a scaling factor between high and low-multiplicity yields.

Template fitting

The ATLAS method used in Ref. [136] is conceptually different from the other two. The low-multiplicity correlations are used as a template for the non-flow. Instead of subtracting the low-multiplicity yields from high-multiplicity yields, a "template fit" method is used, where the low-multiplicity class is subtracted F times, with F a free parameter. The assumption is that the non-flow is not constant as a function of the centrality class and is mainly due to dijet production, which contributes significantly to the v_1 coefficient. As the non-flow is suppressed, the v_1 coefficient becomes therefore equal to zero.

$$Y^{Central}(\Delta\phi) = FY^{Peripheral}(\Delta\phi) + G^{tmp}(1 + \sum_{n=2}^{+\infty} 2v_n\{2, tmp\}^2 cos(n\Delta\phi)) \tag{2.10}$$

In Equation 2.10, v_1 is nullified, and G^{tmp} (the tmp exponent meaning template) is a parameter fixed to ensure that the integrals over the $\Delta\phi$ range on both sides of the equation are equal.

In the analysis work of this thesis we use both the ALICE yield subtraction method and the ATLAS template fit; a more detailed description of the processes in the context of the analysis will be given in

Chapter 5. The CMS method is disregarded as it requires a distinction between short and long-range correlations, which is too unclear considering ALICE pseudorapidity acceptance.

An improved version of the ATLAS template fit procedure, described in Ref. [137], is also used in the literature, especially when studying light particles flow, in an attempt to reduce the impact of the flow dependence on multiplicity. Indeed, by considering both the central and peripheral yields are the sum of a dijet component and a ridge from collective effects, one obtains the following equation.

$$\begin{cases} Y^{Central}(\Delta\phi) = Y^{Central}_{dijet}(\Delta\phi) + G^{Central}(1 + \sum_{n=2}^{+\infty} 2v_n\{2\}^2 cos(n\Delta\phi)) \\ Y^{Peripheral}(\Delta\phi) = Y^{Peripheral}_{dijet}(\Delta\phi) + G^{Peripheral}(1 + \sum_{n=2}^{+\infty} 2v_n\{2, periph\}^2 cos(n\Delta\phi)) \end{cases}. \tag{2.11}$$

By using the assumption that $Y^{Central}_{dijet}(\Delta\phi) = FY^{Peripheral}_{dijet}(\Delta\phi)$ and substituting in Equation 2.10, one gets

$$\begin{aligned} Y^{Central}(\Delta\phi) =& FY^{Peripheral}_{dijet}(\Delta\phi) + FG^{Peripheral}(1 + \sum_{n=2}^{+\infty} 2v_n\{2, periph\}^2 cos(n\Delta\phi)) \\ &+ G^{tmp}(1 + \sum_{n=2}^{+\infty} 2v_n\{2, tmp\}^2 cos(n\Delta\phi)). \end{aligned} \tag{2.12}$$

By identification, using $G^{Central} = G^{tmp} + FG^{Peripheral}$, it follows

$$v_n\{2\}^2 = v_n\{2, tmp\}^2 - \frac{FG^{Peripheral}}{G^{Central}}(v_n\{2, tmp\}^2 - v_n\{2, periph\}^2). \tag{2.13}$$

Equation 2.13 proves that we can extract a "true" $v_n\{2\}$ using the result from the template fit corrected by an estimation of the peripheral $v_n\{2, periph\}$. In practice, this procedure relies on applying the template fit twice. Once between the second-to-lowest multiplicity bin and the lowest, to get $G^{Peripheral}$ and $v_n\{2, periph\}$ the estimates of the fit parameters in the peripheral class. And a second time between the central class and the second-to-lowest multiplicity bin to estimate F, $G^{Central}$, and $v_n\{2, tmp\}$ which ultimately allow one to compute $v_n\{2\}$. However, this method can only be used if there are enough events so that one can define statistically significant centrality classes (especially making a difference between the lowest and second-to-lowest) and obtain meaningful fits. This is the case when studying light particles. However, it is not yet possible with the fewer number of candidates available when studying heavy flavours, as is the case in this thesis.

In this section, we have seen the formal definition of the flow coefficients and why particle correlations, in pairs or with respect to an event plane, are necessary to define meaningful flow observables. We have seen the principal sources of non-flow, how they impact the flow measurements and what methods are currently used to suppress their effects. In the next section, we will focus on reviewing the current status of flow measurements in large A–A systems and smaller collision systems like p–A or pp.

2.2 Review of the results on flow measurements

2.2.1 A–A systems

In the 1990s, following the proposal by Ref. [113] to study elliptic flow as an observable of collectivity, the first measurements at AGS [138, 124], SPS [139] and RHIC [140] were conducted. Initially, the study of the flow was focused on heavy-ion collision systems A–A (typically Au–Au or Pb–Pb) before more recently focusing on medium and small systems in search for collectivity. We will go through some of the main results in the different systems for both light and heavy flavours.

Light particles

Flow measurements essentially focus on the behaviour of the flow coefficients as a function of different variables, which allows for comparison to models and an intuitive understanding of the flow formation and development. The main variables against which one can study flow, and on which we will focus here, are centrality, multiplicity, collision energy, transverse momentum and (pseudo)rapidity.

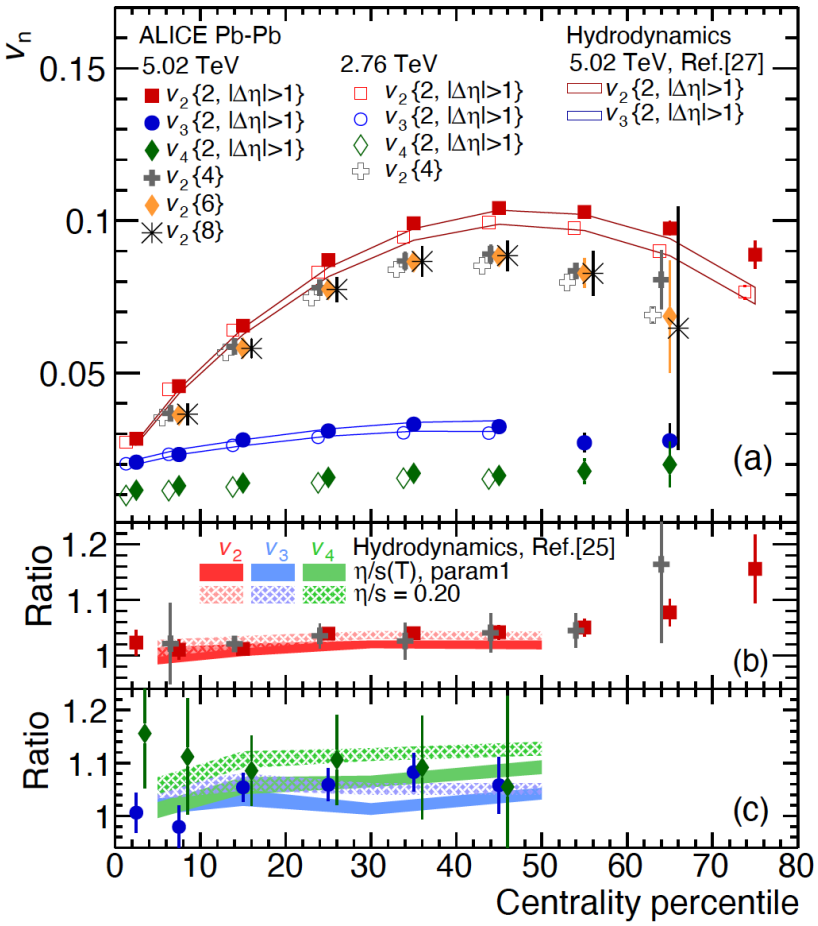

Figure 2.3: From Ref. [141], (a) Anisotropic flow coefficient v_n integrated over $0.2 < p_{\mathrm{T}} < 5.0$ GeV/c as a function of event centrality. (b,c) Ratios of the v_n between 5.02 TeV and 2.76 TeV Pb–Pb collisions. Hydrodynamic models [142, 143] are presented for comparison.

Centrality and multiplicity In Figure 2.3 (a), measurements of elliptic, triangular and quadrangular flow coefficients for identified charged light particles by ALICE in Pb–Pb collisions are presented [141]. From central to semi-central collisions, the flow coefficients increase for all orders. Then, for more peripheral collisions, they start to decrease. This trend is expected by the geometry-based interpretation given of the onset of the flow. In very central collisions, there is collectivity but barely any initial geometric anisotropy from the collision region. As collisions become less central, the collision region becomes more anisotropic due to the increased impact parameter and flow increases before decreasing again in peripheral collisions where there may be too few participants to observe collectivity. This behaviour is confirmed by hydrodynamic models [142] for both v_2 and v_3. On this same figure we also observe a hierarchy of the flow coefficients where $v_2 > v_3 > v_4$. Comparing the different v_2 extractions using multi-particle cumulants, we observe that all cumulants involving four particles or more agree on the value of v_2 which is less than what $v_2\{2\}$ measurements provide. This illustrates the interest of multi-particle cumulants, which, by involving correlations of many particles, can suppress the non-flow effects more efficiently than two-particle pairs [144]. However, it comes at the cost of increasing the statistical uncertainties [127].

Finally, on Figure 2.3 (b,c) we see the ratios of the v_n coefficients between 5.02 TeV and 2.76 TeV Pb–Pb collisions. There is a slight increase of all coefficients with increasing energy, which we will detail in the next paragraph, and which is well predicted, within uncertainties, by hydrodynamic models [143].

The behaviour of the flow coefficients as a function of multiplicity is similar to their behaviour as a function of centrality. This is because centrality is defined from a fit of the energy deposited in the detectors (the V0 for ALICE) which is correlated to the multiplicity of the events [23]. And so, in Figure

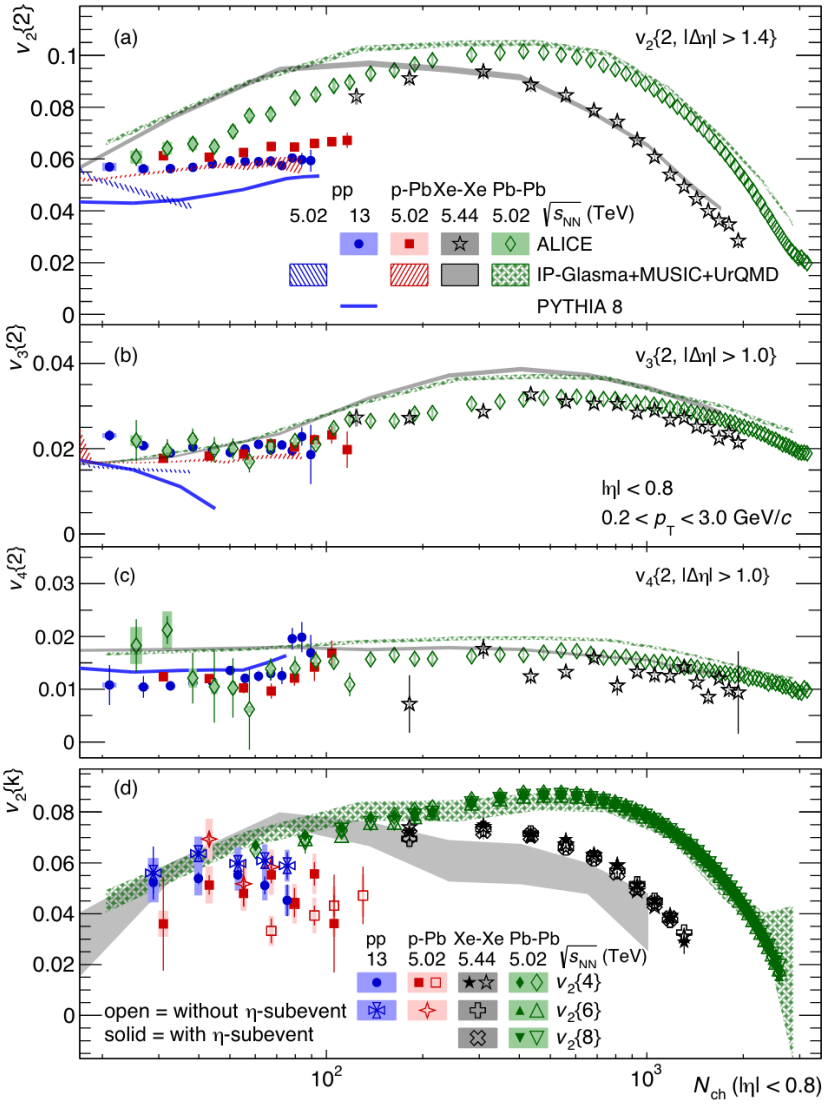

Figure 2.4: From Ref. [144], multiplicity dependence of the k-particle cumulants $v_n\{k\}$ for various collision systems. Data is compared to PYTHIA8.2 Monash [145] simulations for pp collisions at 13 TeV, and IP Glasma+MUSIX+UrQMD [146, 147] calculations for p–Pb and A–A systems.

2.4 showing v_n measurements for different systems as a function of charged particle multiplicity, we observe an increase of the flow coefficients from high multiplicities to medium multiplicities and then a decrease towards low multiplicities. The data from large A–A systems are compared to a IP-Glasma (initial state) + MUSIC (hydrodynamic evolution) + UrQMD (hadronic rescatterings) model [146, 147] which reproduces qualitatively the v_n measurements down to $N_{ch} = 200$ where it overshoots the elliptic flow data.

Collision energy As Figure 2.3 indicates, the flow coefficients are sensitive to the energy of the collision. Figure 2.5 shows this sensitivity using elliptic flow data from light particles in multiple experiments for semi-central collisions, where the flow is expected to be the highest. The measurements span three orders of magnitude in centre-of-mass energy. Between RHIC and LHC energies, there is a 30% increase in the measured flow, which is compatible with predictions from hydrodynamic models using viscosities close to the perfect fluid limit of $1/4\pi$ [148]. This increase with energy is also seen on a smaller scale between ALICE measurements at 2.76 TeV and 5.02 TeV. It could come from an increase in $\frac{dv_2}{dp_T}$, but

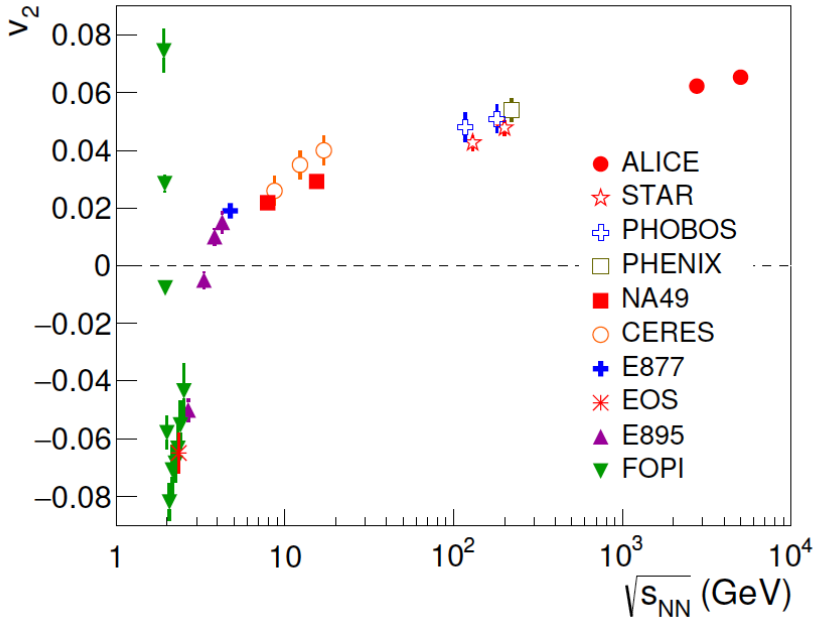

Figure 2.5: From Ref. [144], measurements of the elliptic flow in various experiments as a function of collision energy up to 5.02 TeV. Full references are found in the 2.76 TeV version of this plot in Ref. [148].

this quantity is predicted to be stable with energy in hydrodynamic models. It has been measured not to be impacted by the energy change from STAR to LHC measurements [110]. Therefore, the flow increase with energy must come from the hardening of the p_{T}-spectra, meaning that the mean p_{T} of particles is increased, as predicted by hydrodynamics. At low energy, the trend is different. This effect pushing flow values to the negatives is caused by a shadowing effect called squeeze-out. The spectator nucleons continue to impact the system due to the very long crossing time of the nuclei, which prevents the flow from fully developing in-plane.

Transverse momentum Studying the transverse momentum evolution of the flow highlights different properties of the flow depending on the p_{T} range.

As shown in Figure 2.6, at low-p_{T}, below 2 to 3 GeV/c, there is a mass-ordering of the particle species. At fixed p_{T}, particles with a higher mass will develop lower v_2 [149, 150]. This behaviour has been observed by many experiments, from Au–Au collisions at AGS [151] to Pb–Pb collisions at LHC [28], and agrees with what hydrodynamics predict. This mass-ordering and model agreement also holds for higher flow harmonics, up to v_5 [152]. However, at higher p_{T}, hydrodynamics start to fall out from data, and other processes can explain the behaviour of the flow. At intermediate-p_{T}, starting from 3 GeV/c, the mass-ordering does not hold and can even look inverted. What is observed is a quark-number scaling, where mesons will have similar flow values, separate from baryons. This behaviour is well understood within the coalescence picture, in which the flow of a particle can be explained using the flow from the individual quarks it is composed of [153, 154]. A simple model gives us that the flow of a n-quark hadron is $v_2(p_{\mathrm{T}}) = nv_2(p_{\mathrm{T}}/n)$ by assuming that the spatial distribution of quarks is uniform and other assumptions that hold on a restricted range of p_{T} [153]. This model holds remarkably well as observed at AGS for the directed flow [151], at RHIC first for the elliptic flow of deuterons [155] and then for a larger spectrum of identified hadrons [156], and at LHC [28]. This model implies that the matter is deconfined during the system evolution as quarks develop their own individual flow before coalescing. In this regard, the behaviour of the ϕ meson is particularly interesting, as it weighs as much as the proton while not being a baryon. It exhibits different behaviours between mass-ordering at low-p_{T} and quark scaling at intermediate-p_{T}, as shown on Figure 2.6. When going to even higher p_{T}, typically above 8 GeV/c, the residual flow is coming from path-length dependence

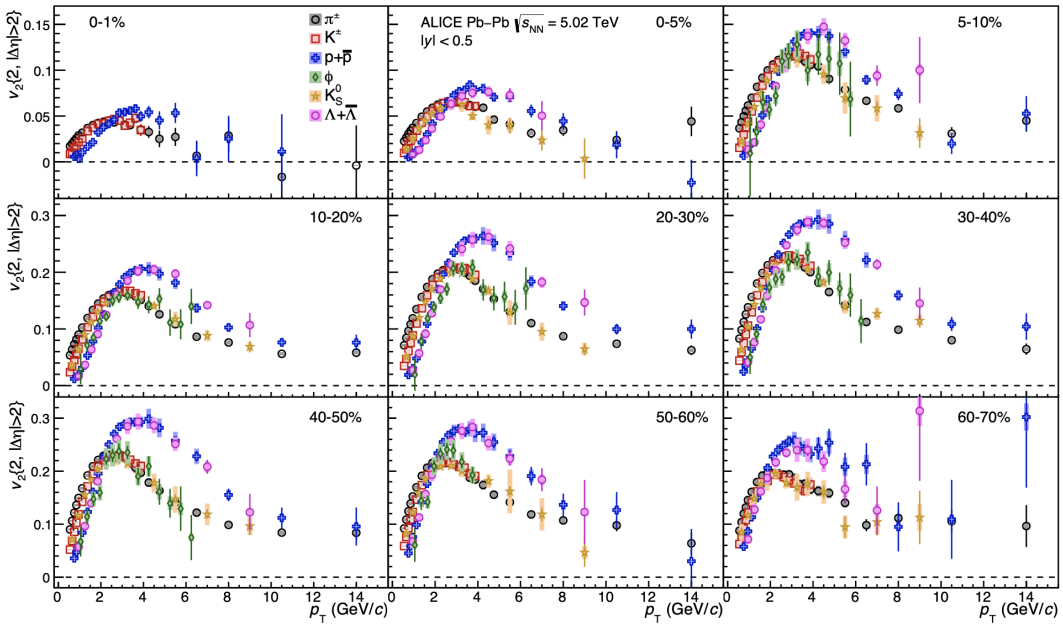

Figure 2.6: From Ref. [28], measurements of the elliptic flow of identified particles as a function of transverse momentum in different centrality ranges, in Pb–Pb collisions at 5.02 TeV.

effects attributed to energy loss [157, 158], as mentioned in Chapter 1.

The p_{T}-dependence of flow coefficients also allows one to evidence scalings between the different coefficients. For instance, ALICE [28] observed a scaling of v_n as a function of the quark number, and at both RHIC [159] and LHC [160, 161], a power law scaling between different harmonics $v_n^{1/n} \propto v_m^{1/m}$ was observed up to intermediate p_{T}. Relationships between different harmonics are particularly studied because they provide additional constraints to models. Hydrodynamics predict [162] that v_2 and v_3 should be proportional to the amount of initial anisotropy ϵ_2 and ϵ_3. However, linearity falls out for higher orders, and an interplay with lower orders is observed [163]. The v_n coefficients are correlated, and studying symmetric cumulants as has been done in recent years allows one to evidence the relationships between the different orders and give new observables for model comparison [144, 164].

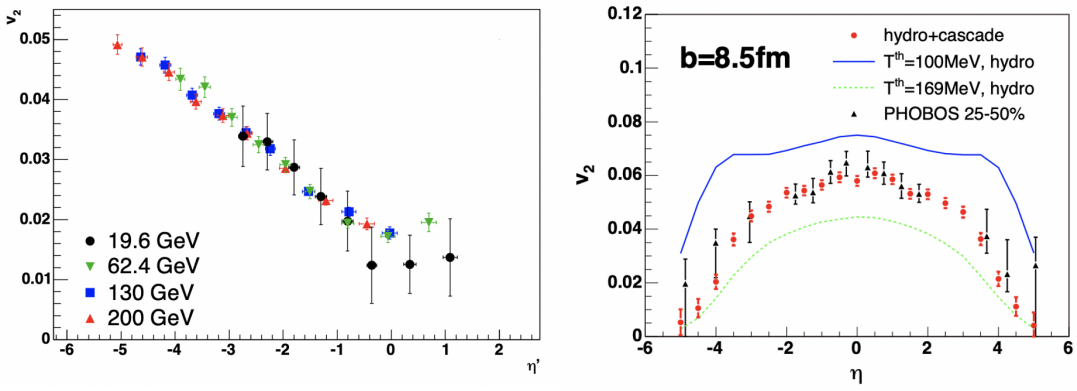

Figure 2.7: (Left) From Ref. [165], charged particles v_2 in Au–Au collisions for different energies as a function of $\eta' = |\eta| - y_{beam}$. (Right) From Ref. [166], v_2 as measured by PHOBOS as a function of pseudorapidity.

(Pseudo)rapidity As seen in Figure 2.7, the elliptic flow shows a maximum at mid-rapidity and decreases as one goes to forward or backward regions. A linear scaling of v_2 as a function of $|\eta| - y_{beam}$ regardless of collision energy was evidenced [165], such that the pseudorapidity dependence cannot be explained by hydrodynamics alone. One needs to incorporate hadronization cascades so that theory can reproduce data correctly [166].

Heavy flavours

Light flavours exhibit anisotropic flow in nucleus-nucleus collisions. The measurements are generally well reproduced by hydrodynamics once hadronization models are added, and they also shed light on deconfined quarks coalescence mechanisms. Is this any different for heavy flavours? Do heavy flavours participate in the collectivity and thermalize as light flavours do? What can we learn about heavy flavour production mechanisms and early stages of the collision that they allow us to access?

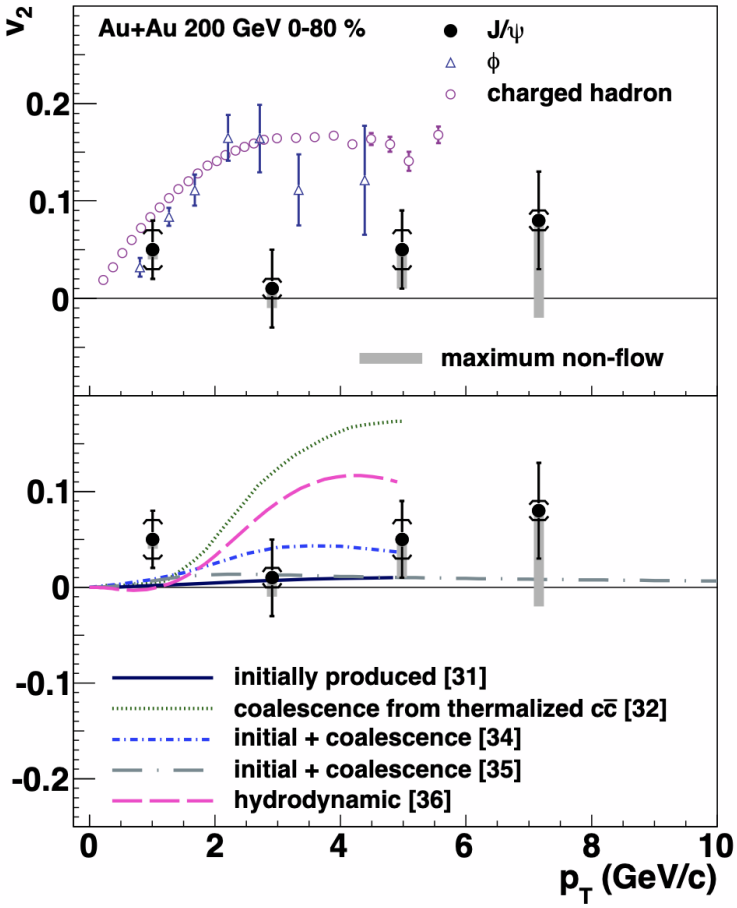

Figure 2.8: From Ref. [167], inclusive J/ψ elliptic flow in the 0-80% centrality range as a function of transverse momentum, studied in Au–Au collisions at 200 GeV via di-electron decay.

Charmonia The study of charmonia states is particularly interesting because they are only made of charm quarks. Hence, if they flow, it would indicate that charm flows as well. In this context, the first measurements of the inclusive J/ψ elliptic flow were made at RHIC [167]. However, no flow was observed within uncertainties over the studied p_{T} range, as shown in Figure 2.8. It is only by accessing LHC energies that J/ψ flow could be observed [100]. The reason is that at RHIC energies, (re)combination of charm quarks is not prevalent, and suppression dominates. As discussed in Chapter 1, (re)combination occurs at LHC energies, and the J/ψ flow develops from the coalescence of the flowing charm quarks, as predicted by transport models.

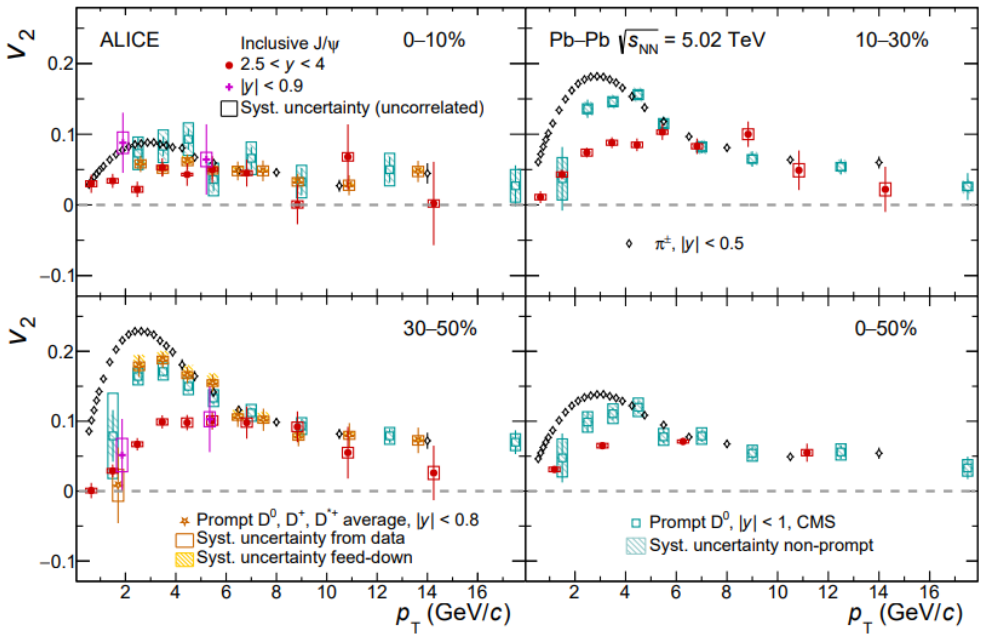

Figure 2.9: From Ref. [100], identified particles elliptic flow as a function of transverse momentum in various centrality ranges, in Pb–Pb collisions at 5.02 TeV.

In Pb–Pb collisions at 5.02 TeV, ALICE measurements [100] show that the elliptic flow of inclusive J/ψ is positive over a large p_{T} range, as seen in Figure 2.9, evidencing that charm participates in collectivity. At high-p_{T}, the flow of various species converges towards a common asymptote, hinting at a common flow mechanism identified previously: energy loss. More generally, the elliptic flow has the same overall magnitude for light and heavy flavours, which shows that charm quarks at least partially thermalize in the QGP. Furthermore, the mass hierarchy observed at low-p_{T} for light flavours extends to heavy flavours, further validating hydrodynamics. The same remarks can be done for the triangular flow v_3 which is significantly positive for p_{T} between 2 and 5 GeV/c [100], highlighting that charm is sensitive to initial fluctuations quantified by v_3.

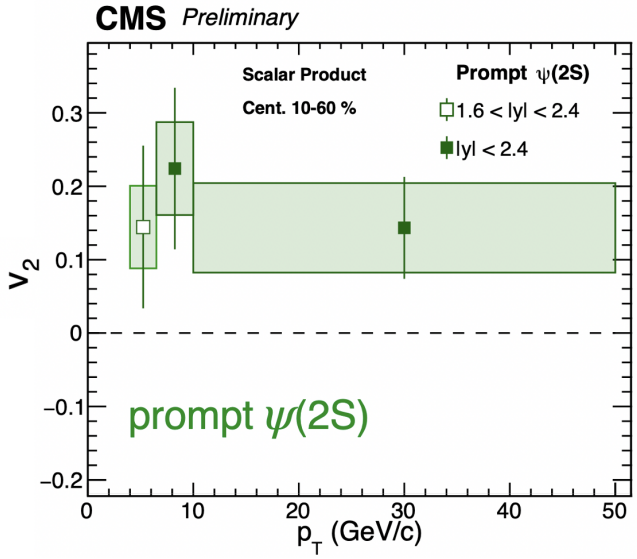

Figure 2.10: From Ref. [168], elliptic flow of prompt $\psi(2S)$ as a function of p_{T}, measured in Pb–Pb collisions at 5.02 TeV in the dimuon decay channel at midrapidity.

In the charmonia sector, the elliptic flow of the excited prompt $\psi(2S)$, seen in Figure 2.10, was measured to be above the elliptic flow of the J/ψ [168] within uncertainties which hints at the importance of recombination processes which are critical to the formation of the loosely bound $\psi(2S)$.

Bottomonia We have seen that the development of anisotropic flow depends on the particle's mass. Studying the bottomonia sector allows one to access the flow behaviour for heavier particles and probe flow's flavour dependence. The elliptic flow of the $\Upsilon(1S)$ was measured by the LHC collaborations [169, 170] to be compatible with zero. This measurement is consistent with the fact that the $\Upsilon(1S)$ bound state is expected to be highly dissociated in the QGP, and (re)combination is expected to be negligible due to the low amount of b quarks produced in heavy-ion collisions. $\Upsilon(2S)$ being less bound than $\Upsilon(1S)$ could have shown a positive flow. However, its elliptic flow is compatible with zero as well [169]. Maybe the situation between the $\Upsilon(nS)$ states is similar to the one of the J/ψ flow at RHIC, where only by going at higher energies could one observe the flow of charmonia from (re)combination effects. In any case, the fact that beauty does not flow is in line with the mass-ordering that is supported by the various studies we presented.

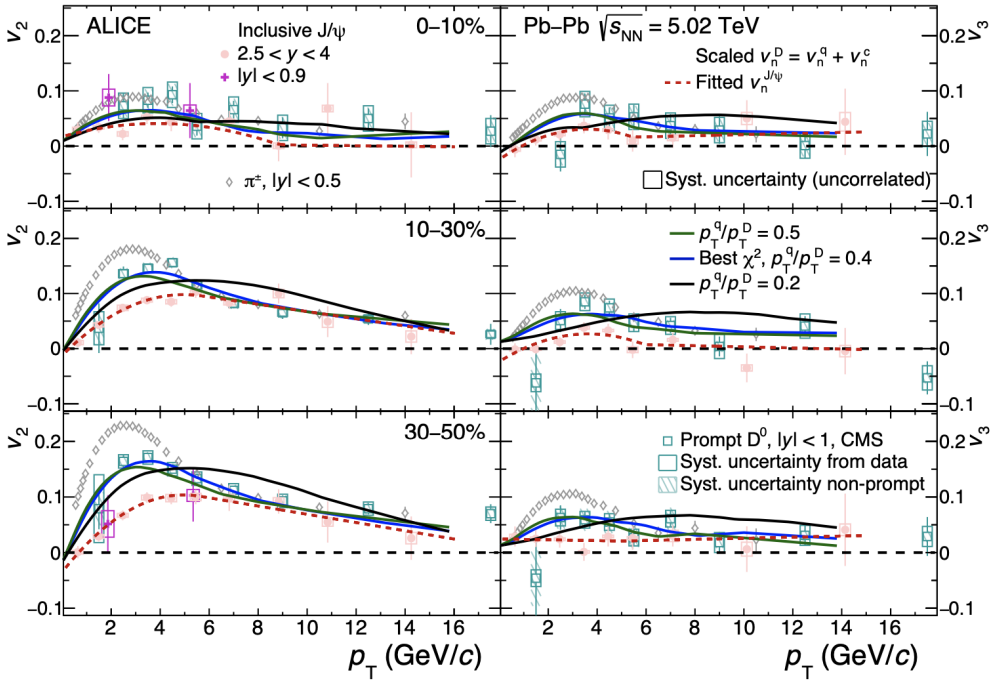

Figure 2.11: From Ref. [100], elliptic (left) and triangular (right) flow of inclusive J/ψ and prompt D^0 meson from CMS [171] as a function of p_T, measured in Pb–Pb collisions at 5.02 TeV.

Open-charm As seen in Figure 2.11, D mesons develop flow. It is expected as both its constituents do. Along with charmonia, they are a handy tool for studying charm flow and coalescence effects. In the same way that light hadrons flow was modeled from the grouping of flowing light quarks, D flow can be modeled as $v_2^D(p_T) = v_2^c(p_T^c) + v_2^q(p_T^q)$ [100, 172]. By fitting the data of J/ψ flow and D flow, an agreement was found when $p_T^q = 0.4p_T$, meaning that the D (elliptic and triangular) flow can be explained by coalescence of flowing light and heavy flavours in the deconfined phase. In comparison, an equal sharing of momentum between light and heavy flavour also gives a good fit to the D v_2 and v_3. In contrast, a distribution of the momentum proportional to the quark masses is quite off data.

Prompt and non-prompt heavy flavours As we have seen, charm participates in collective effects, whereas beauty does not. Studying charmonia and bottomonia is a way to establish this difference. Looking into prompt and non-prompt particles is another way to see how the QGP impacts heavy flavours. For example, ATLAS [173] has looked into prompt and non-prompt J/ψ flow, which evidenced

that both types of J/ψ flow while the p_{T}-dependency and the magnitude of their flow are different. Namely, prompt J/ψ develops more flow than non-prompt. This observation was further validated by CMS for the J/ψ [168] as well as for the D^0 [174] which shows lower non-prompt v_2 and v_3 and is compatible with a variety of theoretical models implementing hydrodynamics, transport, and energy loss. These observations show that b hadrons can be sensitive to initial geometry and fluctuation effects; however, they develop less flow than lighter hadrons.

2.2.2 p-A systems

Light flavours

Small systems are an ideal testing ground for collective effects as they give additional insight into collectivity formation. Historically, following the discovery of collective structures in two-particle azimuthal correlations by CMS in pp collisions [106], similar structures were found in p–Pb collisions systems at LHC [104, 103, 175, 176]. These structures can be explained by a wide variety of models like Color Glass Condensate, in which gluon saturation effects produce near-side contributions [177, 178], hydrodynamics [179], or final state effects like parton-parton scattering [120]. At RHIC, studies of d–Au collision systems [180, 181] showed similar long-range structures of larger amplitude compared to p–Pb systems, which is consistent with hydrodynamics, as initial state anisotropy would be larger in d–Au than in p–Pb. The PHENIX collaboration [182, 183] went further by studying the elliptic and triangular flow patterns in p–Au, d–Au and He^3–Au collisions, thus engineering a circular, elliptic and triangular collision region, respectively. In p–Au collisions, the v_2 was lower than in d–Au. In He^3–Au, the v_3 was the highest, which is in excellent agreement with predictions from hydrodynamics and the geometry-based argument for flow development.

In Figure 2.4, we observe that, as in Pb–Pb, the flow harmonics are ordered in p–Pb [144, 184]. Furthermore, their behaviour with multiplicity is well described by the hydrodynamics and hadronic cascades models [144]. v_3 values are even compatible between the two systems at equal multiplicity, possibly hinting at a common fluctuation-driven origin [184]. Concerning the v_2, it is less developed in p–Pb than in Pb–Pb which is to be expected if collision geometry dominates the formation of elliptic flow [184, 185]. Using many-particle cumulants, the flow observed in p–Pb is due to collective effects and not to non-flow, which is critical in small systems, [186, 185, 187]. This strongly suggests that the flow we observe in p–Pb has common origins with the one in Pb–Pb, and understanding its behaviour and origins in small systems may help us understand it in larger systems.

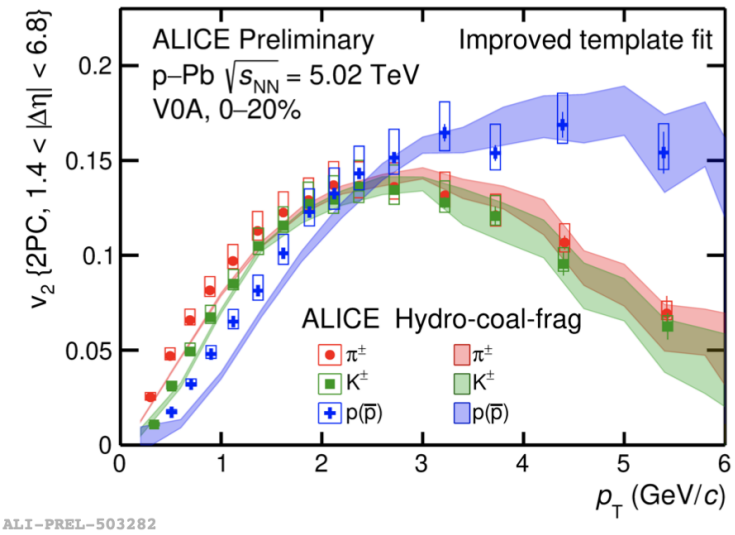

Figure 2.12: From Ref. [188], elliptic flow of various light particles as a function of p_{T} as observed in central p–Pb collisions at $sqrts_{\mathrm{NN}} = 5.02$ TeV by ALICE.

To further underline the similarities with Pb–Pb collisions, it should be noted that flow behaviours like the mass-ordering of species at low-p_{T} and the quark number scaling at intermediate-p_{T} are also seen in p–Pb [188, 189, 190]. Such behaviours are highlighted by Figure 2.12, where models implementing hydrodynamics, quark coalescence and jet fragmentation manage to reproduce the data. Without coalescence, the agreement does not hold [188], indicating that even in p–Pb, quarks seem to develop their flow individually in a deconfined phase before coalescing into flowing hadrons. Studying correlations between harmonics is a powerful comparison tool to theory in Pb–Pb collisions. Studying them in p–Pb allows one to evidence similar behaviours already observed in Pb–Pb, which further demonstrates the similarities between the two systems [137, 191].

Heavy flavours

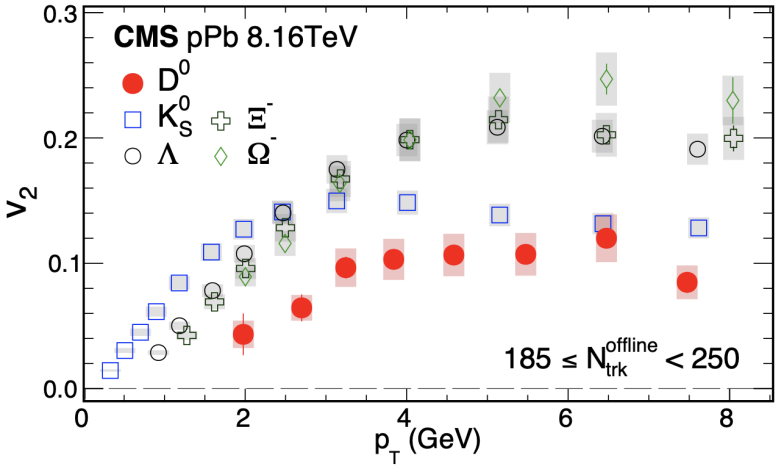

Figure 2.13: From Ref. [192], elliptic flow of various light particles and D^0 mesons as a function of p_{T} as observed in p–Pb collisions at 8.16 TeV.

Concerning heavy flavours, CMS [192] has been the first experiment to measure the elliptic flow of open-heavy flavours. As seen in Figure 2.13, by comparing the D^0 flow to light flavours, CMS indicates that charm develops less flow than light flavours. Moreover, the flow behaviour as a function of p_{T} for various species in p–Pb is reminiscent of Pb–Pb. Indeed, a mass-ordering of the flow is observed at low-p_{T} followed by a meson/baryon splitting at intermediate-p_{T}, underlining the similarities between system sizes in the heavy flavour sector, as evidenced by other flow studies from heavy-flavour decay electrons [193]. However, the low D^0 flow could be attributed to the light constituent quark alone [194]. The study of the charmonium flow is this needed to determine if charm quarks are flowing in p–Pb.

ALICE presented the first study [102] of inclusive J/ψ flow in p–Pb collisions. Following the qualitative agreement between Pb–Pb results and transport models, the expectations were that in p–Pb, barely any flow should be measured. At low-p_{T}, recombination is less prevalent in small systems, reducing the flow. Furthermore, at high-p_{T}, no path-length dependence effect is expected as the system would not be anisotropic enough. This overall behaviour is observed in Figure 2.14. However, in the mid-p_{T} range between 3 and 6 GeV/c, the inclusive J/ψ elliptic flow is positive with a significance above 5σ. Similar results were found by CMS [194] for the prompt J/ψ.

Initial state calculations within the CGC framework reproduce the results consistently [195, 196], contrary to the transport model which did well for Pb–Pb and R_{pA} but dramatically undershoots the J/ψ elliptic flow [109], as seen in Figure 2.14. This failure points to the need for another source to explain heavy flavour flow in small systems, potentially initial state effects. However, Ref. [197] throws shade at initial state interpretations by suggesting that initial momentum anisotropies are fully decorrelated from geometrical anisotropies in p–Pb. The implications would be the measurement of null flows within the CGC framework when correlating heavy flavours to light hadrons.

In order to compare flow measurements between charm and beauty, CMS [198] studied the prompt

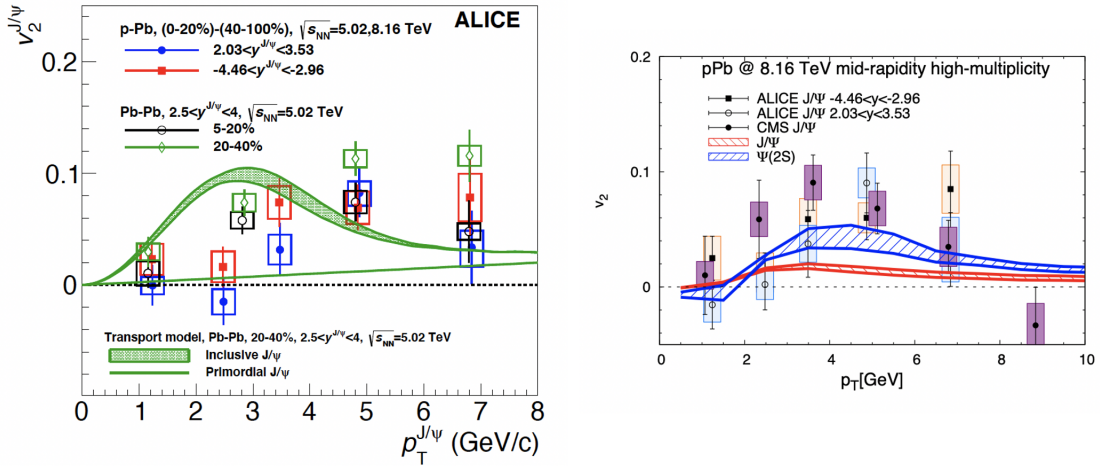

Figure 2.14: (Left) From Ref. [102], elliptic flow of inclusive J/ψ as a function of p_{T} for p–Pb and Pb–Pb collisions at 5.02 TeV and 8.16 TeV. (Right) From Ref. [109], transport model estimation of the charmonium v_2 as a function of p_{T} in p–Pb collisions compared to existing measurements at 8.16 TeV.

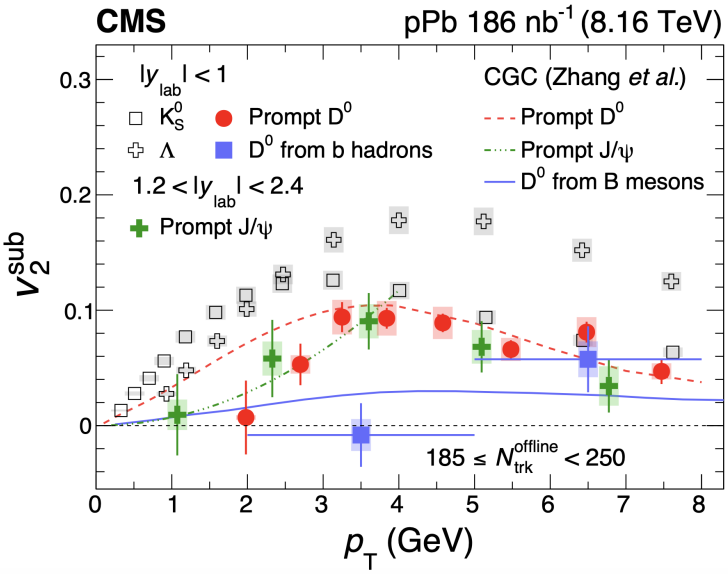

Figure 2.15: From Ref. [198], elliptic flow of various light particles, prompt and non-prompt D^0 mesons and prompt J/ψ as a function of p_{T} as observed in p–Pb collisions at 8.16 TeV.

and non-prompt D^0 flow. As seen in Figure 2.15, this study shows a mass scaling between charm and beauty. Beauty develops less flow than charm, in coherence with the mass-ordering predicted by final state effects and initial state calculations, which agree nicely with the data within uncertainties. However, a recent measurement by CMS [199] in the bottomonia sector shows that the $\Upsilon(1S)$ exhibits an elliptic flow compatible with zero, although the uncertainties are large. This measurement contradicts predictions from the CGC [195, 196] which indicate that both $\Upsilon(1S)$ and J/ψ should develop the same amount of flow. All in all, even if heavy flavours flow in p–Pb, the origin of the flow remains unclear.

2.2.3 pp system

Light flavours

Historically, the first observation of a near-side peak and away-side ridge in pp collisions was made by CMS [106] using particle-pair correlations, as seen in Figure 2.16. Measurements by the other LHC Collaborations quickly followed, with results obtained up to centre-of-mass energies of 13 TeV [135, 144, 105, 136, 107]. These collective effects, evidenced by studying higher-order multi-particle cumulants [135, 144] as in p–Pb, showed many similarities between high-multiplicity pp events and larger systems. This is corroborated by the inability of PYTHIA8 to reproduce flow results in pp [144].

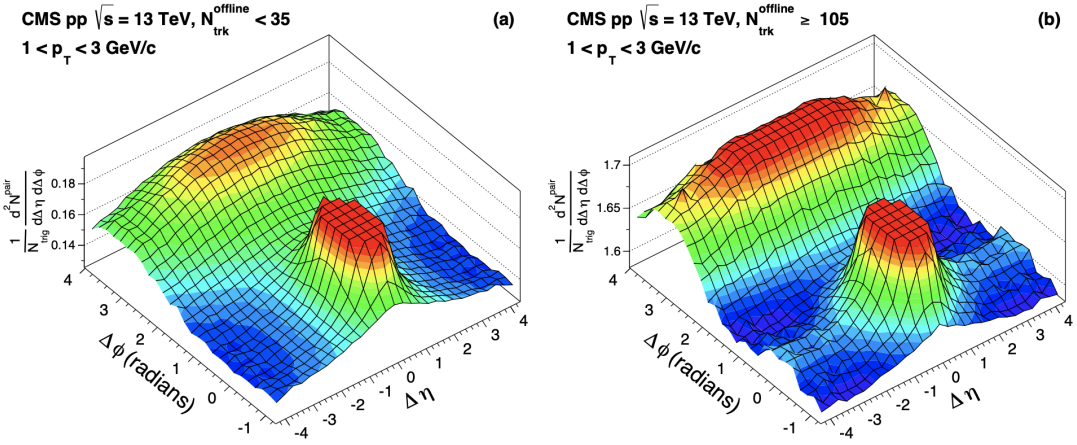

Figure 2.16: From Ref. [105], per-trigger yields of charged particles pair-correlations in (a) low-multiplicity (b) high-multiplicity pp collisions at 13 TeV. They display a (truncated) correlation peak in (0,0) and an away-side extended ridge.

As shown in Figure 2.17, the study of various species of light particles like pions, kaons and lambda, highlights a similar p_{T}-dependence of the elliptic flow [107] to larger systems, with a mass-ordering at low-p_{T} and a quark number scaling at intermediate-p_{T} [135, 188] for high-multiplicity pp events. Figure 2.4 also evidences a v_2 ordering between the different systems, which is to be expected as geometrical anisotropies become less important in small systems, and an equivalent v_3 across system sizes showing a common sensitivity to event-by-event fluctuations [135, 144]. The ordering of the harmonics is also valid through all system sizes [144].

The multiplicity dependence of light particle flow is found to depend strongly on the extraction method. This is somewhat expected, given that the importance of non-flow contributions is amplified compared to heavy-ion collisions, and therefore their subtraction is more critical in small systems. For instance, CMS finds that the elliptic flow tends to decrease [135] at low multiplicities whereas ATLAS measures no dependency on multiplicity [107], as seen in Figure 2.18.

Some models [200, 201, 202] try to reproduce the measurements made by the different LHC collaborations. They are based on the CGC formalism as hydrodynamics and transport model rely on the formation of a QGP fireball which is not expected yet in pp [203]. Some gluon saturation-based models reproduce features of the bulk, like the shape of v_2 as a function of p_{T} [202].

Heavy flavours

The flow of heavy flavours in small systems is a challenging observable. The challenge mainly comes from the low number of candidates available in small systems and the appropriate use of flow extraction techniques. CMS [198] studied the flavour-dependency of elliptic flow using the prompt and non-prompt D^0 meson, thus providing for the first time such measurement in pp collisions. For transverse momentum between 2 and 6 GeV/c, the prompt D^0 shows elliptic flow values close to the ones obtained in p–Pb. An agreement is also found in the multiplicity-dependency of the v_2 where results from both systems coincide. This result indicates that charm seems to develop flow in high-multiplicity pp collisions, to the level of or slightly below light flavours.

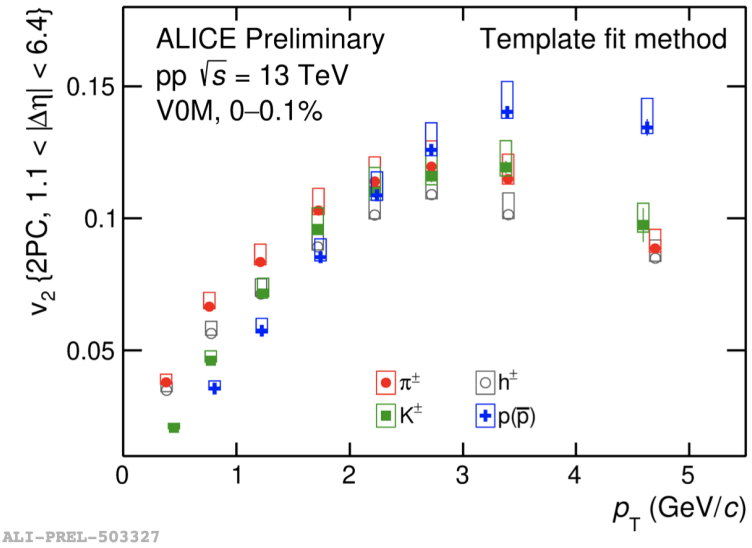

Figure 2.17: From Ref. [188], elliptic flow measurement of light particles as a function of p_{T} in central pp events at 13 TeV using the template fit method.

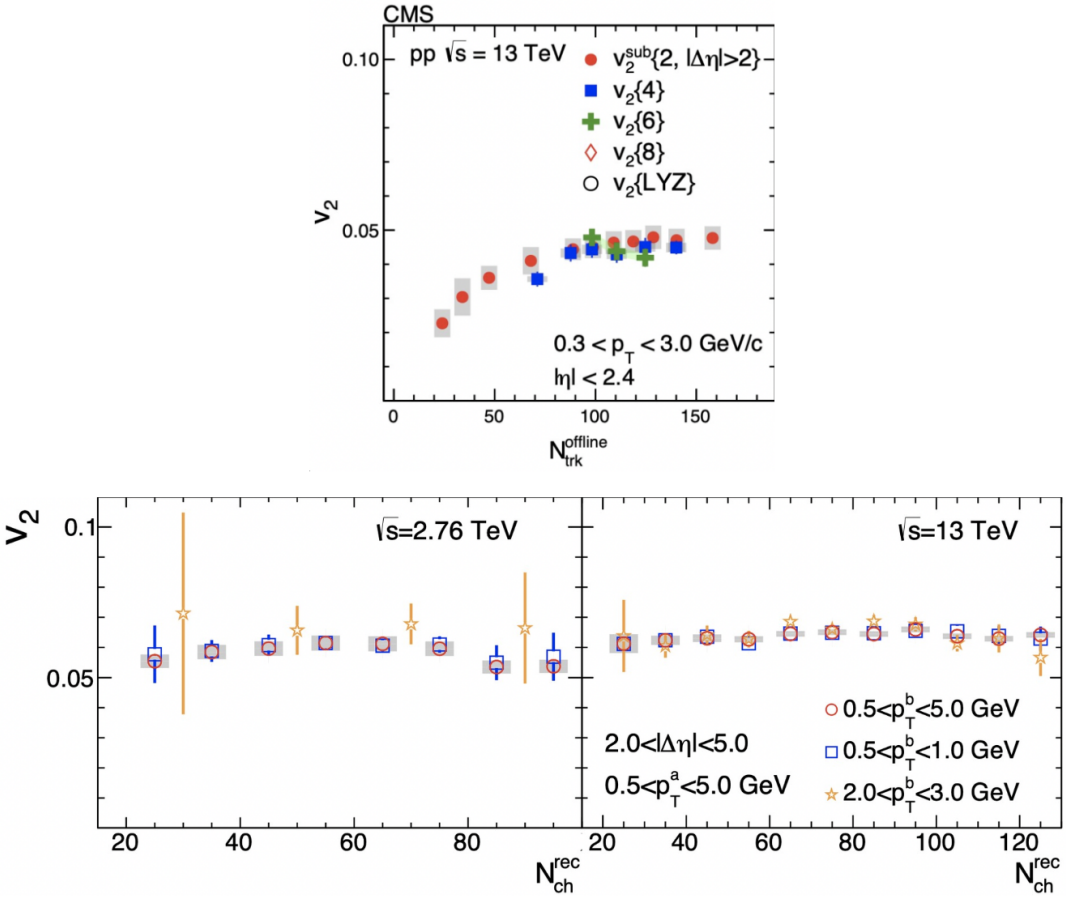

Figure 2.18: Elliptic flow from light particles as a function of particle multiplicity in pp collisions at 13 TeV from (top) CMS [135] (bottom) ATLAS [107].

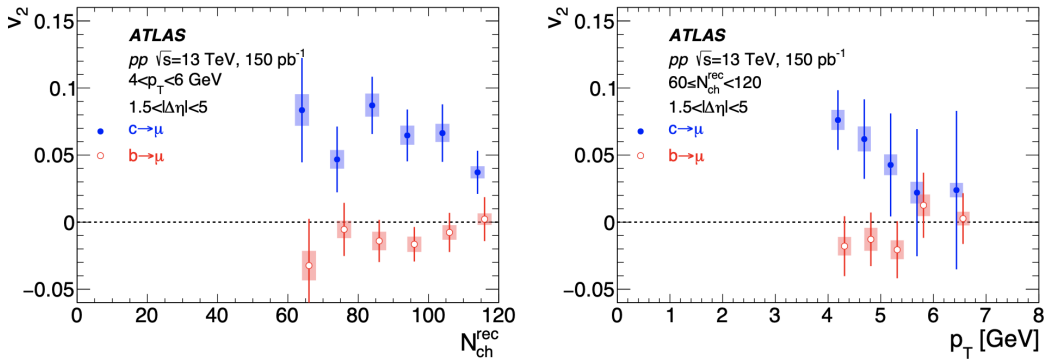

Figure 2.19: From Ref. [108], elliptic flow of muons decaying from charm or beauty hadrons in pp collisions at 13 TeV, as a function of (left) charged particle multiplicity (right) p_{T}.

Charm participation in collectivity is further proven by ATLAS [108] which studied the flow of muons coming from either a charm or a beauty decay. As seen in Figure 2.19, charmed muons exhibit a positive elliptic flow independent of multiplicity within uncertainties and decreasing for p_{T} between 4 and 7 GeV/c. On the contrary, muons from beauty decays exhibit an elliptic flow compatible with zero. While it appears that charm could participate in collective effects, beauty does not.

However, studying charmonia would bring a more compelling argument to charm quark flow in pp collisions. In a $c\bar{c}$ system, the developed flow, if any, can only be due to the heavy flavour and not the accompanying light flavour as in the D^0 meson, for example. Furthermore, as the J/ψ flows in both Pb–Pb and p–Pb systems, the analysis of the J/ψ elliptic flow in pp is deeply motivated, which is why it is the core subject of this thesis' analysis presented in Chapter 5.

Chapter 3

Experimental setup

Toutes les machines ont un coeur, t'entends ? / Toutes les machines ont un coeur dedans / Qui bat, qui bat, qui bat.

– Maëlle, *Toutes les machines ont un coeur*

This chapter will introduce the Large Hadron Collider (LHC) at CERN and one of its main experiments, ALICE, which studies the QGP. We will discuss the different detectors, the recent LS2 upgrades, and future perspectives.

3.1 The Large Hadron Collider (LHC)

In 1994, the LHC was approved by the CERN Council [204]. This new collider was due to replace the Large Electron-Positron collider (LEP), which was dismantled in 2000. The LHC is made of two beam pipes in concentric rings with a circumference of 26.7 km. It is located 100 m underground, close to Geneva at the border between France and Switzerland. The LHC is currently the world's largest and most powerful collider, with centre-of-mass energies going up to 14 TeV in proton-proton (pp) collisions. Using existing accelerators as injectors (see Figure 3.1), highly energetic hadron beams circulate both clockwise and anti-clockwise in the beam pipes.
Along the ring, several experiments have been built around interaction points where the beams can collide. There are four main experiments:

- ATLAS (A Toroidal LHC ApparatuS) is one of the two general-purpose detectors at the LHC. It is the largest experiment of its kind ever and leads various studies, from Higgs searches to tests of the Standard Model or dark matter hunting.
- CMS (Compact Muon Solenoid) is the second general-purpose detector, which essentially has the same objectives as ATLAS, allowing a complementary cross-check between the two collaborations working independently.
- ALICE (A Large Ion Collider Experiment), which will be further detailed in the next section, specializes in measuring heavy-ion collisions to study the QGP.
- LHCb (LHC beauty) is a forward experiment whose fields of study include the imbalance between matter and anti-matter and lepton universality by focusing on the beauty quark.

Other smaller and more specific experiments have also been added to the LHC. As of 2022, there are four of them.

- TOTEM (TOTal, Elastic and diffractive cross-section Measurement) is an experiment placed around the CMS interaction point, studying the behaviour of protons post-collision in the very forward region.
- LHCf (LHC forward) is an experiment placed around the ATLAS interaction point. It studies the particles produced in the very forward region and their cascades to better understand cosmic rays and their cascades in the atmosphere.

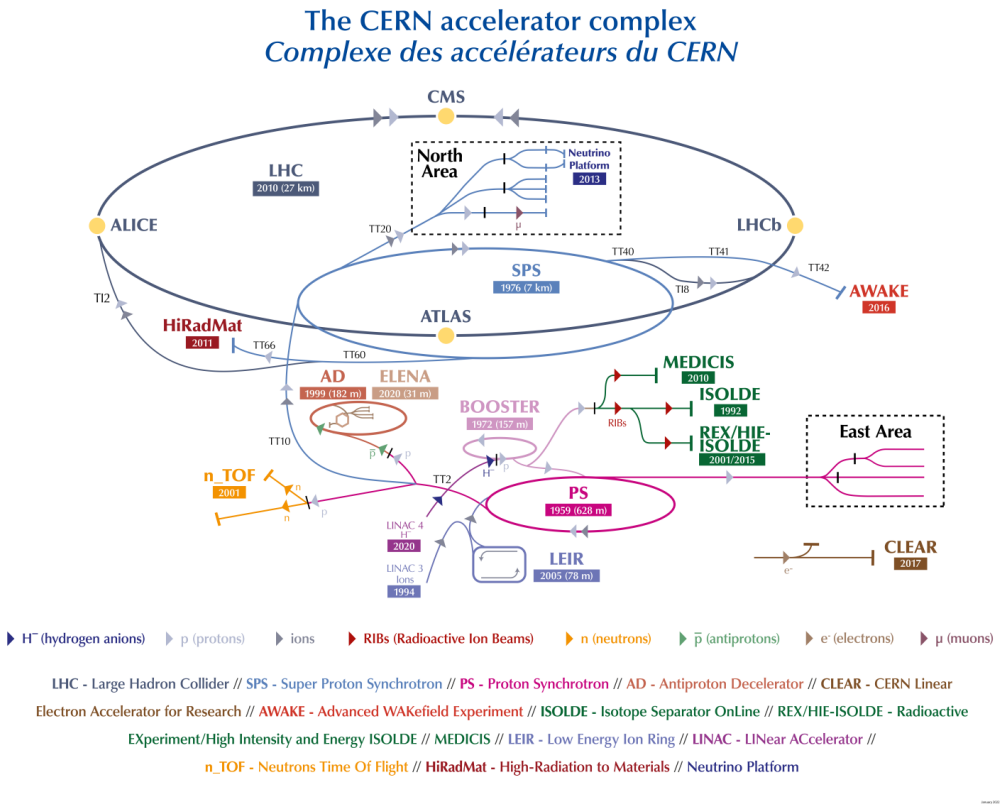

Figure 3.1: Representation of the accelerator complex at CERN (from CERN official website).

- MoEDAL (Monopole and Exotics Detector at the LHC) is an experiment, approved in 2010, situated close to LHCb which searches for magnetic monopoles and exotic particles that LHC collisions could produce.

- FASER (ForwArd Search ExpeRiment) is an experiment placed downstream ATLAS, searching for light and weakly interacting particles, which could solve some of the Standard Model puzzles like the search for dark matter.

After years of construction, in the morning of the 10th of September 2008 [205], the first proton beam was delivered in the beam pipe. Some technical issues surfaced [206] resulting in a cooling agent leak. This issue was more serious than some other data taking challenges coming from the sheer scale of the experiment, like the impact of tidal forces [207] or even train schedules [208] on precision measurements. Despite this fault which was corrected in the following months, September 2008 is a milestone which marked the start of data-taking at high energies at the LHC.

The energies at play at the LHC are the highest ever seen in a collider. The LHC's capacity to study such energetic collisions lies in two factors. First, the collisions are head-on collisions of two facing hadron beams. The centre-of-mass energy is higher than for a single beam colliding with a fixed target. Second, the beams are accelerated to ultra-relativistic speeds, extremely close to the speed of light. The ability that LHC has to accelerate beams to such speeds comes from its size and the interplay between radio-frequency (RF) cavities [204, 209, 210], to accelerate the beam, and different types of magnets to curve the trajectory and focus the beam into shape [204, 209, 210]. To further detail this point, the RF cavities are precisely shaped so that an electric field oscillating at 400 MHz is stationary. The charged particles entering the cavities are then accelerated, and the oscillating electric field makes them regroup in buckets spaced by 2.5 ns. By filling one out of ten buckets, particle bunches can be spaced by 25 ns.

The bunches' trajectory is then governed by supra-conducting dipole magnets which allow for swerving the hadron beams. Typically made of Nb-Ti alloy through which currents as high as 12 kA circulate,

the magnets are cooled down to 1.9 K using superfluid helium and allow the production of a nominal magnetic field of 8.33 T. Sextupoles and higher order magnets correct imperfections while quadrupoles help in focusing-defocusing beams. The latter serve as insertion magnets where triplets of quadrupoles focus the hadron beams to maximize the chances of a collision at the interaction point.

Before being shaped and moved around the collider, particles must be injected into the main ring. The protons for the proton beams are hydrogen nuclei. Until 2020, they came from H_2 gas bottles emptied in a duoplasmotron where electric fields separated electrons from nuclei. The protons were then accelerated in LINAC2 up to 50 MeV [209]. As of December 2020 [211], LINAC4 is used for injecting protons into the Proton Synchrotron Booster (PSB) as it allows to increase beam density by increasing beam intensity without increasing its size. The way LINAC4 produces protons [210] is by using a source of H^- ions. They go through a stripping foil that removes (sometimes part of) their electrons. Dipole magnets deviate the resulting beams of H^-, H^0 and protons. Protons enter the PSB and circle back to the stripping foil where they meet the H^- beam from LINAC4 again, gradually increasing the density of protons in the beam. Meanwhile, H^- and H^0 are dumped. In the Proton Synchrotron Booster, the proton beam is accelerated up to 1.4 GeV. Then it is injected into the PS, where it is further accelerated to 25 GeV. Gradually increasing in energy and size, the SPS brings proton beams to 450 GeV before finally transferring them to the LHC. They are then accelerated up to the nominal energy of 7 TeV, which takes approximately 20 minutes.

Lead nuclei come from a sample of solid and isotopically pure ^{208}Pb. The source is placed in an ECR (Electron Cyclotron Resonance) chamber where a magnetic field oscillating at 14.5 GHz heats the electrons and creates Pb^{29+} ions. They are then accelerated in LINAC3 up to 4.2 MeV/u and stripped of some electrons through a thin carbon sheet of thickness 0.3 µm. The resulting Pb^{54+} ions are then further accelerated to 72 MeV/u in the LEIR ring. With the addition of another complete electron stripping using an aluminium sheet of a thickness of 1 mm, they then go through the PS and SPS and finally the LHC, where they acquire their nominal energy.

After Run 3, which has just started, the event rate will be increased to gather more events which will help in the study of rare candidates. This collision rate (Γ) is linked to a quantity called (instantaneous) luminosity, L. Luminosity reflects the ability of an experiment to make interactions happen. It accounts for the likeliness of a collision. The luminosity is then the proportionality factor between the cross section (σ) of a given process and the event rate of said process. The following equations describe the link between event-rate, luminosity and cross section. They also define integrated luminosity $\mathcal{L}_{int}$ which is a way to express the number of events observed during data taking.

$$L = \frac{1}{\sigma} \times \Gamma,$$
$$\mathcal{L}_{int} = \int L dt = \int \frac{1}{\sigma} \times \Gamma dt = \int \frac{1}{\sigma} \times \frac{dN_{events}}{dt} dt.$$

During Run 3, LHC instantaneous luminosity is expected to plateau at 2×10^{34} cm^{-2}s^{-1}, as seen in Figure 3.2. Perspectives for an upgrade of LHC were envisioned in 2013, and green-lighted by the CERN Council in 2016. The so-called HL-LHC (High Luminosity LHC) [212] aims at increasing the instantaneous luminosity at the LHC up to 5×10^{34} cm^{-2}s^{-1}, which would represent an integrated luminosity of 250 fb^{-1} per year.

The project will be put into place during LS3 in the mid-2020s. It aims to increase the beam intensity. New optics will reduce the focal length at the collision point. A levelling of the luminosity will be necessary to avoid too much pile-up. Challenges concerning beam injection will be faced, like reducing the beam noise and correcting non-linearities from the optics. New technologies will be used to this effect. High-field Nb_3Sn supra-conducting magnets will increase the magnetic field from 8.33 T to 12 T, which is a necessary step in the development of stronger magnets at 15-16 T, in prevision of the FCC (Future Circular Collider). Crab radio-frequencies cavities will allow to rotate bunches without changing their trajectory to maximize chances of collision. High-current power lines using superconductive links will be able to supply currents up to 100 kA. These technological novelties will allow the increase of luminosity, making rarer and more exotic processes accessible at the LHC.

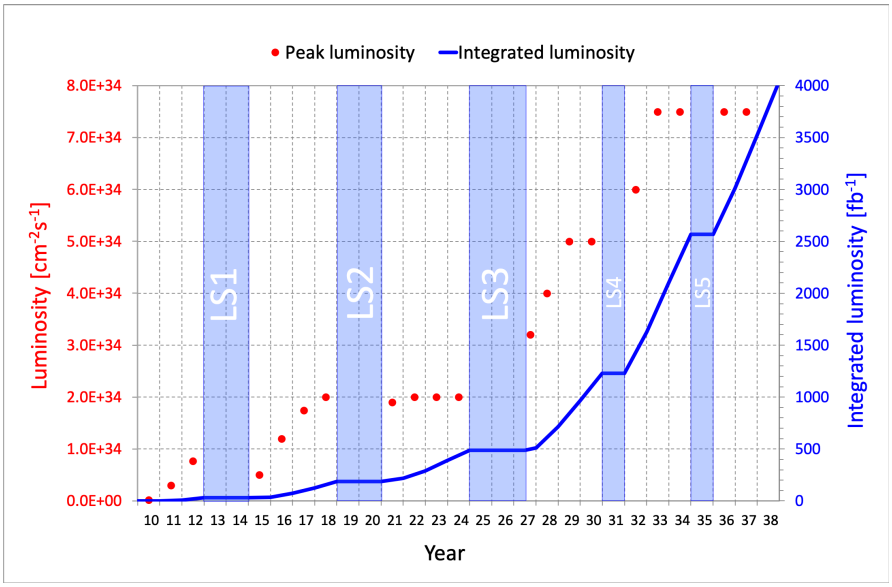

Figure 3.2: Evolution of instantaneous and integrated luminosity at LHC (from https://lhc-commissioning.web.cern.ch/schedule/).

3.2 A Large Ion Collider Experiment (ALICE)

ALICE is one of the four main experiments of the LHC at CERN. It is dedicated to the study of heavy-ion collisions and its history is reported in Ref. [213]. ALICE is inscribed within the study of the QGP started in 1986 at CERN SPS and Brookhaven AGS at centre-of-mass energies of 5 to 20 GeV. ALICE was built in the continuity of the ongoing work at RHIC. In 1993, a Letter of Intent for ALICE was published [214], presenting the extensive physics program such an experiment could offer. A Technical Proposal [215] followed in 1996 before CERN Council approval in 1997. During the better part of a decade, a robust R&D effort was produced to develop new technologies, detectors, and design ideas to face the challenges brought by the environment resulting from energetic heavy-ion collisions. The experiment was designed to handle the very large multiplicities of charged particles expected, at the time, in central Pb-Pb collisions (up to 8000 per unit of rapidity), track every particle and identify them over a wide dynamic range from tens of MeV/c to hundreds of GeV/c. Studying particle energies around 200 MeV is particularly interesting because it can give an insight into the phase transition of QCD matter. According to the Letter of Intent, ALICE needs to:

- be versatile, to assess a variety of observables, including some that may only be relevant in the future.
- have a large enough acceptance, especially at mid-rapidity, to study the region of the phase-space where the baryon density is low and the energy density is high.
- be robust because it will be the only experiment studying specifically heavy-ions at such energy.
- be flexible to accommodate future upgrades or additions to the design.

ALICE is a massive set of detectors sketched in Figure 3.3, 16 m high, 16 m wide, 26 m long, weighing 10000 tonnes, around 50 m under Point 2, at Saint Genis-Pouilly in France. The apparatus comprises a number of subsystems that can be grouped depending on their rapidity coverage. The central barrel, at mid-rapidity ($|\eta| < 1.5$), focuses on particle identification (using a wide variety of methods, including Bethe-Bloch energy loss, time-of-flight, Cerenkov radiation) and tracking. As of Run 2, it comprises the Inner Tracking System (ITS), the Time Projection Chamber (TPC), the Time Of Flight detector (TOF), the Transition Radiation Detector (TRD), the High-Multiplicity Particle Identification Detector (HMPID), the PHOton Spectrometer (PHOS), the ElectroMagnetic Calorimeter (EMCAL), the Dijet Calorimeter (DCAL). At forward-rapidity, we find the Zero-Degree Calorimeter (ZDC), the

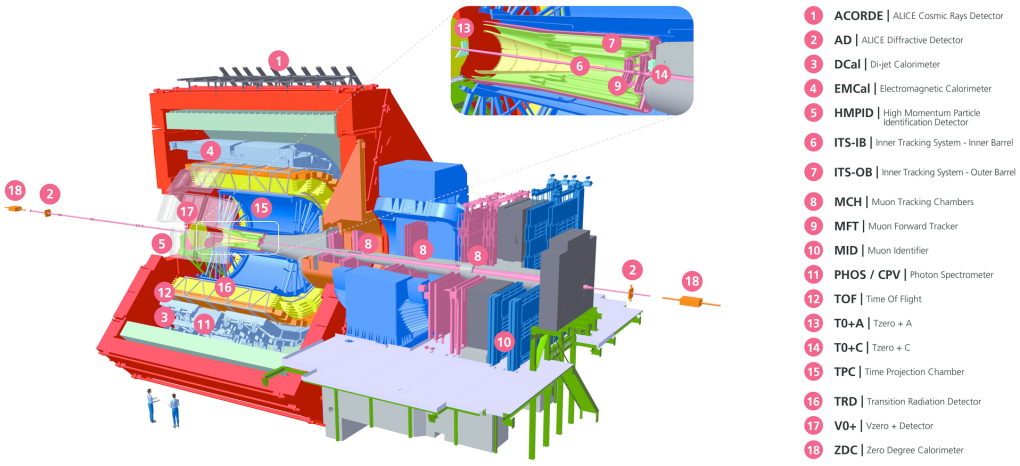

Figure 3.3: Sketch of the ALICE experiment with its subsystems after LS2 upgrade.

Photon Multiplicity Detector (PMD), the Forward Multiplicity Detector (FMD), T0, V0, the Muon spectrometer for tracking and triggering (MCH + MID). For an extensive technical review of ALICE and its detectors, see Ref. [216]. Run 1 performance report is available in Ref. [217]. We will focus on the main subsystems that are relevant for the data analysis presented in this thesis. An overview of recent and future upgrades will be given at the end of this chapter.

3.2.1 Inner Tracking System (ITS)

The Inner Tracking System (ITS) is a cylindrical detector located the closest to the interaction point. Its Technical Design Report (TDR) is available in Ref. [218] and a sketch is visible in Figure 3.4. The ITS is made of six cylindrical layers of silicon detectors representing in total 6.28 m^2 of detection planes, allowing tracking, vertexing and particle identification, in particular at low momentum. The radii of the layers were chosen to optimize the tracking abilities of the ITS. Notably, the outer layer is constrained by the necessity to have a tracking complementary to the one of the TPC, while the beam pipe constrains the inner layer. Inside-out, the two first layers are Silicon Pixel Detectors (SPD), the middle two are Silicon Drift Detectors (SDD), and the last two are Silicon Strip Detectors (SSD). Overall, all six layers cover the pseudorapidity range $|\eta| < 0.9$ simultaneously. The SPD layers cover $|\eta| < 1.4$ and $|\eta| < 2.0$ for the outermost and innermost layer, respectively. They ensure complete coverage in the charged particle multiplicity measurement with the FMD.

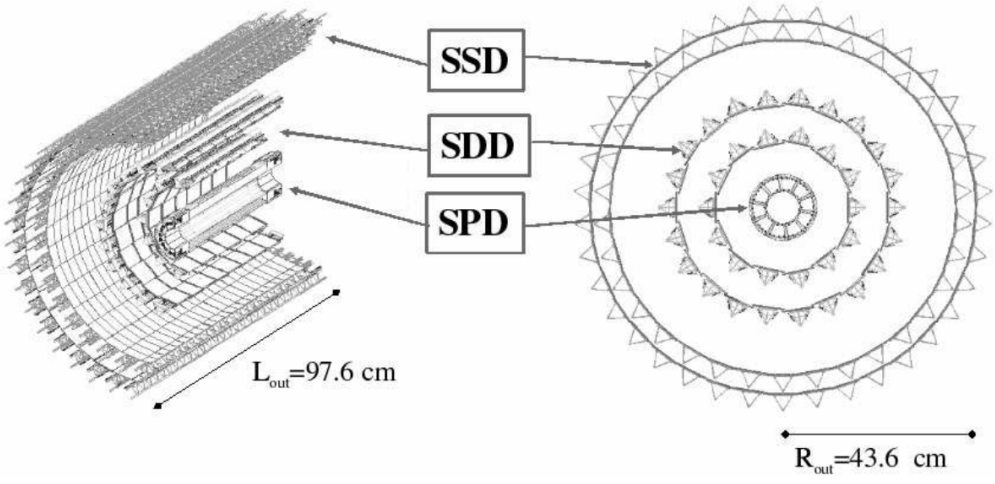

Figure 3.4: Sketch of the ITS, from Ref. [216].

SPD layers (of radii 3.9 and 7.6 cm) are used to determine the primary vertex and possible secondary vertices coming from beauty decays if they are far enough (100 µm away) from the primary vertex. The SPD layers were optimized to work under the expected extreme conditions of heavy-ion collisions, handling more than 8000 charged tracks per unit rapidity, that is to say, up to 15000 tracks simultaneously, according to upper limits from theoretical predictions at the time of design. Several million silicon cells are needed to keep the occupancy at the percent level in these conditions. They have been tested for radiation hardness as they would have handled a total dose of 200 krad in the first ten years of operation. Outer layers making up the SDD (radii of 15 and 23 cm) and SSD (radii of 38 and 43 cm) are subject to lower particle densities, and analogue readout is used to allow for measurement of energy loss and particle identification. Finally, because momentum and impact parameter resolutions are limited at low-p_{T} by multiple scatterings, the ITS material budget has been limited to 7.2% of a radiation length for a trajectory perpendicular to the beam pipe at mid-rapidity.

In the analysis presented in this thesis, the SPD layers of the ITS are used for vertexing by identifying the interaction point, counting and reconstructing light particle tracklets in the central barrel and obtaining their kinematics (transverse momentum, azimuthal angle, pseudorapidity).

3.2.2 Time Projection Chamber (TPC)

The TPC [219] (see Figure 3.5) is the main tracking apparatus of ALICE at midrapidity. It is a cylinder of inner and outer radii of 85 and 250 cm, respectively, 5 m long, spanning from $z = -2.5$ m to $z = +2.5$ m, containing around 90 m^3 of gas. The TPC can track charged particles efficiently for momenta between 100 MeV/c and 100 GeV/c, identify said particles and reconstruct vertices. The TPC works jointly with other central barrel detectors like ITS, TRD and TOF for track reconstruction on the whole radial length within $|\eta| < 0.9$. However, it can also reconstruct tracks on a reduced radial length within $|\eta| < 1.5$. The chamber benefits from a complete azimuthal acceptance, except for some dead zones between the readout chambers.

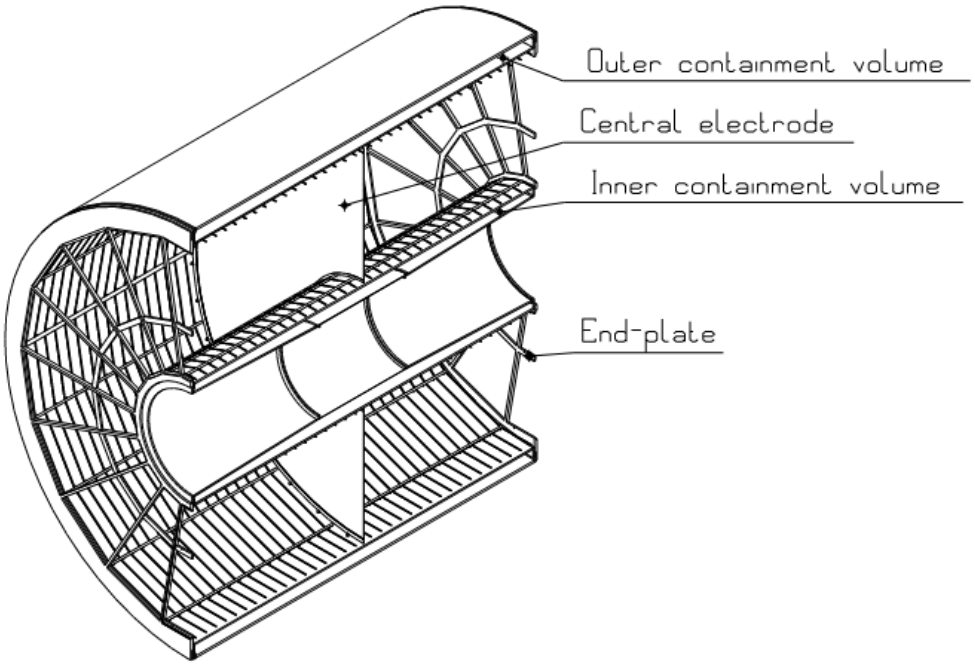

Figure 3.5: Cut view of the TPC without its readout chambers at the end-plates, from Ref. [219].

When charged particles go through the TPC volume, they ionize the gas. The gas is a mixture of Ne/CO_2/N_2 (90/10/5), based on the experience of the NA49 experiment, to which N_2 was added to increase gains [219]. It fills the cylindrical volume in which a uniform electric field of 400 V/cm is applied thanks to a high-voltage electrode at $z = 0$ (100 kV) and two opposite potential dividers.

The ions and electrons from the interaction between a charged particle and the gas will drift towards the electrodes. In particular, the electrons, whose drift time is at most 90 µs, will leave signals in the cathodes at both end caps of the TPC which are instrumented with multi-wire proportional chambers. The principle of such proportional chambers is similar to that of the muon chambers, which is covered further in this chapter. Each endcap of the TPC is subdivided into 18 trapezes. Each trapeze is filled by two planes of readout chambers, whose pad size increases with the radius to accommodate for the increase in occupancy towards small radii. In particular, in central Pb-Pb collisions at 1 kHz, the TPC is designed to ensure a maximal occupancy of 40% at the inner radius and 15% at the outer radius. Central Pb–Pb collisions impose hard design constraints due to the 20000 simultaneous tracks they can create in the TPC, leading to distortions of the electric field due to space-charge effects. Proton-proton collisions show way less activity and barely create any notable distortion. However, their interaction rate is constrained by the drift time of the electrons from prior events.

The TPC is not used in the analysis presented in this thesis due to its unavailability for the data we use. For our concern, the ITS covers the necessary vertexing and tracking at mid-rapidity.

3.2.3 V0 detector

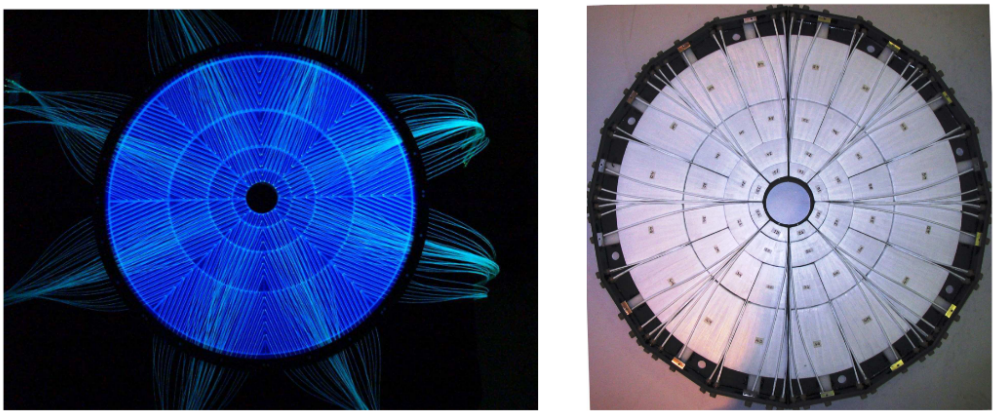

Figure 3.6: Front view of V0A (left) and V0C (right), from Ref. [216].

The V0 [220], visible in Figure 3.6, is a forward and backward rapidity detector. It is made of two arrays of scintillator counters around the beam pipe. V0A, situated at $z = +3.4$m within $2.8 < \eta < 5.1$ and V0C, situated at $z = -0.9$m within $-3.7 < \eta < -1.7$. Both elements consist of 4 concentric rings subdivided into eight sectors each. A crossing particle excites the scintillating medium, which by de-excitation generates light transported to photo-multipliers by sets of optical fibres. In pp, only 1 or 2 particles are expected per segment, they must be efficiently detected. In Pb–Pb, this number ranges from 1 to 1000, which sets constraints on the yield of the scintillators, which must accommodate for the detection of very sparse and very dense signal alike. It also constrains the time resolution and the quick response from the front-end electronics. V0 is used as a low-level trigger, by putting a threshold on deposited energy. A coincidence of signals within V0A and V0C constitutes a Minimum Bias (MB) trigger in which parasitic beam-gas events are rejected. The V0 also acts as a filter for background rejection in the dimuon spectrometer.

In most analyses, the V0 is used to estimate the centrality, especially in Pb–Pb. As the response from the detector increases with particle multiplicity, centrality can be defined for recorded events based on the V0 output. Centrality is a percentile which ranks the events based on the activity of the detectors. 0% corresponds to the most central event, so the most active, with the highest multiplicity. 100% corresponds to the most peripheral event, with the lowest multiplicity. The matching between V0 output and centrality is done using a Glauber fit [23]. In Pb–Pb collisions, centrality can also be linked to the impact parameter of the collision as a smaller impact parameter will lead to more head-on collisions producing more particles.

In the analysis presented in this thesis, the V0 detector is used in triggers and centrality estimation. In Pb–Pb flow analyses, the V0 can estimate the reaction plane of the collision. In pp collisions the

reaction plane estimated from the V0 is not sufficiently accurate, therefore a pair correlation method was used to assess the elliptic flow, as described in Chapter 2.

3.2.4 Muon spectrometer

The muon spectrometer, seen in Figure 3.7, is an example of the modularity and adaptability of ALICE. It was not planned in the original design but was considered in 1995 (see Refs. [221, 222] for its TDR and addendum) and added to the Technical Proposal [223]. This forward rapidity spectrometer ($2.5 < \eta < 4.0$, $2.5 < y < 4.0$ for the J/ψ) allows the measurement of open and closed heavy flavour hadrons, gauge bosons, and low-mass hadrons in their (di)muon decay channel. The muon spectrometer comprises multiple elements: absorbers, tracking chambers, a dipole magnet and trigger chambers.

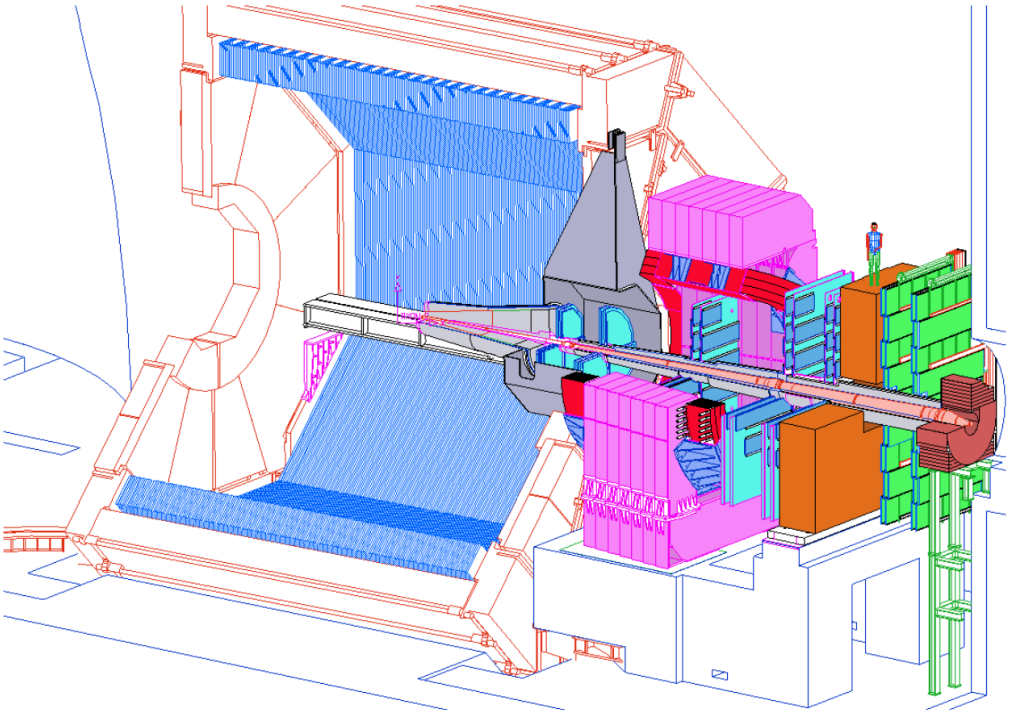

Figure 3.7: Cut view of the muon spectrometer from Ref. [216], displaying the dipole magnet in magenta, the tracking chambers in cyan, the back absorber in orange, the trigger chambers in green and all other absorbers in grey.

The role of the absorbers is to shield the active parts of the muon spectrometer from parasitic background signals. A front absorber in the shape of a cone around the beam pipe protects the muon chambers from hadrons or secondary particles. Around the beam pipe, a lead and steel shielding is added to protect the chambers from high-rapidity particles and beam-gas interactions. A muon filter is located after the tracking chambers and before the trigger chambers. It is an iron wall, 1.2 m thick, that stops the remaining energetic hadrons so that they do not manage to get to the trigger. Finally, an iron wall after the trigger chambers suppresses background particles from beam-gas interactions in the LHC.

The tracking is based on five stations: two before a dipole magnet, one within the dipole magnet, and the last two after it. Each station is made of two detection planes and the detectors are shaped in quadrants for the first two stations. For the other stations, the detectors are slats that are arranged to build circular stations that cover the forward rapidity range and give full azimuthal coverage. The detectors themselves are multi-wire proportional chambers (MWPC, schematically represented in Figure 3.8) where a volume of gas (a mixture of Ar and CO_2) is enclosed between cathode planes with a plane of anode wires in the middle. An electric field is created by applying a voltage of around 1700 V to the anode. Each cathode plane is segmented into pads whose dimensions depend on the expected particle density, making the mesh thinner close to the beam pipe. As charged particles trajectories are

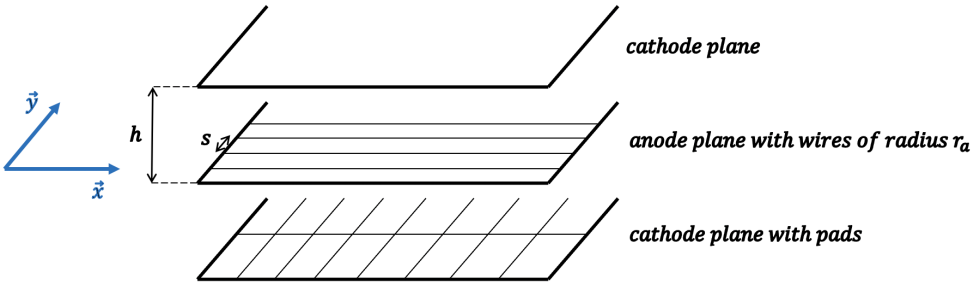

Figure 3.8: Representation of a multi-wire proportional chamber as implemented for muon tracking.

curved vertically under the action of a magnetic field, the cathode plane having the best resolution in the vertical direction is labeled the bending plane, while the other is the non-bending plane. When a particle crosses the detector, it ionizes the gas and the produced electrons drift towards the anode wires. Close to the wire, they are further accelerated, and they produce an avalanche creating other electron-ion pairs. The ions drift towards the cathode planes, where they deposit their charge, creating signals on the pads which can be processed by the electronics as follows.

The front-end electronics read the sampled signal from the cathode pads, and the signal is directly integrated by the ADC (Analog-Digital Converter). Through buses and ribbon cables, data is sent to CROCUS (Cluster Read Out Concatenator Unit System), which concentrates the data from the detectors. Signals are then sent through optical fibers to the RORC (ReadOut Receiver Card), communicating with the LDC (Local Data Concentrators) and the trigger system.

The dipole magnet, within which we find the third muon tracking station, is a resistive magnet producing a magnetic field along the horizontal direction, with a field integral of $\int Bdz = 3$ Tm. The charged muon tracks are then bent vertically by this field. Reconstructing the particle's trajectory from the hits left in the tracking chambers, one can determine the p_{T} of the muons using the curvature of the trajectory.

The two trigger stations are located at the end of the spectrometer. Each is composed of two trigger planes: resistive plates connected to reading strips that detect the signal deposited from a crossing particle. If a muon is detected and has a p_{T} above a certain threshold (to suppress parasitic decays at low p_{T}), the apparatus is triggered, and the current event can be classified as having a muon.

In this analysis, the muon spectrometer is used to reconstruct the forward muon tracks allowing us to study the dimuon decay of the J/ψ. Using kinematic information from the tracks like the transverse momentum deduced from the curvature, the pseudorapidity, or the azimuthal angle of the J/ψ, pair correlations methods can be applied. They evaluate the angular correlations between particles and ultimately allow us to measure the J/ψ flow.

3.2.5 Software

In order to facilitate data acquisition and avoid recording noise, triggering is used at the level of the whole experiment. The triggering is done on three levels, handled by the Central Trigger Processor (CTP). It aims to select events that could be useful for physics studies. Level 0 (L0) is the fastest as it reacts in 1.2 µs after the collision by taking input from fast detectors (including V0 and muon trigger) to start the readout. Level 1 is slightly slower, as it waits for 6.5 µs to take in the input from the TRD, ZDC and EMCal, and Level 2 is the slowest as it waits for 100 µs which is the time needed for the electrons in the TPC to drift. Based on information from the trigger levels and the physics program, which dictates which trigger classes (groups of triggers) should be considered, events are selected or discarded. If selected, the events are stored on disk and are processed offline into ESD (Event Summary Display), which can be further filtered into AOD (Analysis Object Data), containing the information necessary for physics analyses. Due to the vast amount of data saved by the LHC, the data processing and analysis is done offline over a distributed computing grid. Processing units and data storage are dispersed worldwide, allowing parallel data processing. Information concerning the runs, the detectors' status and the alignment are stored in databases to be accessed for analyses.

AliRoot [224], the ALICE analysis software, is based on ROOT [225], a C++ framework dedicated to high-energy physics analysis. AliRoot provides the tools and libraries needed for developing the physics data analysis, as well as to process the distributed AODs on the grid.

On the grid, simulated data from Monte Carlo events are also available. Monte Carlo events are simulated by using an event generator, like PYTHIA [226] for proton-proton collisions or HIJING [227] for larger systems. Then the particles are propagated to the detectors using GEANT software, where hits can be simulated. The resulting data is then stored in ESDs and AODs as any actual event would be.

3.2.6 The LS2 Upgrades towards Run 3 and beyond

Data acquisition architecture

Due to the increased data rate expected in Run 3, a continuous readout architecture was put into place and required a change in the overall structure of the readout electronics and data acquisition systems, as described in Ref. [228]. Raw data from the detectors are sent from the front-end electronics (FEE) to the CRU (Common Readout Unit) via GBT (GigaBit Transceiver) links. The CRU communicates with the Detector Control System (DCS) via high-speed PCI interfaces. The CRU also receives triggering and timing information from the Central Trigger Processor (CTP).

Instead of waiting for Physics triggers, as was the case in Run 2, ALICE can now work in continuous mode. Acquisition happens during dedicated time windows called time frames. All detectors working in continuous mode receive a timing signal from the LHC clock allowing data to be timestamped and time frames to be defined over all detectors. Time frames, which last 11.3 ms, are further subdivided into 128 orbits (also called heartbeat frames) of duration 89 µs. For the muon chambers in continuous mode, the samples from the pads are continuously read. When they exceed a programmable threshold (currently set at three samples at 3 ADC channels each), data is recorded until the samples fall below the threshold. The acquisition window is widened at its start and at its end by three and nine samples, respectively, ensuring that the whole head and tail of the signal are recorded. However, the muon spectrometer can still run in triggered mode by opening a data taking time window if a Physics trigger is received.

For a given time frame, data from the detectors are distributed among the FLPs (First Layer Processors) for fast data treatment. Then, the EPNs (Event Processing Nodes) process the data from all the FLPs corresponding to the same time frame and store the result.

The description of the experiment and its detectors is based on its status before Long Shutdown 2 upgrades [229, 230] between 2018 and 2022. During LS2, the main upgrades were the ITS2, the FIT detector, the TPC, the MFT, the O2 software, and a general revamp of the readout electronics.

ITS2

To face the challenges of data taking in Run 3, namely the increase of the event rate to 50 kHz in Pb–Pb (200 kHz in smaller systems) and the need for a better spatial resolution, especially at low p_{T} (which would facilitate secondary vertexing), the ITS was completely overhauled, as described in Refs. [231, 232]. ITS2, see Figure 3.9, comprises seven layers fully covered with silicon pixel sensors (29.2 µm $\times$ 27.9 µm). Together, the 12.5 billion pixels represent 10 m^2 of active area spanning the mid-rapidity region ($|\eta| < 1.22$). The pixel matrix is mounted on ALPIDE (Monolithic Active Pixel Sensor) chips based on CMOS technology [233]. The seven layers span radii from 23 to 400 mm. The innermost layer is then closer to the interaction point, thanks to the beam pipe radius reduction to 19.2 mm. For the three innermost layers, the Inner Barrel, the thickness of the chips is reduced to 50 µm, keeping the material budget of an inner layer at 0.35% of a radiation length compared to the Run 2 1.14%. This new detector allows for a better tracking efficiency, a better spatial resolution for secondary vertexing and impact parameter determination, and handling of the hundred times increase of the readout rate.

FIT

The Fast Interaction Trigger (FIT), described in the TDR [228] and represented on Figure 3.10, is the assembly of detectors that supersedes the Run 2 V0 detector. It is composed of the FT0, based on Cherenkov modules with an efficiency above 99% and a timing resolution of 13 ps giving a start-time

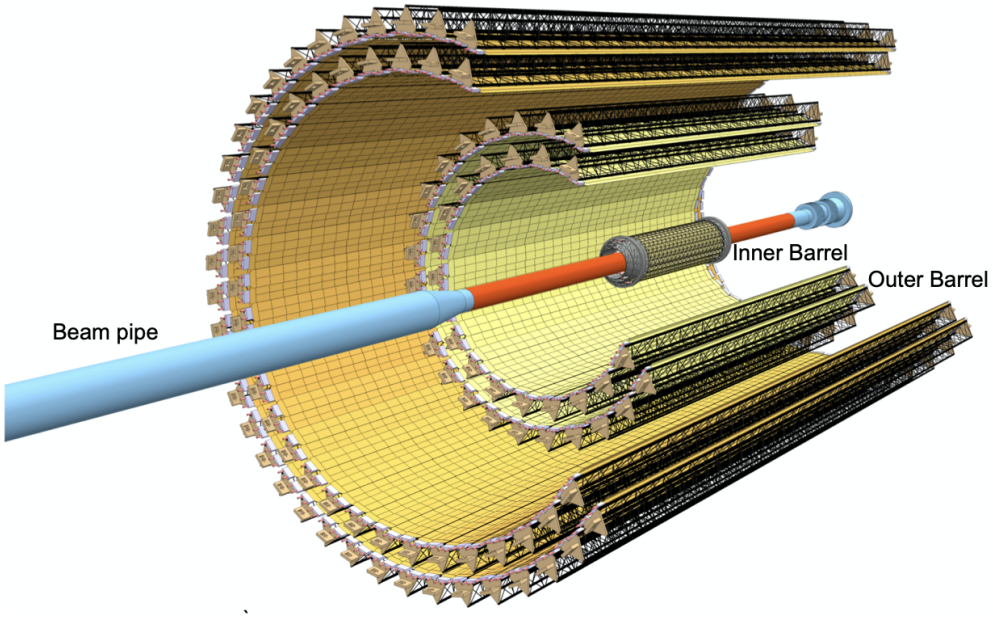

Figure 3.9: Layout of the ITS2, from Ref. [231].

for the TOF. The FV0 and the FDD are improved versions of the V0 and diffractive detectors, using similar electronics as the FT0.

The FIT is the leading fast trigger of the experiment (in minimum bias events, it offers a latency of fewer than 425 ns). It also serves as a tool to measure luminosity, multiplicity, centrality, and the event plane's position.

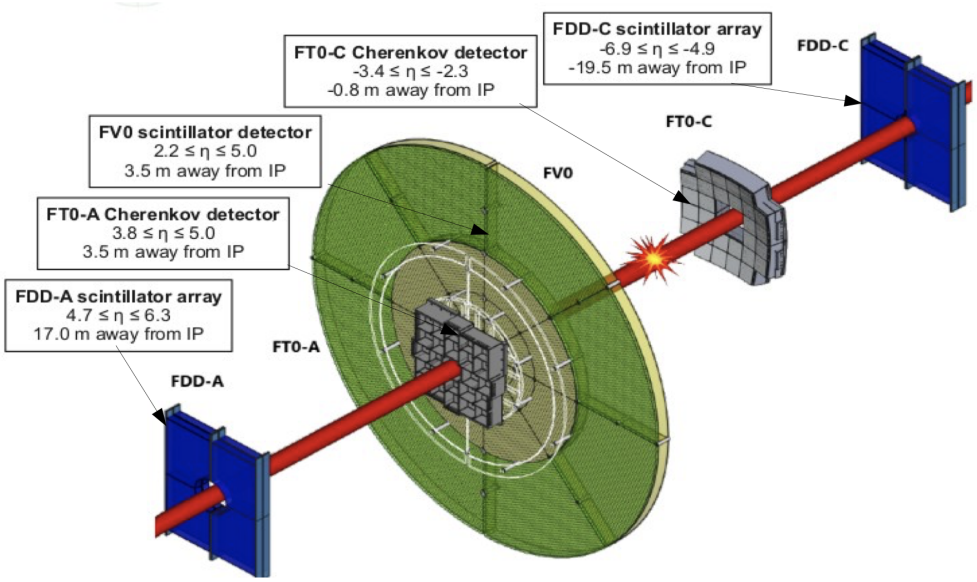

Figure 3.10: Layout of the FIT, from Ref. [234].

TPC

With the event rate increase in Run 3, the TPC faces many challenges. First, there is the need to switch to continuous readout electronics as the electron drift times would mean reading multiple events in the same readout time. The readout must also accommodate the increased data rate of more than 3 TB/s, which also calls for data reduction. The space-charge distortions in the drift volume must be minimized to be corrected in software. However, the current abilities of the TPC in both momentum and dE/dx resolution must be preserved.

In this regard, the main upgrades of the TPC as described in Ref. [228] are: the redesign of the front-end and readout electronics, adapted for continuous readout; the ability to reduce data online; a change of the gas mixture to Ne-CO_2-N_2 for its higher ion mobility, which reduces space-charge accretion; and stacks of four GEMs shown in Figure 3.11 (Gas Electron Multipliers) for the detection of the signals at the cathodes.

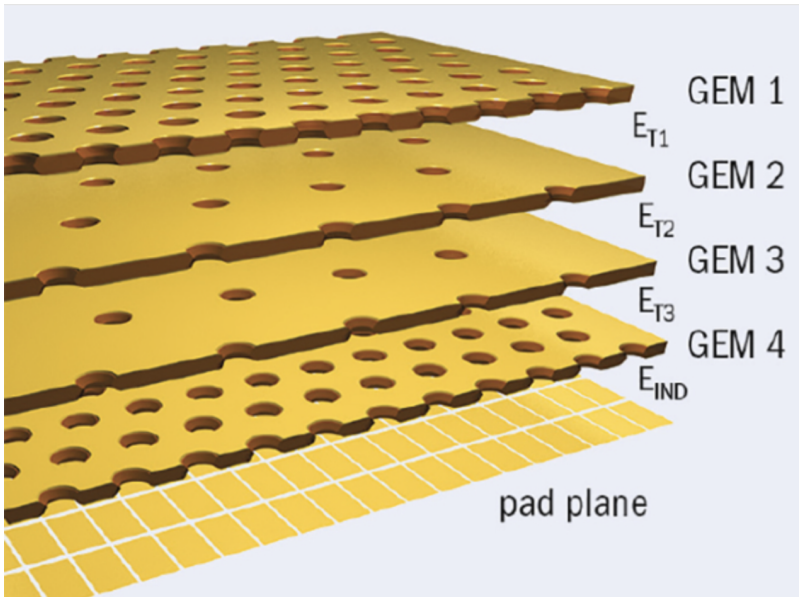

Figure 3.11: Representation of the quadruple GEM layout used for the TPC upgrade, from the ALICE Collaboration.

A GEM is composed of a cathode and an anode plane, between which we find a micro-mesh covered in microscopic holes bathing in gas. When a particle crosses the gas volume, electron-ion pairs are created. An electric field makes electrons drift towards the mesh between the cathode and the micro-mesh. When crossing the microscopic funnels, the electrons are subject to an intense electric field and form electron-ion pairs. On one hand, the electrons drift towards the anode, crossing the amplification region causing cascades which will enhance the signal. On the other hand, the ions drift towards the micro-mesh. However, there is a chance that an ion could escape back from the funnel into the drift volume, creating local field distortions. This process is called ion backflow. Using a stack of four GEMs allows for an amplification of 2000 while minimizing the ion backflow to an acceptable level of less than 1%.

MFT

The Muon Forward Tracker (MFT) [235], shown in Figure 3.12, is a new forward detector added during LS2 ($-3.6 < \eta < -2.5$). It uses silicon tracking to add vertexing capabilities to the muon spectrometer. This apparatus allows new measuring abilities, including separating prompt and non-prompt J/ψ and distinguishing between open-beauty and open-charm production. The MFT comprises two half-cones with five half-disks, each spanning from -460 mm to -768 mm from the interaction point. The same silicon pixel technology and readout electronics as the ITS2 are used. The detector comprises 896 ALPIDE chip sensors arranged in vertical ladders of 1 to 5 sensors each.

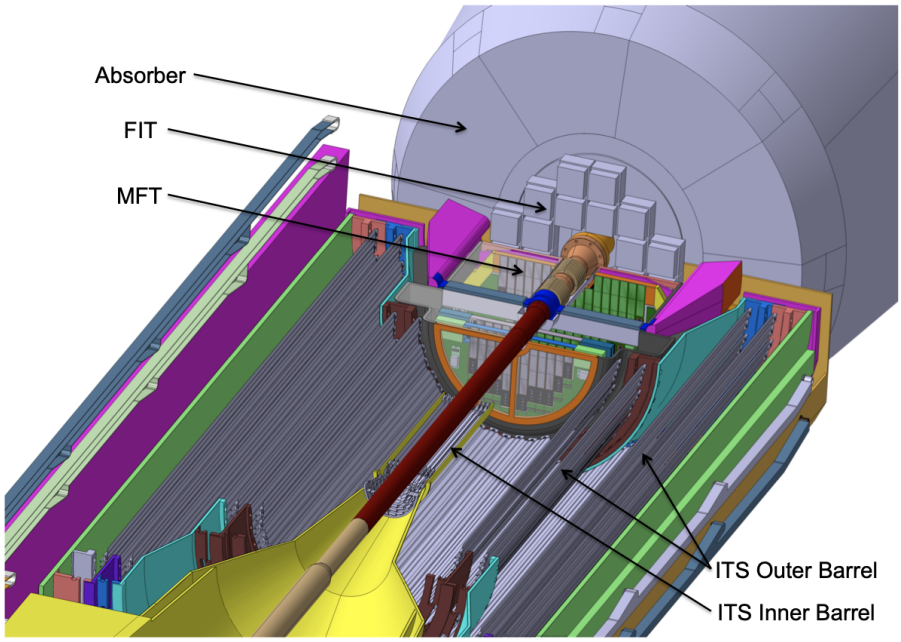

Figure 3.12: Layout of the MFT, from Ref. [235].

Muon Trackers

As of Run 3, the detectors of the muon spectrometer remain unchanged. Only the electronics were modified as discussed in Ref. [228], a diagram of the new electronics is shown in Figure 3.13. Signals from the pads are sent to SAMPA chips which can accommodate for 32 pads at once. The signal is sampled at 10 MHz, once every four LHC clock tics, also called bunch-crossings. The SAMPA chip converts the samples to digital values via a 10-bit ADC (Analog-to-Digital Converter). The pedestal values can be automatically computed and subtracted and only signals exceeding the pedestal by a programmable threshold are transferred to the DAQ (Data AcQuisition).

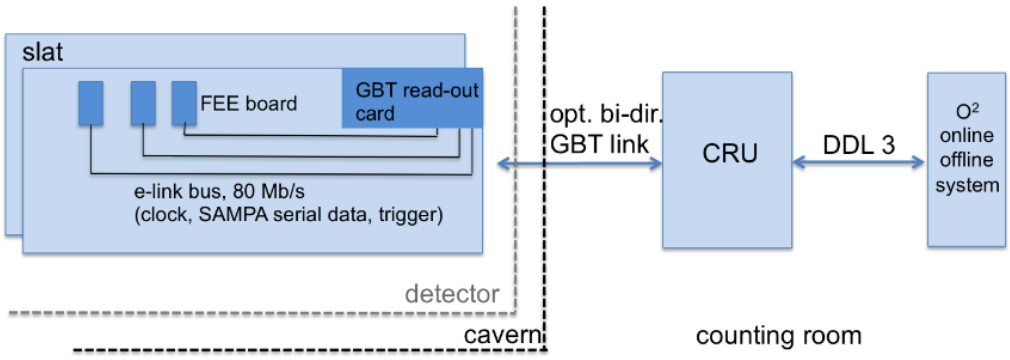

Figure 3.13: Schematics of the post-LS2 electronics of the muon spectrometer from the FEE to O^2, from Ref. [228].

Using flexes and flat cables, DualSAMPA boards (accommodating for two SAMPA chips) are connected to SOLAR boards housing the GBTx [236] chips and the VTRx [237] optical transceivers. The GBTx receives the data from the DualSAMPA boards at a rate of 80 Mb/s, and provides the I2C slow control interface for the configuration of the SAMPA parameters. The VTRx handle the bi-directional communication with the Common Reaout Unit (CRU) boards at a data rate of 3.2 Gb/s. Together, GBTx and VTRx provide the wired and optical connections to the CRU. CRUs send data to the FLPs, followed by the EPNs as discussed previously.

In total, MCH uses 11 FLPs. Each of them accommodates for 3 CRUs at most. Each of the 32 CRUs house 24 SOLAR boards, on each of which 40 DualSAMPA can be connected. Overall, 17000 DualSAMPA are linked to 624 SOLAR boards.

O^2

ALICE has developed a new Online-Offline (O^2) software framework for the processing of Run 3 data, from the low-level data decoding to the high-level physics analysis. For a full technical review, see its TDR [238] and Ref. [239]. It works in a synchronous mode for fast primary data processing and reconstruction and in an asynchronous mode where the data stored in disk buffers are fully processed and converted to AODs for further analysis. O^2 gives a distributed and efficient way to process data. It is divided into three parts: first, the transport layer, which defines the different devices used for data taking and processing; second, the data model which defines the message format as well as the mapping to data objects; third, the data processing layer (DPL), which is a high-level tool hiding the complexity of the two previous layers. Using a unified message format, the DPL connects the data producers to the data consumers and allows for pipelining, making it intuitive for end-users to define analysis workflows by plugging different tasks together. For example, as discussed in the next chapter, the Quality Control workflows are developed in O^2. A first task can decode raw data from the detectors. It can also be converted into a new data format that can be processed by another task that outputs histograms stored on disk.

This high modularity of the workflows allows serializing analyses and using computing power more efficiently. In this regard, various analyses based on the same datasets can be combined together on virtual "analysis trains" (Hyperloop) to optimize the access to grid resources.

Further upgrades

During LS3 (2026-2028), further upgrades are planned for ALICE, seen on Figure 3.14. First, there is ITS3 [240], in the continuity of ITS2, further reducing the material budget. The inner barrel and the beam pipe will be rebuilt to have active detectors even closer to the interaction point, with the first layer at a radius of 18 mm, using bent ALPIDE chips. Second, a set of forward calorimeters (Focal [241]) spanning $3.4 < \eta < 5.8$ will be used to measure direct photons and π^0 and associated hadrons to quantify gluon nuclear modification at small-x and Q^2 and to access non-linear QCD regime.

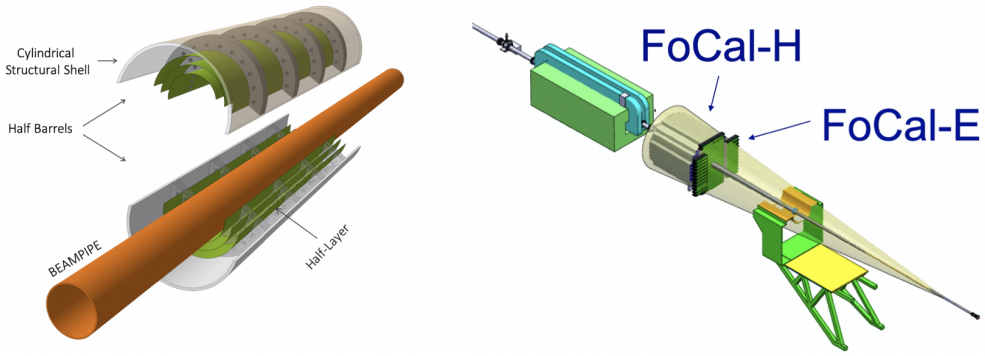

Figure 3.14: Layout of the ITS3 (left) from Ref. [240], and Focal (right).

During LS4 (in the mid-2030s), ALICE3 [242] seen in Figure 3.15, will replace ALICE. Its physics program offers precision measurements of dileptons, which would probe the evolution of the QGP, systematic measurements of heavy-flavour hadrons to study transport properties and hadronization mechanisms, and measurements of hadron correlations. Going to higher energies would necessitate accelerating the beams further, which means building a collider with a higher curvature radius or building more powerful magnets that could swerve the beams more. The larger FCC (Future Circular Collider) should supersede the LHC with its 100 km circumference. The LHC would become an intermediate injector to get the beams into the FCC, as was the case of SPS and others for the LHC.

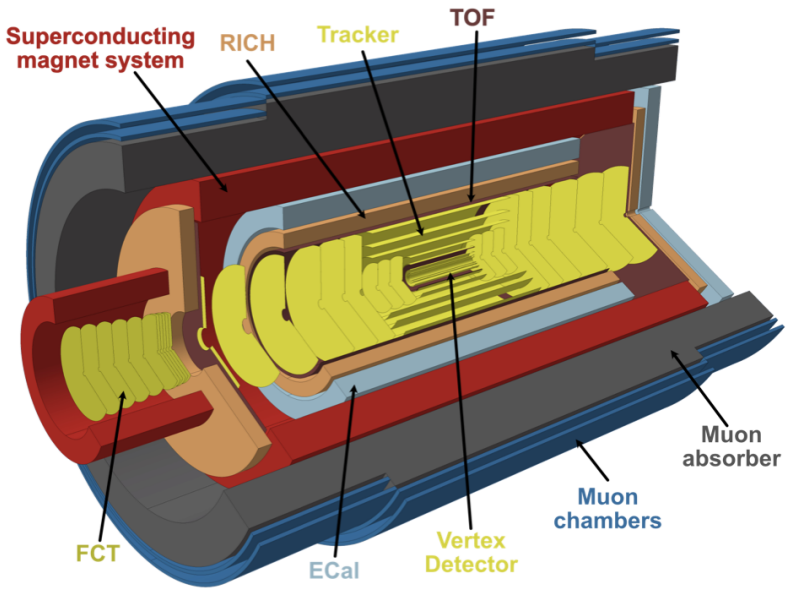

Figure 3.15: Detector concept layout of ALICE3, from Ref. [242].

Chapter 4

Commissioning the muon spectrometer

Cassé, (wo oh) cassé, ça passera avec le temps ou quelqu'un d'autre / Cassé, (wo oh) cassé, ça passera ça prend du temps pour être une autre.

– Nolwenn Leroy, *Cassé*

In this chapter we will discuss two topics related to the processing of the data coming from the upgraded readout electronics of the Muon spectrometer (see Sec. 3.2.6).

In the first part we will describe the upgrades to the cluster fitting procedure that are needed in order to cope with the different signal digitization method of the new electronics. In the second part we will introduce the ALICE Quality Control framework and discuss the development of the data analysis tools that are specific to the muon chambers.

4.1 Upgrade of the hit clustering algorithms

As presented in Chapter 3, the electronics of the muon spectrometer has been upgraded during LS2. While the tracking chambers detectors remain unchanged, the method used to digitize the detector signals differs between Run 3 and Run 2. In particular, we expect differences in the amplitude of the electronics noise superimposed to the charge measurements, and on the effective minimum threshold for signal detection. This change affects the clustering procedure, which allows to estimate the position of the original particle hit from the charge distribution on the cathode pads. Knowing the hit position in each chamber then allows one to reconstruct particle tracks and obtain physical information on the particle. In order to assess the effects of the new front-end electronics on the clustering, test beam data was recorded, which allowed one to study the detector response to a particle hit and compare the clustering results to the real hit positions recorded by a silicon tracker. However, the amount of test beam data is limited. In order to delve deeper into the study of the electronics behaviour and its impact on clustering procedures, we developed a fast Monte Carlo simulation of the electronics response that has been tuned to reproduce the test-beam data as accurately as possible. It also provides accurate detector simulations for future physics analyses.

In this section, we will cover the status of the detector and clustering during Run 2, the test beam data and its results, as well as the Monte Carlo implementation and tuning.

4.1.1 Detector geometry and charge distribution

The description of the muon tracking chambers and their geometry is discussed in Chapter 3. Each chamber is composed of multiple detection elements arranged around the beam pipe. Each detection element is a multi-wire proportional chamber made of two cathode planes enclosing a gas mixture in which bathe anode wires. As a particle crosses the volume, it ionizes the gas and the electrons drift towards the wires under the action of a voltage of around 1700 V. More electron-ion pairs are created in the vicinity of the anode and the ions drift towards the cathodes, segmented into pads, leaving signals

which are read by the electronics [243]. A schematic representation of the anode and cathode planes is shown in Figure 3.8.

The deposited charge on each pad can be described by the Mathieson-Gatti distribution, which gives the normalized charge along any dimension (x, parallel to the anode wires or y, orthogonal to the anode wires) and is defined as follows

$$\frac{\rho(\lambda)}{q_a} = K_1 \frac{1 - tanh^2(K_2\lambda)}{1 + K_3 tanh^2(K_2\lambda)} \text{ with}$$
$$K_1 = \frac{K_2\sqrt{K_3}}{4tan^{-1}(\sqrt{K_3})} \text{ and}$$
$$K_2 = \frac{\pi}{2}(1 - \frac{\sqrt{K_3}}{2}),$$

where λ is the distance along the cathode in units of the anode-cathode separation h, s the anode wire pitch, and r_a the radius of the anode wires, as represented in Figure 3.8. K_n are constants determined by the geometrical parameters of the detector.

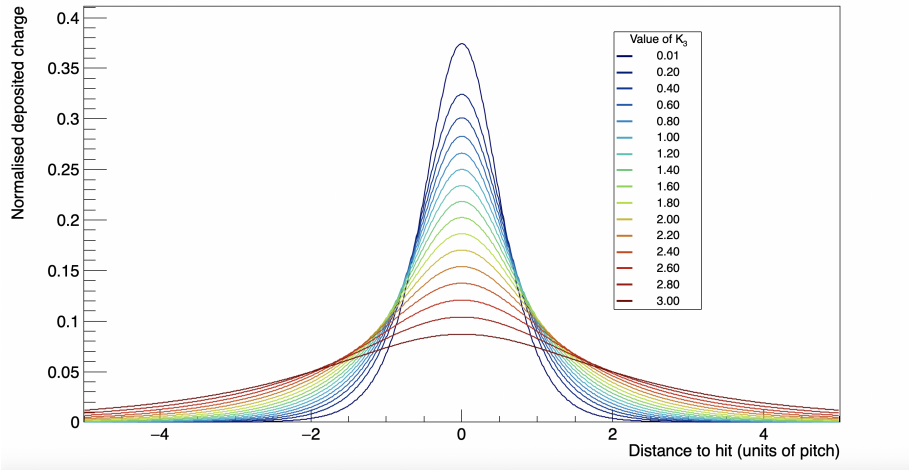

Figure 4.1: Shape of the Mathieson-Gatti distribution for different values of the paramater K_3.

The width of the Mathieson-Gatti distribution is encoded in the parameter K_3, as seen in Figure 4.1 where we see that increasing K_3 spreads the distribution more.

As K_3 depends on the direction of the wires in the detector, two coefficients are in principle needed for the bending ($K_{3x} = 0.5085$) and non-bending ($K_{3y} = 0.5840$). They are obtained using the geometry of the detectors as described in the Technical Design Report [221, 222]: anode-cathode separation and anode wire pitch both equal to 2.5 mm, and radius of the anode wires equal to 10 µm. The quadrants of the first tracking station have a slightly smaller pitch of 2.1 mm, and therefore slightly different K_3 values.

The computation of the Mathieson-Gatti distribution is quite CPU-intensive, therefore we also tested an approximation based on two gaussian distributions: one gaussian reproduces the core of the Mathieson, and another the tails, as seen in Figure 4.2.

4.1.2 Digitization, pre-clustering and cluster fitting

As the charges are deposited on the cathode pads, the DualSAMPA (DS) boards sample the deposited charge every 100 ns. Digits are then constructed from the raw ADC samples; they contain a pad identifier, the time of the hit, and the total amount of charge deposited on the pad obtained by summing the individual samples. Using the detector mapping, which connects the pad identifiers to the actual geometry of the detectors, the digits are then preclusterized.

Pre-clustering is the step during which fired pads on both cathodes that are geometrically correlated are grouped together. Based on hit time and pad positions, preclusters are connex components spanning

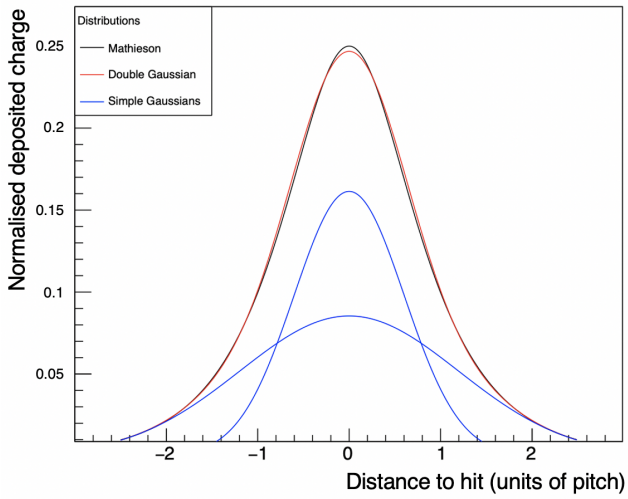

Figure 4.2: Shape of the Mathieson-Gatti distribution ($K_3 = 1$) reproduced using two gaussians.

both cathodes, consisting of digits belonging to neighboring pads. Figure 4.3 represents the simulated charge deposit of hits in a fictitious detector. Each histogram bin with a non-zero charge will be assigned a digit. We can observe two connex groups of digits, each spanning both cathode planes.

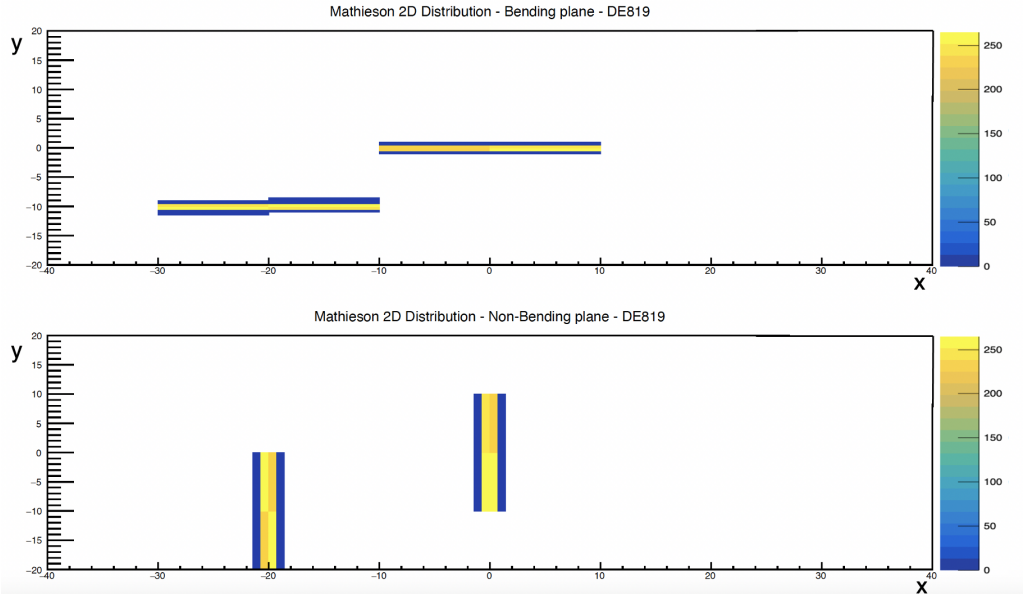

Figure 4.3: Simulation of a pattern of charge deposit, where two particles hit the detector creating two preclusters spanning both cathode planes. Top: bending. Bottom: non-bending.

Next, the pre-clusters are processed in order to estimate the coordinates of the track impact point on the detector (clustering step). Because the pads on the bending plane are thinner in the y direction, the bending plane will constrain the y coordinate of the hit. On the non-bending plane, pads are thinner in the x direction and will constrain the x coordinate better. During the clustering phase, pre-clusters that originate from overlapping charge deposits are also split into separate charge clusters.

Once the coordinates of the particle hits on each detection chamber are determined they can be used in track reconstruction for physics analyses.

In the following we will follow two main approaches to estimate the cluster coordinates: algorithms based on weighted averages and algorithms based on fits of the charge distribution.

Algorithms based on weighted averages are easy to implement and very quick to run. The most simple consists in computing the center of gravity (COG) of the charge distribution as the average of the pad coordinates weighted by their deposited charge.

Algorithms based on fitting the charge distribution are more complex than the weighted average and take more time to run. A template for a theoretical charge distribution is assumed and fitted to the experimental data. The coordinates where both ideal and experimental distributions match best define the hit position. The fitting procedure is based on a χ^2 minimization, where

$$\chi^2 = \sum_{\text{fired pads}} \frac{(q_{exp} - q_{fit})^2}{q_{exp}^2},$$

q_{exp} is the actual charge on a pad, whereas q_{fit} is the charge predicted on this pad by the distribution we fit with. MIGRAD [244] then handles the minimization process and outputs the predicted hit position and precision. In the analysis we compared various theoretical charge distributions: a Mathieson-Gatti distribution [245], which should theoretically match the detector response the best as it was developed specifically for this type of gaseous detectors; and a simple or double gaussian.

Comparison of the clustering algorithms accuracies

In order to determine how accurate a clustering algorithm is, a useful tool is to study the behaviour of the residuals, which are the difference between the theoretical hit position and the reconstructed one. In the Run 2 data reconstruction, the typical accuracy of the cluster determination was of the order of 70 µm, and we expect to achieve similar figures in Run 3. Moreover, the residuals should not be biased, i.e. the mean value of the residuals should be close to zero regardless of the position of the hit.

To illustrate the different clustering methods, we simulate Monte Carlo events where a muon hits a detection element (DE) perpendicularly to the cathode planes. For simplicity's sake in this discussion, we chose to simulate events on DE819: the pads are all of the same size and large (0.5 cm by 10 cm on the bending plane), which facilitates the plotting, and DE819 was used for data taking during TB runs and was available to take new data on the fly. An example of simulated hits on both planes of DE819 is seen in Figure 4.3.

For every event and on each cathode, the charge distribution is randomly drawn from a Mathieson-Gatti distribution with the expected width given by $K_3 = 0.5840$. The charges are then mapped, and preclustering and clustering algorithms can be run on this set of generated digits. Before extracting the digits, however, an additional layer of realism is added by simulating electronic noise following a gaussian distribution of width 1 ADC on each pad and rejecting some pads if their charge is too low. This pad rejection aims to reproduce the threshold applied by the DualSAMPA on samples, which are only recorded if they exceed a given threshold. A first criterion was to select pads with a total charge above 6 ADC, as it was roughly the amount of charge needed to pass the threshold in the DualSAMPA logic.

Overall, this simulation is rudimentary and does not perfectly simulate the response from the electronics. However, this first toy model can help visualise the effects of the various clustering methods. Over the course of this study, it will evolve and be tuned to reproduce real events with much more accuracy.

Bias of the residuals In order to check if a clustering algorithm produces results independently of the position of the hit, we have simulated single hits at different positions on a pad and looked at the corresponding residual.

By simulating 50 events, with x fixed at 0 and y uniformly distributed between 0 cm and 0.5 cm, we generate particles that hit along the y side of a bending pad, as represented in Figure 4.4. The charge of each event is uniformly chosen between 20 and 2000 ADC, and electronics cuts are applied. By plotting the residuals as a function of the position of a hit, we can estimate the spatial bias. The results obtained for the different clustering procedures are presented in Figure 4.5.

The residuals in the COG clustering case (see Figure 4.5a) exhibit a wave-like shape, with the mean value of the residuals that depends on the hit position. Residuals improve when y is 0 cm, 0.25 cm, or 0.5 cm, that is when the hit is located on the borders of the pad or in the middle, and charges

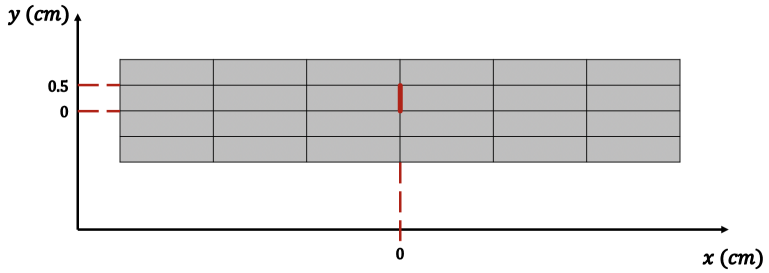

Figure 4.4: Representation of a part of the bending plane from DE819. The red line represents the positions where the particle hits were first simulated.

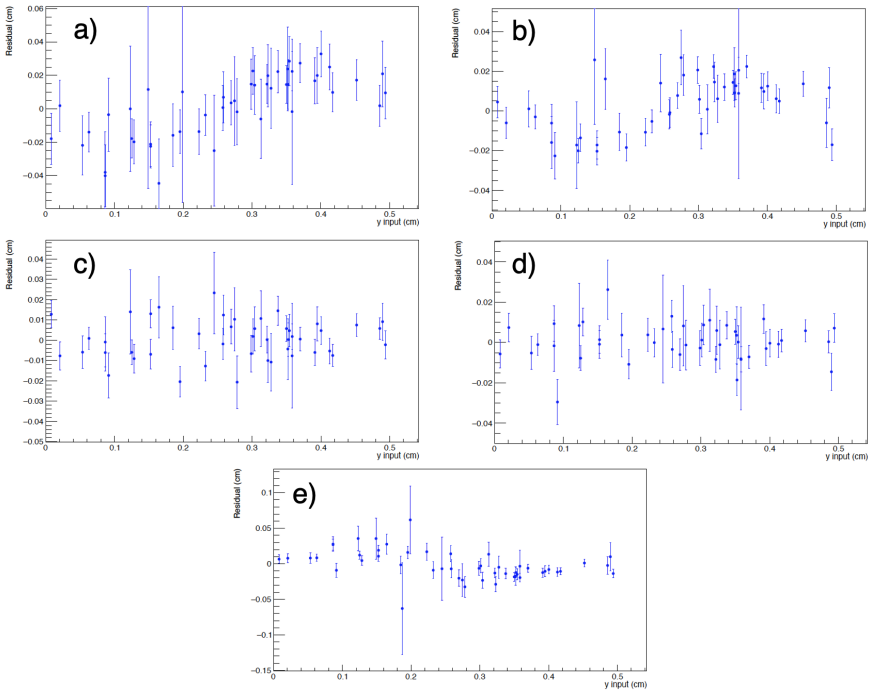

Figure 4.5: Distribution of residuals as a function of the y coordinate, for 50 events using various clustering procedures. a) Center of Gravity (COG), b) Gaussian fit, c) Mathieson fit ($K_3 = 0.5840$), d) Double gaussian fit, e) Mathieson fit ($K_3 = 0.2$). The uncertainty is defined as the fit error on the position.

can distribute symmetrically between neighboring pads. Fitting the charge distribution with a gaussian (see Figure 4.5b) still exhibits this wave-like pattern even though the uncertainties and residuals are reduced compared to COG. On the other hand, fitting the same Mathieson distribution that was used to simulate the data ($K_3 = 0.5840$), we observe no significant spatial bias as expected.

A double-gaussian distribution mimicking the Mathieson distribution also provides un-biased fit results, which validates the possibility of replacing the complex Mathieson distribution with two gaussians.

K_3 is the most crucial parameter in the Mathieson distribution. It is fixed by the geometry of the detectors and describes the spread of charges. Smaller values make the distribution more peaked, as shown in Figure 4.1. For example, trying to fit the charge distribution using a very narrow distribution with $K_3 = 0.2$, we observe a spatial bias in the results as the function cannot reproduce the charge distribution. The wave-like pattern is noticeable again, with a reversed sign compared to the COG case.

Accuracy of the residuals Now that we know which algorithms are not spatially biased, we need to check if their results are accurate. We generate 2000 single events as before and fit the distribution of

the residuals with a gaussian to estimate its width. The results are presented for various algorithms in Figure 4.6

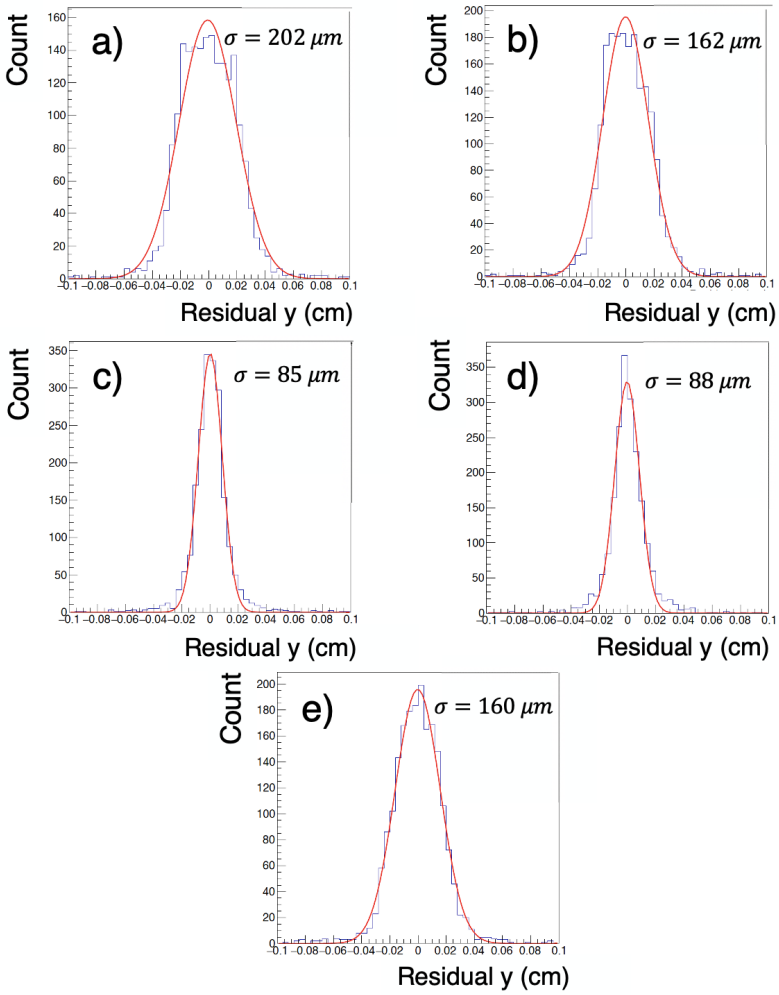

Figure 4.6: Distribution of residuals and resolution extraction, for 2000 events using various clustering procedures. a) Center of Gravity (COG), b) Gaussian fit, c) Mathieson fit ($K_3 = 0.5840$), d) Double gaussian fit, e) Mathieson fit ($K_3 = 0.2$).

The simple COG clustering gives a resolution of 202 µm. The gaussian fit is slightly better at 162 µm but still not meeting our requirements. A Mathieson fit gives a resolution of 85 µm, which is acceptable but can be improved. Using a double gaussian gives a resolution of 88 µm. Finally, if we try to change the K_3 of the Mathieson, for example, to 0.2, the resolution worsens to 160 µm. So changing the value of K_3 has a drastic impact on the clustering accuracy.

One can also look qualitatively at the impact of the cluster charge on the resolution for different clusterings, as seen in Figure 4.7. By simulating events at fixed charges, we observe that there is little impact of the clustering method at low charges, up to 100 ADC. Few charges are deposited, not many pads can be hit at once, and no method is significantly more accurate. Above this threshold of 100 ADC, we see that a better description of the charge deposit gives a better resolution. That is why COG is consistently the worst, followed by a simple gaussian, which does not fully reproduce a Mathieson-Gatti distribution whose characteristics become more visible as the cluster charge increases. We see, again, that a double gaussian and a Mathieson distribution give equivalent results.

The same qualitative analysis can be done for Mathieson-Gatti distributions at different K_3, as shown in Figure 4.8. The closer K_3 is to the K_3 used to simulate the event, the better. By gradually increasing K_3 towards this ideal value, we see that the resolution is improved on a gradually larger cluster charge range.

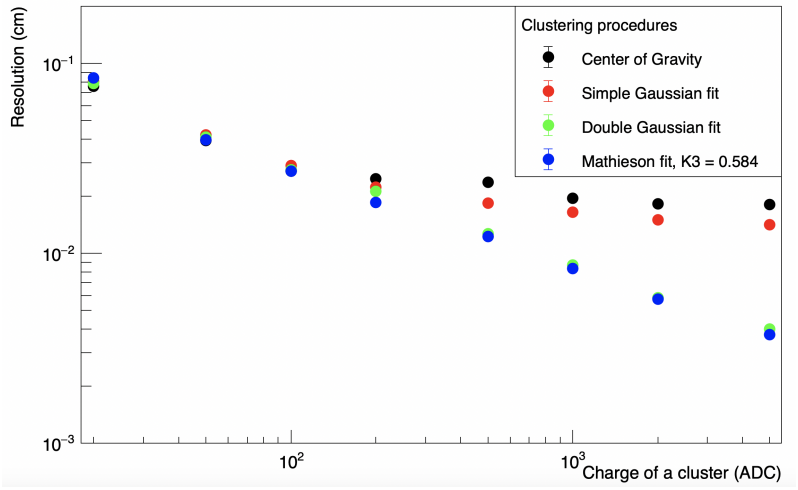

Figure 4.7: Resolution as a function of cluster charge obtained by applying various clustering procedures.

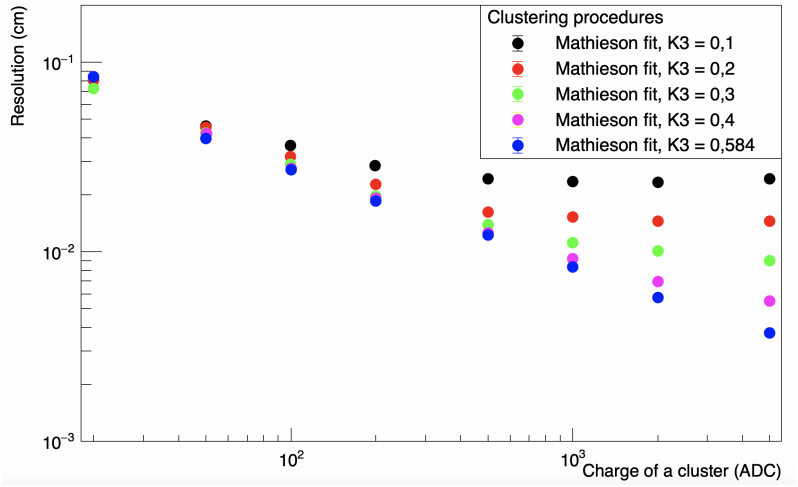

Figure 4.8: Resolution as a function of cluster charge obtained by using the Mathieson fit clustering procedure for various values of K_3.

4.1.3 Test beam (TB) setup and analysis

The performances of the upgraded electronics for the muon trackers (see Section 3.2.6) has been extensively characterized during two test-beam campaigns using few GeVs muon beams provided by the CERN SPS accelerator complex. The test beam set-ups (see Figure 4.9) comprised two muon tracking detectors, one quadrant and one SLAT, equipped with the new DualSAMPA readout boards. A telescope of three silicon pixel detector planes, based on the ALPIDE ASIC, provided a very precise reconstruction of the straight muon track trajectories. The impact point of the beam muons on the quadrant and SLAT detectors could thus be estimated with a precision $O(10\ \mu m)$, much better than the intrinsic resolution of the muon trackers. The data acquisition was triggered by the coincidence of two 5×5 cm^2 plastic scintillators placed at about 50 cm of distance on either side of the SLAT detector and centred along the nominal beam trajectory. The SAMPA readout chips were configured with zero-suppression mode enabled, with the nominal threshold settings foreseen for the Run 3 data taking.

The data acquired from TB can be used to test the clustering algorithms and how they respond to the new electronics. Fitting clusters with the Mathieson-Gatti distribution, as was done in Run 2, brings a better resolution with $K_3 = 0.2$ (68 µm) than with $K_3 = 0.5840$ (82 µm), as seen in Figure 4.10. Our toy model does not reproduce this effect and must be tuned to simulate events and the electronic response better. However, as seen in Figure 4.11 the wave-like pattern of the residuals as a function

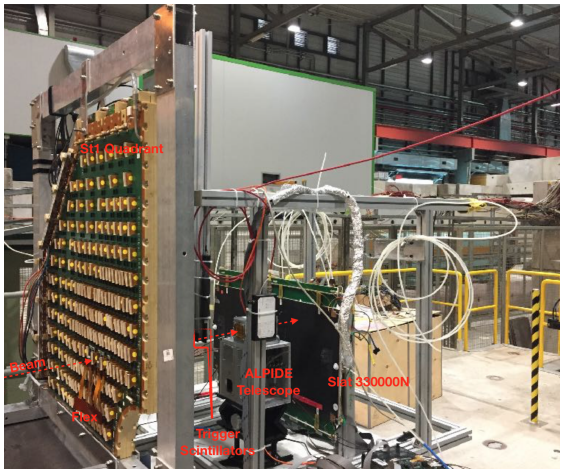

Figure 4.9: Picture of the CERN SPS test-beam set-up used to characterize the upgraded readout electronics for the muon trackers.

of the y coordinate can be observed in TB data as is the case for our toy model. We also see an improvement of the resolution from the COG algorithm to Mathieson fit, the only difference being that the pattern is more pronounced for $K_3 = 0.5840$ than for $K_3 = 0.2$. Overall, our toy model already manages to reproduce some of the features expected from TB data. However, some key aspects of the electronics response are still lacking. This motivates the improvement of the simulation by tuning its parameters and implementation to match TB data the best it can.

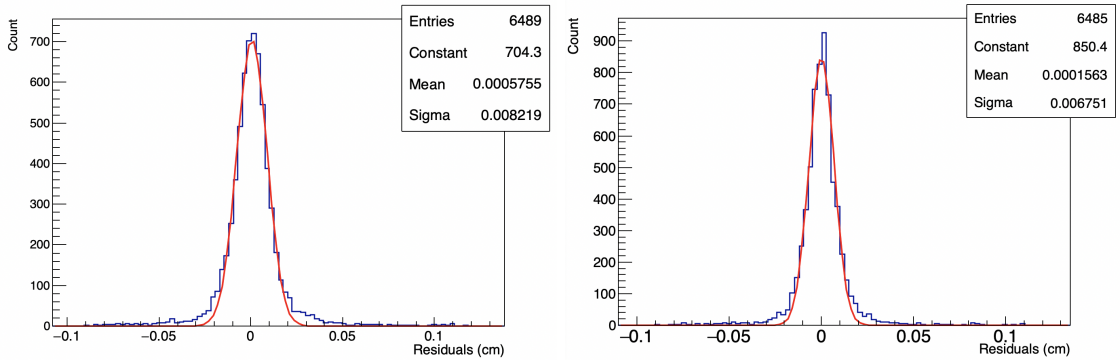

Figure 4.10: Distribution of the residuals obtained from TB dataset using a Mathieson-Gatti fit (Left) with $K_3 = 0.5840$ (Right) with $K_3 = 0.2$.

4.1.4 Simulation and tuning to TB data of charge spread, electronic digitization and noise distribution

So far the pad hits have been uniformly distributed in charge amplitude and hit positions, affecting the distribution of the residuals (as an event with more charge should be reconstructed more accurately than an event that barely passed electronic cuts). One way to make simulations more realistic is to tune them to Test Beam data. Information from available Test Beam runs allows us to compare a physical set of events to simulated events and make them coincide. The results on the clustering of Test Beam data with Run 2 algorithms would be directly comparable to results on simulated data with ported algorithms.

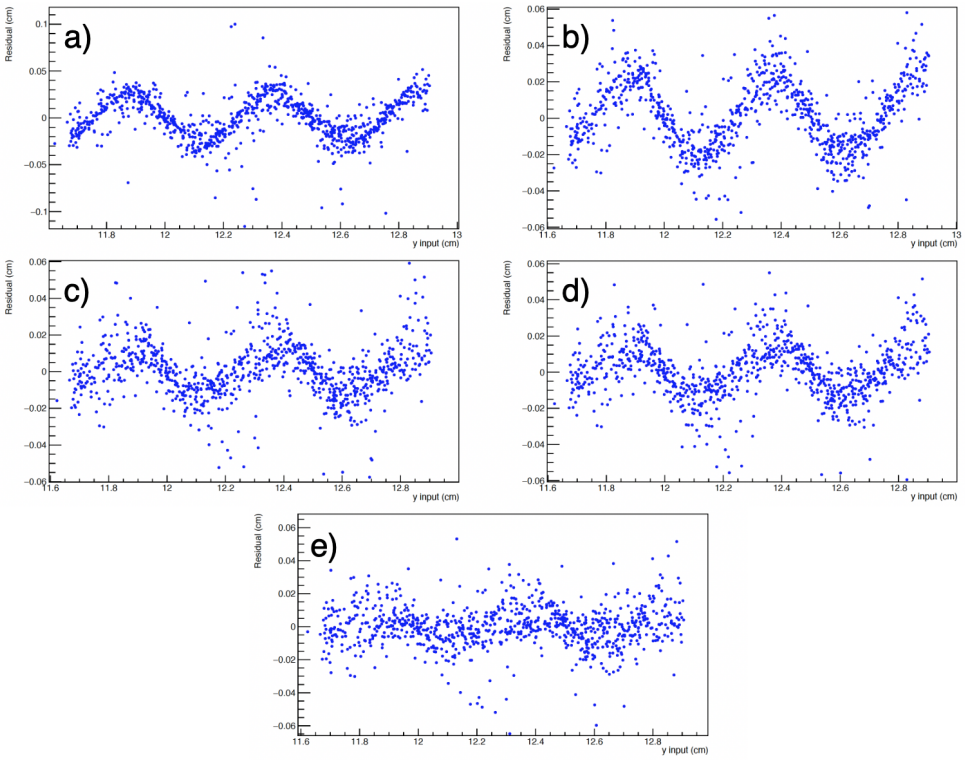

Figure 4.11: Distribution of residuals as a function of the y coordinate, for 1000 events from TB data using various clustering procedures. a) Center of Gravity (COG), b) Gaussian fit, c) Mathieson fit ($K_3 = 0.5840$), d) Double gaussian fit, e) Mathieson fit ($K_3 = 0.2$).

Parameters refinement based on TB data

To simulate realistic events, we need to match 3 elements between simulation and real data: the global charge distribution of the hits, the position of the hits, and the shape of the charge deposit. For simplicity we will focus on the data from the bending plane of DE819, whose pads measure 5 mm in the vertical y direction and 100 mm in the horizontal x direction.

The charge distribution of the clusters follows a Landau distribution. By fitting the TB distribution with a Landau function, we obtain a most probable value of 555 ADC with a sigma of 185 ADC. Our simulation should be close to this instead of a uniform random draw. By simulating a Landau distribution with parameters close to the TB ones, we see in Figure 4.12 that the noise and cuts have little impact, so the input distribution is close to the distribution after cuts from the electronics (which is what we measure in TB data). Using as an input for our simulation events following a Landau distribution of most common value 565 ADC and sigma 195 ADC, the cluster charge distribution from TB data and simulation match.

Concerning the position of events, we can use the information on x and y coordinates from TB data, as seen in Figure 4.13. The y coordinate was directly measured thanks to a silicon tracker, while the x coordinate was manually adjusted such that the beam impinged in the area between two pads, approximately 10 cm from the edge of the active area. This is confirmed by the fact that about one-third of the muon tracks leave charges in two pads in x. In the simulation the events have been uniformly distributed between 8.75 cm and 11.25 cm along x and between 11.5 cm and 13 cm along y.

Realistic electronics response simulation

To simulate the electronics response accurately, we need to match two elements: the noise and the cuts on individual pad charges.

The noise comes from the SAMPA boards and the intrinsic capacitance of the detector pads. It can be modeled by a gaussian component of width ≈1 ADC superimposed to each ADC sample. The total

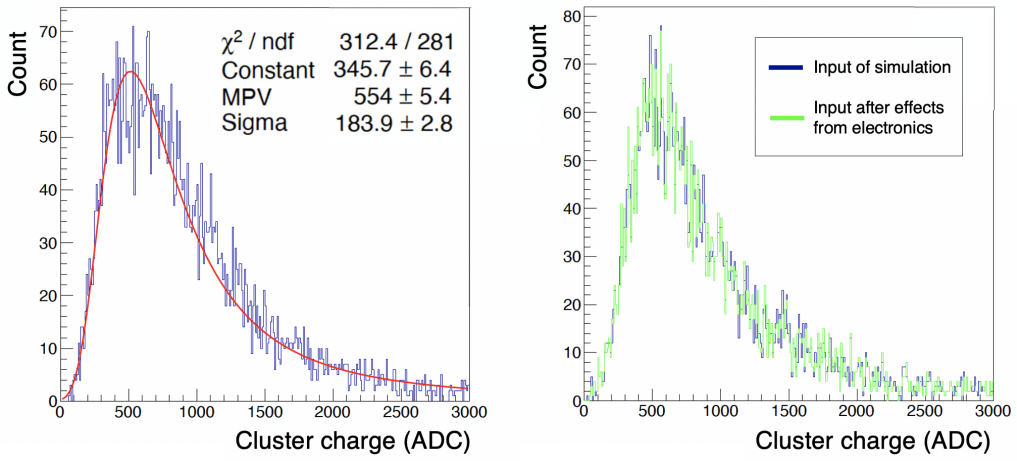

Figure 4.12: Left: Distribution of cluster charges from TB events. Right: Distribution of cluster charges from a random draw from a Landau distribution before any cut (in blue), after noise and electronics cuts (in green).

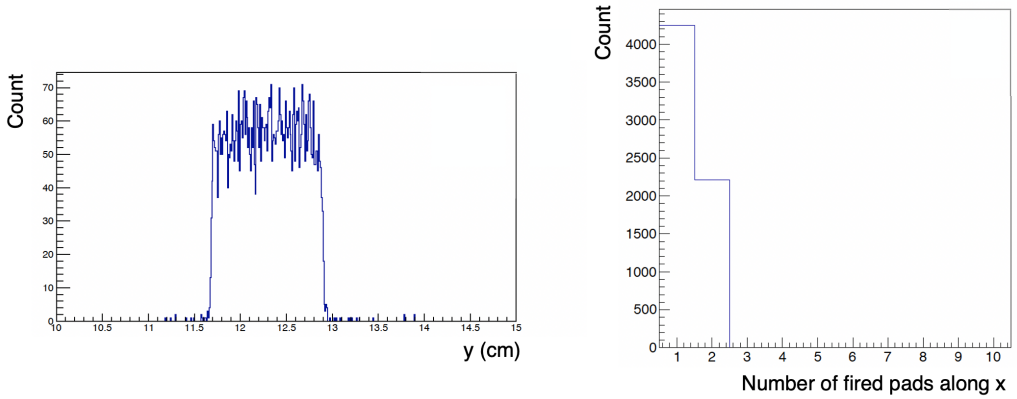

Figure 4.13: Left: y coordinate distribution of TB events. Right: Distribution of the number of fired pads in x from TB events.

noise contribution to the integrated pad charge is therefore given by the sum of the contributions from the individual ADC samples.

The rejections applied by the SAMPA boards are the following: a pad charge is kept if the SAMPA measures three consecutive samples of at least 3 ADC each. A first assumption is that three samples of 3 ADC each are 9 ADC, so one should discard pads whose charge after noise is below 9 ADC. The effect of such cuts is to eliminate pads of small charge. The stricter the charge cut, the narrower the charge distributions become because the tails are discarded. To check the validity of our rejection, we can look at the multiplicity of fired pads in the y direction and compare it with TB data, as seen in Figure 4.14. A straightforward cut at 9 ADC is not enough to reproduce the fired pads distribution. By looking at the individual pad charge distribution in TB data shown in Figure 4.15, we see that indeed there is no event below 9 ADC, but between 10 and 20 ADC, events are progressively rejected; the reason being that SAMPA boards may miss the first and last charge samples of an event, which would reduce the measured charge of the pad. To model this progressive rejection of pads of low charge, pad signals below 20 ADC were suppressed randomly so that the distribution of pad charge mimics the TB distribution, as shown on the right plot of Figure 4.15.

In order to study a possible saturation effect on the pad charge, we looked at the distribution of the pad with maximum charge in a cluster. Without applying any additional cut, the distributions were matching between simulation and TB data as seen in Figure 4.16.

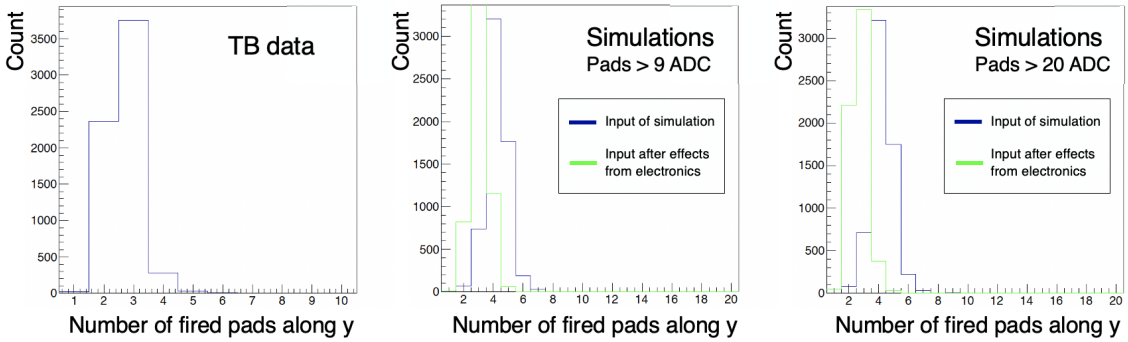

Figure 4.14: Left: Distribution of the number of fired pads along y in TB data. Middle: Distribution of the number of fired pads in simulated data before cuts (in blue), after cuts on pad charge at 9 ADC (in green). Right: Distribution of the number of fired pads in simulated data before cuts (in blue), after cuts on pad charge at 20 ADC (in green).

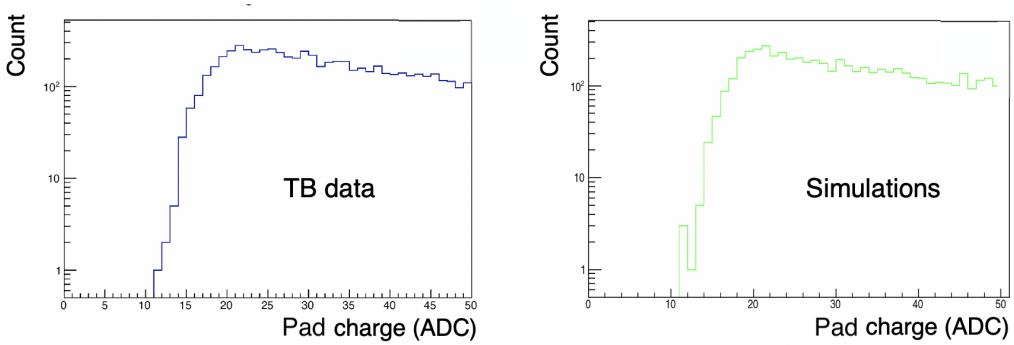

Figure 4.15: Distribution of individual pad charge after electronics cuts in TB data (left) in simulated events (right).

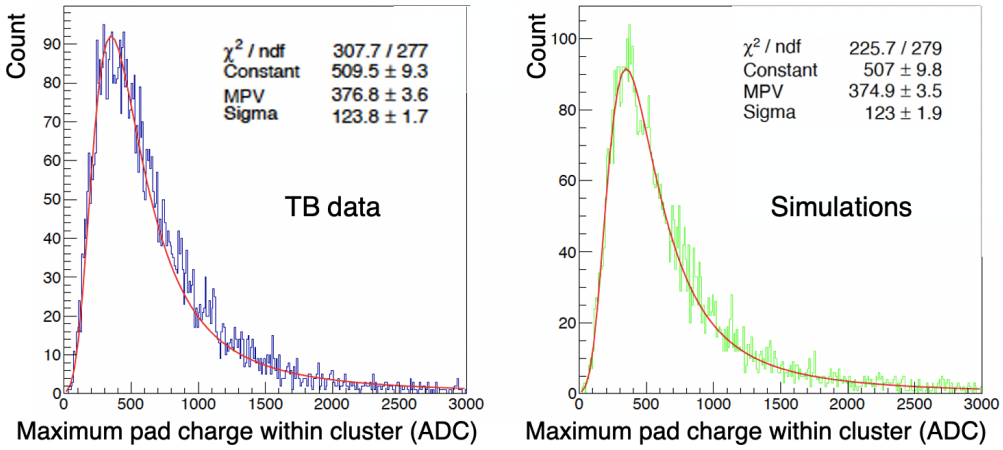

Figure 4.16: Distribution of maximum individual pad charge in a cluster in TB data (left) in simulated events (right).

Tuning of the Mathieson K_3 parameter

The last parameter that remains to be tuned on TB is the width of the charge distribution, controlled by the K_3 parameter of the Mathieson function. Despite the tuning performed so far, we observe in Figure 4.17 that in the y direction and overall, simulated events are too spread out compared to TB data. Too many pads are fired, which cannot come from the way the electronics or the event was

simulated as other tuning observables already match. Having no more leverage, the only way to reduce the spread of events is to lower K_3 compared to the 0.5085 value that is expected from the detector geometry.

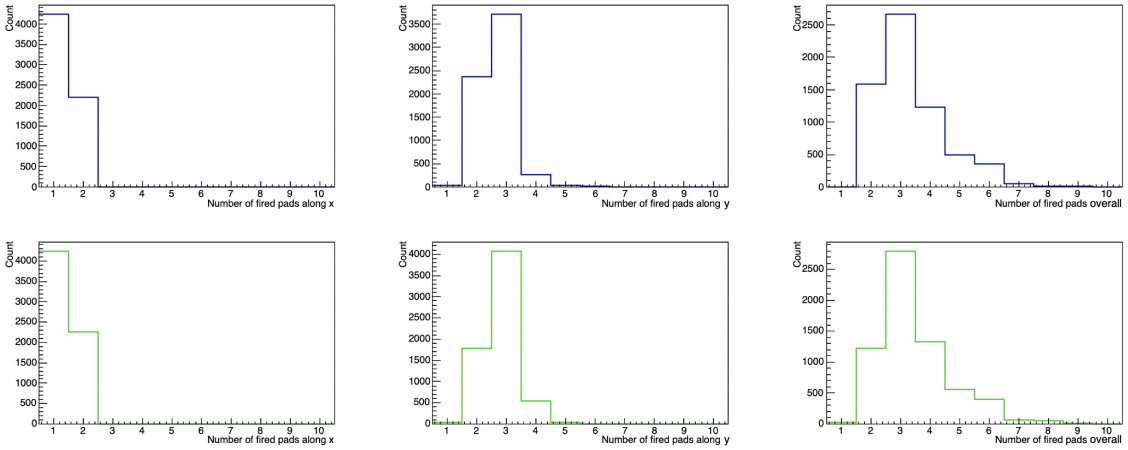

Figure 4.17: Distribution of number of fired pads along x (left), along y (middle), in total (right). Top: TB data. Bottom: Simulated events.

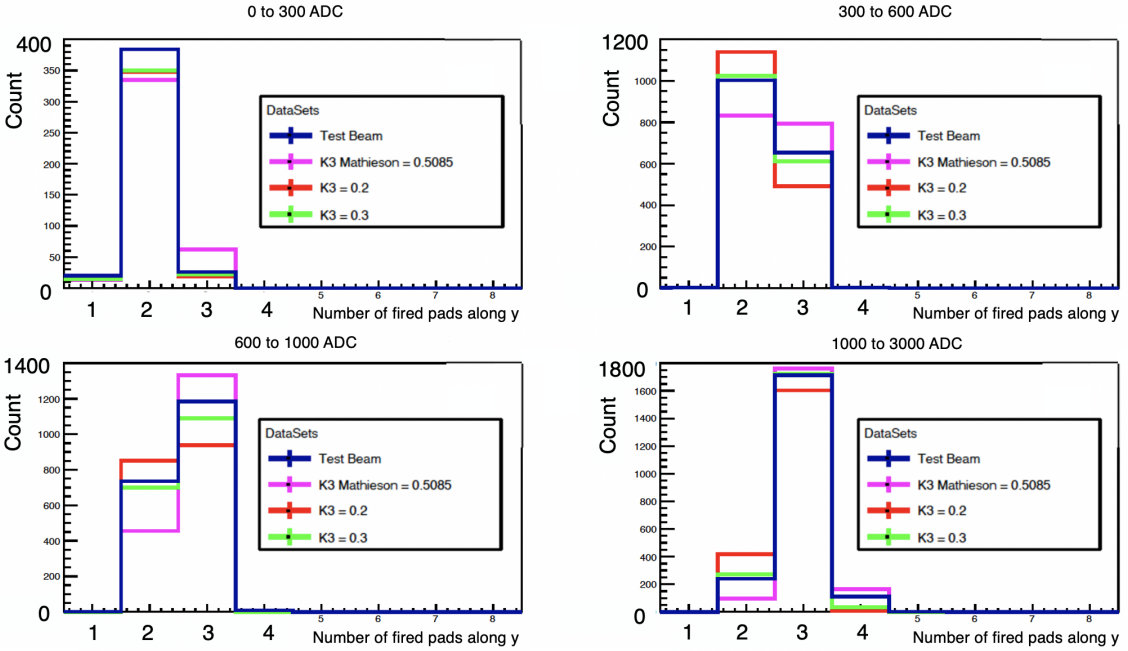

Figure 4.18: Distribution of the number of fired pads along y for TB data and simulated events of different K_3, grouped by bins of cluster charge.

This preference for narrower charge distributions is confirmed when splitting the data into four charge bins:

1. from 0 to 300 ADC, the ascending part of the Landau distribution
2. from 300 to 600 ADC, the peak
3. from 600 to 1000 ADC, the sharp decrease
4. from 1000 to 3000 ADC, the slowly decreasing plateau

Comparing TB distributions to simulated ones for different values of K_3, as presented in Figure 4.18, it seems that a value lower than the Mathieson prescribed one and closer to $K_3 = 0.3$ would match best TB data.

This analysis was repeated using TB data at 1700 V instead of 1650 to gather more insight using another dataset. The change from 1650 V to 1700 V impacts the Landau event charge distribution by multiplying the charge by 2, thus reducing the impact of the charge detection threshold (see Figure 4.19). In this case we observe that no value of K_3 seems to perfectly reproduce TB data behavior. However, low values around 0.3 to 0.4 would match best.

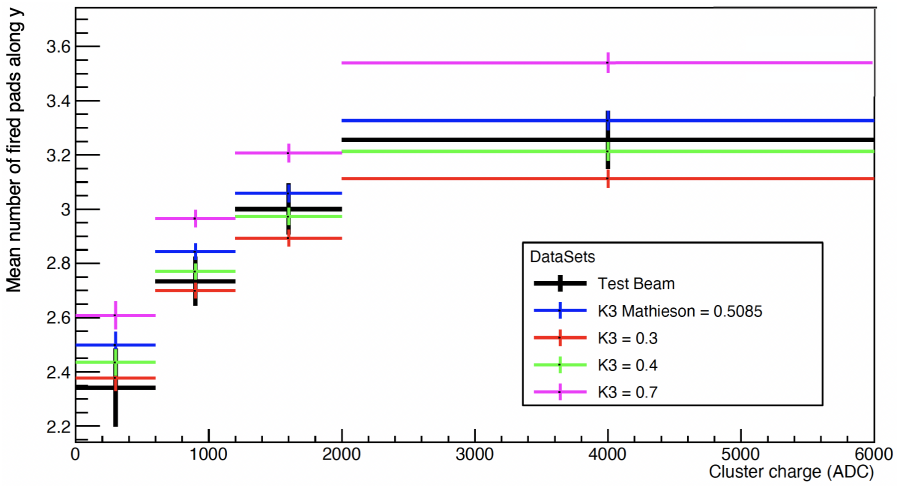

Figure 4.19: Mean number of fired pads along y for TB data at 1700V and simulated events of different K_3, as a function of cluster charge.

Another way to find the optimal K_3 for simulating the TB data consists in looking at the bias of the residuals as a function of the hit position along y.
As seen in Figure 4.20, fitting TB data at 1650 V using $K_3 = 0.2$ leads to no spatial bias. On the contrary, using $K_3 = 0.5085$ leads to a pattern where only the symmetric charge deposits (pad hit at a pad border or center) would be accurate. This pattern is reproduced in simulated data, which further shows the robustness of our simulations.

If, instead, we use $K_3 = 0.5085$ to simulate events that we then fit with $K_3 = 0.2$, the pattern is inverted, as we see in Figure 4.21. The "sign" of this pattern depends on whether K_3 used for fitting is higher or lower than the one associated with the actual charge deposit. If the fitting shape is too narrow or too wide, the fit will be biased either by being drawn towards the highest charge peak or away from it.

In TB data, it is observed that the resolution is optimal when using $K_3 = 0.2$ for fitting. That would mean that the charge reconstructed from Run 3 electronics follows a Mathieson distribution of $K_3 = 0.2$ (if it is still a Mathieson). This effect is currently not fully understood, and will be subject of further studies in the laboratory.

4.1.5 Comparison of residuals and resolutions between TB data and simulation

Now that we have all the simulation elements, we can check the performance of the clustering algorithm on TB data which would complete the workflow. As seen in Figure 4.22, on nearly all events at 1700 V, compared to the clustering that was used in a prior analysis of TB data, the difference in residuals is 0. Some outlier events disagree, but this is due to a slight correction in the implementation of the preclustering. In the end, both clustering implementations agree. However, on 1650 V data, our resolution (76 µm) is still slightly above the one obtained in the previous TB data analysis (68 µm). This difference may come from a different definition of the uncertainty on each pad charge which would be less visible on 1700 V data due to the higher charges.

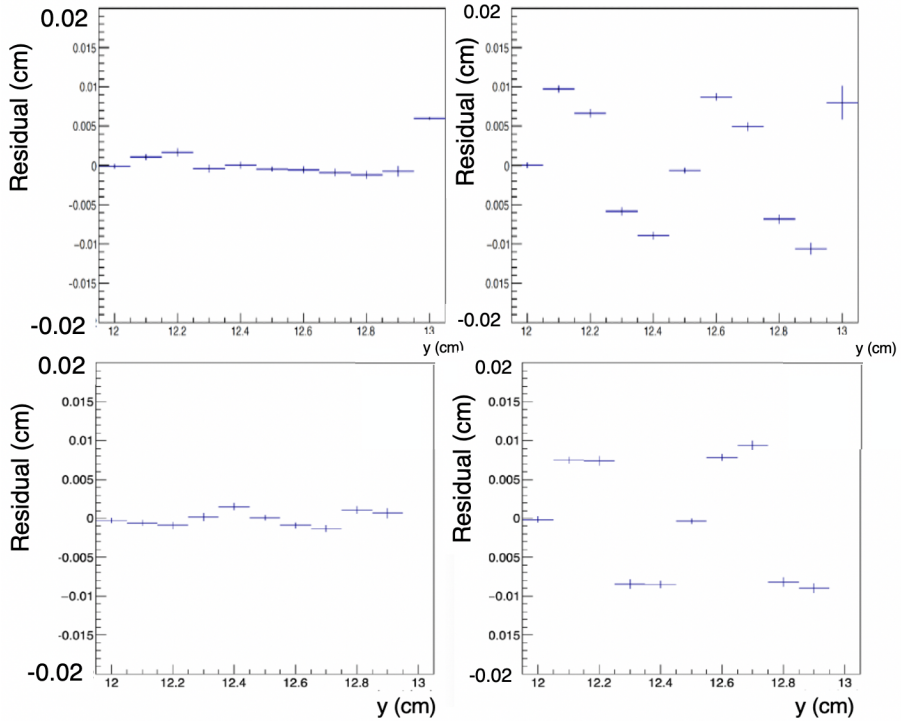

Figure 4.20: Residuals as a function of the y position of a cluster. Top: For TB events. Bottom: For events simulated with $K_3 = 0.2$. Left: Fit using $K_3 = 0.2$. Right: Fit using $K_3 = 0.5085$.

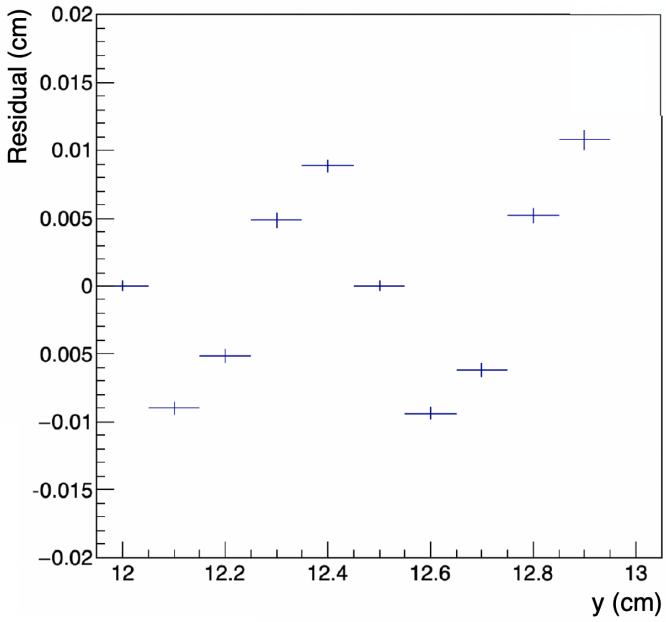

Figure 4.21: Residuals as a function of the y position of a cluster for events simulated with $K_3 = 0.5085$ obtained by fit using $K_3 = 0.2$.

We can now use the complete simulation-clustering chain to try and reproduce TB results. All this tuning has dramatically improved our resolution. Assuming TB data to be reproduced by a Mathieson distribution of $K_3 = 0.2$, we can compare our simulation and TB data in terms of the final resolution. We see that if the fit is done using $K_3 = 0.2$ or $K_3 = 0.5$, the results agree between simulation and TB data, showing a minimum resolution for $K_3 = 0.2$.

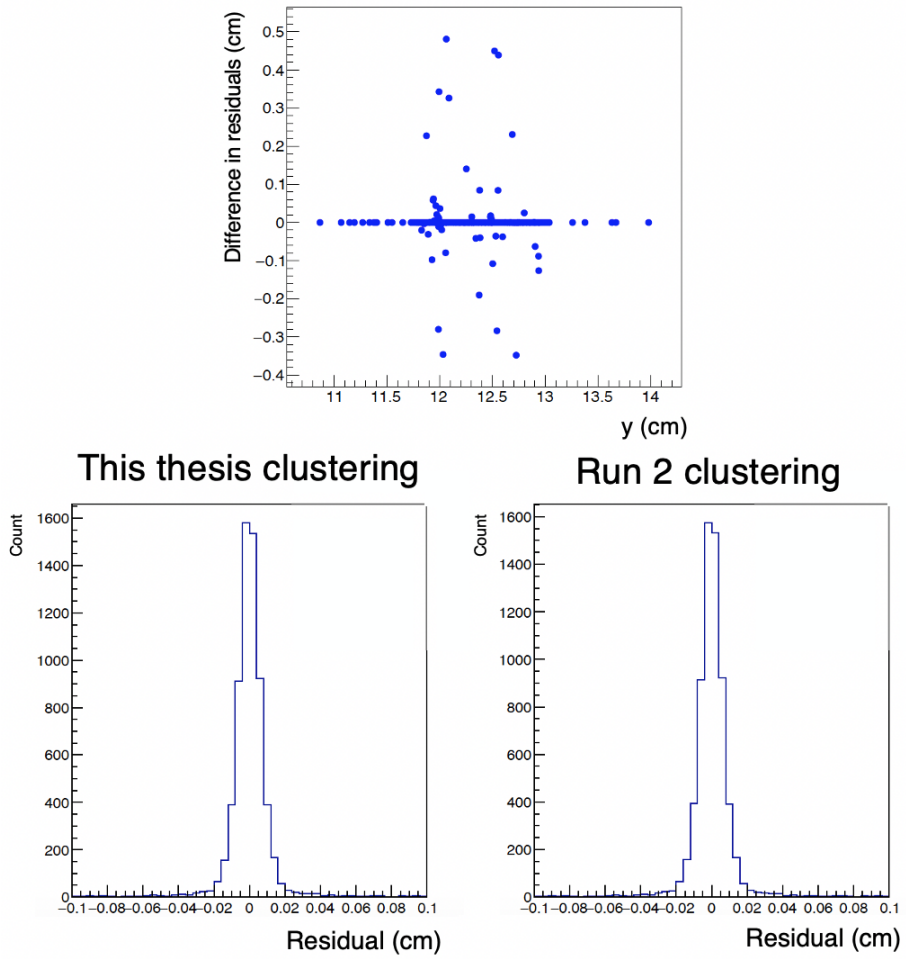

Figure 4.22: Top: Difference in residuals obtained in TB data at 1700V between legacy Run 2 code and this re-implementation. Bottom: Distribution of residuals for this re-implementation (left) and legacy code (right).

We studied the distributions of residuals between simulations and TB data shown in Figure 4.23. Even though the resolutions obtained in the end are similar, the tails of the distribution are more prominent in our simulations and the core of the distribution is higher in TB data, indicating there are still differences between simulations and TB data. Indeed, looking at clusters of fixed charges, the resolution we obtain in our simulations is consistently slightly worse than the TB resolution. So, there is still room for improvement. However, the basic tuned simulation implemented here shows enough similarities with real events and manages to reproduce physical behaviors. Hence, we can use it to determine the impact of various physical parameters on the resolution.

4.1.6 Impact of parameters on resolution

In this subsection, we look at the impact of some physical parameters on the resolution. The parameters we focus on are the pad size, the cluster charge, the cluster position, the noise and cuts, and the uncertainty on the pad charge. Because we want to study the individual impact of parameters, we have to shield ourselves from the effects of others. When we are not studying the parameter in question, the simulations are as ideal as possible, done at fixed charges, giving residuals following a gaussian from which resolution extraction is reliable. In particular, wherever possible we computed the resolution for the case of "ideal" charge distributions, obtained by discretizing a perfect Mathieson distribution on the pads without any randomization. The results are then compared with the "realistic" case in which the theoretical Mathieson distribution is randomly sampled, leading to an uncertainty of $\sqrt{ADC}$ on each

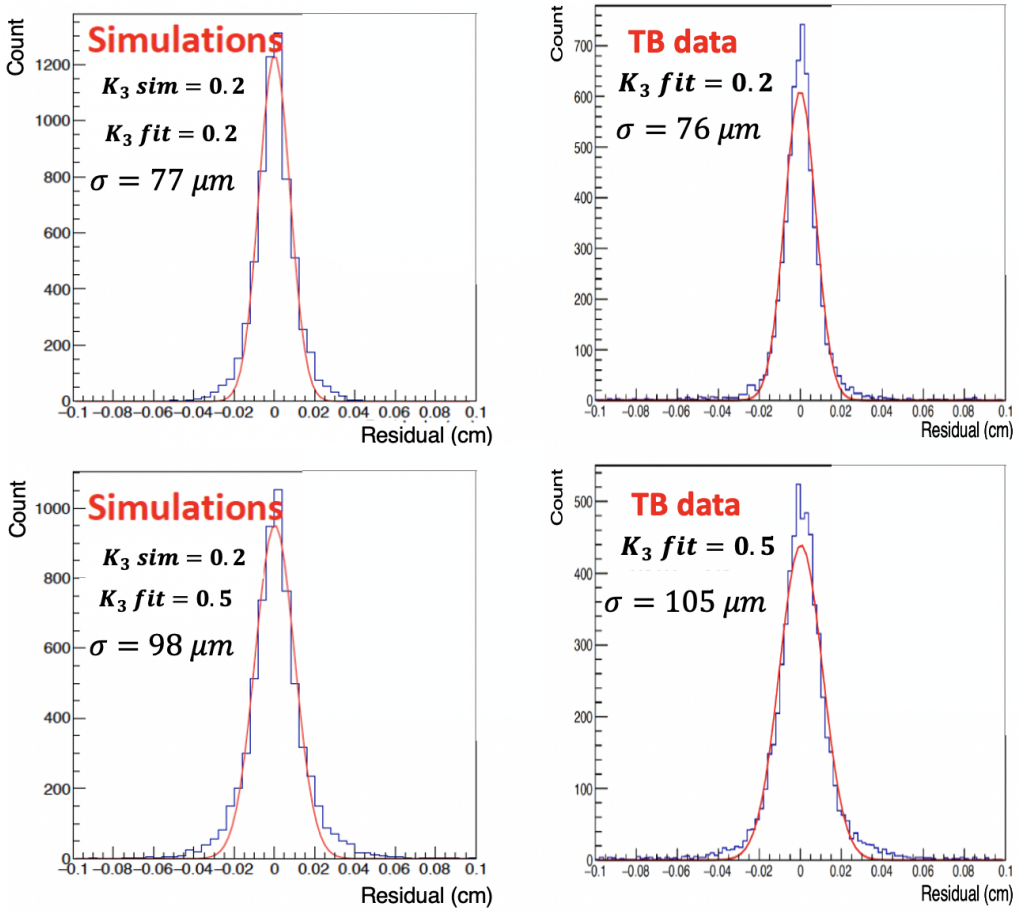

Figure 4.23: Distributions of residuals for TB data at 1650V and simulated data with $K_3 = 0.2$ obtained by Mathieson fit at various K_3.

pad.

Pad size

To study the impact of pad size, we simulated 2000 events at a fixed charge and random coordinates, without cut or noise, using $K_3 = 0.2$ for both simulation and fitting procedures. The case where the simulation is done by a random draw of the charges (leading to statistical uncertainties on pad charge) and where the simulation is ideal are presented.

Only the pad size in the y direction is studied as the pad size in the x direction does not impact the resolution on the y coordinate. It would just spread the charges and make the events more sensitive to cuts. In Figure 4.24, we observe that in ideal events, the resolution does not seem to follow any trend as a function of the change in pad size. When we add (statistical) uncertainties to the pad charge, the resolution worsens the larger the pads are.

That is expected because when the events are ideal, the fitting procedure will always nicely match the charge deposit. After all, the simulated shape is rigorously identical to the one we use for fitting. When fluctuations are introduced, the charge deposit deviates from the ideal Mathieson distribution we then fit with, which explains the sudden increase in resolution from 10 µm to 100µm. Furthermore, in this case, the bigger the pads, the less information from charge measurement is accessible to the fit, so the resolution worsens.

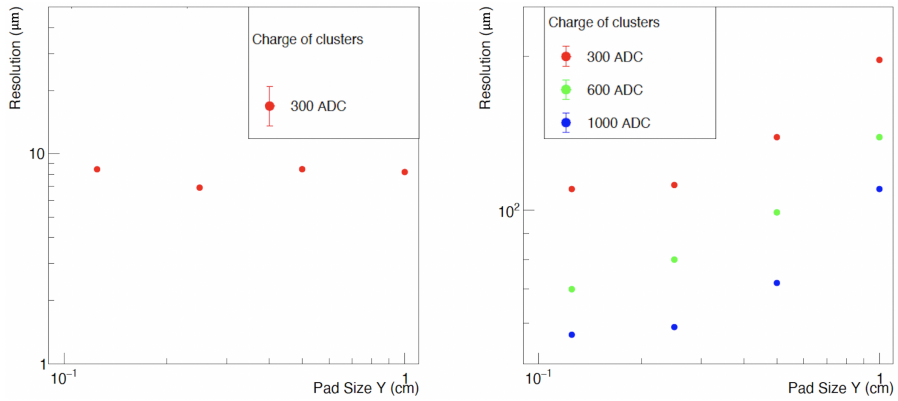

Figure 4.24: Resolution as a function of pad size. Left: For ideal events. Right: For events with statistical uncertainties on individual pad charges.

Cluster charge

We also studied the behavior of resolution as a function of cluster charge. The results are presented in Figure 4.25.

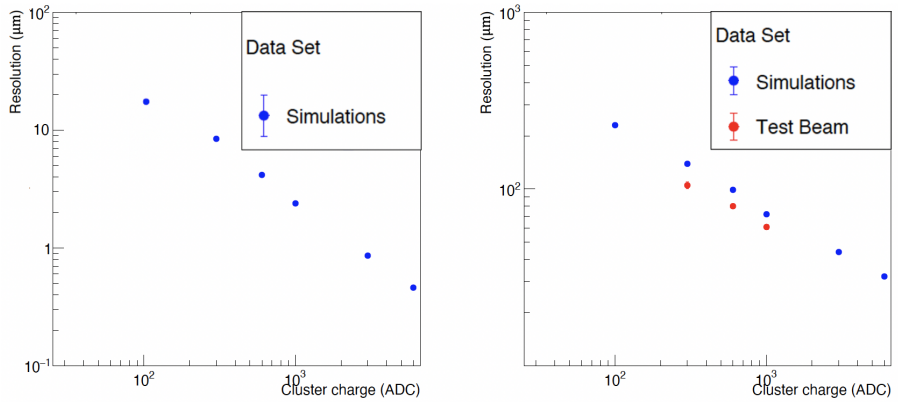

Figure 4.25: Resolution as a function of cluster charge. Left: For ideal events. Right: For events with statistical uncertainties on individual pad charges.

A similar trend is observed for both the "ideal" and "realistic" cases: the resolution improves with increasing values of the charge, with a linear trend in log scale. However, the resolution degrades by a factor ~ 10 when charge fluctuations are introduced.

Considering how much the introduction of fluctuations on pad charge deteriorates our resolution, one may start to consider that what drives our resolution away from TB results is the way those fluctuations are simulated.

Cluster position

To study the influence of the hit position on the resolution, events have been generated and fitted using $K_3 = 0.2$. The x coordinate was left free, but y was constrained between -0.5 cm and $+0.5$ cm to focus on two pads in the y direction. The charge of clusters was fixed, and no noise or cuts were applied. Trying with ideal events (no fluctuation of pad charge), we obtained resolutions of around the tens of micrometers without any y dependence.

Once more, interesting effects appear when statistical fluctuations are added to the pad charges. Results are presented for clusters of 300 ADC in Figure 4.26. The simulated data results show that the resolution is the best at y values of -0.5 cm, 0 cm, and $+0.5$ cm, which are borders of pads. In contrast, the resolution is the worst at the centers of pads. The fact that the resolution is worst at the

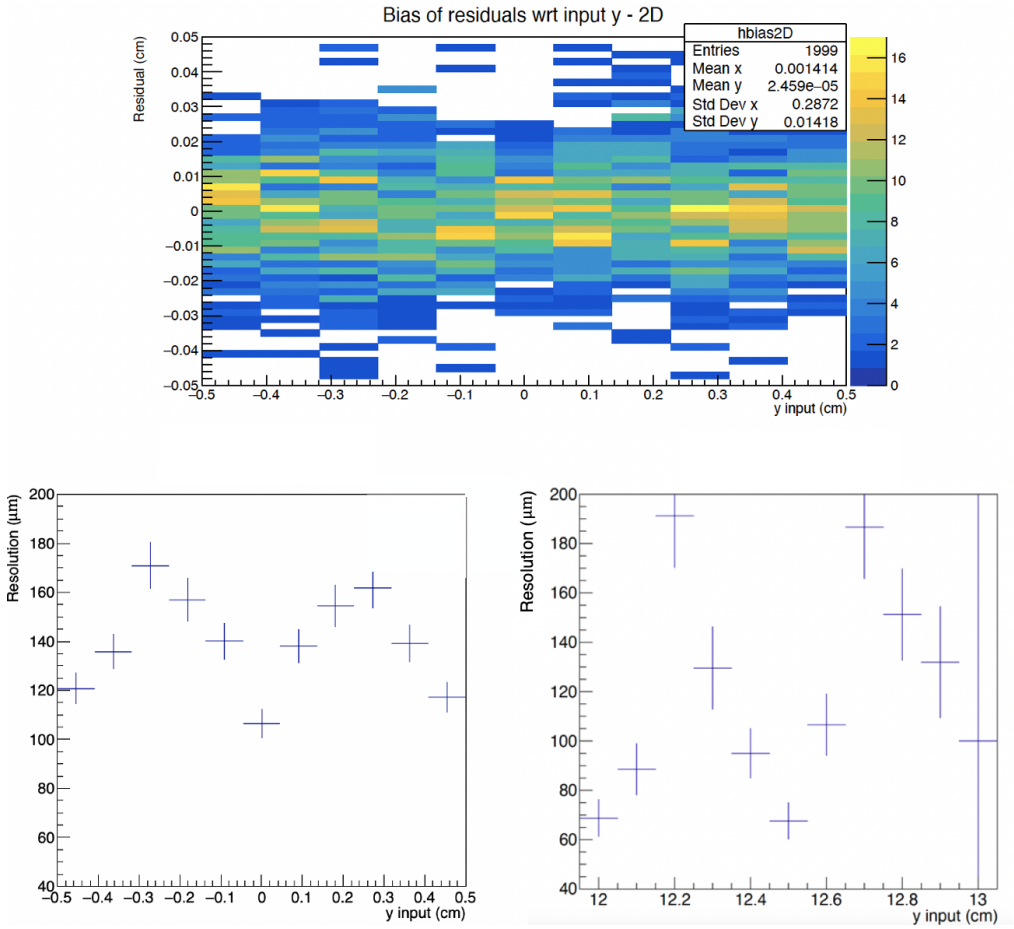

Figure 4.26: Top: Distribution of simulated events as a function of resolution and y, for clusters of 300 ADC. Bottom: Resolution as a function of y for simulated events (left) for TB data (right).

center of the pads even though the charge distribution is symmetric may tell us that the fit converges better between pads than at the center of a pad, or, more plausibly, that when a particle hits the center of a pad, there is a larger probability of losing signal in the tails which will prevent the fit from being accurate.

Comparing these results to TB data, the same behavior is observed, which shows that our simulations are accurate enough to reproduce such an effect. We also see that the resolution is better in TB data, which we had already noticed. This behavior as a function of the y coordinate is seen for other cluster charges, both in simulation and TB data but seems to fade away with increasing charge, as seen in Figure 4.27. It corroborates the intuition that the decrease in accuracy is due to signal loss in the low-charge tails. As clusters have more charge, signal lost in the tails has less impact over the accuracy of the fit.

Noise and electronic cuts

In order to study the impact of noise and cuts, we simulated and reconstructed 2000 events on the whole detector at a fixed charge. We did so, changing the value of the cluster charge and the values of the cuts (either none, cut similar to the ones in TB data, or stricter cuts) and fluctuations (which account for both the electronic noise and the uncertainty on pad charge, so everything that could modify pad charges). In each case, the resolution was obtained by fitting the distribution of residuals with a gaussian. Results are reported in Table 4.1.

First, if we look at the number of events reconstructed in each case, we see that the stricter the cuts the more events are lost because the number of fired pads is not enough to perform the fit of the charge distribution.

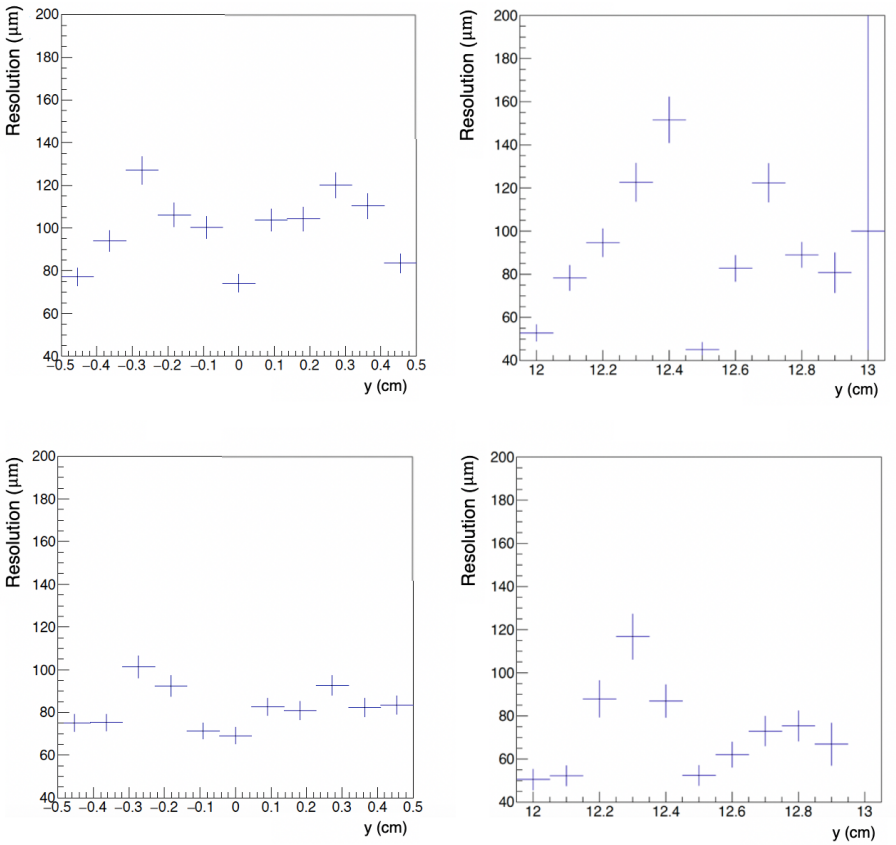

Figure 4.27: Resolution as a function of y, for clusters of 600 ADC (top), 1000 ADC (bottom). Left: For simulated data. Right: For TB data.

	300 ADC	600 ADC	1000 ADC
No fluctuation, No cut	8.45 [2000]	4.17 [2000]	2.39 [2000]
No fluctuation, Cut TB-like	4.94 [1981]	2.62 [1990]	1.68 [1993]
Statistical fluctuation, No cut	168 [2000]	121 [2000]	83.5 [2000]
No fluctuation, Cut 50 ADC	NA [1226]	1.5* [1840]	1.6* [1984]

Table 4.1: Resolution obtained (in μm) and the number of reconstructed events out of 2000 (in brackets) for various cluster charges and various cuts and fluctuations conditions.
*The distribution of residuals was not gaussian, the resolution loses its meaning.

We also see that apart from reducing the efficiency, especially on low-charge events, the cuts do not affect the resolution too much. Again, the largest contribution comes from the fluctuations on the pad charge, being from the electronic noise or any other source. The resolution worsens as soon as the pad charge fluctuates away from its ideal value.

Uncertainty on pad charge

Through the studies presented in this section we have seen that the fluctuations on pad charge have a significant impact. When events are ideal, other parameters like cluster charge, pad size, or cuts barely impact the resolution, which is close to 10 µm. Nevertheless, as soon as there is any source of pad charge fluctuation (electronic noise, statistical uncertainties due to random simulation process), the resolution worsens to around 100 µm, and some cross-effects start to appear.

However, the resolutions measured in our simulations and TB data are different. Likely, the bone of contention between our simulation and TB data resides in the way fluctuations are simulated. Indeed, making a random draw to simulate the deposit of charges on the pads, as it has been done for most

of the whole analysis, leads to statistical fluctuation (of $\sqrt{\text{ADC}}$) on each pad. If one wants to improve this toy model, the aim in the future will be to see what fluctuation we need to add to each pad in order to match the reference TB data. Attention will also have to be directed toward the simulation of the noise from the electronics.

4.1.7 Outlook of clustering and event simulation

To summarise this work on clustering and event simulation, we have implemented a way of building and reconstructing realistic events in the muon spectrometer. From the basic principles of the simulation through comparisons with actual TB data; parameters have been identified and tuned to make the simulations as close to reality as possible.

Different clustering algorithms have also been tested, and the fitting procedure and its parameters have been improved to optimize the output resolution. The current simulation-reconstruction process allows us to reproduce Test Beam data quite accurately, although some tuning remains to be done on identified parameters, namely pad charge fluctuations.

The shape of the charge deposits of the pads has also been studied, where we observed a clear discrepancy between TB data and the Mathieson prediction, which was found to be valid for Run 2 data. Indeed the events seem less spread out than they should be, which should be investigated further.

This simulation-reconstruction chain also allowed us to study the impact of various parameters on the resolution, like the pad size, the cluster charge, the cluster position, the electronics threshold, and the fluctuations of the pad charge. This study proved helpful in identifying the fluctuations of pad charge (e.g., from electronic noise and charge deposition uncertainty) as the leading candidate to account for resolution deterioration.

4.2 MCH Quality Control

In this section, we focus on the development of the Quality Control (QC) software for the muon spectrometer (MCH). We cover the principles of the QC, what variables it allows to monitor and the use we have of it during both Long Shutdown 2 (LS2) and Run 3.

4.2.1 Principles of the Quality Control

The QC is a software framework that allows one to process the online data stream produced by detectors and provide a real-time monitoring of the quality of the recorded data. The QC can process the output of any step of the online processing chain, from low-level raw data to reconstructed tracks and vertices. As an output, the QC returns histograms monitoring the observables we judge relevant. As the QC runs, its output is updated periodically. Every cycle, we get a snapshot of the observables we monitor.

The QC framework is based on a set of routines that receive data from the detectors or other QC components and process them periodically. The processing is defined as a "task". Each QC task receives a specific input and runs a dedicated algorithm. In the MCH case the QC currently processes the following data streams:

- **Pedestals** calibration data
- **Digits**, which are produced by the raw data decoder
- **Errors**, also generated by the raw decoder together with digits
- **ReadOut Frames** (ROFs), which are the output of the time clustering step
- **Pre-clusters**, from the preclustering step
- **Tracks**, either reconstructed from the MCH detectors alone or matched with the Muon Identifier (MID) and Muon Forward Tracker (MFT)

The output of the QC is then saved on a database (CCDB) which both shifters and experts can access during commissioning and data taking to monitor the detectors. QC outputs presented to the experts are more detailed and exhaustive than the ones accessible to shifters for whom the information

must be presented in the clearest way possible. Information stored on the CCDB can then be re-used and post-processed. It allows one to study the time-evolution of the detector observables, merge information from different time frames, or study the quality of the output.

During LS2, we had to install new front-end electronics to accommodate the increased event rate in Run 3 and the online reconstruction and triggering process. This new configuration had to be checked because we had to make sure that its behaviour conforms to what we expect. In this regard, the QC provided an excellent tool for assessing the status of the new electronics during installation and commissioning, as it provided an immediate visual feedback of the readout status and possible errors.

4.2.2 The MCH QC Tasks

Pedestals calibration monitoring

Pedestals calibrations are collected with a special configuration of the SAMPA front-end chips, requiring a fixed number of samples and no zero suppression. The Pedestals QC task measures the average and rms noise fluctuations of the ADC offsets, to identify the electronics channels that behave incorrectly or are too noisy. Such information is stored in the CCDB and the identified bad channels are excluded from the physics data taking. An example of output produced by the pedestals task is given in Figure 4.28 and Figure 4.29.

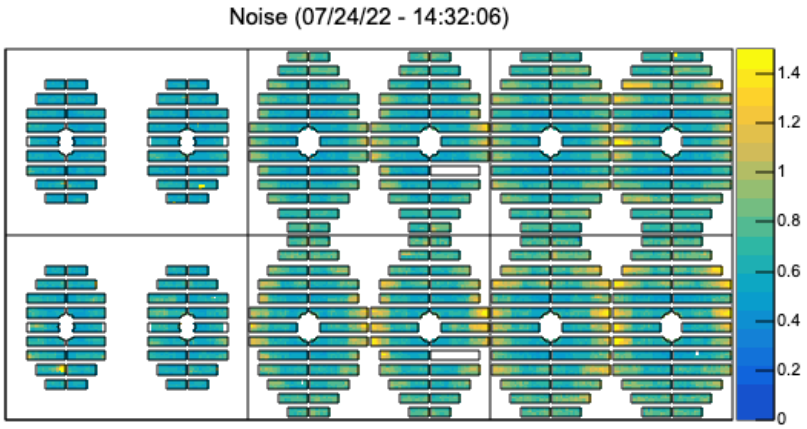

Figure 4.28: Noise values for pads of Stations 3, 4, and 5.

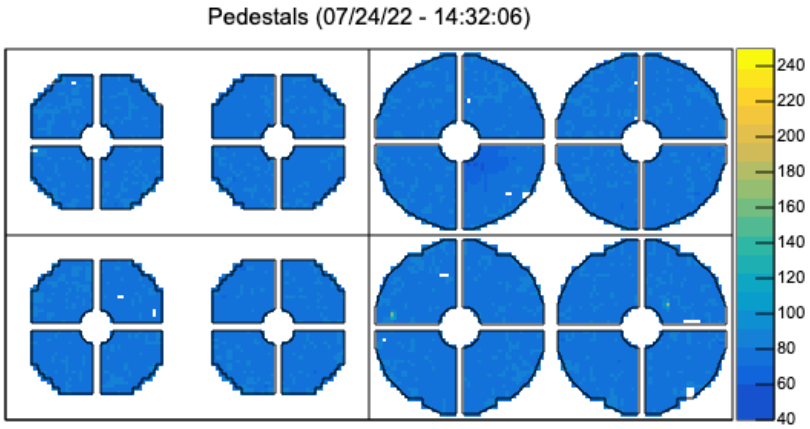

Figure 4.29: Average pedestal values for pads of Stations 1 and 2.

The most direct input for a QC task is raw data, the crudest information form. It is directly output by the detector electronics. It contains the samples coming from the fired pads before they are grouped into digits and the error codes. There are two QC tasks implemented to process raw data: "ErrorsTask" and "DigitsTask".

Raw decoding monitoring

The raw data decoding step produces as an output a set of digits and a list of decoding errors, which are monitored by two dedicated QC tasks. As introduced previously in this chapter, a digit is an object containing information about a fired pad, like the time of the hit, the integrated charge received by the pad and the pad identifier, which allows knowing the pad's position in the spectrometer using the detector mapping.

The Digits task uses the digits as input to measure the occupancy of each pad, defined as

$$Occupancy = \frac{N_{hits\ seen}}{N_{orbits\ seen}},$$

where an orbit is a time window of about 90 µs.

The processing routine counts how many digits have been seen in a given orbit for each pad. If no digit is seen, it may mean that we have no information coming from the pad, which must be corrected. If the occupancy is too high, it may indicate a noisy pad or some other electronics problem that should be investigated. Occupancy can be visualized in a histogram where each bin is a pad, as in Figure 4.30. The coordinates of the bin depend on pad identifiers (e.g., the identifier of the DualSAMPA it sends data to, the identifier of the SOLAR board linked to the DualSAMPA). Alternatively, we can use the mapping to draw the muon chambers and survey which physical parts of the detectors are facing occupancy issues, as shown in Figure 4.31.

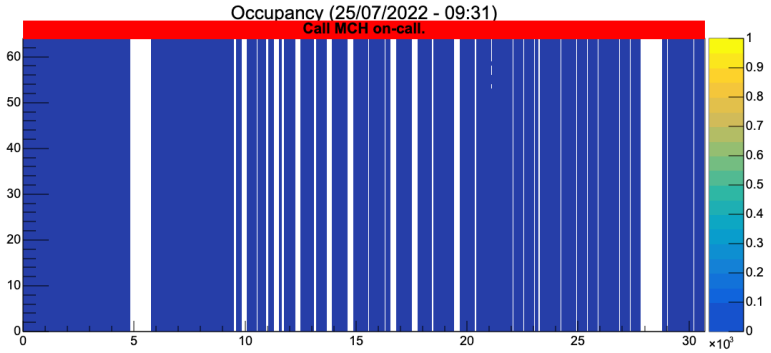

Figure 4.30: Pad occupancy displayed on a histogram based on electronics identifiers.

The Errors task receives the error codes reported by the raw data decoder. It allows knowing if specific detectors see a particular type of error more than others. Examples of errors include an invalid electronic identifier, incomplete incoming messages, and poorly formed packets, as shown in Figure 4.32.

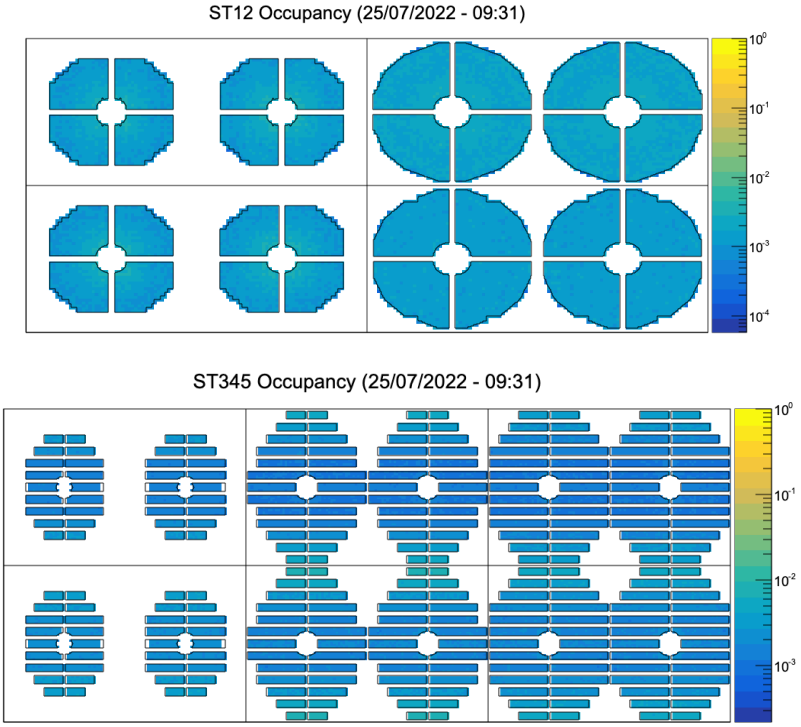

Figure 4.31: Occupancy displayed on a histogram using the mapping to represent the geometry of the muon spectrometer. Top: Stations 1 and 2, Bottom: Stations 3, 4 and 5.

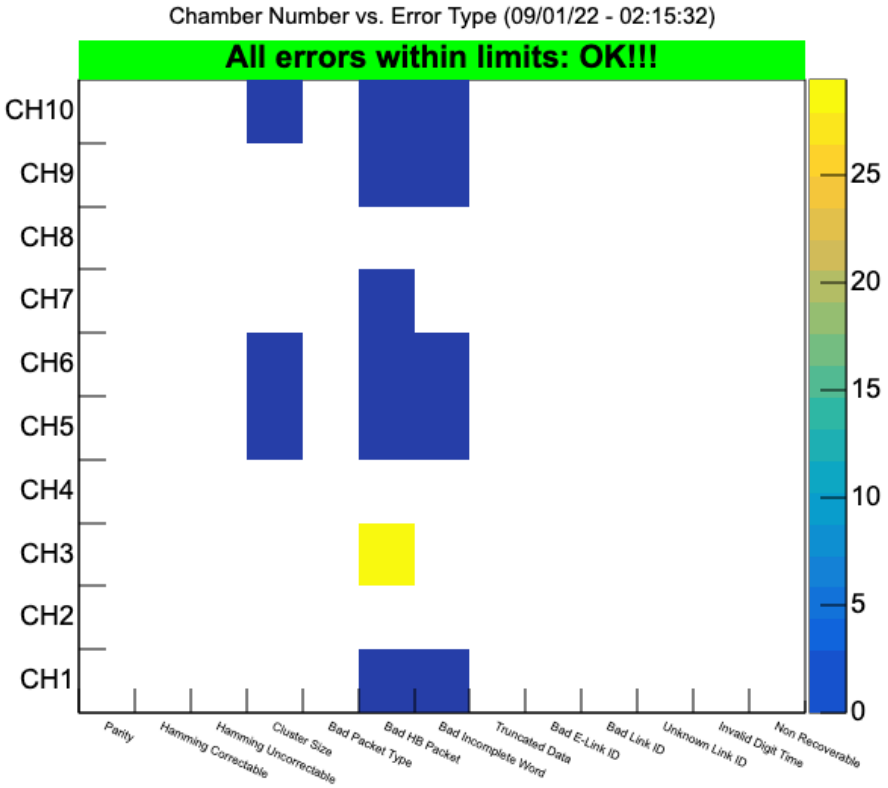

Figure 4.32: Output histogram from ErrorsTask, showing the error sources coming from each detection chamber.

Preclusters monitoring

A precluster is a group of fired pads belonging to the same particle hit. So, it contains physical information regarding the position where the particle crossed the detector, as well as the response of the detector.

The main goal of the Preclusters task is to measure the detector's pseudo-efficiency. Pseudo-efficiency measures the geometrical correlation between both cathode planes for the same detection element. We count "good clusters" on a cathode, which are defined as clusters spanning at least two pads with at least one pad having a minimal amount of charge (of the order of 50 ADC). Then, we see if the good clusters are associated with a signal on the other cathode.

For each cathode, we define the pseudo-efficiency as:

$$Pseudo\text{-}efficiency_{cathode} = \frac{N_{good\ clusters\ cathode\ \cap\ clusters\ other\ cathode}}{N_{good\ clusters\ cathode}}$$

where $N_{good\ clusters\ cathode\ \cap\ clusters\ other\ cathode}$ is the number of times a good cluster on the cathode was associated to signal on the other cathode, and $N_{good\ clusters\ cathode}$ the number of times a good cluster was seen on the reference cathode. This definition gives a quantity between zero and one. The closer the pseudo-efficiency is to one, the more the cathode planes are correlated, showing a robust measurement of a particle hit. If the pseudo-efficiency is too low, it might mean that a plane is not working properly and fails to identify a particle hit that was seen by the other cathode.

In practice, the location of clusters is defined by applying the quick centre of gravity clustering algorithm to the preclusters within some margin of error, which allows getting a quick and acceptable way to measure the position of the clusters. We can then compare the cluster-position distributions between both cathodes and compute the pseudo-efficiency described above. In Figure 4.33 we see an example of the display of pseudo-efficiency for both sides of DE100. Most of the detector has a pseudo-efficiency equal to one. However, some areas in the middle of the non-bending side show a null pseudo-efficiency, and the same areas on the bending side are empty which shows that no good cluster was found in this zone.

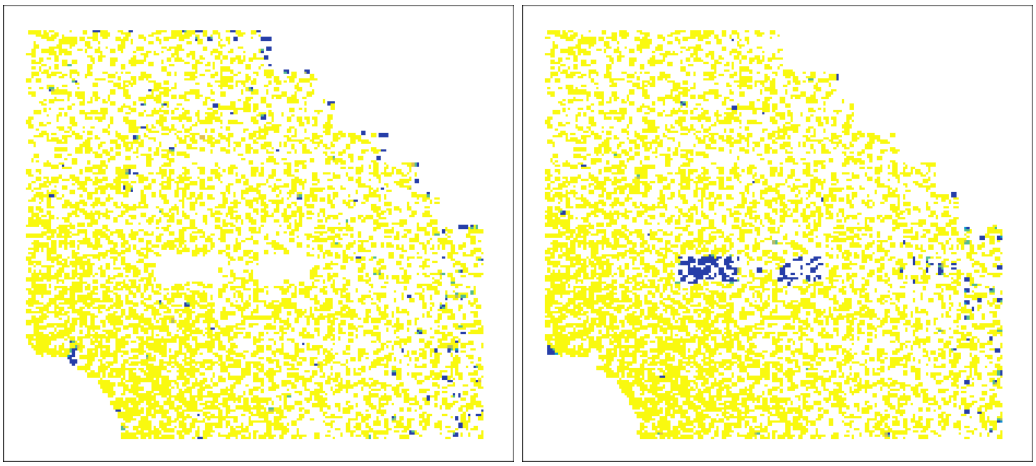

Figure 4.33: Pseudo-efficiency measurement on DE100. Top: Bending side, Bottom: Non-bending side.

The Preclusters task also monitors the amplitude of the total charge in the pre-clusters, which should follow a Landau distribution. The charge distribution is plotted separately for each detection element, and fitted with a Landau function when a minimum statistics is reached. The information on the fitted parameters of the Landau distribution (MPV and width) gives us information regarding the response of the detectors, in particular the relative value and stability of the gas gain.

Tracks monitoring

A fraction of the recorded data goes through full event reconstruction in real time on the online computing farm, and the resulting tracks and vertices are available for further processing in dedicated

QC tasks.

In the MCH case we monitor two categories of tracks:

- "standalone" tracks, which are reconstructed using exclusively clusters from the MCH detectors
- "matched" tracks, which consist of MCH tracks combined with those from the Muon Identifier (MID) and the Muon Forward Tracker (MFT)

For both track categories we monitor various parameters of the track candidates, like the average time, the geometrical distribution (azimuthal angle and pseudo-rapidity), the momentum distribution, and the average number of MCH charge clusters associated to the tracks. The framework also allows one to plot correlations between tracks, like dimuon invariant mass distributions, where the J/ψ resonance peak is visible.

An example of the output of the tracks monitoring is given in Figure 4.34. The monitoring of the tracks' parameters allows one to assess the overall performances of the event reconstruction, and spot at a very early stage possible inaccuracies or abnormal acceptance distortions.

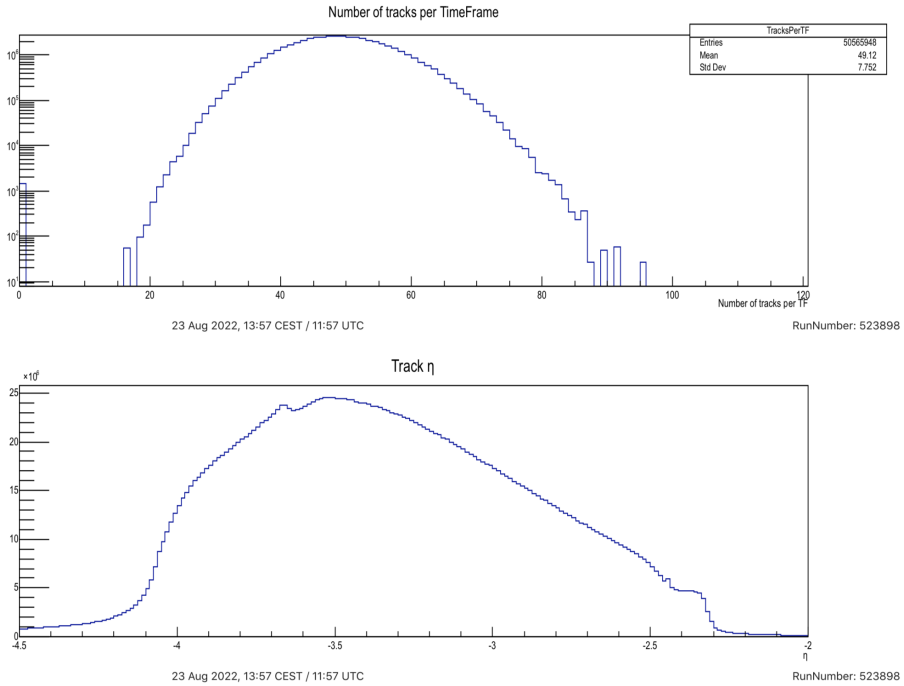

Figure 4.34: Example of MCH tracks monitoring. Top: number of reconstructed tracks in each Time Frame. Bottom: pseudo-rapidity distribution.

4.2.3 Post-processing

Once the observables have been measured and stored in the CCDB, they can be processed further before being output by the QC. In particular, the evolution with time of a specific observable can be studied. The quality of the output can also be assessed, which is particularly helpful to signal shifters and experts if the subsystem is working as expected or failing.

Trending: Assessing the evolution of an observable with time

The trending is a first tool of post-processing that can be applied to the monitored observable. Trending is an additional task, independent of the main QC task. It takes a plot stored in the CCDB and displays its time evolution.

In the MCH case, we mainly follow the evolution of occupancies and pseudo-efficiencies. A sudden change in either observable would indicate a modification of the working conditions of the detector,

which should be addressed. In Figure 4.35 an example of trending of the pseudo-efficiency of Chamber 4 is presented.

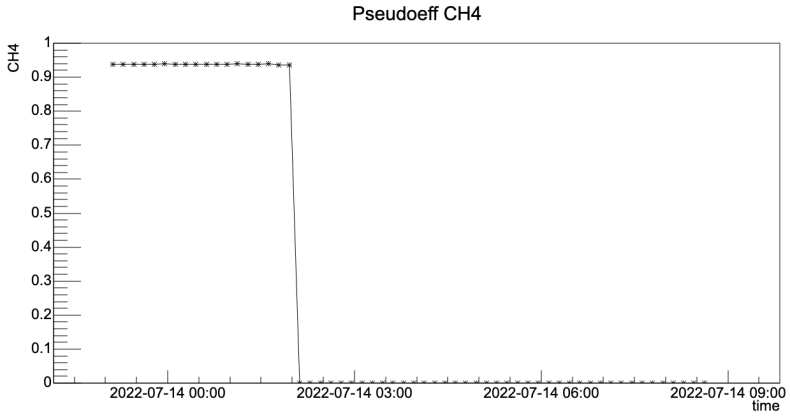

Figure 4.35: Trending of pseudo-efficiency measurement on Chamber 4.

Checking: Assessing the quality of the output

The last post-processing tool applied to QC outputs is checking. Checking routines are tasks that judge the quality of QC output. In the checking tasks, we define a set of criteria to determine if the quality of a given monitored quantity is satisfactory or not. For example, it means checking if too many pads are too noisy, or if the occupancy or pseudo-efficiency we measure are within reasonable bounds.

From the checks we can attribute a quality to the output. Essentially, it is a way to grade the output as "Good" or "Bad", label it and beautify it. The checking task is beneficial for the shifters that need to monitor the detectors during data taking. Whenever an output does not satisfy a check, the failure should be clearly visible to take action quickly. For example, in Figure 4.36 the mean value of occupancy for each detection element is plotted on a single plot. Each QC cycle, this plot is updated. Here, the occupancies are deemed too low, which may indicate a data taking issue (maybe parts of the detectors do not detect hits). We need to signal this in the most user-friendly way possible, so messages are displayed and the histogram is coloured in red to indicate the issue. On the contrary, if the observables indicate no specific issue, the histograms are coloured in green.

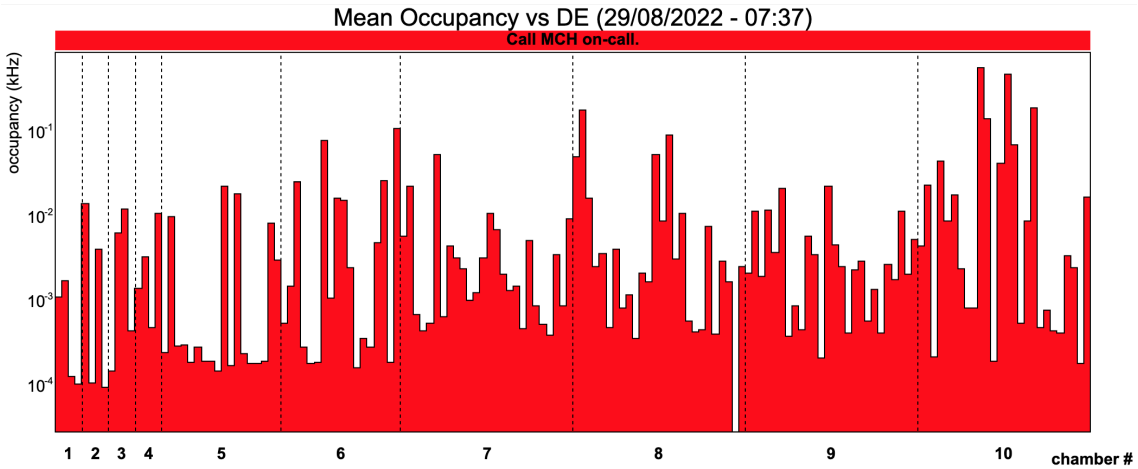

Figure 4.36: Display of the mean occupancy for each detection element.

4.2.4 Practical use

The tasks and post-processing techniques described in this section were used during the installation and commissioning of the muon spectrometer. They are also being used during Run 3 data taking. This subsection reviews examples of results we obtained thanks to the QC.

During commissioning

During commissioning we mainly focused on the monitoring of pedestals data. It allowed one to measure the pedestals and noise of each pad and to verify the mapping implementation by checking that each front-end component was correctly placed in the spectrometer. For example, as the SOLAR boards were progressively connected to the detectors, the QC task was run to see if the new data appeared at the correct place in the histograms. Failures in the filling of the QC histograms (if the wrong parts of detectors started receiving data for example) could signal a mapping issue or a hardware failure. For example, a failing DualSAMPA board would not send messages and remain blank in the QC plots. Furthermore, it allowed scanning of the noise of each pad.

In particular, the QC output let us identify a substantial noise during the commissioning. It was coming from the ventilating equipment of the ALICE cavern, controlled by variable-speed electronic motors, which generated parasitic noise on the chamber supports that was then injected into the detectors.

During data taking

During data taking, the QC output is typically used by shifters to make sure the detectors are working correctly in real-time. Information is presented in layout panels that display the various observables of interest.

The tasks that have been implemented allow monitoring of the error sources in raw data for the different detector chambers and the detector occupancy on different scales of the spectrometer. We monitor the occupancy at the level of individual pads, detection elements or chambers. Detector experts mostly use layouts based on the electronics, while layouts based on an overall view of the spectrometer are preferred for shifters because the display is more user-friendly.

The behavior of the MCH system and its QC was tested during pilot beams at the LHC and allowed the full-system validation with beam. An example of displays during this test is shown in Figure 4.37. Some issues in the mapping, in the power supplies and in the QC implementation were identified and subsequently corrected to have the MCH system ready for Run 3.

4.2.5 Outlook of MCH QC development

The muon spectrometer Quality Control is an ensemble of tasks that allows assessing the system's functionality. By processing data from the detectors, we can extract a set of observables to monitor that inform us of the health of the spectrometer. These physical observables, such as error codes, occupancy or pseudo-efficiency, are periodically measured and stored in a database where they can be post-processed. This post-processing allows one to study their behavior more thoroughly and, in particular, to judge whether it is satisfactory. This "satisfaction" level can then be displayed to shifters during data taking to communicate the good or bad running of the system.

The QC was used as a helping tool during the commissioning phase and during pilot beam tests to ensure the readiness of MCH for Run 3 data taking. However, further developments of the QC could be envisioned. For now, the main one is improving the user interface for the shifters by making the display of information from the QC more user-friendly. We will also need to define precise validity ranges to decide whether the detector behaviour is satisfactory or not. These bounds will have to be tuned to "ideal" data. Also, existing observables could be improved, or more could be monitored to give an insight into other detector issues we try to discern. For example, the monitoring of the charge distribution shape (which should follow a Landau distribution) could be made more robust as fitting procedures can fail depending on the amount of data available in each cycle.

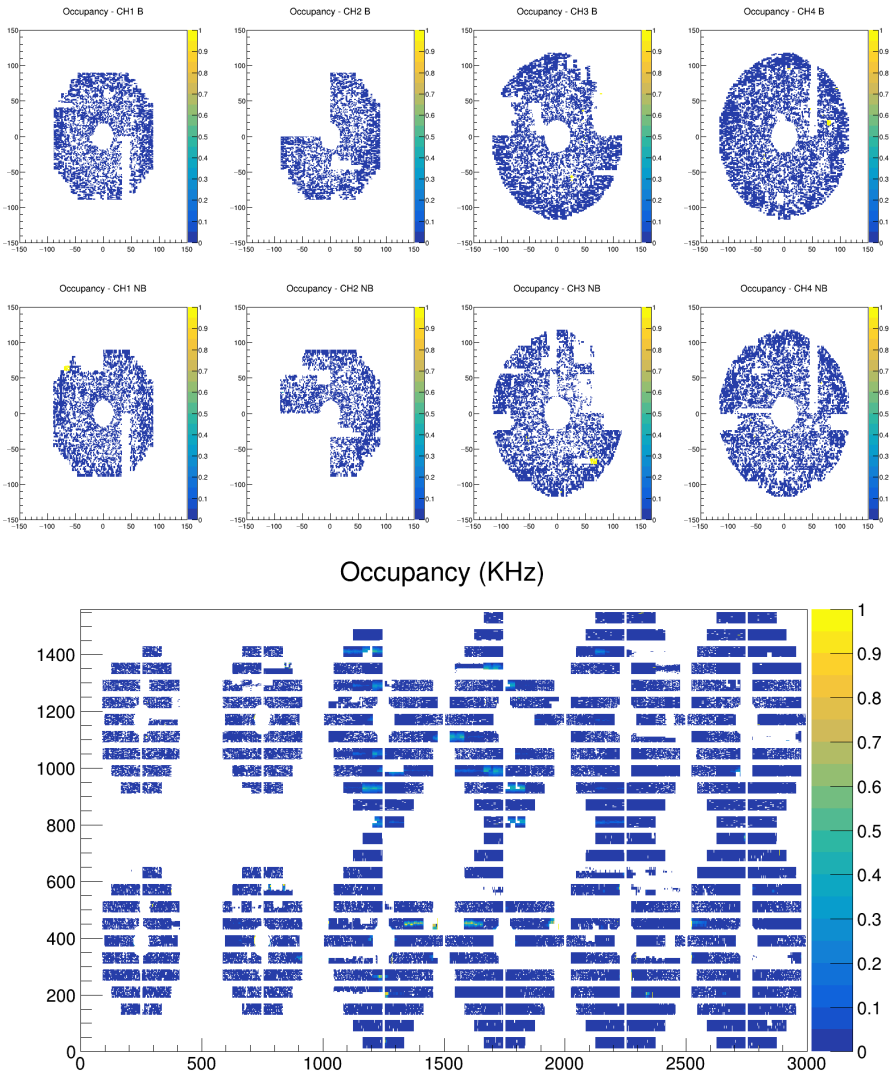

Figure 4.37: Display of the occupancy for all stations using data from pilot beams. Parts of detectors did not receive data, either due to a power supply issue or a mapping issue. Top: Stations 1 and 2, Bottom: Stations 3, 4, and 5.

Chapter 5

Flow analysis

Aujourd'hui j'aimerais mieux qu'le temps s'arrête, c'qui compte c'est pas l'arrivée c'est la quête.

– Orelsan, *La quête*

In this chapter, we detail the analysis of the elliptic flow of inclusive J/ψ in pp collisions at centre-of-mass energy $\sqrt{s} = 13$ TeV using the ALICE apparatus. It rests on two previous analyses. The dataset is the one previously used in Ref. [246] and the main analysis procedure is based on the one used in Ref. [102] as it already produced results in small systems on inclusive J/ψ anisotropic flow. In this chapter, we will go through the dataset and selection of events and particles, the different steps of the analysis and alternatives in view of systematic uncertainties evaluation, and various sanity checks and cross-checks allowing us to validate the analysis procedure and implementation.

5.1 Data selection

5.1.1 Datasets

For this analysis, data from pp collisions at $\sqrt{s} = 13$ TeV acquired during Run 2 is used. The periods used span from 2016 to 2018. The detail of the data processed in this analysis, with the different periods, the passes used, and the complete list of runs can be found in Table B1. The events studied amount to a luminosity of 24.38 ± 0.87 pb^{-1} [246].

5.1.2 Event selection

Two types of events are processed, based on two trigger classes. "CINT7-B-NOPF-CENT" are minimum bias (MB) events which only require a coincidence of signals in both V0 elements. They are used for centrality (rather multiplicity in the case of small systems) determination. "CMUL7-B-NOPF-MUFAST" are minimum bias events requiring an unlike sign dimuon with $p_{\mathrm{T}} > 0.5$ GeV/c, which will be used for the core of the analysis (correlations and flow extraction). The events used in this analysis are required to pass the following selection criteria:

- the Physics selection
- a multiplicity-dependent pileup cut
- have a primary vertex within $|z_{vtx}| < 10$ cm
- have a primary vertex reconstructed with a resolution $\sigma_z < 0.25$ cm
- have at least a contributor to the primary vertex (a reconstructed track which crosses the vertex)
- have at least one SPD tracklet within $|\eta| < 1$

The Physics selection framework is widely used in ALICE analyses and allows one to select events with the relevant trigger, and to reject background (like beam-gas events), pile-up, and poor quality events in general. The justification of the other requirements lies within the need to reject events that would not be useful in correlation analyses because they are of poor quality or because they do not provide reliable tracks to use. In Figure 5.1, we see examples of their effects, like the multiplicity-dependent pileup cut which suppresses events based on the proximity of reconstructed vertices, or the cut on z_{vtx} resolution. The latter typically shows that some events having few contributors do not manage to obtain a good enough resolution on z_{vtx} and should be ignored.

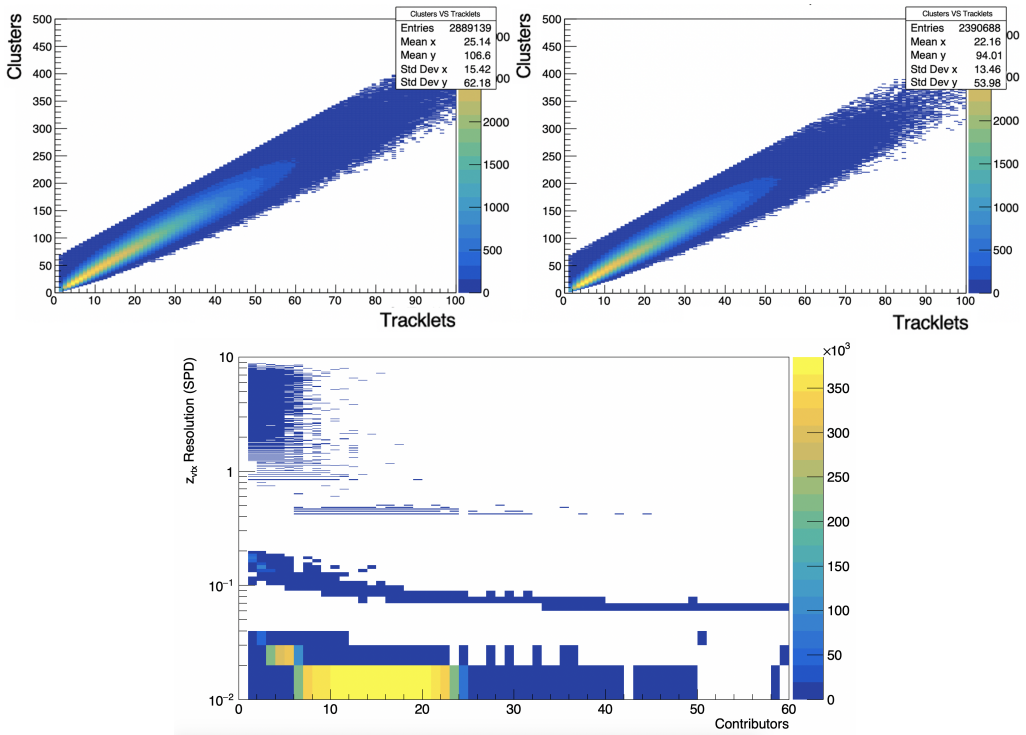

Figure 5.1: Top left: Distribution of events depending on the number of tracklets and clusters in the SPD, when correct pileup cuts are applied (Group8_LHC18m). Top right: Distribution of events depending on the number of tracklets and clusters in the SPD, when events tagged as pileup are removed regardless of multiplicity, wrongfully removing a fifth of the events (Group_LHC18m). Bottom: Distribution of resolution on z_{vtx} depending on the number of contributors to the primary vertex. The distribution is similar to Ref. [246] (Group4_18o).

During the analysis, forward dimuons are correlated to light particle tracks reconstructed in the SPD at mid-rapidity. However, the acceptance of the SPD is not uniform between the different data taking runs. In order to compute meaningful correlations and estimate detector effects properly thanks to event mixing, runs need to be grouped based on the status of the individual SPD modules. In each group, the SPD acceptance must stay unchanged. Based on the status of individual inner and outer SPD modules as stored in ALICE databases, groups of at least 5 runs were formed. The same procedure was also applied in Ref. [246].

Figure 5.2 shows an example of the SPD modules status for two runs. As they are identical, the runs belong to the same group (in this case Group 1). The detailed composition of each group, including the periods and number of runs, and the number of MB events and CMUL7 events in each case is reported in Table 5.1.

The selection criteria and grouping method being identical between this analysis and Ref. [246], we expect to be able to compare the number of events in each group. This reference number of CMUL7 events is also reported in Table 5.1. The agreement is within the percent level, failed jobs on the distributed ALICE computing grid accounting for the differences. In Table B2, we can see the impact of the different event selections in each group.

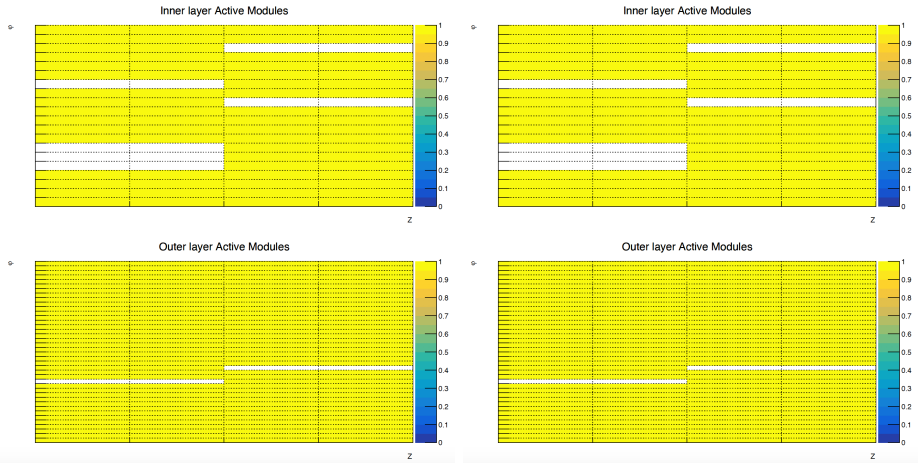

Figure 5.2: Layout of active/inactive SPD modules on inner and outer layers for Run 254419 (LHC16h) (left), Run 256512 (LHC16k) (right), both belong to Group 1.

Group	Period (# runs)	Total runs	#CMUL7 events ref	#CMUL7 events	#CINT7 events
1	LHC16h(68) LHC16j(49) LHC16k(170) LHC16o(100) LHC16p(39) LHC17i(56) LHC17k(95) LHC17l(4)	581	191,220,395	193,548,144	625,630,249
2	LHC17h(36)	36	8,494,516	8,402,198	25,374,721
3	LHC17h(67)	67	14,988,321	14,394,161	110,841,469
4	LHC17k(3) LHC18l(84) LHC18m(29) LHC18o(38) LHC18p(75)	229	77,389,191	77,880,45	226,075,743
5	LHC17l(110) LHC17m(116) LHC17o(168) LHC17r(31) LHC18c(46) LHC18d(44) LHC18e(44) LHC18f(67)	626	224,825,177	228,347,622	684,986,553
6	LHC18m(26)	26	8,663,725	8,584,444	21,538,912
7	LHC18m(9)	9	1,737,121	1,710,711	4,303,643
8	LHC18m(8)	8	2,926,354	2,898,949	6,864,366
9	LHC18m(14)	14	4,163,175	4,125,084	10,197,463
10	LHC18m(22)	22	8,016,626	7,975,941	21,417,693
11	LHC18m(11)	11	5,241,085	5,207,719	13,054,951
12	LHC18m(55)	55	17,294,586	17,547,676	43,897,670
Total		1684	564,960,272	570,530,694	1,794,183,433

Table 5.1: Repartition of runs into groups of similar SPD acceptance.

5.1.3 Tracklet and (di)muon selection

Tracklet selection

Once events have been selected, tracklets from those events need to be selected as well. They are reconstructed from hits in the SPD (the two inner layers of the ITS), and are paired with either a forward dimuon or with themselves in the course of this analysis. The quality of the tracklets used in the analysis is enhanced by applying two selection cuts to their direction and kinematics, as described below.

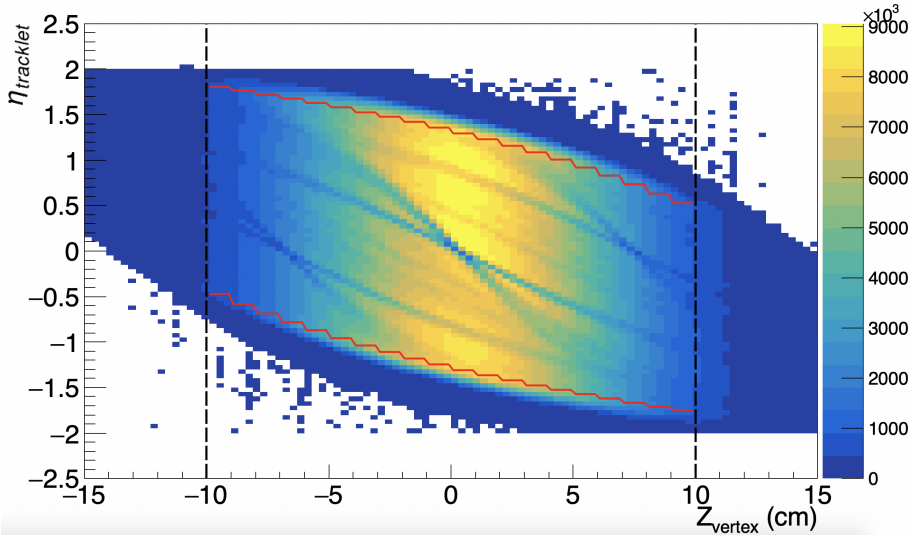

Figure 5.3: Distribution of selected tracklet η as a function of z_{vtx} on Run 2 data, the red curves show the variable cuts on η.

As seen in Figure 5.3, the tracklet distribution as a function of z_{vtx} and η is not uniform. To avoid selecting tracklets in domains of low acceptance, a cut on z_{vtx} is already applied in the event selection, and a z_{vtx}-dependent cut on the tracklet pseudorapidity η is added, mimicking the boundaries of the acceptance region. Formally, the η acceptance cuts follow the following equation:

$$\begin{cases} \eta_{low} = \log(\tan(\frac{1}{2}\arctan\dfrac{7.6}{14.1 + (\lfloor z_{vtx} \rfloor + 0.5)})) + 0.1 \\ \eta_{high} = -\log(\tan(\frac{1}{2}\arctan\dfrac{7.6}{14.1 - (\lfloor z_{vtx} \rfloor + 0.5)})) - 0.05 \end{cases} \tag{5.1}$$

Another cut is applied to the tracklets based on the angle between both of their hits in the SPD layers, denoted $\Delta\Phi$. This value is capped to $\Delta\Phi_{max}$ which is set by default at 10 mrad. The reason of such a cut is that if $\Delta\Phi$ is too large, the tracking and matching abilities of the SPD are deteriorated, which would cause an increase of combinatorial background with fake non-physical tracklets. This $\Delta\Phi_{max}$ requirement is in fact equivalent to a $p_{\mathrm{T},min}$ cut which is standard in flow analyses from other collaborations. We'll now delve more into the equivalence between $\Delta\Phi$ and p_{T} cuts which will be useful in comparing results from different analyses down the line.

As represented in Figure 5.4, due to the existing magnetic field in the central barrel, charged particles move along a portion of a circle whose radius of curvature is $R = \dfrac{p_{\mathrm{T}}}{0.3B}$ with R in metres, p_{T} in GeV/c, B in T. In the ALICE case we have $R = \dfrac{p_{\mathrm{T}}}{0.15}$. As a consequence, the coordinates (x, y) of the hit of a charged particle in a SPD layer satisfy

$$\begin{cases} x^2 + y^2 = r_{SPD}^2 \\ x^2 + (y - R)^2 = R^2 \end{cases} . \tag{5.2}$$

which yields

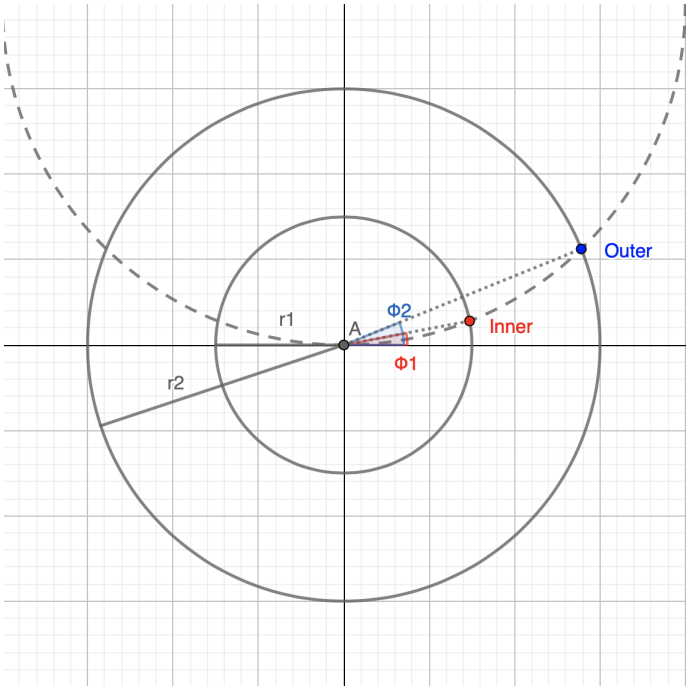

Figure 5.4: Representation of a particle going through the two layers of the SPD by the points labelled Inner and Outer. $\Delta\Phi$ is the difference between the angles labelled Φ_2 and Φ_1.

$$\begin{cases} x = \sqrt{r_{SPD}^2 + y^2} \\ y = \dfrac{0.15 \times r_{SPD}^2}{2p_{\mathrm{T}}} \end{cases} . \tag{5.3}$$

The Φ angles of each hit being $\Phi = \arctan\dfrac{y}{x}$, it follows that

$$\Delta\Phi = \Phi_2 - \Phi_1 = \arctan\frac{y_2}{\sqrt{r_2^2 + y_2^2}} - \arctan\frac{y_1}{\sqrt{r_1^2 + y_1^2}} \tag{5.4}$$

Plugging the SPD layers radii ($r_1 = 3.9$ cm and $r_2 = 7.6$ cm) into Equation 5.4, we obtain the equivalence between $\Delta\Phi$ and p_{T} cuts. For the $\Delta\Phi$ that were considered over the course of this analysis, the corresponding p_{T} cuts are of order 0.1 to 1 GeV/c, as shown in Table 5.2, which is the order of magnitude in existing flow analyses from ATLAS and CMS.

Cut on $\Delta\Phi$	Cut on tracklet p_{T}
10 mrad	0.28 GeV/c
5 mrad	0.56 GeV/c
2.8 mrad	1.00 GeV/c

Table 5.2: Equivalence between $\Delta\Phi$ cuts and p_{T} cuts.

Using the cut on η and on $\Delta\Phi$, we ensure the tracklets we select are of good quality. However, one last correction must be applied before using them in the analysis. The information regarding each tracklet is stored in AODs. ϕ, the azimuthal angle of the tracklet, is stored as the azimuthal angle of the tracklet as it hits the first layer of the SPD (Φ_1). In the analysis, we need the angle at which the tracklet is produced at the primary vertex, which is different from Φ_1 as shown in Figure 5.4. To correct the value of ϕ stored in the AOD, we need to add a corrective factor that is a function of $\Delta\Phi$, following Equation 5.5.

$$\phi_{corr} = \phi_{uncorr,AOD} + \frac{R_{SPD1}}{R_{SPD2} - R_{SPD1}}\Delta\Phi \tag{5.5}$$

where R denotes the radius of a given layer of the SPD. Having $R_{SPD1} = 3.9$ cm and $R_{SPD2} = 7.6$ cm, one obtains $\phi_{corr} = \phi_{uncorr,AOD} + \frac{39}{37}\Delta\Phi$. This correction was applied for completeness but this corrective effect is of order $\mathcal{O}(1 \text{ mrad})$, so it has very little impact on any of the final results. Some analyses (for example in Ref. [102]) use effective radii which slightly modifies the correction factor but the impact is small compared to the correction itself so both parametrizations are equivalent.

(Di)muon selection

The muon and dimuon candidates are selected based on the following criteria, the usual ones in dimuon analyses with ALICE.

Muon selection:

- The muon track must match a trigger track
- The pseudorapidity η of the muon must fall within the spectrometer acceptance $[2.5, 4.0]$
- The radial distance to the beam axis at the end of the absorber must satisfy $17.6 < R_{abs}(\text{in cm}) < 89.5$ (to avoid the absorber edges)
- The $p \times DCA$ cut is fixed at 6σ. DCA is the distance of closest approach, defined as the distance in the transverse plane between the interaction vertex and the extrapolated muon track.

Dimuon selection:

- It must be composed of two unlike sign muons
- The rapidity y of the dimuon must fall within the spectrometer acceptance $[2.5, 4.0]$
- The invariant mass falls between 2 and 5 GeV/c^2 (by default, varied for the systematic uncertainties study)
- The p_{T} of the dimuon is required to be below 12 GeV/c

5.1.4 Centrality selection and estimators

Centrality estimation in small systems

As was discussed in previous chapters, in the small pp system the pair-correlation method is used to extract the flow. The consequence is the need to separate central and peripheral (high-multiplicity and low-multiplicity) events to suppress non-flow effects. While in Pb–Pb collisions, centrality has a geometrical meaning (as discussed in Chapter 3), this meaning is lost in small systems. One could try to count the selected tracklets in an event and use this as a way to classify what is high or low-multiplicity. However, as seen in Figure 5.5, the distribution of the number of tracklets is not uniform along z_{vtx} and changes between groups.

Although this issue can be avoided by a data-driven method which defines centrality percentiles in each bin of z_{vtx} to account for some non-uniformities, it is better to use the existing calibrated centrality estimators from the ALICE framework. These estimators have been calibrated (for instance along z_{vtx}) to make them as event-independent as possible without the need for such additional data-driven calibration by hand, as seen in Figure 5.6. For this analysis, three estimators are used:

- V0M, which uses the signals from both V0A and V0C
- SPDTracklets, which uses the tracklet count in the SPD
- SPDClusters, which uses the cluster count in the SPD

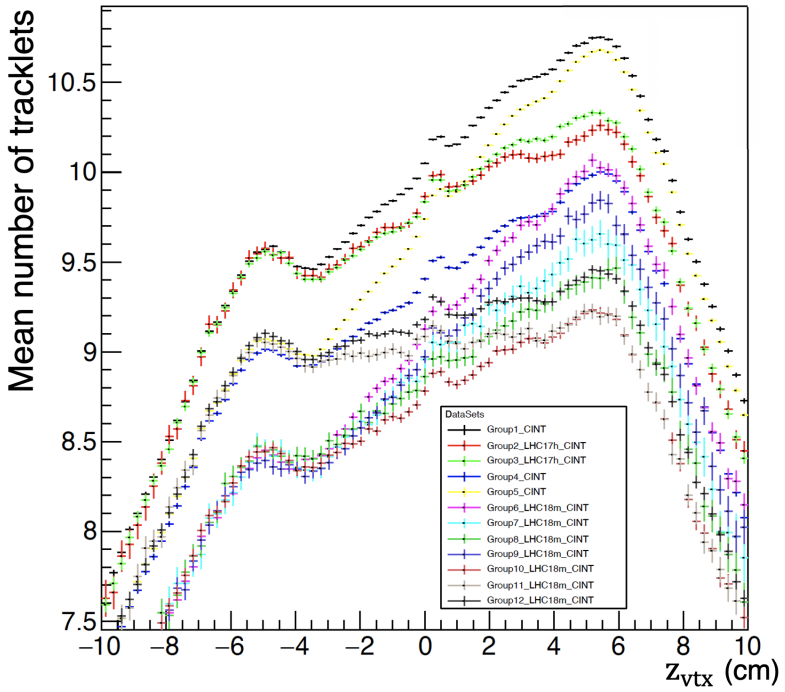

Figure 5.5: Distribution of the mean value of the number of SPD tracklets as a function of z_{vtx} for the different run groups.

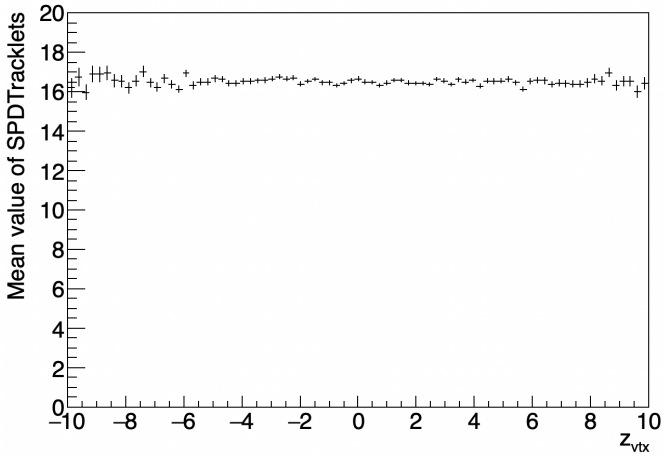

Figure 5.6: Distribution of the mean value of the calibrated SPDTracklets estimator as a function of z_{vtx} for period LHC16h.

These estimators represent three ways of defining centrality. They are based on different observables within a different acceptance. The SPD measures activity at mid-rapidity, while the V0M measures activity at forward and backward-rapidity. Both SPD-based estimators are strongly correlated, whereas V0M is very loosely correlated with any of them, as seen for example in Figure 5.7. Results from the analysis might be highly influenced by the choice of the centrality estimator.

Now that the concept of centrality in pp collisions is defined, we need to introduce classes for central events, where we expect high enough multiplicity to see collective effects, and peripheral events, where we expect no collective behaviour. Based on the available number of events in each class and documentation from ALICE framework concerning the estimators (see for example a table concerning SPDTracklets in Figure 5.8), the default peripheral class was defined as 40-100% as the mean multiplicity of this class is close to the pp dataset mean multiplicity. The default central class was defined as 0-

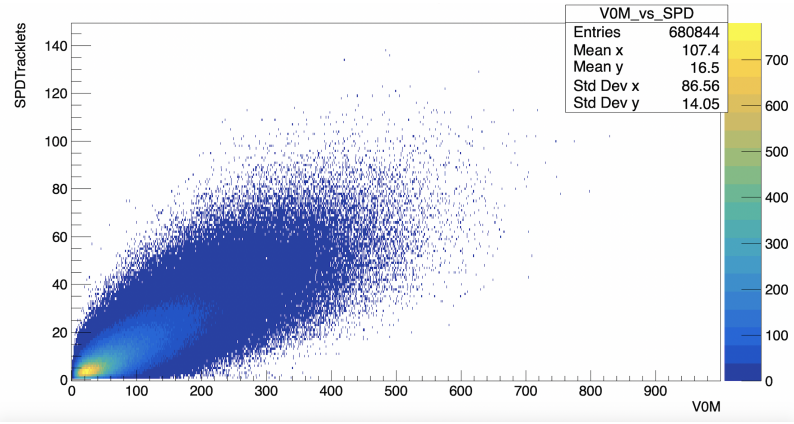

Figure 5.7: Correlation between SPDTracklets and V0M estimators on events from LHC16h.

5% as the mean multiplicity of this class is close to five times the pp mean multiplicity which should be enough to observe collective effects while keeping enough events. This motivated but still arbitrary choice of centrality classes will be further discussed during the evaluation of the systematic uncertainties and cross-checks.

Multiplicity dependent pp at 13 TeV: SPDTracklet multiplicity estimator

0 - 1	INEL>0	$\|\eta\|<0.5$	33.01	+0.55 -0.49	$\|\eta\|<1$	33.29	+0.57 -0.51	link	in preparation
1 - 5			23.18	+0.35 -0.32		23.44	+0.37 -0.33		
5 - 10			18.00	+0.26 -0.24		18.25	+0.28 -0.25		
10 - 15			14.91	+0.21 -0.19		15.13	+0.22 -0.20		
15 - 20			12.67	+0.18 -0.16		12.88	+0.19 -0.17		
20 - 30			10.32	+0.15 -0.13		10.50	+0.16 -0.14		
30 - 40			8.02	+0.12 -0.11		8.18	+0.12 -0.11		
40 - 50			6.17	+0.09 -0.08		6.30	+0.10 -0.09		
50 - 70			4.04	+0.06 -0.05		4.13	+0.06 -0.06		
70 - 100			1.80	+0.04 -0.04		1.87	+0.04 -0.04		

Mult (%)	Class	η	$dN_{ch}/d\eta$	sys	AN	Paper
0 - 100	INEL>0	$\|\eta\|<0.5$	6.89	± 0.11	link	updated from published

Figure 5.8: Top: Table taken from ALICE centrality framework TWiki showing the mean multiplicities in various centrality classes using the SPDTracklets estimator. Bottom: Mean multiplicity on the whole dataset.

V0M and SPD mixed estimator

Results will highly depend on the choice of the centrality estimator. For now, the ALICE framework offers two alternatives. Counting activity in the SPD or counting activity in the V0M. However, we could imagine events that would be very active in the V0M and not at all in the SPD (like dijet events forward and backward), and vice versa. This is why the resulting estimators do not correlate strongly and this estimator-dependent centrality selection will lead to different flow extractions.

In an effort to account for a larger coverage of the experiment, we tried to devise an estimator that would use information from both the V0 and SPD detectors. The first step is to look at the distribution of V0M and SPDTracklets in Minimum Bias events, as shown in Figure 5.9.

V0M yields higher values than SPDTracklets. Averaging the raw distributions as-is would let V0M fully dominate and would be useless. The distributions need to be normalized so that the averaging makes sense. Instead of equalizing the means or the maxima of the distributions, we opted to equalize

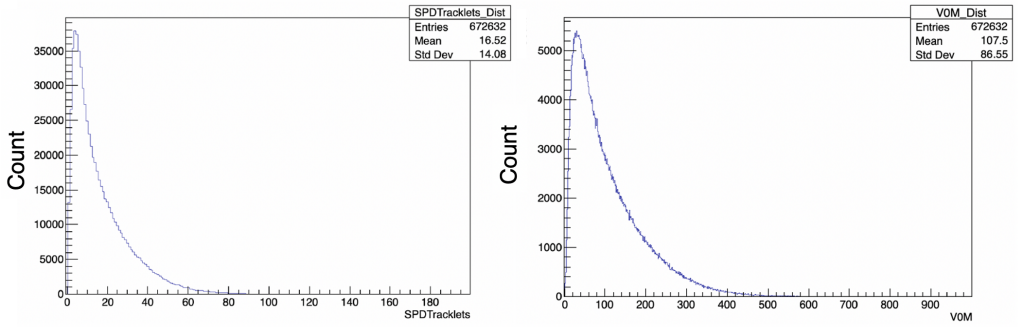

Figure 5.9: Left: Values distribution of SPDTracklets estimator. Right: Values distribution of V0M estimator.

the median values, as they would be less sensitive to extreme events. The normalized distributions are shown in Figure 5.10, where the median of each normalized distribution is arbitrarily fixed at 10 [1].

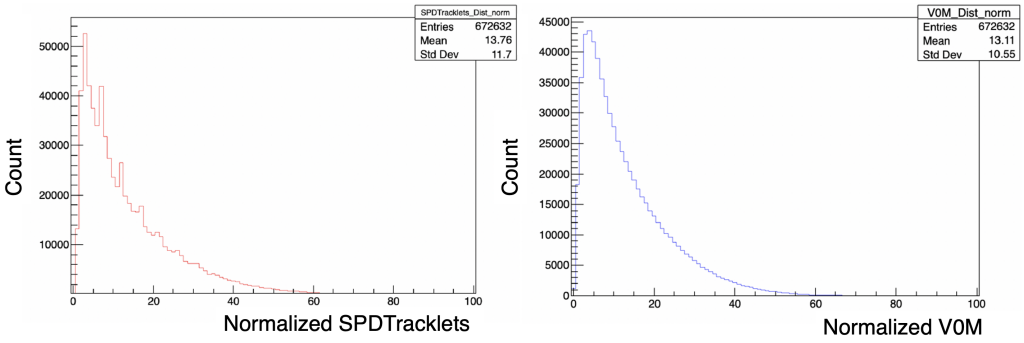

Figure 5.10: Left: Values distribution of SPDTracklets estimator normalized. Right: Values distribution of V0M estimator normalized.

Before averaging those normalized distributions, one also needs to account for the fact that the charged particle pseudorapidity density $\frac{dN_{ch}}{d\eta}$ is not constant with η which means that the V0 and the SPD do not "see" the same amount of charged particles. The V0 being forward and backward will see a lower density compared to the SPD so the relative importance of the V0M estimator in the averaging needs to be scaled down slightly.
Using current results on the charged particle pseudorapidity density in pp (5 TeV) from Ref. [247] shown by the blue curve in Figure 5.11, we can measure that the mean charged particle density for the SPD (whose tracklets are considered within [-1,+1]) is 5.62, and for the V0 ([-3.7,-1.7] + [2.8,5.1]) 5.39. The value of the mixed estimator can then be computed as the average of the values of the two normalized estimators weighted by their acceptances:

$$Value_{Mixed} = \frac{Acc_{V0} \times Value_{V0M,norm} \times \frac{\frac{dN_{ch}}{d\eta}_{V0M}}{\frac{dN_{ch}}{d\eta}_{SPD}} + Acc_{SPD} \times Value_{SPDTracklets,norm}}{Acc_{V0} + Acc_{SPD}}$$
$$= \frac{4.3 \times Value_{V0M,norm} \times \frac{5.39}{5.62} + 2 \times Value_{SPDTracklets,norm}}{6.3}.$$

The limits on the centrality classes of this new estimator are obtained by computing the quantiles of the distribution seen in Figure 5.12 (in magenta). This set of limits should be valid for all periods as it is based on centrality estimators that have been calibrated.

[1] Such scaling causes issues with the binning of SPDTracklets normalized distribution which only impacts the visual representation of the distribution without hurting the physics or our ability to use it to define a meaningful mixed estimator.

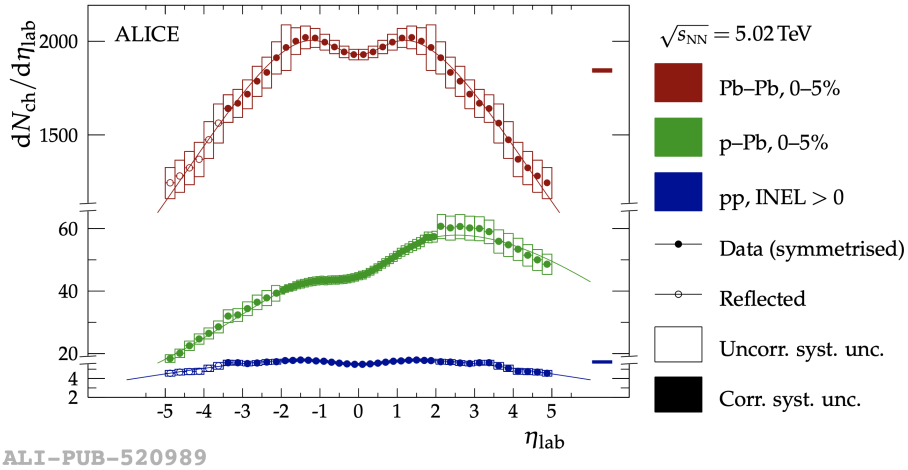

Figure 5.11: Charged particle pseudorapidity density versus pseudorapidity in the laboratory frame in collisions at 5.02 TeV for various collision systems from Ref. [247].

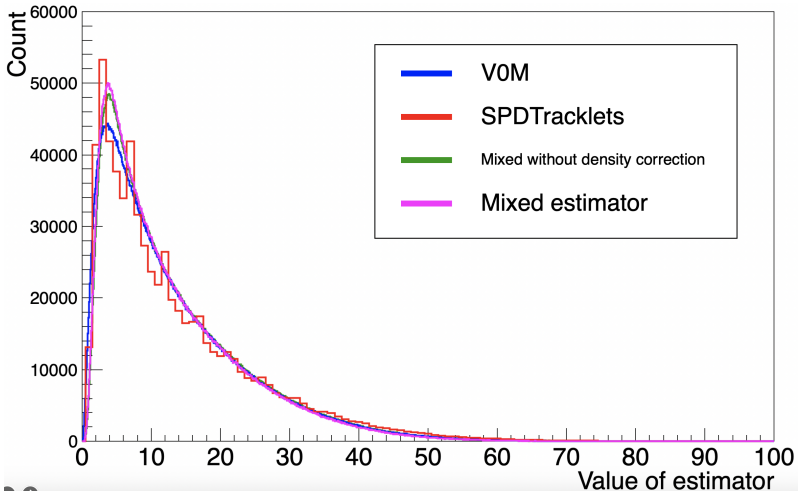

Figure 5.12: Distributions of SPDTracklets normalized (red), V0M normalized (blue), the V0M and SPD weighted average without accounting for density correction (green), and the correct weighted average (magenta).

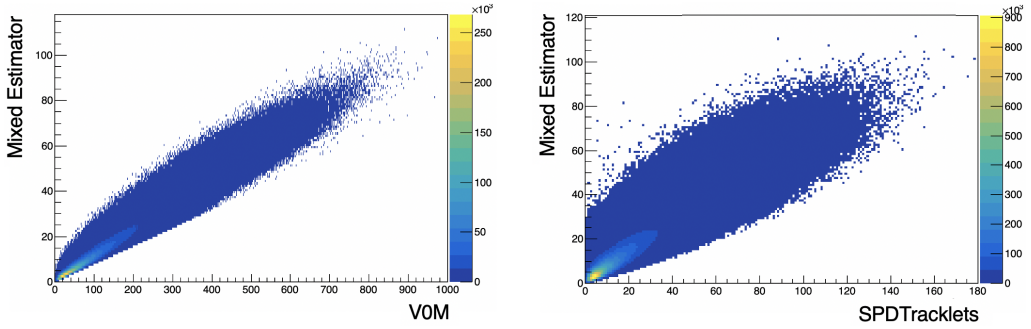

Figure 5.13: Correlation between the mixed estimator and V0M (left) and SPDTracklets (right) estimators on events from LHC16h.

As a check, we can look into the correlation of this estimator with the existing ones. In Figure 5.7 we saw that V0M and SPDTracklets were loosely correlated. In Figure 5.13, we see the correlation between the mixed estimator and both V0M and SPDTracklets. If the new estimator is well defined,

it should correlate with both. Indeed, we observe that the mixed estimator correlates nicely with both estimators, maybe even more so with V0M than with SPDTracklets, which may lead to similar results between V0M and the mixed estimator in the end, which we will discuss in the next chapter when presenting the results.

5.1.5 Dimuon invariant mass

Now that the event selection, dimuon selection and centrality classes are defined, one crucial tool in the analysis is the dimuon invariant mass spectra. The reason is that, while we will correlate dimuons with tracklets, to extract the J/ψ flow we need to separate signal J/ψ from background dimuons. This separation is done through fits of the invariant mass spectrum. Fitting the dimuon invariant mass spectrum also serves as a cross-check with Ref. [246] which applied the same selection criteria to the dataset. This cross-check will be discussed further in this chapter.

Function shapes and tail parameters used for this analysis can all be found in Appendix C.1. By default, the fit was done between 2 and 5 GeV/c^2. Within this range, the invariant mass spectrum was fit using a Double Crystal Ball (CB2) to reproduce the signal, and a Double Exponential to reproduce the background. The tails of the signal were fixed to Run 2-extracted values as found in Ref. [246]. For the $\psi(2S)$, the signal shape was the same however, the mass difference with the J/ψ was fixed to the PDG value and the width ratio was 1.05 by default. Other function shapes, and alternative parameters were used in the assessment of the systematic uncertainties and the cross-check with Ref. [246] and they will be detailed in Section 5.5.2.

The top panel of Figure 5.14 shows the dimuon invariant mass fit using the default functions and parameters. The bottom panel shows the pulls from the fit which measure the difference between each data point and the value predicted by the fit. Candidates in the dataset amount to 3.76 million J/ψ and 70 thousand $\psi(2S)$ which is in reasonable agreement with the results from Ref. [246], but some tensions remain between the fit and data especially on the level of the signal tails. From this fit, we can obtain the templates of the signal and background dimuons which will be used in extracting the flow by disentangling signal and background contributions to the measured flow. The fit will also have to be carried out in thinner bins of p_{T} or centrality, as shown in Figure 5.15, depending on the specific binning used in the analysis because the templates will change depending on the dimuon p_{T} requirements and the centrality, compared to the full Run 2 dataset.

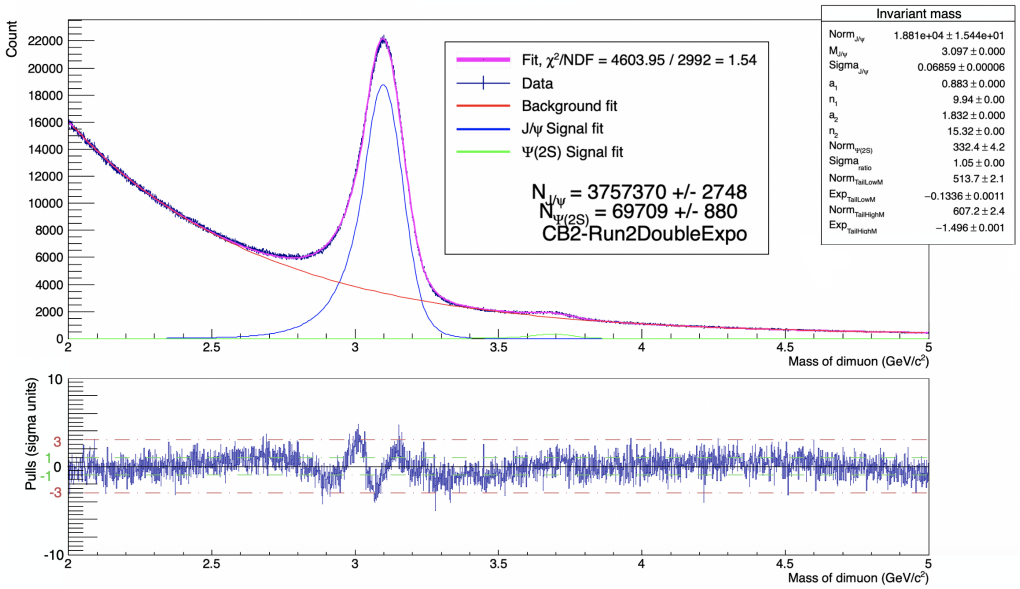

Figure 5.14: Example of dimuon invariant mass fit using default configuration on the whole Run 2 dataset - CB2 - Run 2 tails - DoubleExponential background - 2 to 5 GeV/c^2 mass range - 1.05 sigma ratio.

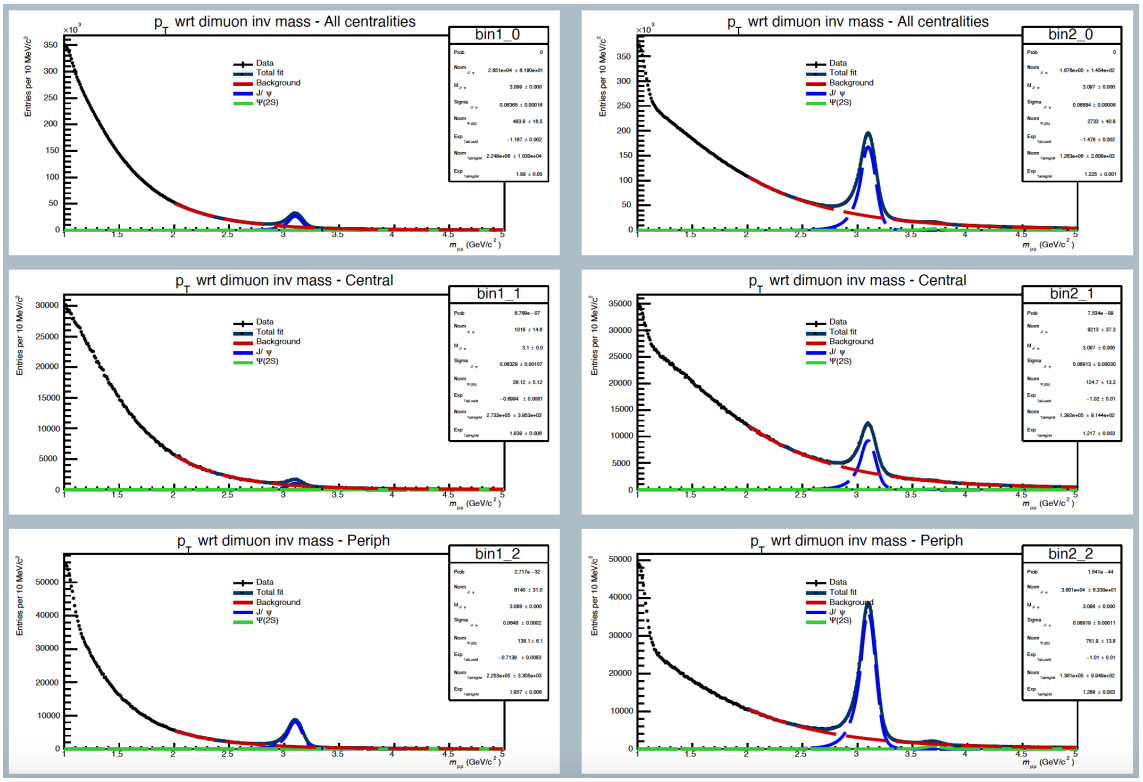

Figure 5.15: Invariant mass fits using the default procedure, binned in centrality and p_{T}. The rows are respectively 0-100%, 0-5% and 40-100%. The columns are respectively 0-1 and 1-12 GeV/c.

5.2 Overview of the analysis method

This section outlines the analysis procedure used to extract the elliptic flow of the J/ψ, based on the work described in Ref. [102]. The general idea is to measure correlations of pairs of particles, in both high and low-multiplicity events to be able to apply the flow extraction methods we discussed in previous chapters. In each event, one correlates a dimuon with tracklets to get a sense of how tracklets arrange around the dimuon. One also correlates tracklets together to see how they themselves arrange around one another, which is a behaviour dictated by light particle flow, so that this effect can be factored out. The same correlations must be carried out in non-physical mixed events where pairs are made from particles in different but similar events. This process allows one to assess detector effects. By normalization, summation and projection steps, dependencies on parameters like z_{vtx} can be suppressed. Then, using the invariant mass templates to separate background and signal dimuons and applying the existing flow extraction techniques, we can finally obtain the flow of the J/ψ.

5.2.1 Counting the correlations: the per-trigger yield

The per-trigger yield is the observable used to properly count the particle correlations with a reference particle, also called trigger particle. The reference particle is for example the dimuon in dimuon-tracklet correlations. The per-trigger yield is defined following:

$$Y_{ijk}(\Delta\phi,\Delta\eta) = \frac{1}{N_{ijk,trig}}\frac{d^2N_{ijk,assoc}}{d\Delta\phi d\Delta\eta} = \frac{1}{N_{ijk,trig}}\frac{SE_{ijk}(\Delta\phi,\Delta\eta)}{ME_{ijk}(\Delta\phi,\Delta\eta)}, \tag{5.6}$$

with Y, the per-trigger yield in a given $(\Delta\phi,\Delta\eta)$ bin, N_{trig} the number of reference particles that have been triggered on, N_{assoc} the number of associated particles that have been observed (the number of pairs that have been counted), SE the same event distribution (the counting of pairs where the reference particle and the associated particle come from the same physical event) and ME the mixed event distribution (the counting of pairs where the reference particle and the associated particle come

from different events but have been mixed together to factor detector effects). The per-trigger yields are defined in bins of centrality (index i), z_{vtx} (index j), and $m_{\mu\mu}$ (index k). Other variables like p_{T} or $\Delta\Phi$ are kept apart and the analysis can be done separately for each bin of these variables. z_{vtx} bins are of size 1 cm and mass bins are of variable width from 0.5 GeV/c^2 at low and high masses to 0.3 GeV/c^2 at the J/ψ peak.

Intuitively, the per-trigger yields describe how particles tend to arrange spatially around a reference particle. And this is why one needs to correlate dimuons to tracklets as well as tracklets together, because one needs to account for the fact that trackelts flow so if we observe collectivity in dimuon-tracklet pairs, we need to make sure what we observe is not fully coming from the tracklet flow itself. For dimuon-tracklet pairs we define $\Delta\phi$ and $\Delta\eta$ as:

$$\Delta\phi = \phi_{tracklet} - \phi_{dimuon}, \text{ mod}[2\pi] \text{ so that the result falls within } [-\frac{\pi}{2}, +\frac{3\pi}{2}]$$
$$\Delta\eta = \eta_{tracklet} - y_{dimuon}$$

$\Delta\phi$ is then further reduced to fall within $[0, \pi]$ only, by symmetry. Due to the muon spectrometer and SPD acceptances, $\Delta\eta$ is required to fall between 1.5 and 5.0 by default, typically the bin size is taken to be 0.5 units, while the bin size for $\Delta\phi$ is $\frac{\pi}{6}$ by default.

For tracklet-tracklet correlations, a reference tracklet is chosen and assumes a role similar to the dimuon in dimuon-tracklet correlations except this time $\Delta\eta$ is required to fall between 1.2 and 2.4 by default. The lower limit is imposed by the need of a sufficient η-gap to reduce short-range non-flow correlations, the upper limit by the acceptance of the tracklets in the SPD.

5.2.2 Assessing detector effects: the event mixing

As per their definition in Equation 5.6, per-trigger yields computation requires both same event correlations and mixed event correlations. While same event correlations are straightforward, mixed event correlations require to clarify what it means for two events to be "similar". Such events belong to the same pool and each time an event is studied, it is stored in a pool and its dimuon is correlated to the tracklets in its pool.

Pools definition

Similar events should have similar "activities" and, because z_{vtx} highly impacts the SPD acceptance, pools of similar events are made based on the existing centrality and z_{vtx} bins. The maximum number of events stored in a pool is 100. The minimal number of events needing to be stored in a pool before starting using this pool for mixing is 10. If we do not impose a threshold and a pool has a low number of events, all events will have been mixed with the first events of the pool which will greatly contribute to the final mixed event distribution. The use of such a threshold is to make the impact of the first events stored less important, which allows one to avoid statistical effects. The existing p–Pb analysis [102] used a similar definition for its event mixing pools.

For tracklet-tracklet correlations, it has been checked that 30 events instead of 100 were enough to reproduce well the detector acceptance effects. This is due to the fact that the number of tracklet pairs scales as N_{tkl}^2. This reduction allows quicker processing of data without deteriorating the results.

Normalization

After computing the mixed event distribution, it must be normalized. By default in the dimuon-tracklet study, each $ME_{ijk}(\Delta\phi, \Delta\eta)$ is projected along $\Delta\eta$. The normalization factor is taken to be the maximum of $ME_{ijk}(\Delta\eta)$, as was the case in Ref. [102]. In the tracklet-tracklet study, by default the normalization factor is taken as the number of pairs in the $(\Delta\phi, \Delta\eta) = (0, 0)$ bin for $|z_{vtx}| < 10$ cm.

In Figure 5.16, a basic example of the event mixing technique is shown. On the left, we see a 2D distribution of the same event dimuon-tracklet pairs and the 1D projection along the $\Delta\phi$. On the right, there is the same 2D distribution but for mixed events. The latter is only due to detector effects. Other event mixing criteria and normalization methods are employed as alternatives to the default presented here. They will be detailed in Section 5.5.

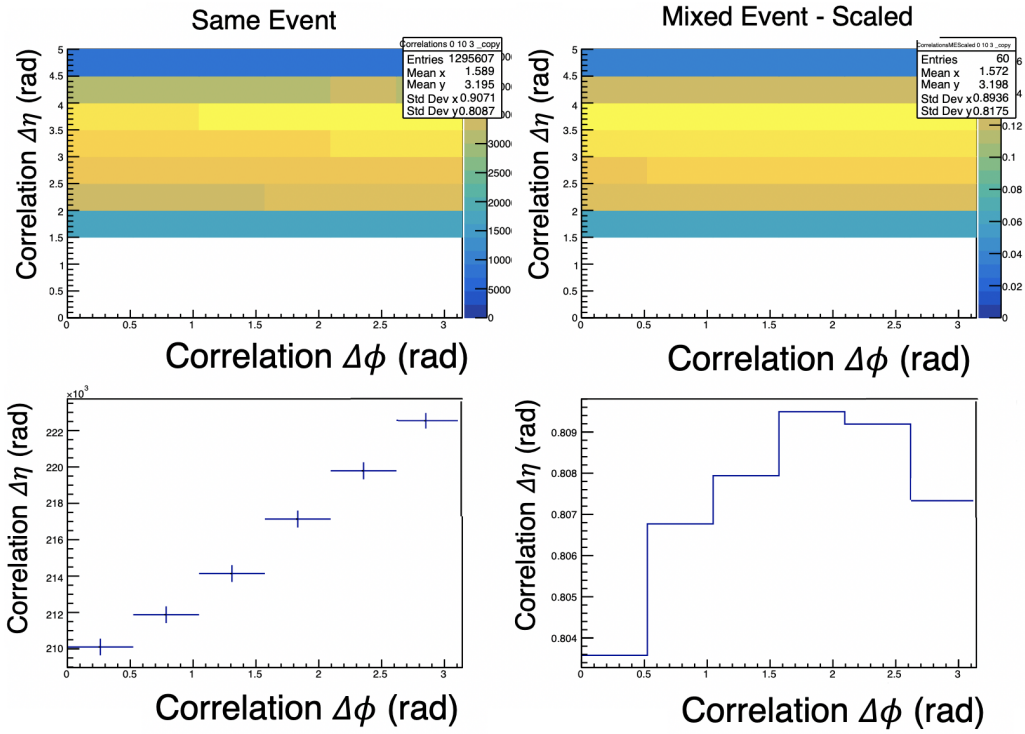

Figure 5.16: Same event (left) and Mixed event (right) distributions in 2D and their 1D projections for dimuon-tracklet pairs, in a given bin of centrality, z_{vtx} and mass.

5.2.3 Removing dependencies - Summation on z_{vtx} and $\Delta\eta$

Because of non-uniformities of observables as a function of z_{vtx}, as seen for example on the tracklet distribution in Figure 5.3, one needs to properly handle the yields in the different z_{vtx} bins to obtain a z_{vtx}-independent result. The default method, as in Ref. [102], consists in fitting $\frac{SE_{ik}(z_{vtx})}{N_{ik,trig}ME_{ik}(z_{vtx})}$ in each bin of $\Delta\phi$ and $\Delta\eta$ with a constant, which is denoted as Y_{ik} in the following. By doing so one obtains the distribution of $Y_{ik}(\Delta\phi, \Delta\eta)$, as exemplified in Figure 5.17. To suppress the dependency on $\Delta\eta$, the yield distribution is then projected on $\Delta\phi$ and the final value of each $Y_{ik}(\Delta\phi)$ is computed as $\int_{\Delta\eta} Y_{ik}(\Delta\phi, \Delta\eta) d\Delta\eta$ using a linear fit, which suppresses the dependency on $\Delta\eta$, as shown in Figure 5.18. The error on $Y_{ik}(\Delta\phi)$ is taken as the error on the integration.

There are two ways of handling the fit of the same and mixed event profiles. It can be done as usual via a χ^2 fit. However, because in the dimuon-tracklet analysis there are some bins, especially at high-mass and/or high p_{T} that have low numbers of candidates, it is false to assume that the errors on the distributions are gaussian (as assumed by the χ^2 fit). In this case, a Poisson-likelihood fit dedicated to studying rarely occurring events is more appropriate.

Overall, this procedure allows the per-trigger yields to be freed from the z_{vtx} dependence because they are defined using information from same and mixed events z_{vtx}-profiles. The $\Delta\eta$ dependence of the yields is then dropped by integrating on this variable to define $Y_{ik}(\Delta\phi)$ which are only dependent on centrality, mass and $\Delta\phi$.

5.3 Flow extraction from the per-trigger yields

5.3.1 Dimuon-tracklet flow

Once the dimuon-tracklet per-trigger yields $Y_{ik}(\Delta\phi)$ have been computed, two things must be done to get to the $V_{2,J/\psi-tracklet}$.

- Subtract the non-flow effects (via $\Delta\phi$-dependent plots)

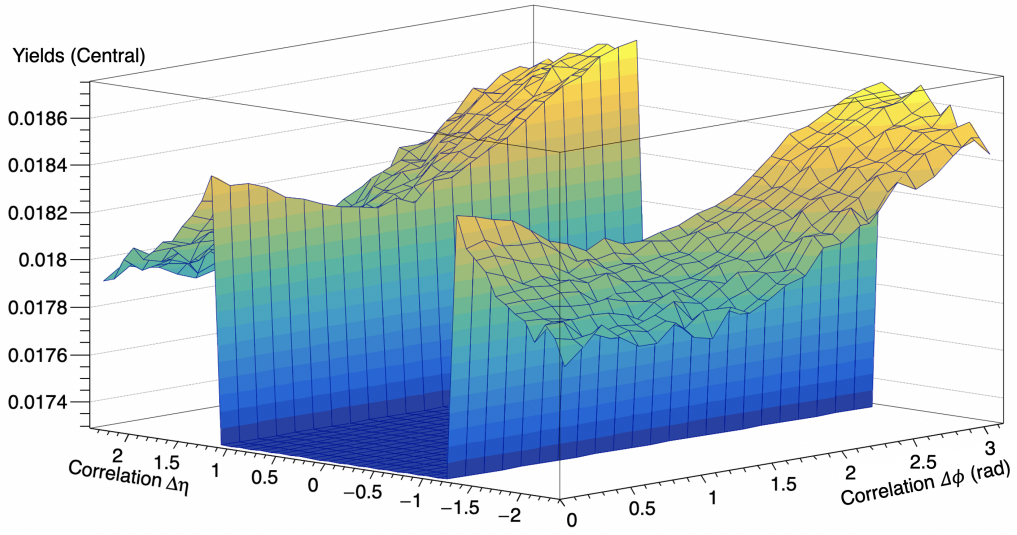

Figure 5.17: Per-trigger yields in central collisions form tracklet-tracklet correlations (on LHC16h period) as a function of $\Delta\eta$ and $\Delta\phi$.

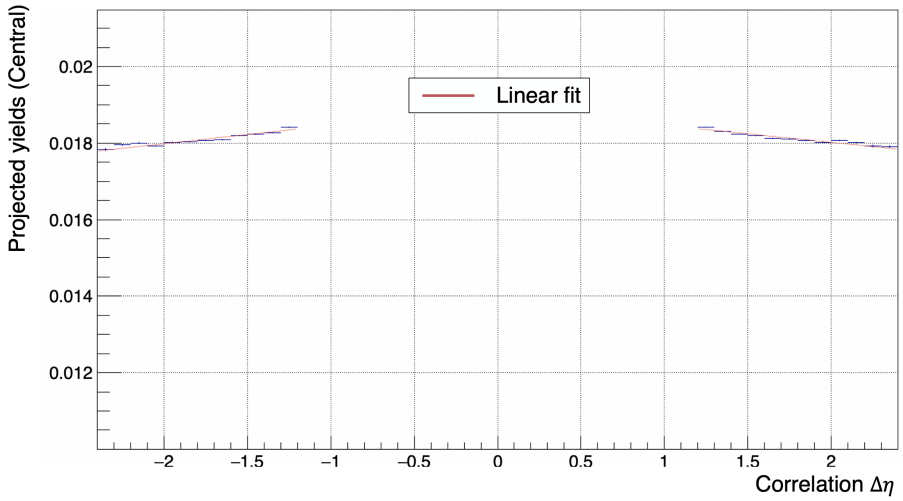

Figure 5.18: Projection in the first $\Delta\phi$ bin of per-trigger yields in central collisions form tracklet-tracklet correlations (on LHC16h period) as a function of $\Delta\eta$. The integral obtained from the linear fit of this distribution gives the value of the per-trigger yield for this specific $\Delta\phi$ bin. The error on the integral is taken as the error on the yield.

- Disentangle signal from background (via mass-dependent plots)

The second step uses the dimuon invariant mass spectrum fit that we have presented at the beginning of this chapter. The first step however can be done in multiple ways as was presented in Chapter 2. The historical approach in ALICE is to consider that non-flow effects are centrality-independent and so one can define subtracted yields as $Y^{sub} = Y^{Central} - Y^{Peripheral}$, in which non-flow effects are cancelled out. On the other hand, the ATLAS collaboration uses template fitting which defines subtracted yields as $Y^{sub} = Y^{Central} - F \times Y^{Peripheral}$ where F is a free parameter. These two methods present different behaviours and results and so they have both been used in the present analysis.

Considering we already applied an η-gap suppressing short-range correlations, the main source of non-flow that we are yet to suppress at this point in the analysis is part of the dijet contribution, that is characterised by an increased yield around $\Delta\phi = \pi$.

Yield subtraction methods

In yield subtraction methods (like ALICE usually uses), non-flow is suppressed by subtracting once the peripheral yields to the central ones. The two steps on the $V_{2,J/\psi-tracklet}$ extraction can be done in either order.

Extraction method 1 starts by taking the $Y_{ik}(\Delta\phi)$ distribution and changing its variables so that in each bin of $\Delta\phi$ and centrality we have a $Y(m_{\mu\mu})$ distribution. Each of these are fit using the following function:

$$\frac{S}{S+B}Y_{J/\psi} + \frac{B}{S+B}Y_B(m_{\mu\mu}). \tag{5.7}$$

S is the signal shape of the dimuon invariant mass fit, B is the background shape of the dimuon invariant mass fit, $Y_{J/\psi}$ is the J/ψ yield, and $Y_B(m_{\mu\mu})$ is the background dimuon yield taken as a second order polynomial. An example of this fitting procedure is shown in Figure 5.19.

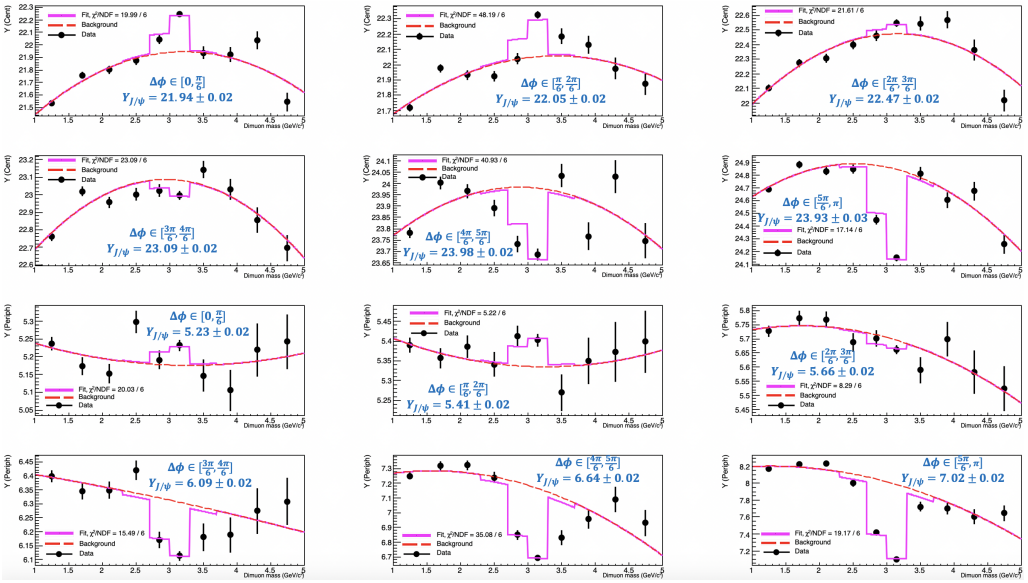

Figure 5.19: Signal/Background extraction step of Extraction method 1 - Run 2 data for p_{T} between 4 and 6 GeV/c.

Using the extracted $Y_{J/\psi}$ in each $\Delta\phi$ bin, one can build the J/ψ $Y_i(\Delta\phi)$ distributions for central and peripheral events and subtract the central and peripheral one as shown in Figure 5.20. The Fourier coefficients of $Y^{sub}(\Delta\phi)$ are then extracted using:

$$a_0 + 2a_1 cos(\Delta\phi) + 2a_2 cos(2\Delta\phi). \tag{5.8}$$

The $V_{2,J/\psi-tracklet}$ is then obtained as $\frac{a_2}{a_0+B_p}$ where B_p is the peripheral baseline. It is defined as the minimal value of $Y^{periph}(\Delta\phi)$, which is typically $Y^{periph}(0)$ due to the small (usually nonexistent) impact of collective effects in peripheral collisions. The use of the peripheral baseline in the computation of the flow coefficients is an artifact from the Zero Yield At Minimum (ZYAM) hypothesis.
The ZYAM hypothesis relies on the following assumption. Because of the absence of collective effects in peripheral collisions we can consider that the peripheral yields have an offset (the minimum of the distribution) that is not due to collective effects, and so, this offset B_p can be subtracted away. This is why $V_{2,J/\psi-tracklet}$ is computed as $\frac{a_2}{a_0+B_p}$ and not simply $\frac{a_2}{a_0}$. In fact, using the ZYAM hypothesis on the peripheral yields is equivalent to computing the subtracted yields as $Y^{sub} = Y^{Central} - (Y^{Peripheral} - B_p)$ and then computing V_2 as $\frac{a_2}{a_0}$. ATLAS typically puts into question the validity of this hypothesis in Ref. [136], and we will do so in order to check the impact of this hypothesis on the measured values of v_2 for J/ψ and for tracklets.

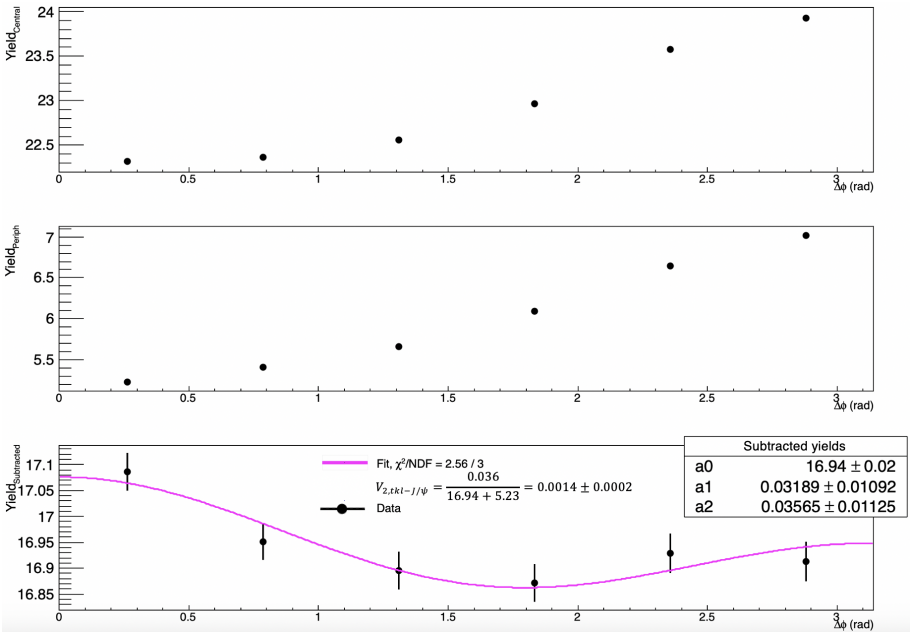

Figure 5.20: Yield subtraction and Fourier step of Extraction method 1 - Run 2 data for p_{T} between 4 and 6 GeV/c.

Extraction method 2 is the same as method 1 except the two steps are reversed. First, in mass bins, the central and peripheral yields are subtracted to obtain $Y_{ik}^{sub}(\Delta\phi)$, as shown in Figure 5.21. Using Equation 5.8, the Fourier coefficients are extracted as a function of $m_{\mu\mu}$, allowing one to compute $V_{2,dimuon-tracklet}(m_{\mu\mu})$.

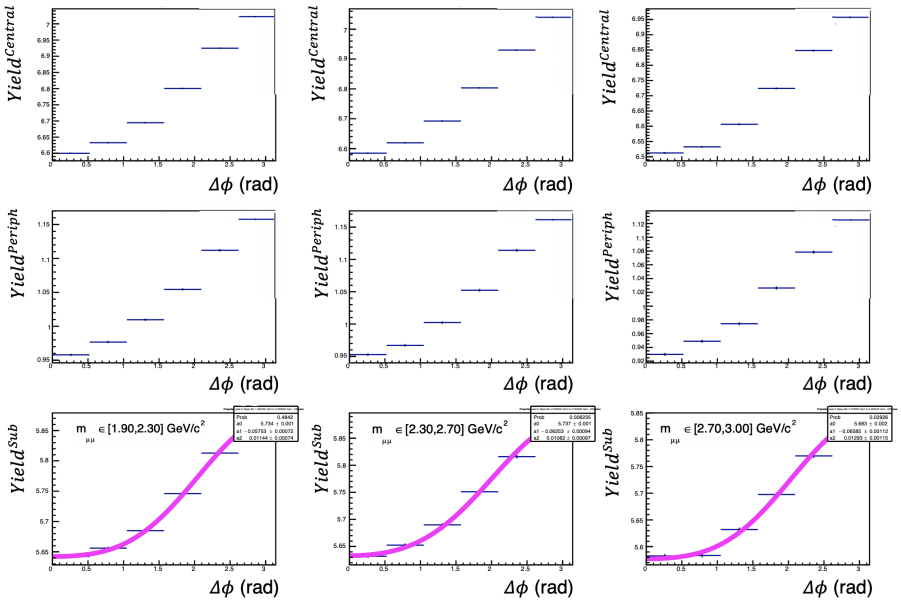

Figure 5.21: Yield subtraction and Fourier step of Extraction method 2 - Run 2 data for p_{T} between 0 and 12 GeV/c.

Then, we disentangle signal and background using the following equation, in an analogous way to method 1:

$$\frac{S}{S+B}V_{2,J/\psi-tracklet} + \frac{B}{S+B}V_B(m_{\mu\mu}). \tag{5.9}$$

One finally obtains the value of $V_{2,J/\psi-tracklet}$, as shown in Figure 5.22.

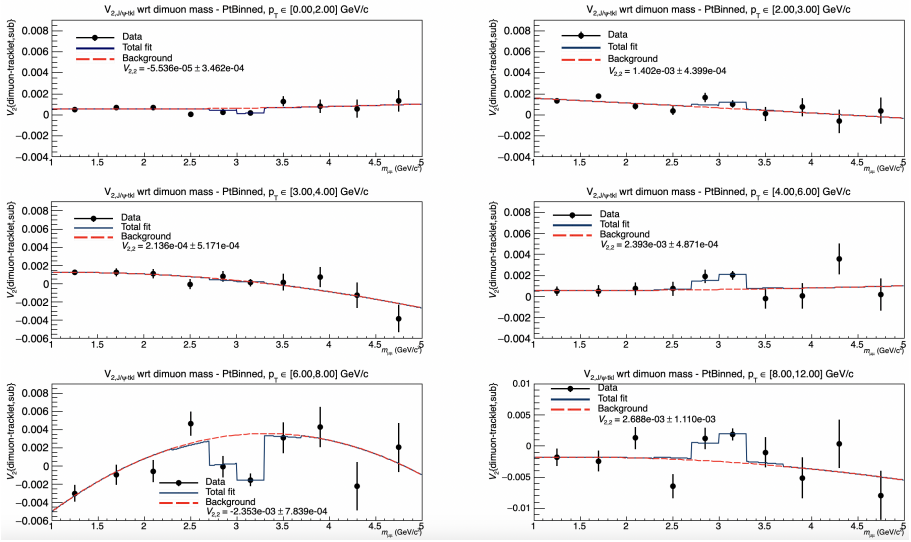

Figure 5.22: Signal/Background extraction step of Extraction method 2 - Run 2 data binned in p_{T}.

Extraction method 3, shown in Figure 5.23, is very similar to method 2. The difference lies in the use of the Fourier coefficients. In method 2, the Fourier coefficients a_0, a_1, and a_2 are used to compute $V_{2,dimuon-tracklet}$ on which the signal extraction is then carried out. In method 3, the signal extraction is done on the Fourier coefficients themselves. This then gives $a_{0,J/\psi}$, $a_{1,J/\psi}$, and $a_{2,J/\psi}$ from which one can directly compute $V_{2,J/\psi-tracklet}$.

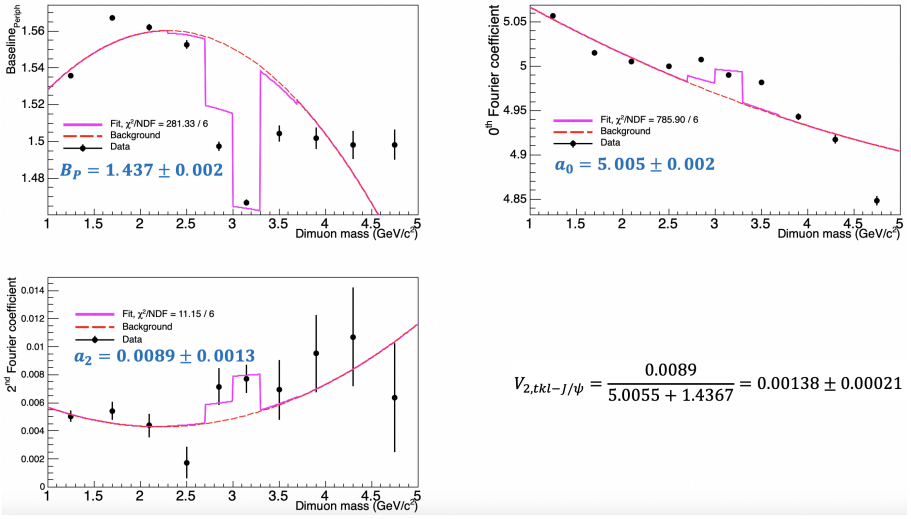

Figure 5.23: Signal/Background extraction step of Extraction method 3 (done at the level of the Fourier coefficients) - Run 2 data, p_{T} from 0 to 12 GeV/c.

The extraction method 1 will be taken as default, as is the case in the p–Pb analysis [102], the others will be used for systematic uncertainties estimation.

Template fit methods

While in yield subtraction methods the non-flow is removed by subtracting once the peripheral yields to the central yields, in template fit procedures, as used in ATLAS, the removal of non-flow is different. Such procedures are shown in Figure 5.24. Contrary to yield subtraction methods, template fit methods assume that the non-flow is dependent on centrality. In order to fully remove it, one needs to subtract

the peripheral yields not once but F times, where F is a free parameter of the procedure. This F factor accounts for the full removal of the non-flow. The direct flow coefficient v_1 being regarded as mainly driven by non-flow by ATLAS, it is not needed anymore after subtraction because it is assumed that all non-flow has been removed. All in all, the template fit procedure boils down to:

$$Y^{Central} - F \times Y^{Periph} = G(1 + 2V_{2,dimuon-tracklet}cos(2\Delta\phi)) \tag{5.10}$$

G is a fixed parameter ensuring that the integrals on both sides of the equation are equal. There are only two free parameters: F, and $V_{2,dimuon-tracklet}$.

To this fit method, we can apply the ZYAM hypothesis, which changes the fit into:

$$Y^{Central} - F \times (Y^{Periph} - B_{Periph}) = G(1 + 2V_{2,dimuon-tracklet}cos(2\Delta\phi)) \tag{5.11}$$

A variant of this method, used in an exploratory study, is to fix G to be the baseline of central yields, B_c. Although this approximation of G works well in the dimuon-tracklet case, it fails in tracklet-tracklet where there are way fewer uncertainties due to the higher number of correlations, as shown in the bottom panel of Figure 5.24.

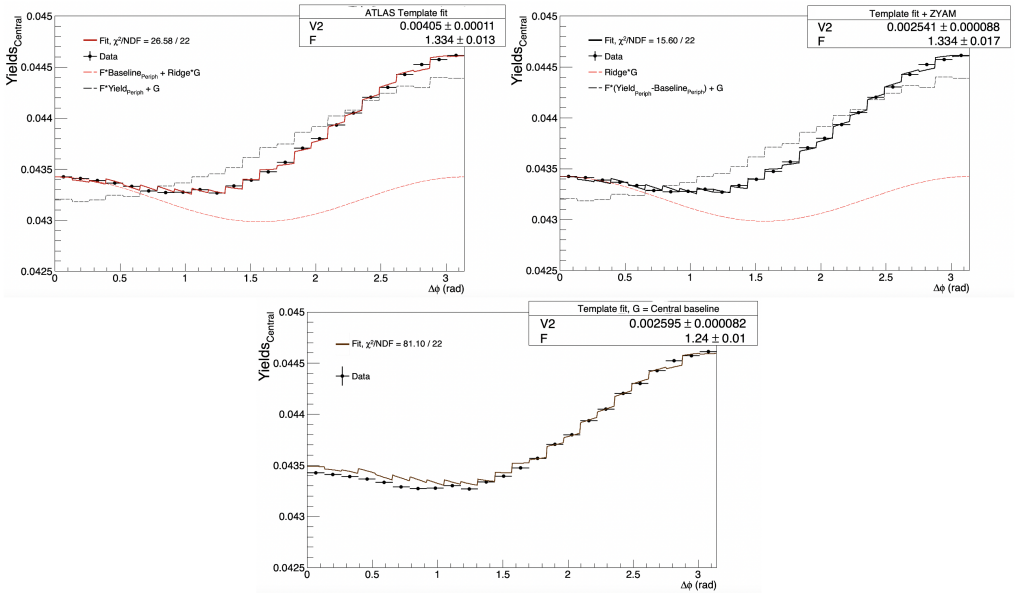

Figure 5.24: Tracklet-tracklet correlations data from the LHC16h dataset - Top left: Fitting procedure using the default template fit. Top right: Fitting procedure using the template fit in which the peripheral ZYAM hypothesis is used. Bottom: Fitting procedure using a variant of the template fit where G is fixed to be the baseline of central yields B_c.

A detailed description of the template fit is given in Ref. [136]. It is noted that the ZYAM hypothesis should never be applied to yields showing collective effects because the measurement of the ridge and of the position of the minimum would vary nonphysically and be biased. That is why we do not apply the ZYAM hypothesis to the central yields where we expect collective effects. We only apply it to peripheral yields. However, Ref. [136] states that even then, in the case where both soft and hard effects are present in the peripheral yields, the measured $V_{2,dimuon-tracklet}$ can be biased. In practice, one would measure less $V_{2,dimuon-tracklet}$ using the ZYAM hypothesis. This statement will have to be checked by evaluating the impact of the ZYAM hypothesis on the results from the different extraction methods.

The impact of physics on the F factor is not discussed in the literature. However, what we can expect is: the more the F factor is above 1, the more non-flow was suppressed which will give a large difference between the simple yield subtraction method and template fits.

Like for yield subtraction methods, the same extraction method alternatives are used for template fits and will be used in the systematic uncertainties evaluation.

5.3.2 Tracklet-tracklet flow

In order to measure the J/ψ v_2 we need to measure both J/ψ-tracklet V_2 and tracklet v_2. If factorisation of flow holds, which will be checked in this chapter, we can compute $v_{2,J/\psi}$ from:

$$v_{2,J/\psi} = \frac{V_{2,J/\psi-tracklet}}{v_{2,tracklet}}. \tag{5.12}$$

The overall analysis procedure in tracklet-tracklet correlations is simpler due to the absence of dependencies on dimuon kinematics, like mass and p_{T}. Once we have computed the tracklet-tracklet per-trigger yields $Y_i(\Delta\phi)$, only one thing must be done to get to the $V_{2,tracklet-tracklet}$: subtract the non-flow effects (via $\Delta\phi$-dependent plots), because disentangling signal and background does not mean anything in the tracklet-tracklet study. As a consequence, we can directly apply the yield subtraction or template fit methods, which give the $V_{2,tracklet-tracklet}$, and then obtain the tracklet $v_{2,tracklet}$ as $\sqrt{V_{2,tracklet-tracklet}}$.

5.4 Sanity checks

The analysis of heavy flavour flow is implemented for the first time in pp collisions using the ALICE apparatus. This smallest hadronic system calls for caution when applying non-flow extraction procedures or defining centrality. In an effort to proceed carefully, many sanity checks and cross-checks have been implemented to ensure the validity of the implementation of the analysis and its methods.

5.4.1 Is the event mixing correctly implemented ?

A simple cross-check of the event mixing is to take the single tracklet ϕ distribution, and make random draws of pairs using said distribution as a probability distribution. Plotting the random pairs $\Delta\phi$ distribution should give a shape similar to the mixed event pairs $\Delta\phi$, and the mixed event distribution should not depend on centrality as is the case for the detector acceptance times efficiency.

In Figure 5.25, we observe that the mixed event pairs distribution is independent of centrality. the only difference comes from the uncertainties on the data points (as in peripheral collisions there are fewer tracklets so fewer possible pairs). The main features of the theoretical random drawn distribution are also reproduced, even though the yields around $\Delta\phi = 0$ could have been expected to be lower than what is measured here.

5.4.2 Are the errors propagated well between the invariant mass fit and the signal/background flow extraction ?

By default, the dimuon invariant mass is fit in order to obtain the shape of the J/ψ and the shape of the background contribution. The shapes are fixed and used as a template for the Signal/Background extraction step in the $V_{2,J/\psi-tracklet}$ extraction method. This procedure is shown in Figure 5.26.
By fixing the shapes, we effectively lose the information on the precision of the fit parameters. The impact of the uncertainty propagation has been checked in two ways: by fitting simultaneously the invariant mass and the $V_{2,dimuon-tracklet}(m_{\mu\mu})$, or by fitting the invariant mass, taking each parameter and creating multiple fit templates where parameters are fixed to a random value around the central value with a standard deviation being the precision obtained in the fit. Each template is used to fit $V_{2,dimuon-tracklet}(m_{\mu\mu})$ and the uncertainty on the extracted value is compared to the type A uncertainty from the propagation of invariant mass uncertainties.

Simultaneous fits

For simplicity, to validate this check, only one fitting range of 1 to 5 GeV/c^2 was used for all fits (invariant mass and signal over background extraction). The impact of this range (instead of a smaller one like 2 to 5 GeV/c^2) is that the invariant mass fit has a large χ^2 due to the poor low-mass description.

In Figures 5.26 and 5.27, for p_{T} between 0 and 2 GeV/c, fit results are similar regardless of whether or not the fits are simultaneous. The impact of the error propagation on the final $V_{2,J/\psi-tracklet}$ result is negligible. This makes sense because the mass binning is very large on the $V_{2,dimuon-tracklet}(m_{\mu\mu})$

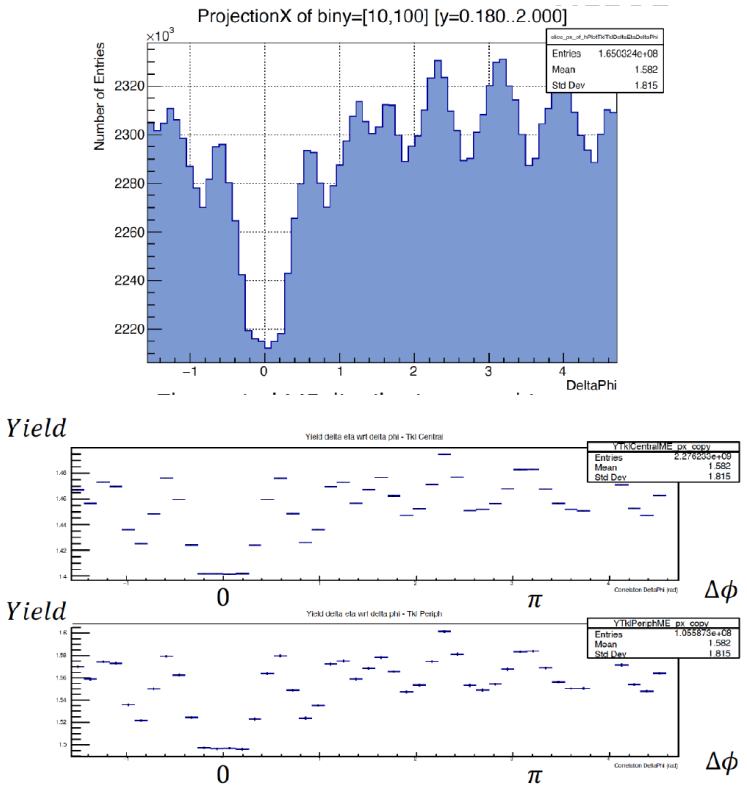

Figure 5.25: Top: Theoretical mixed events tracklet-tracklet yield distribution from random draws (LHC16h, $0 < z_{vtx}$ (in cm) < 1), Bottom: Measured mixed events tracklet-tracklet yield distribution from random draws (LHC16h, $0 < z_{vtx}$ (in cm) < 1) in central and peripheral collisions.

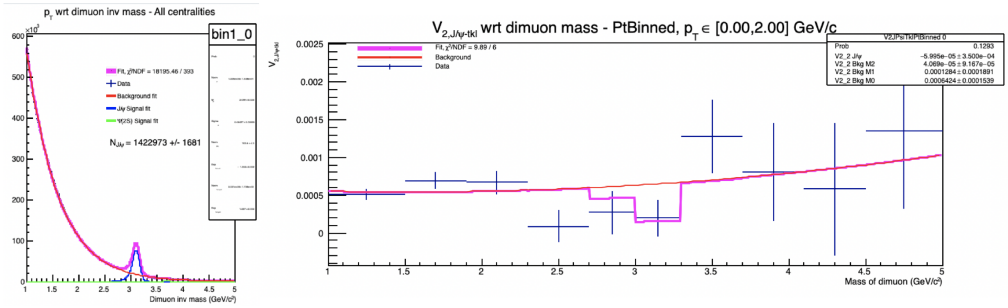

Figure 5.26: Errors not propagated, Run 2 data p_{T} from 0 to 2 GeV/c - Left: Invariant mass fit. Right: V_2 fit.

extraction plot compared to the invariant mass plot. So the invariant mass parameters will only really be constrained by the invariant mass fit. The $V_{2,dimuon-tracklet}(m_{\mu\mu})$ extraction plot will not constrain the invariant mass parameters enough to have a noticeable impact. This test was repeated on the other p_{T} bins and showed negligible impact on all the results.

Random templates

For this test, we start by fitting the invariant mass plot alone. Each parameter of the fit p_i has its own error σ_i. The set of p_i defines the best fit template. Then, we create a template that is close to the best template by taking each parameter and making a random choice of its new value p_i'. The probability distribution of p_i' is a Gaussian centered in p_i with standard deviation σ_i. We repeat this process to create N templates. Each template is then used in the signal over background extraction step of the analysis. With N templates, we make N fits giving us a set of N yields Y_j and their errors

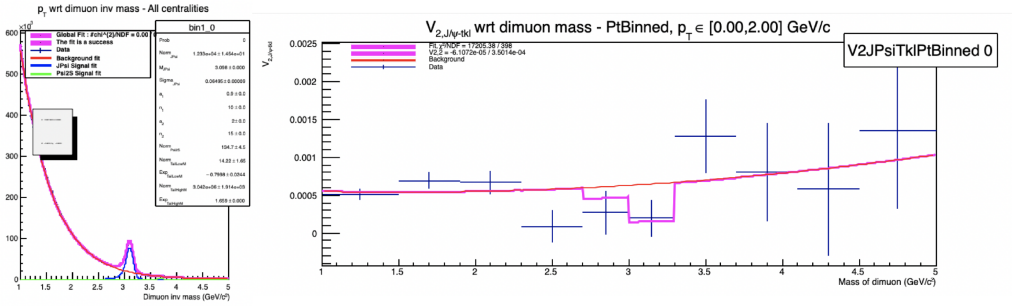

Figure 5.27: Errors propagated by simulataneous fitting, Run 2 data p_{T} from 0 to 2 GeV/c - Left: Invariant mass fit. Right: V_2 fit.

ϵ_j.

We then define the "true" result and its error as $Y = \langle Y_j \rangle \pm \sqrt{\langle \epsilon_j \rangle^2 + \sigma_A^2}$, where σ_A is the type A uncertainty on the result defined as $\sigma_A = \sqrt{\frac{1}{N(N-1)} \sum_j (Y_j^2 - \langle Y_j \rangle^2)}$. ϵ encapsulates the error of the fitting procedure, and σ_A the impact of the error propagation. If σ_A is negligible in front of ϵ, the error propagation has a negligible impact on the final result and can then be neglected, which is what we expect from the previous paragraph.

This test was made on Extraction method 1. The error on the central yields extracted in each $\Delta\phi$ bin was monitored and, at the time of testing, $\Delta\phi$ was divided into 12 bins, hence the 12 results. In each bin, the relationship between ϵ and σ_A was checked.

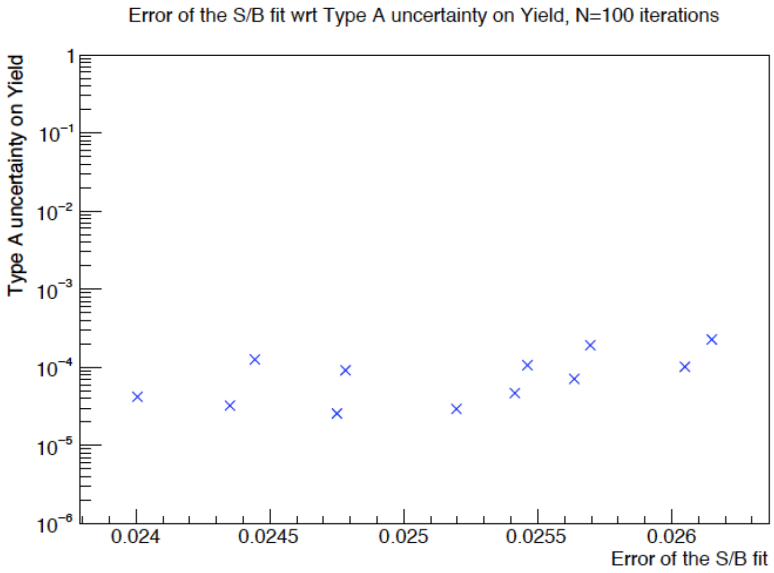

Figure 5.28: Comparison of errors coming from the V_2 fit itself and the amount of error propagation.

As shown in Figure 5.28, for each of the 12 extractions, σ_A is 2 orders of magnitude below ϵ, making it negligible. As a consequence, the error propagation from the invariant mass fit can be neglected. This statement is backed by two different checks on the different extraction processes of the analysis.

5.4.3 Is factorization valid ?

Computing $v_{2,tracklet}$ and $v_{2,J/\psi}$ from $V_{2,pairs}$ relies on the assumption that the elliptic flow can factorize. That is to say that for any p_{T}^a and p_{T}^b, the following equation should hold:

$$V_{2,pair(a,b)}(p_{\mathrm{T}}^a, p_{\mathrm{T}}^b) = v_2(p_{\mathrm{T}}^a) \times v_2(p_{\mathrm{T}}^b) \tag{5.13}$$

As is done in the analysis of muon-tracklet angular correlations in p–Pb [248], a check of factorization validity can be done for the tracklet-tracklet pairs as well as for the dimuon-tracklet pairs.

Tracklet-tracklet factorization

In order to check that the factorization is valid for tracklet pairs, we measured the $v_{2,tracklet}$ applying different cuts on the $\Delta\Phi$ of the tracklets (which is equivalent to cuts on their p_{T}). Cuts at 1, 2, 5 and 10 mrad were applied to the reference tracklets. Cuts at 1, 2, 5 and 10 mrad or no cuts at all were applied to the associated tracklets. If factorization holds, the value of the $v_{2,tracklet}$ at a given reference cut should be independent of the associated cut. This has been checked for V0M and the SPD estimators, as shown in Figure 5.29.

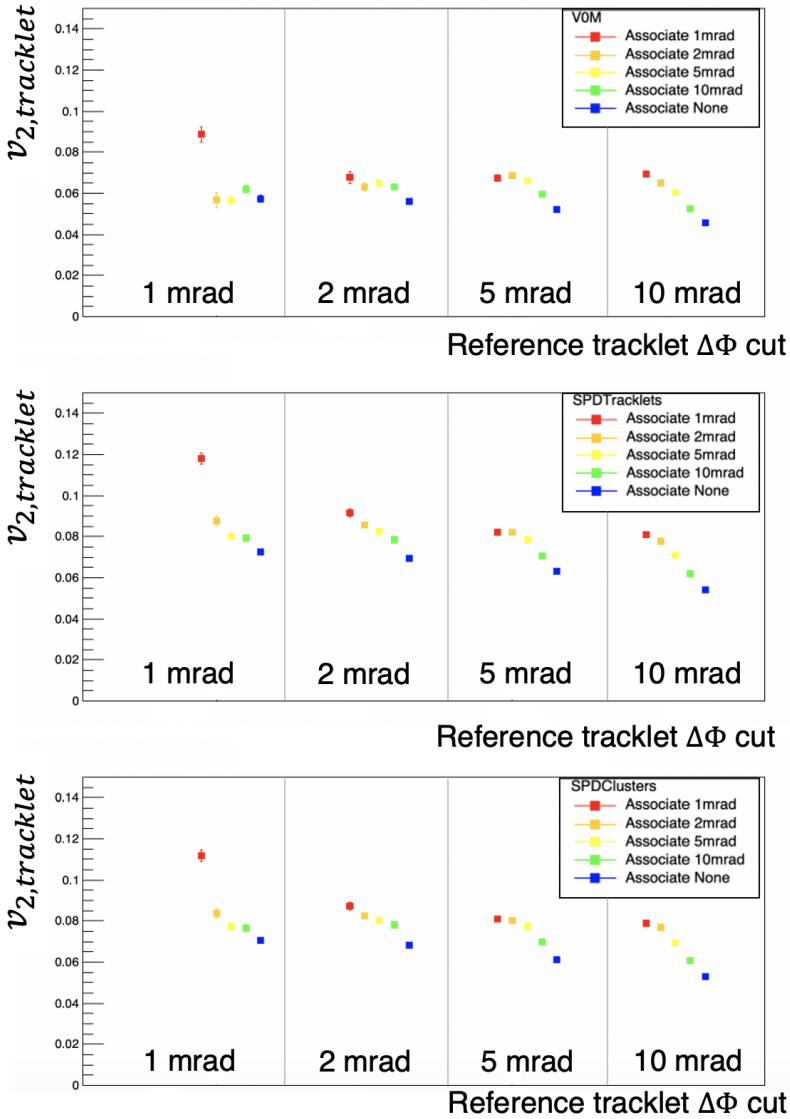

Figure 5.29: $v_{2,tkl}$ as a function of the reference tracklet $\Delta\Phi$ cut, colours depend on the associated tracklet $\Delta\Phi$ cut.

For V0M, as was the case in Ref. [248], the values for cuts at 1 mrad do not match the others. Factorization does not hold at a cut so low, and Ref. [248] attributed it to the non-flow from jets that could be prevalent. As far as our measures are concerned, factorization seems to hold up to 5 mrad cuts, but seems to deteriorate at 10 mrad. SPDTracklets and SPDClusters yield nearly identical results between them, and the conclusions concerning $v_{2,tkl}$ factorisation are identical to V0M.

Maybe it is an indication that it would be worth looking into the results using a 5 mrad cut by

default instead of 10 mrad. To be sure if such change is needed, we'll have to see what happens for the J/ψ elliptic flow. If factorization holds there, there would be no need to change the default cuts. Furthermore, in the next chapter, we will discuss the impact of the systematic uncertainties. As we will see, they are quite substantial, of the order of the statistical uncertainties. Overall, within uncertainties (statistical and systematic), factorization holds for tracklet pairs.

Dimuon-tracklet factorization

For the dimuon-tracklet case, Ref. [248] computes the behaviour of $v_{2,J/\psi}$ with p_{T} using different $\Delta\Phi$ cuts on the tracklets. Where factorization holds, we should expect the results to coincide.

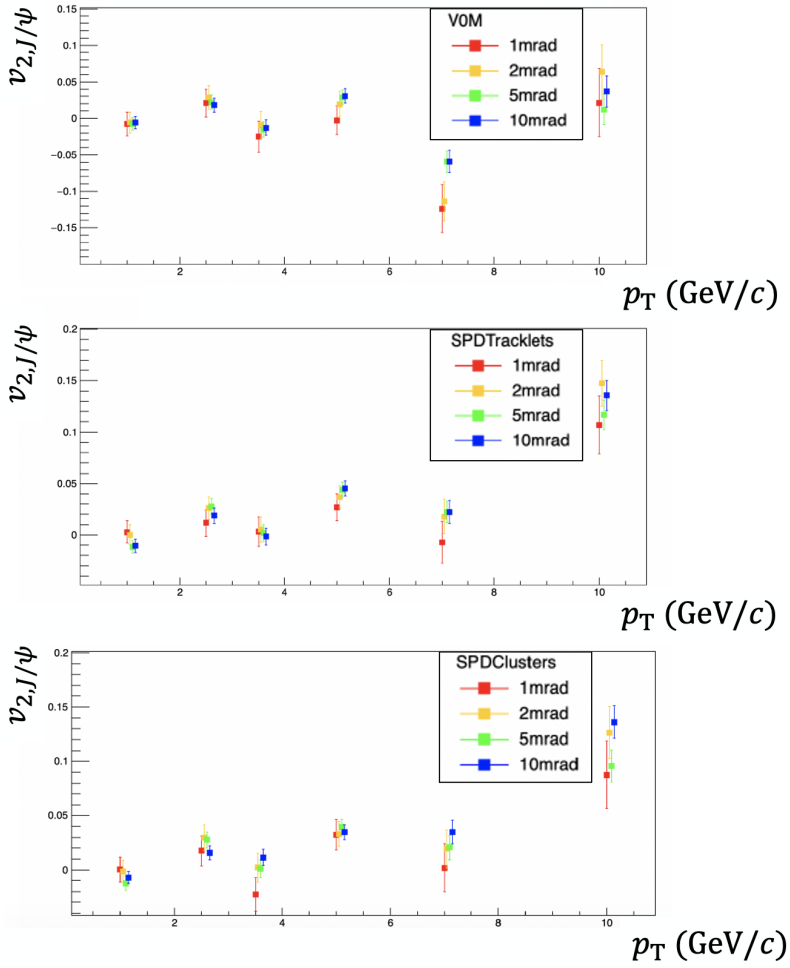

Figure 5.30: $v_{2,J/\psi}$ as a function of p_{T}, colours depend on the associated tracklet $\Delta\Phi$ cut.

We observe in Figure 5.30 that due to the uncertainties especially for strict cuts, one would need to use more data to definitely conclude, however, for all estimators and p_{T} bin there is an agreement on the values of the $v_{2,J/\psi}$ (except maybe for V0M in the 6-8 GeV/c bin which anyway as we will see has very large uncertainties).

From these observations, J/ψ factorization holds regardless of the chosen tracklet cut between 1 and 10 mrad, which is reassuring. So changing the value of the default tracklet cut is not really needed as the change on $v_{2,J/\psi}$ between 10 mrad and 5 mrad is negligible, and the change on $v_{2,tracklet}$ itself is not too dramatic and well within uncertainties.

5.4.4 Does the trigger impact the light particle flow ?

As an aside, it was checked whether or not the tracklet v_2 could be impacted by the trigger selection. The idea is that maybe requiring events containing a dimuon was in fact selecting events where the

spatial distribution of the light tracklets was very distorted by the presence of a heavy dimuon, maybe increasing the tracklet flow. This could then prevent us from directly comparing our result with analyses based on a CINT7 trigger for example.

The tracklet-tracklet analysis was run on CMUL7 events and CINT7 events from 10% of LHC16h using the V0M estimator and the default analysis procedure. The $V_{2,tracklet-tracklet}$ extraction is shown in Figure 5.31.

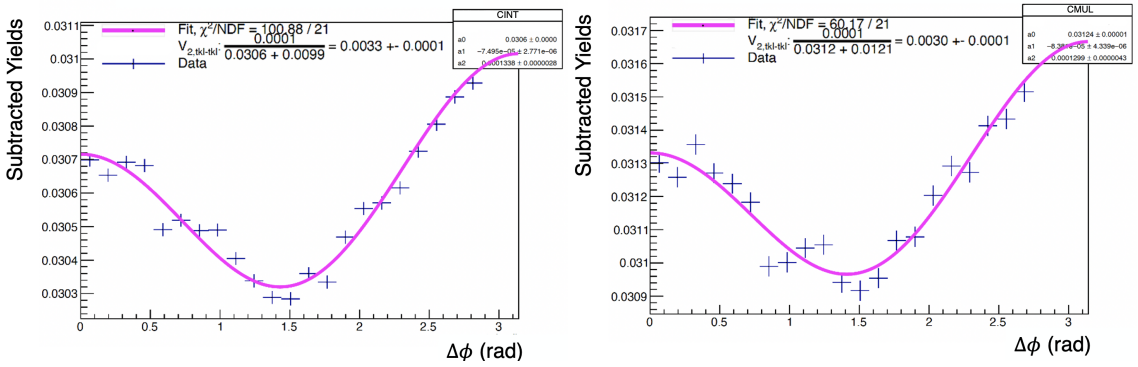

Figure 5.31: $V_{2,tracklet-tracklet}$ extraction on 10% of LHC16h data - Left: CINT7 events. Right: CMUL7 events.

There is indeed a slight difference in the measured $V_{2,tracklet-tracklet}$ which seems to go in the other direction than the one that could have been expected. Slightly more tracklet flow is extracted on CINT7 than on CMUL7 events. The difference on $V_{2,tracklet-tracklet}$ is of order 0.0003 with statistical uncertainties of 0.0001 for each measurement which gives compatibility within 2σ only based on statistical effects. Therefore, comparisons could be made between CINT and CMUL analyses regardless of the trigger.

5.4.5 Can this analysis reproduce p-Pb results ?

Because the default analysis is based on the p–Pb analysis [102] procedure, by using p–Pb data we should be able to reproduce the existing results. Some minor changes had to be made in adapting for p–Pb data (using the same pile-up cuts, using similar fit ranges and binning, etc.). By comparing the existing intermediate and final plots from Ref. [102], we managed to reproduce them all within uncertainties as shown in Figures 5.32 and 5.33.

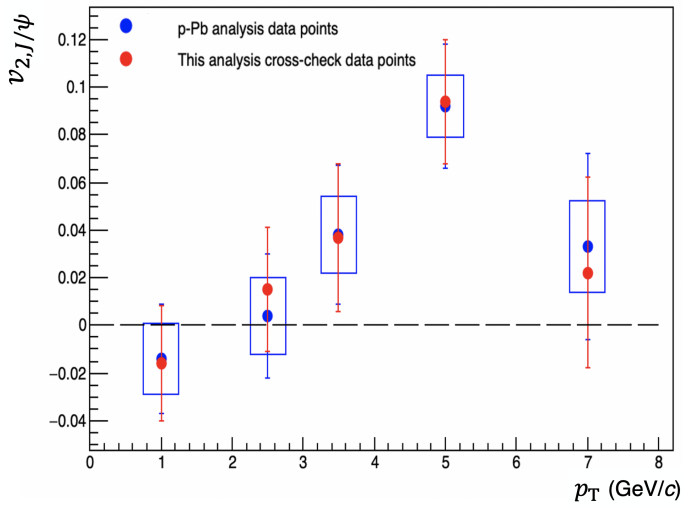

Figure 5.32: Agreement between Ref. [102] and this analysis concerning $v_{2,J/\psi}$ as a function of p_T on LHC16r data.

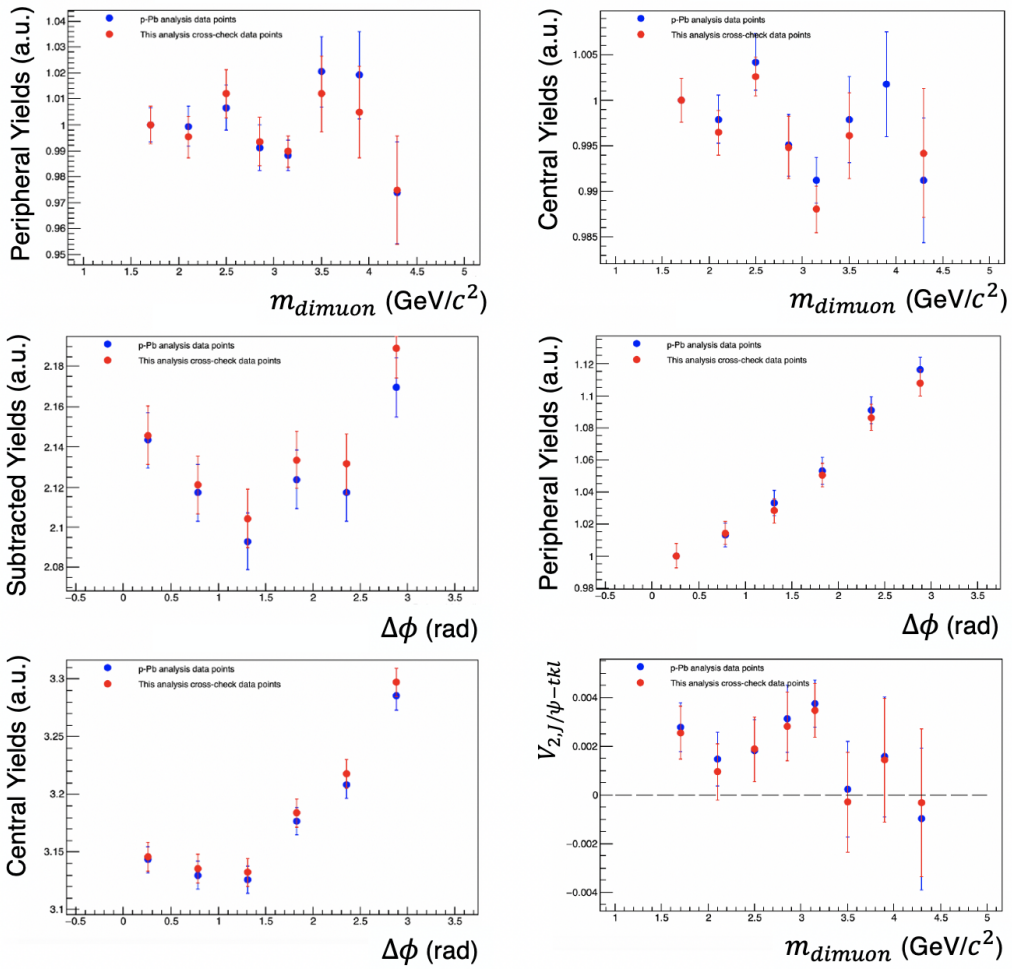

Figure 5.33: Agreement between intermediate plots in Ref. [102] and this analysis.

This analysis is able to reproduce Ref. [102] final and intermediate results, based on data with p_{T} between 3 and 6 GeV/c from period LHC16r, which validates fully the analysis procedure implementation for pp. The slight differences, especially in intermediate plots could be accounted for by a difference in the implementation of the event mixing. In the existing p–Pb analysis, the event mixing and the analysis was fully done on the ALICE distributed grid. In this thesis, the ALICE grid served as a way to select events from the Run 2 dataset and store the event information so that they could be post-processed. This allowed to have a better feel of the implementation of the analysis, and be able to vary parameters on the fly instead of running the whole selection and analysis each time something had to be changed. On the other hand, this choice also means that the event mixing had to be implemented "by hand" by defining, filling, and using the event pools. Therefore, some differences may occur in the selection of events used in the mixing or the filling of the pools which could affect the final yields.

5.4.6 Is the invariant mass fit compatible with existing analyses ?

The dimuon invariant mass spectra that is used to fit the signal and background functions can also serve to cross-check the previous pp analysis of Ref. [246]. The fit procedure was therefore repeated with other parameters and shapes to reproduce the previous results.

The Double Exponential function used in this analysis and Ref. [246] are different. In Ref. [246], both exponentials have a scaling coefficient, while in this analysis only one coefficient is used. This allowed us to reduce the number of parameters and improve the fit convergence. We also checked that changing the definition of the Double Exponential has a negligible impact on the final v_2 values.
The following sets of functions and parameters have been used to cross-check the results of Ref. [246]:

- CB2 or NA60 parametrization of the signal shape
- Tails sets from either Run 2 or Monte Carlo (only MC are available for NA60).
- Background functions: Double Exponential (from Ref. [246]), Variable Width Gaussian or a Ratio of polynomials (Pol1/Pol2).
- Width ratio between $\psi(2S)$ and J/ψ fixed to either 1.05 or 1.00.
- Fit range set to either $[2.4, 4.7]$ or $[2.3, 4.9]$ GeV/c^2.

The tail parameters are taken directly from Ref. [246] and they stay fixed to these values regardless of centrality or p_{T} range. This cross-check then consists of 36 different templates to extract the signal and background from the invariant mass distribution. The fitting procedure is the following: first, the parameters are set to values close to convergence, and the background is set free and fitted. Then the peak parameters (width, mass) are set free one by one while tail parameters are kept fixed.

Other alternatives were tried, like a Chebychev polynomial background, or bigger fit ranges, but they did not change the results or they were similar enough to implemented methods. Furthermore, it was not used in Ref. [246] so it was decided to leave it out of this cross-check, but such tests are kept in the full systematic uncertainties study of this analysis for completeness.

In Ref. [246], the main driver of the difference in J/ψ population is the set of tails. Run 2 tails give slightly less than 3.8M J/ψ whereas MC tails give around 4.0M J/ψ. All the other variables do not change this amount by much. In our case, we expect to see slightly more candidates because we have roughly 1% more CMUL7 events. Essentially we expect Run 2 tails to yield around slightly less than 3.85M raw J/ψ and MC tails around 4.05M raw J/ψ.

In Figure 5.34, we observe indeed that the set of tails is the main driver of the difference in number of candidates in our case, reproducing the results from Ref. [246]. The final number of J/ψ is taken as the mean of all methods, the statistical uncertainty is defined as the mean of all statistical uncertainties and the systematic uncertainties are taken as the rms of all methods. Doing so we obtain that $N_{J/\psi} = 3972300 \pm 3270_{stat} \pm 132755_{syst}$.

If we factor in the fact that this analysis has 1% more triggered events, we find that there is a very good agreement between both analyses on the number of J/ψ. The only difference comes from the value of the systematic uncertainty which is higher in our case by 30%. It appears our methods using Run 2 tails give results a bit on the low side, increasing the systematic uncertainty.

Taking the $\psi(2S)$ results from Figure 5.35 we obtain $N_{\psi(2S)} = 80376 \pm 1000_{stat} \pm 4850_{syst}$. Here again, factoring in the 1% difference for triggered events, the agreement with Ref. [246] is satisfactory as the number of $\psi(2S)$ agree within the statistical uncertainties, and both statistical and systematic uncertainties are of the same order between the analyses.

We can also compare the ratio of $\psi(2S)$ over J/ψ which should be independent of the number of triggered events. Doing so, we obtain $\frac{N_{\psi(2S)}}{N_{J/\psi}} = 0.0202 \pm 0.0003_{stat} \pm 0.0007_{syst}$, again compatible with Ref. [246] within the statistical uncertainties.

Figure 5.36 shows the χ^2/ndf values for the various fit methods; the values around 1.5 and 2 are equivalent to what was seen in the previous pp analysis. However, due to the large number of degrees of freedom, we cannot say that the fit is really satisfactory. Looking at pulls shows that the main issue with the fits is the signal part which is the main driver of the χ^2.

We can also look at individual fits taken from Ref. [246] to see if we have a local agreement on each method and not just a global agreement. For each fit, found in Appendix C.2, the pulls show us that the main fitting issue comes from the signal, and particularly the tails, regardless of the background function used. There is a relative agreement on the number of J/ψ and $\psi(2S)$ in each fit, even though our J/ψ measurement from the available examples is a bit on the high side, and the $\psi(2S)$ a bit on the low side.

An overall agreement on the number of each particle can be found even though some local differences arise fit by fit. In any case, we do not expect the shape of the invariant mass to have an effect that would be noticeable on the final v_2 results as the very large mass binning in the v_2 extraction will make the variations, brought by alternative signals or backgrounds or tail parameters, practically irrelevant.

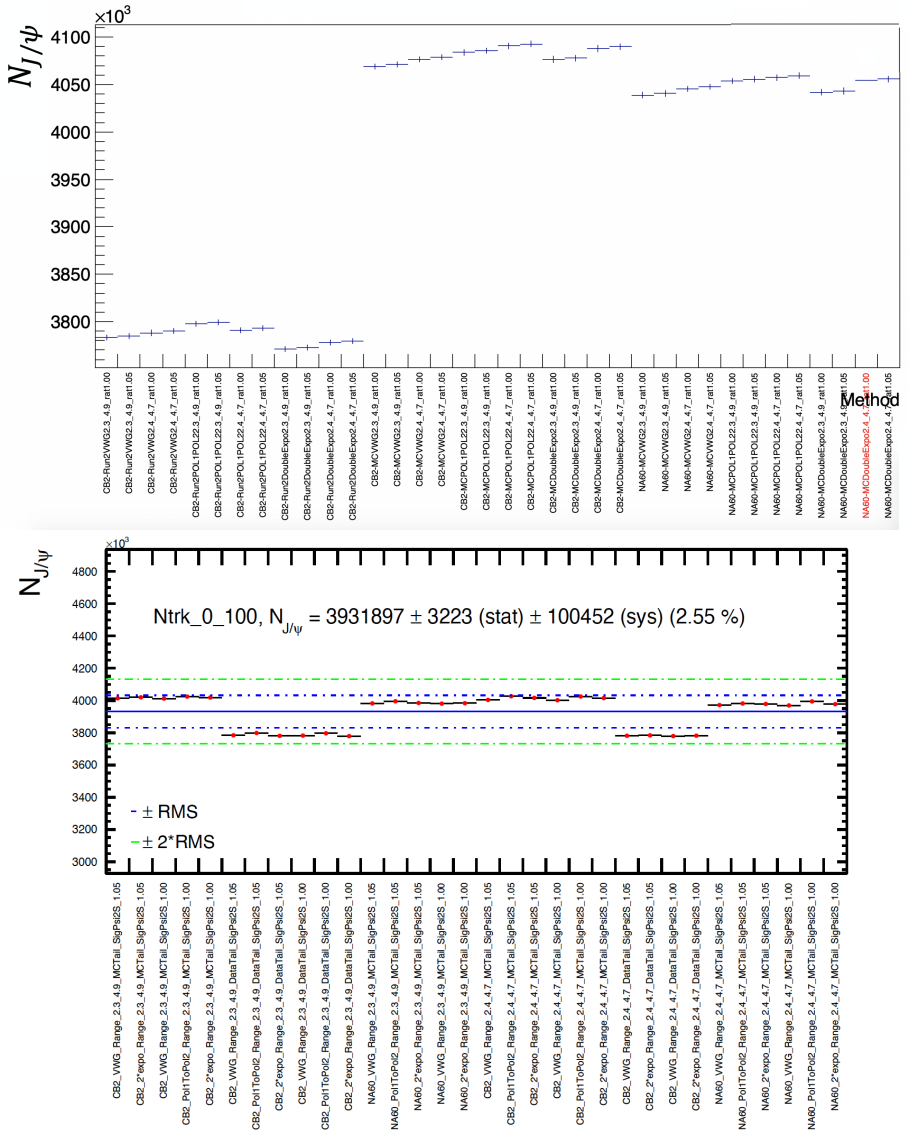

Fig. F.5: $N_{J/\psi}$ signal extraction for integrated N_{trk}^{Corr} ([0;100]).

Figure 5.34: Raw number of J/ψ for each fit method, similar to the systematic study done in Ref. [246], Top: This analysis, Bottom: Ref. [246] (red labels correspond to methods having encountered problems during fit procedure, essentially an error matrix not positive-definite).

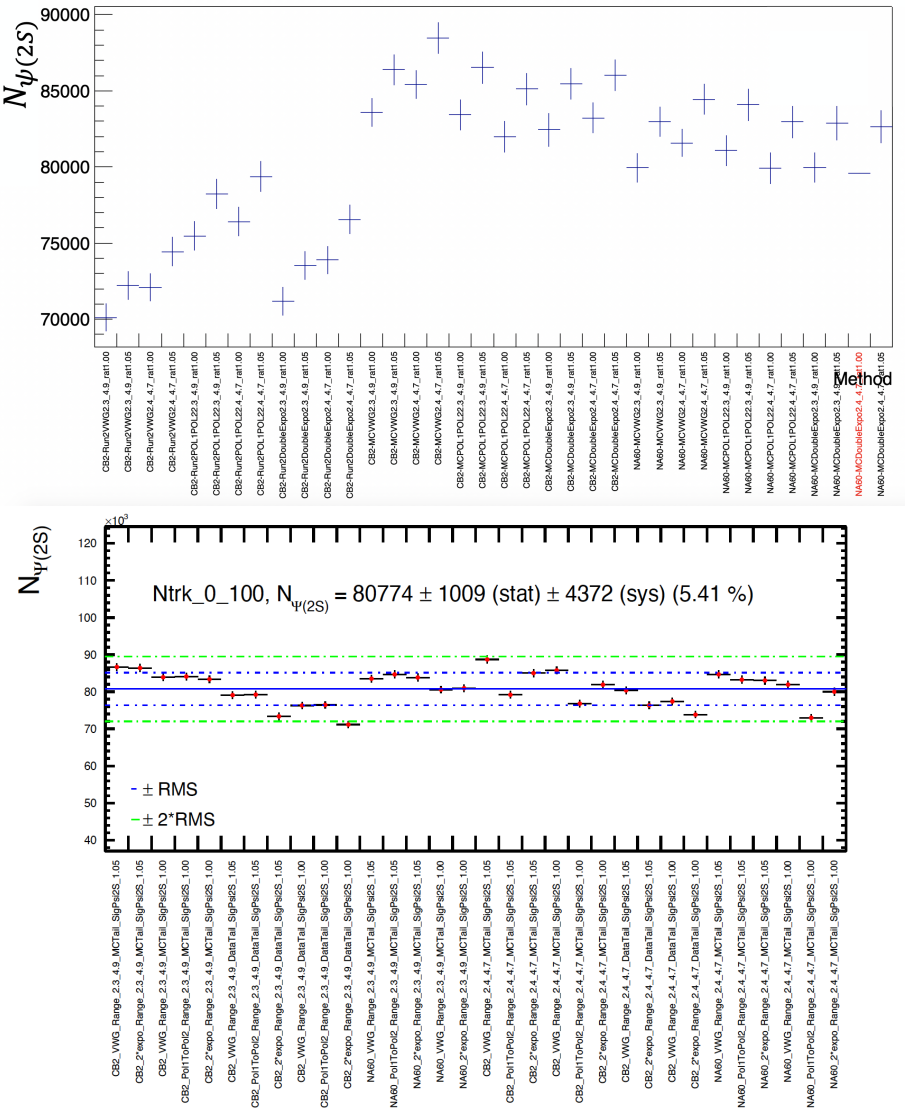

Fig. F.4: $N_{\psi(2S)}$ signal extraction for integrated N_{trk}^{Corr} ([0;100]).

Figure 5.35: Raw number of $\psi(2S)$ for each fit method, similar to the systematic study done in Ref. [246], Top: This analysis, Bottom: Ref. [246] (red labels correspond to methods having encountered problems during the fit procedure, essentially an error matrix not positive-definite).

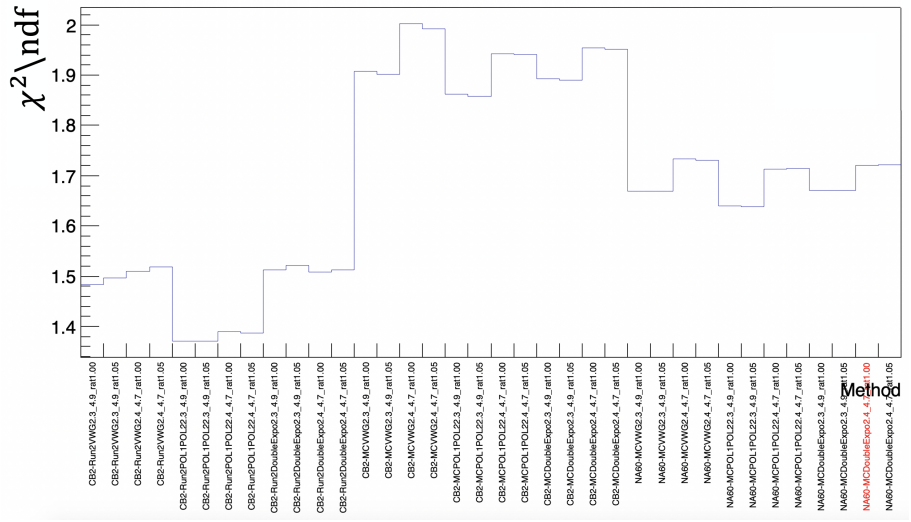

Figure 5.36: χ^2 for each fit method, similar to the systematic study done in Ref. [246].

5.4.7 Is non-flow suppressed well ?

In the previous sections we have shown that this analysis is able to reproduce existing p-Pb results, therefore we can conclude that its implementation is correct. However, it is legitimate to ask whether the procedure is valid also in the case of pp collisions. To check this, we can use Monte Carlo (PYTHIA8) simulations, in which only non-flow is simulated and there are no collective effects. If the flow extraction implemented in the analysis is efficient, it should suppress the non-flow without introducing biases. Therefore, running the tracklet-tracklet correlation analysis on PYTHIA8 data should provide a measurement of tracklet flow compatible with zero.

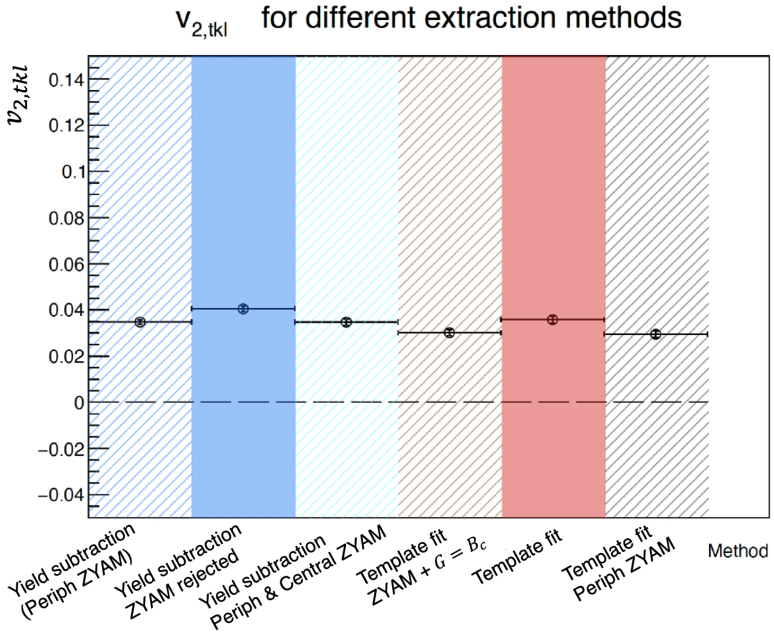

Figure 5.37: $v_{2,tkl}$ values obtained using various extraction methods on LHC17f5 PYTHIA8 dataset (anchored to LHC16h) - V0M estimator. From left to right, methods are: yield subtraction (the default one which includes peripheral ZYAM), yield subtraction without ZYAM, yield subtraction with ZYAM in peripheral and central yields, template fit with $G = B_C$, template fit (default one), template fit with peripheral ZYAM.

However, as seen in Figure 5.37, a non-zero flow is measured. It amounts to around $v_2 = 3.5 - 4\%$

with V0M but is even larger (around 5%) with SPDTracklets. If the treatment of Monte Carlo data is correct, this would mean that our extraction methods cannot extract flow with enough accuracy in pp. To this measurement, we can associate a new source of systematic uncertainty quantifying this inability to extract flow properly. This "PYTHIA systematic uncertainty" will be covered in the next section with all the other identified sources.

Checking the MC data treatment

In order to check that the data selection using PYTHIA8 is correct, we tried to reproduce a reference study [134] on PYTHIA pp collisions at 13 TeV, carried out using ATLAS/CMS kinematics and acceptance cuts.

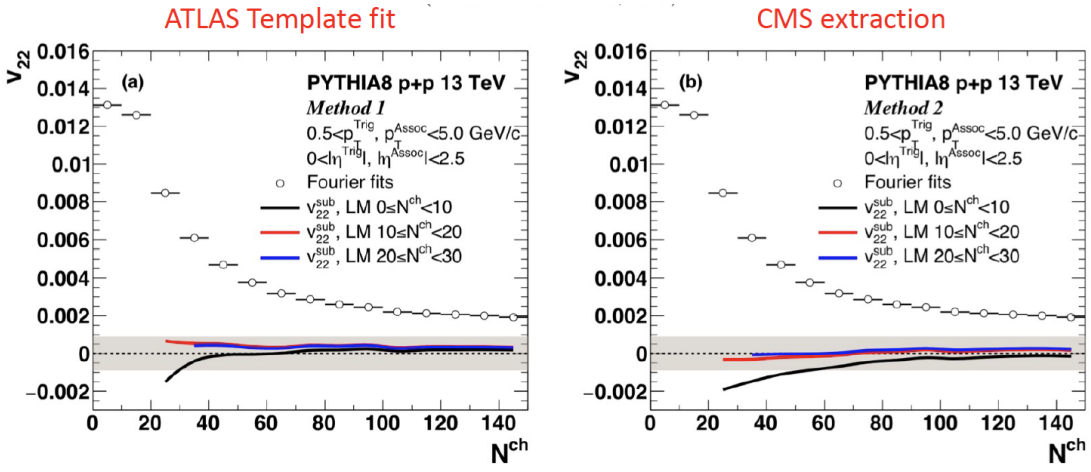

Figure 5.38: Plots of V_{22} from tracklet-tracklet correlations extracted using PYTHIA8 simulated data and ATLAS template fit or CMS method, from Ref. [134].

In Figure 5.38, we see some results of this reference study, showing the multiplicity behaviour of tracklet-tracklet V_{22} for different extraction methods. The charged particle multiplicity N^{ch} is defined as the number of simulated charged particles within $|\eta| < 2.5$ and having $p_{\mathrm{T}} > 0.4$ GeV/c. By applying similar selections as this study we manage to have an analogous multiplicity definition.

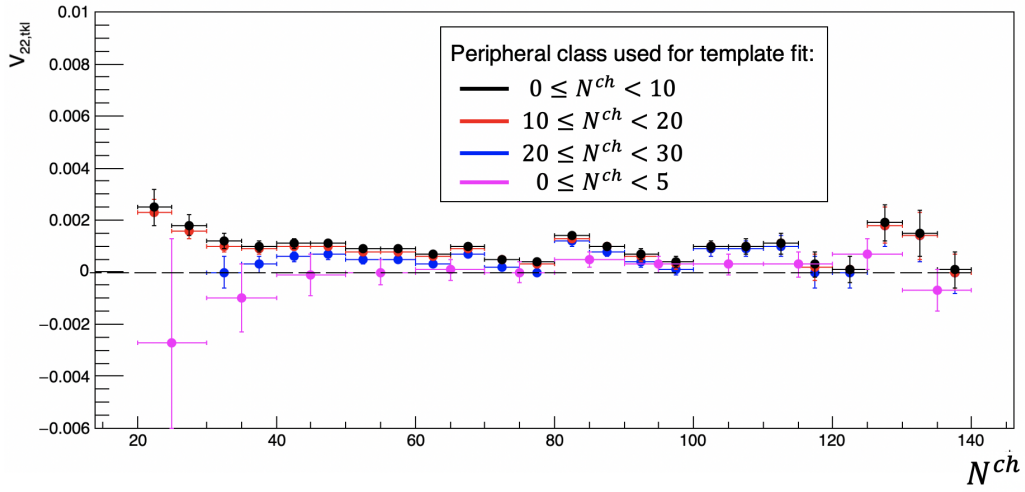

Figure 5.39: Reproduction of ATLAS template fit results using the same colour code for the peripheral class with the additional 0 to 5 peripheral class (magenta).

As shown in Figure 5.39, we reproduced the results obtained using ATLAS template fit method. Using 10-20 (in red) or 20-30 (in blue) as the peripheral class shows a behaviour somewhat reminiscent

of the reference study within uncertainties but the V_{22} is higher than expected. For 0-10 (in black), the behaviour is unexpected and clearly not in line with the reference study.

By using a lower class 0-5 (in magenta) instead of 0-10 for the peripheral class, the same behaviour as was seen for 0-10 in the reference study is observed, with V_{22} values going to the negatives at low N^{ch}. Overall, we are not able to reproduce the results from the reference study. This difference is currently under investigation. The handling of the PYTHIA generated tracks seems right, maybe differences in the parameters of PYTHIA can be a cause of such differences...

From the analysis of tracklet flow in Monte Carlo data, we can conclude that the extraction methods we use in pp collisions measure a tracklet flow from 3 to 4% with V0M. As the tracklet flow in data is of order 6%, the methods that we employ are not good enough to extract flow reliably as the relative mis-estimate is close to 50%. The systematic uncertainty associated with this inefficiency will be substantial.

5.5 Systematic uncertainties

In order to evaluate the systematic effects brought by our optimal choice of selection cuts and methods, the following procedure was used. The analysis has a default setting, where every parameter is set to a nominal value, usually what was used in previous studies like Ref. [102]. This default configuration determines the central values of the final data points and the statistical errors. To evaluate the systematic uncertainty associated with each source, the corresponding parameter or method is varied. The amplitude of the variation is set on a case-by-case basis, usually matching previous flow analyses. If there is only one alternative to the default configuration, the distance between the final values obtained by the two configurations gives the value of the systematic uncertainty. If there are two alternatives or more, the uncertainty is defined as the rms of all the configurations (default and alternatives). Each source is evaluated using this procedure, and then they are all added in an uncorrelated way (by summing their squares) to obtain the total systematic uncertainty.

The advantage of this procedure is to avoid the computation of correlations between parameters that should not be too correlated which would multiply the number of cases to run. And the differentiated way of computing the systematic uncertainties based on the number of alternatives naturally increases the weight of sources where only one alternative exists which models the fact that we have less grip over the behaviour of such variables. We will now go through the various sources that have been studied for this analysis. The detailed results of the analysis including these systematic uncertainties will be presented in the next chapter.

5.5.1 Tracklet flow

The systematic uncertainties study of tracklet-tracklet correlations has been carried out on LHC16h period alone. This reduced dataset still provides results within a statistical uncertainty between 0.5% and 1% depending on the yield subtraction method and the centrality estimator, which is enough to see any significant systematic effect. More precisely yield subtraction method gives a relative statistical uncertainty on the final tracklet flow result of, 0.67% for SPDTracklets, 0.52% for SPDClusters, 1.14% for V0M. By default, the systematic uncertainties analysis was conducted using 0-5% as the central class, 40-100% as the peripheral class, and a $\Delta\Phi_{tkl}$ cut of 10 mrad as standard. It was also carried out, albeit less thoroughly and as a simple check, using a $\Delta\Phi_{tkl}$ cut of 5 mrad in order to check the impact of this cut on the systematic uncertainties (5 and 10 mrad being values for which they were minimal in Ref. [102]).

The different sources of systematic uncertainties identified in this study are:

- The z_{vtx} cut
- The $\Delta\eta$ gap
- The summation method on z_{vtx}
- The normalization of the event mixing
- The $V_{2,tracklet-tracklet}$ fit method

- The choice of centrality classes
- The non-flow subtraction inaccuracies (from PYTHIA study)

z_{vtx} cut The default cut on z_{vtx} is 10 cm. It is varied to 8 and 12 cm to account for inaccurate detector acceptance description. This is a systematic check that was done in the same way in Ref. [102], where it had a negligible impact on the final result.

$\Delta\eta$ gap The default gap is 1.2 units. It is varied to 1.0 and 1.4 to account for the inaccurate removal of the non-flow peak at the origin. The variation is small because going to higher gaps starts deteriorating the correlations, as it enhances the contribution of particles that are on the borders of the SPD acceptance, and tracklets with median values of η get more and more suppressed.

Summation method on z_{vtx} The default method, as is the case in Ref. [102], is a Poisson likelihood fit as described before in this chapter: in each bin of $\Delta\phi$ and $\Delta\eta$, a value of Y_{ik} is obtained by fitting $\frac{SE_{ijk}(z_{vtx})}{N_{trig}^{ijk} ME_{ijk}(z_{vtx})}$ and then the $Y_{ik}(\Delta\phi, \Delta\eta)$ are integrated over $\Delta\eta$. The first natural alternative to this method is to use χ^2 fit, which has gaussian errors and is adapted to many-event distributions, instead of using a Poisson-likelihood fit adapted to samples with a low number of correlations. However, in the tracklet-tracklet case, as the number of correlations we can make scales as $N^2_{tracklets}$ for each event, the two fitting methods are equivalent as we have enough correlations for the errors to be gaussian. In the tracklet-tracklet case, the alternative fit is therefore disregarded, which will not be the case in the dimuon-tracklet case where fewer correlations are expected.

Another approach suggested in Ref. [102], can be described as follows. The same event $SE_{ij}(\Delta\phi, \Delta\eta)$ and mixed event $ME_{ij}(\Delta\phi, \Delta\eta)$ distributions are projected on $\Delta\phi$ by summing over the range of $\Delta\eta$. This removes the $\Delta\eta$ dependency from the start. Then the yields are computed by calculating their weighted average over z_{vtx}, where the weights are the numbers of trigger particles N^{ij}_{trig}, as shown in Equation 5.14.

$$Y_i(\Delta\phi) = \frac{1}{\sum_j N^{ij}_{trig}} \sum_j \frac{SE_{ij}(\Delta\phi)}{ME_{ij}(\Delta\phi)} \tag{5.14}$$

Normalization of the event mixing In the tracklet-tracklet study, by default the normalization factor is taken as the number of pairs in the $(\Delta\phi, \Delta\eta) = (0, 0)$ bin for $|z_{vtx}| < 10$ cm. An alternative is to make the normalization factor dependent on z_{vtx}. So, instead of having one factor common to all z_{vtx}, an alternative is to normalize each z_{vtx} binned mixed event distribution by the number of pairs in the $(\Delta\phi, \Delta\eta) = (0, 0)$ for this particular z_{vtx} bin.

However, using the Poisson fit (or even a χ^2 fit for that matter) as a summation method, we fit $SE(z_{vtx})$ and $ME(z_{vtx})$. Both these functions are expected to have the same shape. Using an alternative method of mixed event normalization that is dependent on z_{vtx} changes the shape of $ME(z_{vtx})$ which cannot be fitted with $SE(z_{vtx})$ anymore. In other words, using our default summation method, there is no reasonable alternative to the event mixing normalization. Therefore no systematic uncertainty is assigned to the event mixing normalization.

For completeness, it was tried to vary the normalization while using the weighted average along z_{vtx} as a summation method, which is described by Equation 5.14. In this case, $SE(z_{vtx})$ and $ME(z_{vtx})$ are not required to have the same shape. But even then, the systematic uncertainty obtained from this variation is around 0.5% for all estimators. Therefore, it is negligible, and we can reasonably disregard mixed event normalization systematic uncertainty in this analysis.

V_2 fit method By default, we fit the subtracted yields with a second-order Fourier expansion. As was done in Ref. [102], we can go up to the third order.

Another alternative relies on the way the non-flow peak in $\Delta\phi = \pi$ is modelled in the peripheral per-trigger yields. Instead of using a v_1 term in $cos(\Delta\phi)$ to describe it, one could fit the peripheral yields with a constant and a gaussian on the away-side to reproduce the non-flow peak. The subtracted yields can then be fitted with a second order Fourier expansion and a gaussian whose width is set to

the width extracted from peripheral yields (as shown in Figure 5.40) and which replaces the v_1 term. This systematic uncertainty is here to account for the fact that the choice of a Fourier expansion is arbitrary and the v_{2k+1} contributions could be modelled in another way.

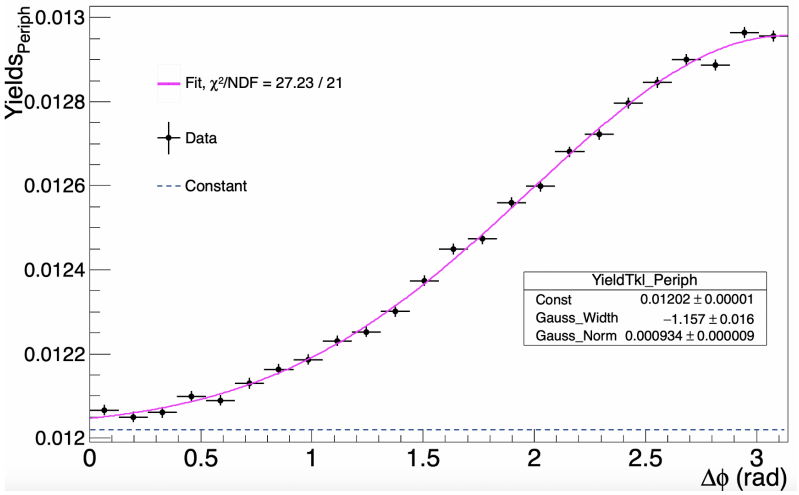

Figure 5.40: Fit of the peripheral yields in tracklet-tracklet correlations (from period LHC16h), using a constant and a gaussian on the away-side. The parameters of the gaussian are then fixed and used to fit the subtracted yields.

Even though this alternative is possible for the subtracted yields extraction where we have a v_1 we can replace, it is not possible to accommodate it in the template fit method where v_1 is considered null. Only adding a v_3 remains as an alternative in this case.

Centrality classes Because the choice of centrality is arbitrary, it was decided to assign a systematic uncertainty to the centrality ranges used for the analysis. 0-5% was varied to 0-3% and 0-10%. 40-100% was changed to 40-80%, 30-100% and 50-100%.

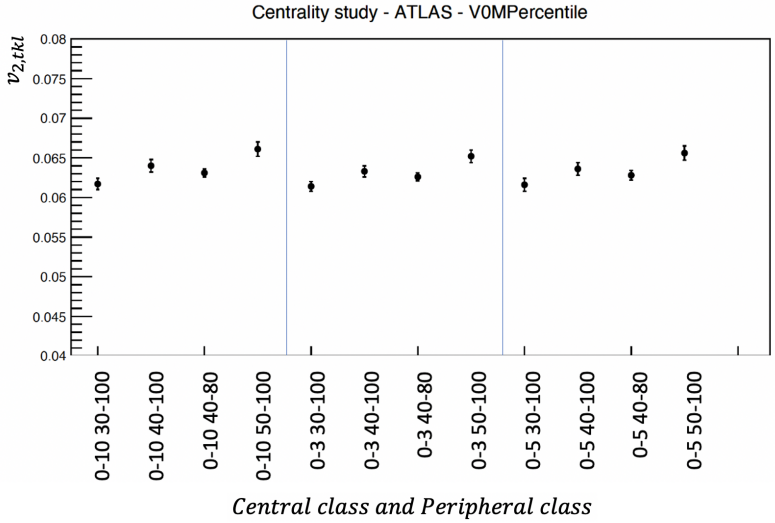

Figure 5.41: Values of tracklet elliptic flow obtained when varying the central and peripheral classes, used to determine the systematic uncertainty attached to the arbitrary choice of centrality classes. Results obtained with the V0M estimator using the template fit method.

We see in Figure 5.41 that the choice of a central class has a marginal impact. However, making the peripheral class less peripheral or stopping at 80% lowers the measured flow. In the first case, we may start to pick up collective effects which increase peripheral v_2. In the second case, maybe removing

events with very low numbers of tracklets which probably do not have jets makes that our non-flow description ends up being better.

Non-flow subtraction inaccuracies - The "PYTHIA systematic uncertainty" As we previously said, this systematic uncertainty is linked to the inability of our extraction methods to measure a zero flow in PYTHIA8 simulations. It reflects the inaccuracies of our methods in pp.

The computation of this source of systematic uncertainty is different from the others. Here, what the PYTHIA simulations show us is that we measure a $V_{2,PYTHIA,tracklet-tracklet}$ that is non-zero. This will in turn cause a non-zero $v_{2,PYTHIA,tracklet}$. However, due to the square root the v_2 cannot be directly compared or summed. We should compare the $V_{2,pairs}$ because this is the physical correlations we make and this is the process that is prone to errors. In more practical terms, once $V_{2,PYTHIA,tracklet-tracklet}$ is extracted from PYTHIA simulations to show by how much we are unsure of the non-flow suppression methods, a corrected value $V_{2,corr.,tracklet-tracklet}$ is computed from the $V_{2,data,tracklet-tracklet}$ measured in real data: $V_{2,corr.,tracklet-tracklet} = V_{2,data,tracklet-tracklet} - V_{2,PYTHIA,tracklet-tracklet}$.

This corrected V_2 then gives a corrected v_2 and the distance between this corrected flow and the default one is taken as the systematic uncertainty. Because this uncertainty stems from the amount of residual non-flow that is not suppressed by the extraction methods, this systematic uncertainty will be asymmetric, contrary to all other systematic uncertainties evaluated here, causing a decrease of the measured tracklet flow.

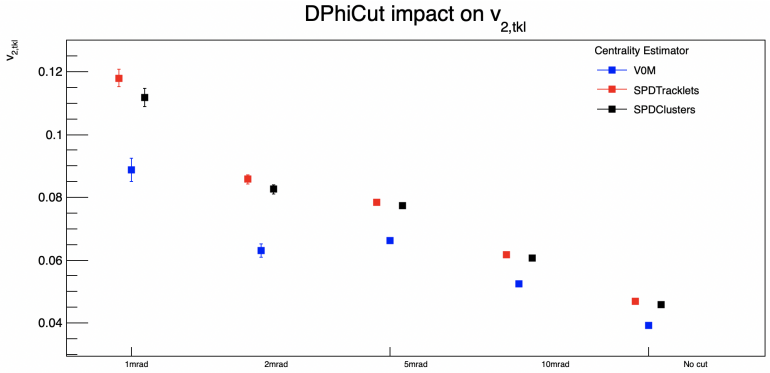

Figure 5.42: Values of tracklet v_2 obtained for different centrality estimators and different tracklet $\Delta\Phi$ cuts.

Tracklet $\Delta\Phi$ cut This cut is in fact a tracklet p_{T} cut. Tracklet v_2 is highly dependent on it, as evidenced in Ref. [102] and when comparing flow measurements between different studies. However, changing the $\Delta\Phi$ cut changes the physical result we are looking at. It is not considered as a source of systematic uncertainty.

For completeness, the evolution of flow with this cut has been looked at and we observe in Figure 5.42, as was the case for Ref. [102] that the tracklet v_2 increases as the cut on $\Delta\Phi$ becomes more strict. Slight deviations from this behaviour can be observed on the stronger cuts (especially 2 mrad) as the number of correlations becomes low as fewer trackelts are selected and the fit uncertainty increases.

5.5.2 J/ψ flow

In each p_{T} bin, the $V_{2,J/\psi-tracklet}$ is computed and divided by the $v_{2,tracklet}$ for the used centrality estimator. We then estimate the systematic uncertainty on the computed $v_{2,J/\psi}$, as we did for the tracklet-tracklet case, which will also be increased by the global systematic uncertainty that propagates from the $v_{2,tracklet}$ extraction.

The systematic uncertainties sources studied in the dimuon-tracklet case are:

- The cut on z_{vtx}

- The $\Delta\eta$ gap
- The maximum value of $\Delta\eta$
- Summation on z_{vtx}
- Normalization of the event mixing
- Pools definition for the event mixing
- Dimuon invariant mass fit functions and parameters
- Shape of background V_2
- Fit range of V_2 extraction
- Flow extraction method
- Centrality classes

The z_{vtx} cut This is exactly the same procedure as tracklet-tracklet case. The default is 10 cm, alternatives are 8 cm and 12 cm and they account for detector acceptance effects.

The $\Delta\eta$ gap The acceptances of the SPD and the muon spectrometer already impose a gap of order 1.5 units. This gap is varied to 1.3 and 1.7 units (which is a 0.2 unit difference with default as was the case for tracklet-tracklet) to account for acceptance effects.

The maximum of $\Delta\eta$ By default, the maximum value is 5.0 units. It was varied by 0.2 units both ways to 4.8 and 5.2 to account for detector acceptance effects.

Mixed event normalization In the default dimuon-tracklet analysis, each $ME_{ijk}(\Delta\phi, \Delta\eta)$ is projected along $\Delta\eta$. The normalisation factor is the maximum of $ME_{ijk}(\Delta\eta)$.

Other alternatives are possible, as used in Ref. [102]:

- Each $ME_{ijk}(\Delta\phi, \Delta\eta)$ is normalized to its integral over $\Delta\phi$ and $\Delta\eta$.
- Each $ME_{ijk}(\Delta\phi, \Delta\eta)$ is normalized to the integral of $\sum_j ME_{ijk}(\Delta\phi, \Delta\eta)$ over $\Delta\phi$ and $\Delta\eta$.
- Each $ME_{ijk}(\Delta\phi, \Delta\eta) = 1$ to neglect the detector acceptance correction

The last one will not be used to assess systematic effects, as we absolutely need to factor in detector acceptance effects. It is especially true for tracklet-tracklet correlations where nothing can be properly extracted from the yield distributions if the detector effects are not factored in. For example, in Figure 5.25, we saw that the mixed event distribution of tracklet pairs was highly non-uniform and would not allow a smooth flow extraction.

In any case, this systematic uncertainty is, as in the tracklet-tracklet study, useless. This is due to the fact the yields are obtained by fitting $SE(z_{vtx})$ to $ME(z_{vtx})$. Some alternative normalizations of the event mixing just scale the values of $ME(z_{vtx})$ uniformly, so changing the method will just scale the yields but will not affect their shape or the subtraction in any way. And, as in tracklet-tracklet, using an alternative normalisation method that would change the shape of $ME(z_{vtx})$ would just make the Poisson fit fail because it could not fit the $SE(z_{vtx})$ profile to the $ME(z_{vtx})$ profile anymore.

Summation on z_{vtx} This is exactly the same procedure as the tracklet-tracklet case. The default is the Poisson-likelihood fit. The alternatives are a χ^2 fit or a weighted average on z_{vtx}.

This time, as we have a lower number of same event correlations than for tracklet-tracket correlations, we can therefore expect a difference between the Poisson fit and the χ^2 fit, which will provide a systematic uncertainty associated with the handling of sparsely populated bins.

Pools definition for event mixing This has been considered in Ref. [102]. When mixing events, they are grouped in pools of z_{vtx}, $p_{\mathrm{T}}^{\mu\mu}$ and centrality. The centrality bins for the pools are thinly cut and we don't use the full central (0-5%) and peripheral (40-100%) classes directly: we use 0-1%, 1-3%, 3-5%, 5-10%, 10-15%, 15-20%, 20-30%, 30-40%, 40-50%, 50-60%, 60-70%, 70-80%, 80-90%, and 90-100%.

That is an arbitrary choice. A first alternative could be using the very large 0-5 and 40-100 classes directly, in fact really having only 3 classes for mixing: central, peripheral, neither. This was also tried with an intermediate case (typically, bins of size 20% between 40 and 100). This gives a first systematic uncertainty based on centrality binning.

Another way of grouping the events could be based on the properties of the dimuon. That is why additional binnings using $\phi_{\mu\mu}$ or its mass are used.

The binning in $\phi_{\mu\mu}$ goes from $-\pi/2$ to $3\pi/2$ in 6 bins of size $\pi/3$. The idea is that the azimuthal distribution of dimuons is anisotropic due to detector effects when really it should be isotropic. We define pools in $\phi_{\mu\mu}$ and for each event, we mix the dimuon with tracklets from all the pools. The pools all have the same size so, artificially, the mixed event distribution corresponds to a flat azimuthal distribution of dimuons. This systematic uncertainty tells us by how much we expect the flow to vary were we to fully correct for this anisotropy. Through trial and error, it was checked that requiring pools of size 10 was enough to ensure no statistical effects on the distributions.

The binning on the mass of the dimuon comes from the fact that maybe similar events should have dimuons of similar masses because the dimuon mass is a good indicator of whether a dimuon is from the background or the signal. After trying to use the same mass binning as in the rest of the analysis, it was observed that high-mass and high-p_{T} bins were subject to large variations from default. This is typically the sign of an insufficient number of events in the pooling. By using only 3 mass bins, one below the J/ψ peak (< 2.7 GeV/c^2), one for the J/ψ peak (2.7 GeV/c^2 to 3.3 GeV/c^2), and one after the peak (> 3.3 GeV/c^2), event mixing pools have enough events to extract a meaningful systematic uncertainty.

The mass pooling was not considered as a systematic uncertainty source in Ref. [102] and the others were negligible or at least not dominant. Just as a check, the systematic uncertainty analysis on p–Pb data was run for these three alternative poolings to see their individual impact and if they allowed one to define meaningful uncertainties.

Regardless of the alternative used on the pooling in p–Pb data, there are slight deviations from default especially at high-p_{T} but not limited to high-p_{T} which suggests that it is not a issue caused by a low number of events. The variations are comparable to other systematic uncertainties in the analysis and do not dominate which validates their implementation and motivates their use in the pp study.

Invariant mass fit The impact of the shape of the signal and background dimuon contribution must be studied, as they are used in extracting the J/ψ contribution to the v_2. However, due to the very large mass binning used in the extraction step, we do not expect this systematic uncertainty to be impactful.

The same alternatives as for the cross-check of [246] are used and some have been added, which gives 72 fit alternatives:

- CB2 or NA60 parametrization of the signal shape.
- Tails sets from either Run 2 or Monte Carlo (only MC are available for NA60).
- Background functions: Double Exponential (from Ref. [246]), Variable Width Gaussian, Ratio of polynomials (Pol1/Pol2) or Chebychev polynomials.
- Width ratio between $\psi(2\mathrm{S})$ and J/ψ fixed to either 1.05 or 1.00.
- Fit range set to either $[2.4, 4.7]$, $[2.3, 4.9]$, or $[2.0, 5.0]$ GeV/c^2.

In order to prevent the systematic uncertainty to be driven upwards by any fitting failure, which is bound to happen considering we can look at 6 p_{T} bins, in 3 centrality ranges (integrated, peripheral, central) and for 72 alternatives, an additional treatment of the results was used. First, the rms of all the v_2 was computed, and then, any value of v_2 that was too far from the mean would be discarded and the iterative process of computing the new rms and discarding outliers would continue until no

outliers would be found. Applying a 3σ cut (meaning a value was considered an outlier if it was not within 3 rms of the mean), we rejected in a given p_{T} bin at most 7 outliers out of 72 values, which is reasonable. Furthermore, they did not correspond to a particular fit function. This allowed computing a meaningful systematic uncertainty that was not biased by outliers.

Shape of background V_2 extraction During the $V_{2,J/\psi-tracklet}$ extraction step from the $V_{2,background}$, assumptions are made on the shape of $V_{2,background}(m_{\mu\mu})$. A second-order polynomial was used by default, and first or third-order polynomials were checked as alternatives. This choice is expected to have a significant impact due to the small number of mass bins.

Range of the V_2 extraction fit By default, the V_2 extraction fit is made from 1.0 to 5.0 GeV/c^2. An alternative was to use 1.5 to 4.5 GeV/c^2, rejecting the lowest and highest mass bins, which were low in stats but may influence drastically the fit of the background as they can constrain the parameters of the background polynomial V_2 pretty strongly, especially at higher orders.

V_2 extraction method The method labelled 1 is used as default. We first extract the signal from background yields in each $\Delta\phi$ bin before suppressing the non-flow using central and peripheral yields. Method 2 and method 3 (where the steps are reversed) give nearly identical results, as shown in Table 5.3 comparing results from method 2 and 3 on the same dataset. Only method 2 will be considered as an alternative in the systematic uncertainty evaluation to avoid redundancy.

	Method 2	Method 3
0 to 2 GeV/c	-0.00003 ± 0.00026	-0.00004 ± 0.00027
2 to 3 GeV/c	0.00108 ± 0.00033	0.00108 ± 0.00034
3 to 4 GeV/c	0.00017 ± 0.00039	0.00016 ± 0.00039
4 to 6 GeV/c	0.00179 ± 0.00036	0.00180 ± 0.00037
6 to 8 GeV/c	-0.00174 ± 0.00058	-0.00173 ± 0.00058
8 to 12 GeV/c	0.00197 ± 0.00082	0.00197 ± 0.00081

Table 5.3: Table of $V_{2,J/\psi-tracklet}$ results for method 2 and method 3 in various p_{T} bins, obtained from dimuon-tracklet correlations in Run 2 collisions using V0M estimator.

Centrality classes This is exactly the same procedure as the tracklet-tracklet case. The choice of centrality classes for central and peripheral events is arbitrary so the classes are slightly varied and the impact on the v_2 is accounted for as a systematic uncertainty source. In this case, the tracklet v_2 used in the computation of the multiple J/ψ v_2 is the default one from the 0-5% and 40-100% case, because changing the tracklet v_2 while computing the J/ψ systematic uncertainty would account for centrality effects on tracklet flow extraction twice.

Non-flow subtraction inaccuracies - The "PYTHIA systematic uncertainty" As we have said, there are too few dimuons in PYTHIA8 simulations to be able to extract a meaningful Monte Carlo J/ψ v_2. However, one could argue that the inaccuracies of non-flow subtraction that have been evaluated on tracklet-tracklet correlations should be of the same order as the ones we would get in dimuon-tracklet correlations. Effectively, the "PYTHIA uncertainty" puts a limit on the sensitivity of our flow measurement. To avoid double counting, the PYTHIA uncertainty on the tracklet flow measurement is the only one not to be propagated to the J/ψ measurement when we use tracklet v_2 to compute J/ψ v_2. The impact of this propagation is in general small compared to all other systematic uncertainties from J/ψ-hadron correlations anyway. Therefore, when presenting J/ψ results, the systematic uncertainty of each point will contain all sources mentioned in this subsection and the ones propagated from the tracklet flow measurement. The "PYTHIA systematic" for the J/ψ will be shown separately, as a limit on the measurement sensitivity (which will depend on the estimator and centrality classes but which is of around 3-4% based on the tracklet flow in PYTHIA for the V0M estimator, for example). Hence, the J/ψ datapoints we will show can be seen as the "upper limits" of v_2 (if all non-flow was fully suppressed by the extraction methods), which will still allow us to compare this analysis to others and draw conclusions despite the inaccuracies of the methods in pp.

Summary

To summarize, in this section we covered the various selections and steps of the J/ψ elliptic flow analysis. The implementation of the analysis was validated through multiple cross-checks and sanity checks, among which the full reproduction of p–Pb results is in my opinion the strongest advocate. In this last section, the protocol for the evaluation of the systematic uncertainties was detailed as well as all the possible sources and the alternative methods that were implemented to evaluate them. In the next and final chapter, we will cover the results of the analysis which we described here and we will discuss them.

Chapter 6

Results and discussion

C'est peu de choses mais moi tout ce que j'ai je le dépose là, voilà. / Voilà, voilà, voilà...
– Barbara Pravi, *Voilà*

In this chapter, we present and discuss the results obtained from the analysis of the inclusive J/ψ elliptic flow in pp collisions at $\sqrt{s} = 13$ TeV described in the previous chapter.

6.1 Tracklet flow

6.1.1 Default values

First, even though this thesis focuses on the J/ψ elliptic flow, the light-particle flow is needed as an intermediate step. By factorization, $v_{2,J/\psi} = \frac{V_{2,J/\psi-tracklet}}{v_{2,tracklet}}$. This equation holds for the J/ψ in this analysis, as checked in the previous chapter. In order to study the behaviour of $v_{2,J/\psi}$ as a function of p_{T}, $v_{2,tracklet}$ was computed using the same centrality classes and selection cuts. Using V0M as the centrality estimator, the per-trigger yields as a function of $\Delta\phi$ are shown in Figure 6.1.

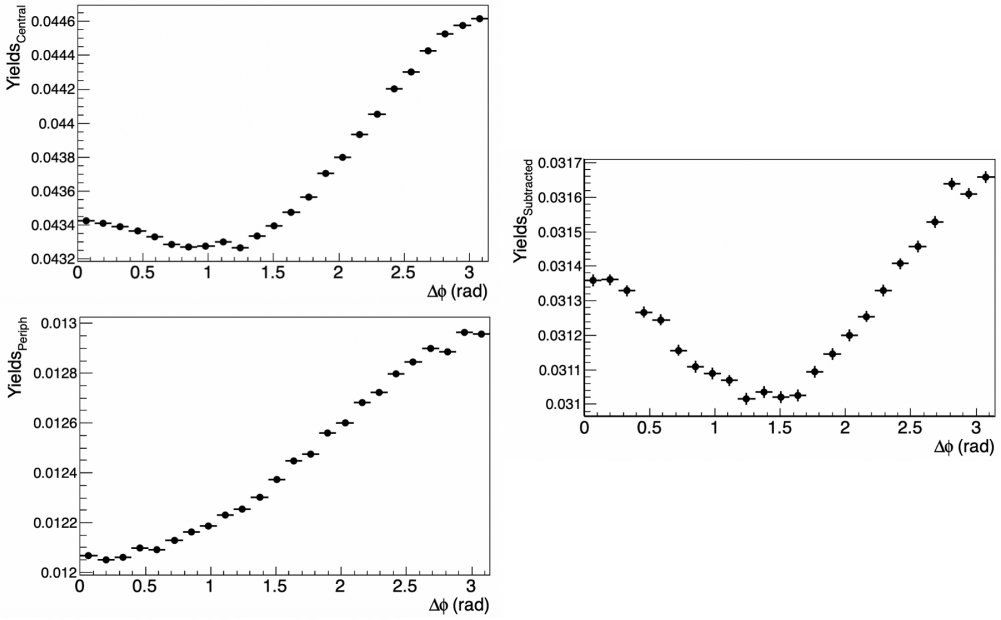

Figure 6.1: Yield subtraction on tracklet-tracklet correlations from LHC16h data using V0M as centrality estimator. Top left: per-trigger yields in the central class (0-5%). Bottom left: per-trigger yields in the peripheral class (40-100%). Right: subtracted per-trigger yields.

In the peripheral yields, a ridge is only visible on the away-side, presumably driven by the dijet non-flow, whereas no yield increase is visible on the near-side, sign that most near-side non-flow is suppressed by the η-gap. On the contrary, both an away-side and a near-side structure are visible in the central class, indicating the presence of collective effects with a non-zero $cos(2\Delta\phi)$ term. In Figures 6.2 and 6.3 we see the results of the tracklet elliptic flow extraction using various methods.

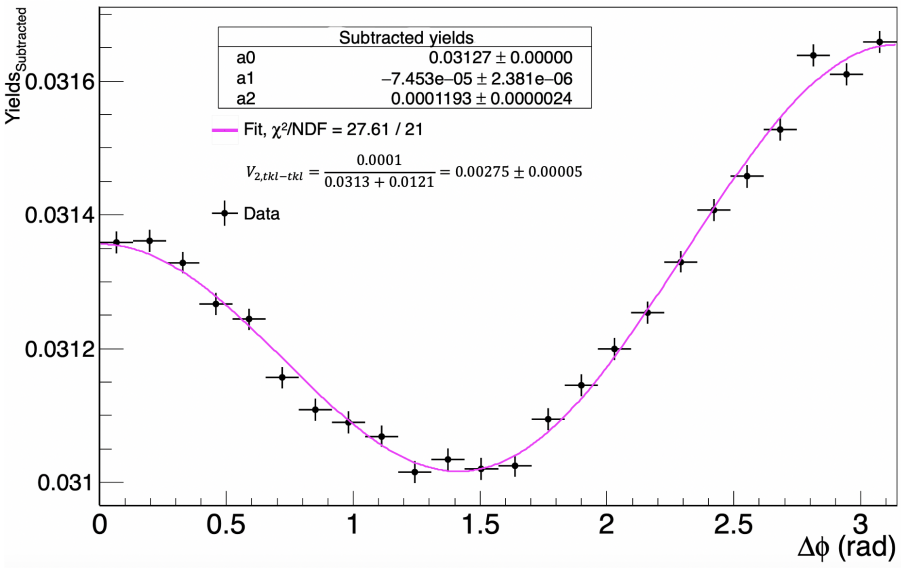

Figure 6.2: Fourier extraction of the tracklet v_2 from tracklet-tracklet correlations and yield subtraction method on LHC16h data, using V0M estimator.

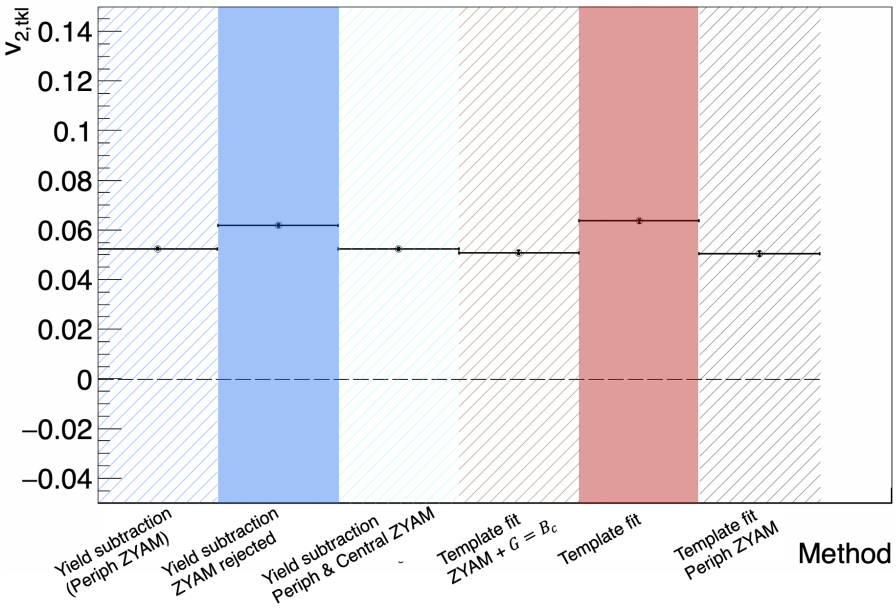

Figure 6.3: Measured values of tracklet v_2 depending on the method used on LHC16h data, using V0M as estimator. From left to right, methods are: yield subtraction (the default one which includes peripheral ZYAM), yield subtraction without ZYAM, yield subtraction with ZYAM in peripheral and central yields, template fit with $G = B_C$, template fit (default one), template fit with peripheral ZYAM.

After the yield subtraction method and Fourier extraction, one obtains the following result for the tracklet flow: $v_{2,tracklet} = 0.05248 \pm 0.0005$. Using various extractions, it is evidenced that the main

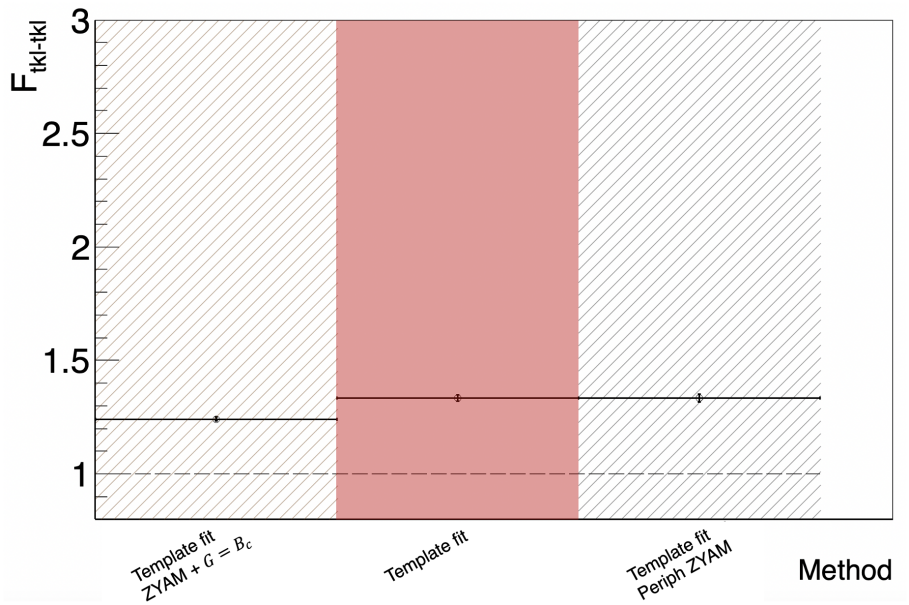

Figure 6.4: Measured values of template fit F parameter depending on the method used on tracklet-tracklet correlations from LHC16h data using V0M. From left to right, methods are: template fit with $G = B_C$, template fit (default one), template fit with peripheral ZYAM.

driver of difference between them is the ZYAM assumption, and, as expected [136], assuming ZYAM reduces the measured v_2. Using a template fit or the yield subtraction procedure does not change the result much, mainly because v_1 is small and the value of the F factor is close to 1 (around 1.3, as seen in Figure 6.4) making the template fit and the yield subtraction procedures nearly equivalent. Using an SPD-based centrality estimator like SPDTracklets drastically changes the result and its behaviour.

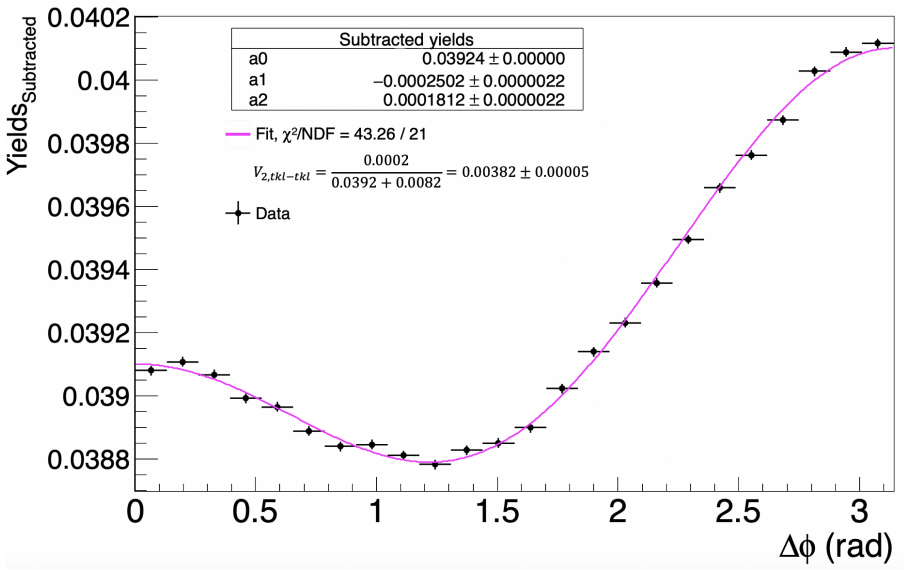

Figure 6.5: Fourier extraction of the tracklet v_2 from tracklet-tracklet correlations and yield subtraction method on LHC16h data, using SPDTracklets estimator.

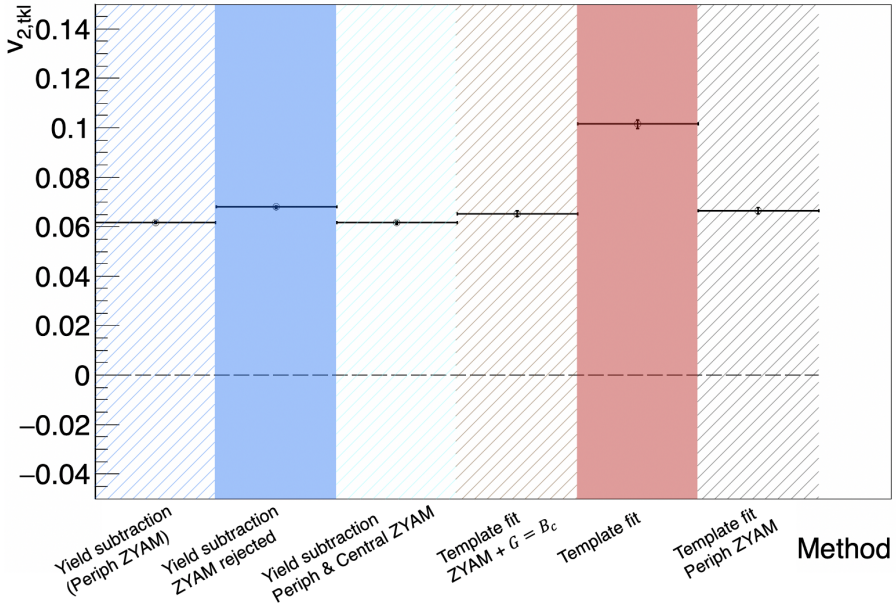

Figure 6.6: Measured values of tracklet v_2 depending on the method used on LHC16h data, using SPDTracklets as estimator. From left to right, methods are: yield subtraction (the default one which includes peripheral ZYAM), yield subtraction without ZYAM, yield subtraction with ZYAM in peripheral and central yields, template fit with $G = B_C$, template fit (default one), template fit with peripheral ZYAM.

With SPDTracklets, using the subtraction method as in Figure 6.5, $v_{2,tracklet} = 0.06178 \pm 0.0004$. this result is higher than what was found for V0M. However, the strongest difference lies in the behaviour of the ATLAS template fit extraction as shown in Figure 6.6. Because the F factor is close to 3 with this estimator, the result obtained by template fitting is around 1.7 times as high as the yield subtraction method. This will be discussed further but it shows how drastic the impact of the centrality estimator can be. Similar behaviour is found using SPDClusters which is expected from the strong correlation between both SPD-based estimators. It gives $v_{2,tracklet} = 0.0607 \pm 0.0004$ using the yield subtraction method.

Systematic uncertainties evaluation

Applying the systematic uncertainties study detailed in the previous chapter, the impact of each possible variation from default was studied. Detailed plots showing the changes of v_2 in each case are presented in Appendix D. The systematic uncertainties are compiled in Table 6.1 for the various centrality estimators.

0-5% - 40-100%	V0M		SPDTracklets		SPDClusters		Mixed (V0M+SPDT)	
Source	Yield sub.	Template fit	Yield sub.	Template fit	Yield sub.	Template fit	Yield sub.	Template fit
Default v_2 value	**0,05248**	**0,06364**	**0,06178**	**0,10149**	**0,06065**	**0,09216**	**0,05816**	**0,07435**
Statistical unc.	0,00052	0,00084	0,00038	0,00176	0,00040	0,00151	0,00044	0,00096
z_{vtx} cut	0,056%	0,104%	0,073%	0,491%	0,090%	0,369%	0,056%	0,154%
η-gap	0,888%	0,355%	1,360%	3,858%	1,460%	2,973%	1,216%	0,775%
Summation method	2,017%	1,364%	2,685%	8,685%	2,879%	7,048%	2,408%	2,192%
Fit method	3,792%	0,000%	6,547%	0,000%	2,775%	0,000%	0,849%	0,000%
Centrality choice	4,00%	2,30%	3,40%	6,60%	3,60%	7,50%	3,669%	4,086%
Syst. Uncorrelated	**5,94%**	**2,70%**	**7,97%**	**11,58%**	**5,58%**	**10,72%**	**4,63%**	**4,70%**
PYTHIA v_2	0,036272	0,0372714	0,0544471	0,0652683	0,0501714	0,0535331	0,0435581	0,0434326
PYTHIA syst.	**27,74%**	**18,94%**	**52,74%**	**23,42%**	**43,81%**	**18,60%**	**33,73%**	**18,84%**

Table 6.1: Table of relative systematic uncertainties for the measurement of $v_{2,tracklets}$ using 0-5% and 40-100% as default centrality classes, 10 mrad tracklet cut and various centrality estimators and extraction methods. A bar chart of these uncertainties can be found in Figure D.7.

The impact of the sources of systematic uncertainties was evaluated for the measurement of the light particle elliptic flow using 0-5% and 40-100% as the central and peripheral classes and a $\Delta\Phi$ cut of 10 mrad. In order of appearance, the sources are the cut on z_{vtx}, the value of the η-gap, the summation method on z_{vtx}, the fitting method to extract the V_2 (which is only defined for the yield subtraction procedure and not for the template fit), and the choice of centrality classes. These systematic uncertainties are assumed uncorrelated and we further add the one coming from PYTHIA simulations which reflects the limits of the methods to accurately measure flow in pp. For each estimator, the systematic uncertainties are evaluated for both the yield subtraction method and the template fit method. The colour coding of each cell represents the relative strength of a particular systematic uncertainty compared to the others. Another visualisation of the relative importance of each systematic uncertainty using bar charts is found in Appendix D.

Discussion on the systematic uncertainties and the tracklet flow

Overall, regardless of the centrality estimator that is chosen, the light particle elliptic flow systematic uncertainties are completely dominated by the PYTHIA one. However, while the z_{vtx} cut and the η-gap have a negligible impact, the others do produce significant variations of the measured flow.

It is interesting to note that what we started to see in the default case is further confirmed by the systematic uncertainties study, namely the similarity between V0M and the mixed estimator and between both SPD-based estimators, which is to be expected.

Concerning V0M, we observe that yield subtraction and template fit methods give results that are quite close overall, caused by the fact that the F factor from the template fit is close to unity, making both methods nearly equivalent. All systematic uncertainties are negligible but the ones on the fit method, the centrality class choice, and the PYTHIA extraction. Where applicable, the systematic uncertainties on the yield subtraction method and on the template fit method are similar. This similarity indicates that for this analysis, when using V0M, both procedures are equally good at measuring flow. This is corroborated, but also nuanced, by the PYTHIA extraction systematic uncertainty, which shows a slightly better non-flow suppression from the template fit procedure, while not being particularly efficient.

For SPD-based estimators, there is a neat difference between yield subtraction and template fit procedures. The extracted flow is nearly doubled using a template fit method and yields values that are not found anywhere in the literature. This highlights the impact of the choice of centrality estimator on the final result. Furthermore, the systematic uncertainties are generally higher for the template fit procedure, possibly because the F factor is around 3, so all changes to the peripheral yields are strongly emphasized. However, these increased systematic uncertainties are counterbalanced by the PYTHIA one, as yield subtraction is unable to extract flow reliably compared to template fitting. This strongly suggests that, when using an SPD-based estimator, non-flow description is drastically different from V0M estimator. When centrality is estimated using SPD activity, it uses the same tracklets as the ones used for the correlations, creating biases in the centrality classes definition and the flow extraction which may be the reason the template fit procedure measures such high tracklet flow. The consequence of this estimator choice is that the template fit needs to subtract the peripheral yields three times to fully suppress non-flow and doing it only once is not enough (because the non-flow in central yields and in peripheral yields do not match anymore), so it seems that template fitting is a robust extraction method as it adapts to various estimators.

6.1.2 Behaviour with centrality

As has been done for the 0-5% central class, the same work can be carried out for various central classes to study the evolution of the light particle elliptic flow with centrality. The centrality classes are disjoint and span from 0-1% to 20-30%, still with 40-100% as the peripheral class.

Systematic uncertainties evaluation

As the mixed estimator and SPDClusters showed similar results to V0M and SPDTracklets, respectively, this work was carried out only for the two latter estimators and the results are shown in Tables 6.2 and 6.3 for V0M and SPDTacklets, respectively.

V0M	0-1%		1-3%		3-5%		5-10%		10-15%		15-20%		20-30%	
Source	Yield sub.	Template fit	Yield sub.	Template fit	Yield sub.	Template fit	Yield sub.	Template fit	Yield sub.	Template fit	Yield sub.	Template fit	Yield sub.	Template fit
Default v_2 value	**0,05314**	**0,06229**	**0,05250**	**0,06460**	**0,05122**	**0,06496**	**0,04958**	**0,06543**	**0,04801**	**0,06719**	**0,04739**	**0,07017**	**0,04210**	**0,06855**
Statistical unc.	0,00061	0,00087	0,00070	0,00107	0,00087	0,00135	0,00084	0,00140	0,00109	0,00188	0,00134	0,00236	0,00156	0,00313
z_{vtx} cut	0,0000	0,0000	0,0001	0,0001	0,0001	0,0001	0,0001	0,0001	0,0002	0,0004	0,0001	0,0002	0,0001	0,0002
η-gap	0,0005	0,0003	0,0004	0,0001	0,0005	0,0003	0,0008	0,0006	0,0006	0,0005	0,0004	0,0001	0,0006	0,0004
Summation method	0,0010	0,0007	0,0010	0,0008	0,0013	0,0013	0,0017	0,0019	0,0017	0,0021	0,0011	0,0012	0,0015	0,0017
Fit method	0,0018	0,0000	0,0021	0,0000	0,0022	0,0000	0,0023	0,0000	0,0023	0,0000	0,0022	0,0000	0,0025	0,0000
Syst. Uncorrelated	**0,0021**	**0,0008**	**0,0024**	**0,0008**	**0,0026**	**0,0013**	**0,0029**	**0,0020**	**0,0030**	**0,0022**	**0,0025**	**0,0012**	**0,0029**	**0,0017**
Syst. Uncorrelated (%)	**3,94%**	**1,27%**	**4,53%**	**1,20%**	**5,02%**	**2,03%**	**5,92%**	**3,02%**	**6,24%**	**3,25%**	**5,18%**	**1,69%**	**7,00%**	**2,55%**
PYTHIA v_2	0,03329	0,03228	0,03639	0,03778	0,03840	0,04061	0,03921	0,04093	0,04086	0,04559	0,04273	0,05102	0,04348	0,05627
PYTHIA syst.	**0,0117**	**0,0090**	**0,0147**	**0,0122**	**0,0173**	**0,0143**	**0,0192**	**0,0144**	**0,0228**	**0,0178**	**0,0269**	**0,0220**	**0,0530**	**0,0294**
PYTHIA syst. (%)	**22,05%**	**14,47%**	**27,92%**	**18,88%**	**33,83%**	**21,96%**	**38,79%**	**21,98%**	**47,51%**	**26,54%**	**56,75%**	**31,34%**	**125,83%**	**42,88%**

Table 6.2: Table of absolute systematic uncertainties for the measurement of $v_{2,tracklets}$ as a function of centrality for V0M. A bar chart of these uncertainties can be found in Figure D.8.

SPDTracklets	0-1%		1-3%		3-5%		5-10%		10-15%		15-20%		20-30%	
Source	Yield sub.	Template fit	Yield sub.	Template fit	Yield sub.	Template fit	Yield sub.	Template fit	Yield sub.	Template fit	Yield sub.	Template fit	Yield sub.	Template fit
Default v_2 value	**0,06241**	**0,09687**	**0,06172**	**0,10436**	**0,06069**	**0,10816**	**0,06055**	**0,11416**	**0,05994**	**0,12519**	**0,05813**	**0,13274**	**0,05676**	**0,14855**
Statistical unc.	0,00045	0,00157	0,00054	0,00205	0,00069	0,00251	0,00066	0,00283	0,00087	0,00401	0,00114	0,00546	0,00124	0,00780
z_{vtx} cut	0,0000	0,0003	0,0000	0,0004	0,0001	0,0010	0,0001	0,0007	0,0001	0,0008	0,0002	0,0010	0,0001	0,0015
η-gap	0,0008	0,0035	0,0008	0,0041	0,0009	0,0046	0,0010	0,0056	0,0010	0,0066	0,0014	0,0082	0,0013	0,0087
Summation method	0,0016	0,0077	0,0015	0,0094	0,0018	0,0107	0,0017	0,0128	0,0018	0,0161	0,0029	0,0188	0,0022	0,0218
Fit method	0,0039	0,0000	0,0041	0,0000	0,0042	0,0000	0,0042	0,0000	0,0042	0,0000	0,0041	0,0000	0,0038	0,0000
Syst. Uncorrelated	**0,0043**	**0,0085**	**0,0045**	**0,0103**	**0,0047**	**0,0117**	**0,0046**	**0,0140**	**0,0047**	**0,0174**	**0,0052**	**0,0205**	**0,0046**	**0,0235**
Syst. Uncorrelated (%)	**6,90%**	**8,76%**	**7,23%**	**9,84%**	**7,71%**	**10,81%**	**7,65%**	**12,29%**	**7,76%**	**13,91%**	**9,00%**	**15,45%**	**8,14%**	**15,85%**
PYTHIA v_2	0,05391	0,06278	0,05481	0,06561	0,05439	0,06705	0,05551	0,07179	0,05975	0,08341	0,06163	0,09288	0,06556	0,11170
PYTHIA syst.	**0,0310**	**0,0231**	**0,0334**	**0,0232**	**0,0338**	**0,0233**	**0,0364**	**0,0254**	**0,0551**	**0,0318**	**0,0786**	**0,0379**	**0,0896**	**0,0506**
PYTHIA syst. (%)	**49,61%**	**23,84%**	**54,04%**	**22,24%**	**55,64%**	**21,54%**	**60,07%**	**22,25%**	**91,99%**	**25,43%**	**135,19%**	**28,56%**	**157,78%**	**34,08%**

Table 6.3: Table of absolute systematic uncertainties for the measurement of $v_{2,tracklets}$ as a function of centrality for SPDTracklets. A bar chart of these uncertainties can be found in Figure D.9.

The only difference with the previous systematic uncertainties study is that in this case the systematic uncertainty attached to the choice of centrality classes was not evaluated as it is precisely the dependency that we are studying.

Discussion on the systematic uncertainties

One can notice that, regardless of the centrality estimator, the systematic uncertainties show the same behaviour for the various central classes. As a result, all previous remarks still apply. One can also observe a tendency for systematic uncertainties to increase as multiplicity decreases, which is a behaviour mainly driven by the PYTHIA source. It underlines the stronger inability to extract flow reliably as multiplicity decreases. From these tables, plots showing the behaviour of the light particle elliptic flow as a function of centrality can be extracted for both V0M and SPDTracklets estimators, as shown in Figures 6.7 and 6.8, respectively.

Discussion on the centrality behaviour of tracklet flow

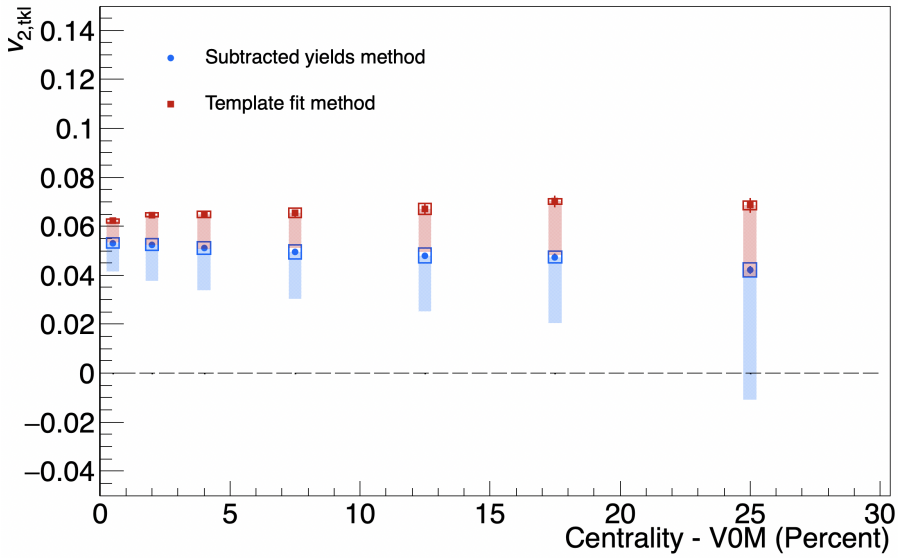

Figure 6.7: $v_{2,tracklet}$ from tracklet-tracklet correlations in LHC16h data as a function of the V0M centrality class. Each point is set at the middle of the centrality class used. The centrality clases used are: 0-1%, 1-3%, 3-5%, 5-10%, 10-15%, 15-20%, 20-30%. The uncorrelated systematic uncertainties are represented by the empty boxes and the PYTHIA systematic uncertainty is apart from the others and is represented by the filled boxes.

No definite conclusion can be drawn due to the large systematic uncertainties except that, within uncertainties, the behaviour of the light tracklet flow is flat for both yield subtraction and template fit using V0M. Nevertheless, some hints of yield subtraction making the flow diminish at low multiplicity could be seen, were the PYTHIA systematic uncertainty assumed to be fully correlated with centrality. In fact, this assumption could hold well as the PYTHIA systematic uncertainty relies on the bad non-flow suppression and so the bad non-flow estimation from the peripheral yields distribution. In this study of tracklet flow as a function of centrality, the peripheral class is fixed to 40-100%. The non-flow estimation is the same regardless of the central class making the PYTHIA systematic uncertainty fully correlated with centrality and so the effects of the PYTHIA systematic uncertainty should be equivalent for all points. With this in mind, the remaining uncorrelated systematic uncertainties (line "Syst. uncorrelated" in Table 6.2) are small enough to note that the behaviour of tracklet elliptic flow with centrality is decreasing with decreasing multiplicity for the yield subtraction method and is either flat or decreasing with decreasing multiplicity for the template fit method, depending on the actual effect we estimate using PYTHIA.

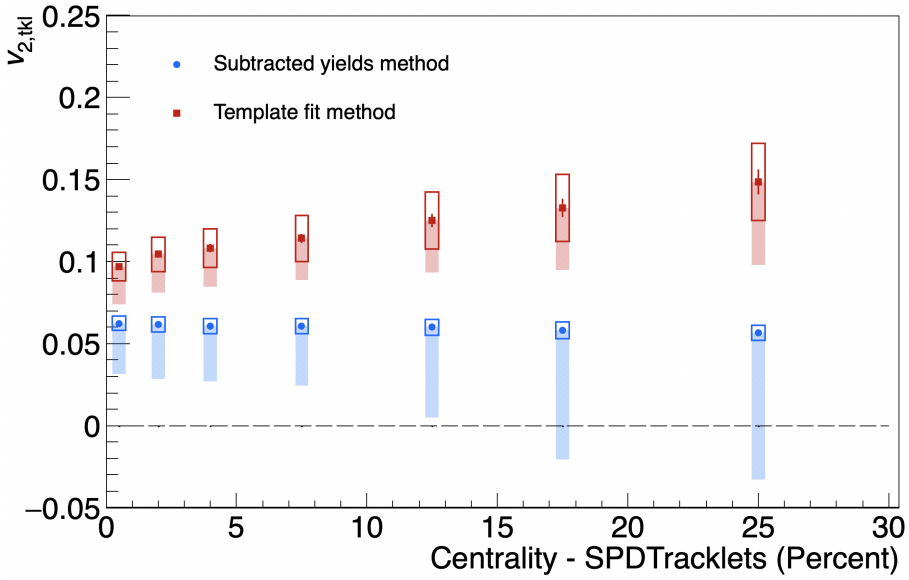

Figure 6.8: $v_{2,tracklet}$ from tracklet-tracklet correlations in LHC16h data as a function of the SPDTracklets centrality class. Each point is set at the middle of the centrality class used. The centrality clases used are: 0-1%, 1-3%, 3-5%, 5-10%, 10-15%, 15-20%, 20-30%. The uncorrelated systematic uncertainties are represented by the empty boxes and the PYTHIA systematic uncertainty is apart from the others and is represented by the filled boxes.

For SPDTracklets in Figure 6.8, the systematic uncertainties are equally large. However, the same argument concerning the PYTHIA systematic uncertainty being fully correlated with centrality still holds. We then see that the template fit gives v_2 values systematically higher than yield subtraction (sometimes by a factor 2) and the behaviour of tracklet flow is either flat or increasing as multiplicity lowers (depending on the systematic effect estimated with PYTHIA) which seems counter-intuitive.

One can try to compare observations from this analysis with previous results from ATLAS [107] and CMS [135] regarding the behaviour of light particle elliptic flow with multiplicity, as shown in Figure 6.9. One can use information from the centrality framework to form an equivalence between multiplicity and centrality classes, allowing one to compare ALICE, ATLAS, and CMS results. One can take the charged particle density per unit pseudorapidity measured by the centrality framework in the 0-1% and 20-30% classes and multiply it by five to cover the 5-unit wide ATLAS and CMS tracklet acceptance ($|\eta| < 2.5$). This hypothesis assumes that the density is flat on a 5-unit range which is an acceptable rough assumption judging from results from Ref. [247]. In doing so, we obtain that the equivalent number of charged particles in $|\eta| < 2.5$ for the 0-1% class could be as high as 150 and for 20-30% around 50, which approximately corresponds to the amplitude of variation seen in Figure 6.9.

Of course, because the PYTHIA systematic uncertainty is so large, one cannot strictly compare this analysis results with ATLAS and CMS, but some elements can still be noted from the trends. ATLAS and CMS measurements were done with a tracklet p_{T} cut of 0.5 and 0.3 GeV/c, respectively. This is equivalent to a 5 mrad and a 10 mrad $\Delta\Phi$ cut in this analysis framework, which makes our results directly comparable to the existing ones. As shown in the previous chapter, a decrease of the $\Delta\Phi$ cut from 10 to 5 mrad leads to an increase of the measured tracklet v_2 by around 30% which could explain the difference between ATLAS and CMS results at high multiplicities.

CMS flow results show a decrease as multiplicity decreases. Other than being intuitive (less particles means less collectivity so a less pronounced flow), it is a behaviour that is compatible with our measurements for the V0M estimator within uncertainties. Assuming the systematic effect from PYTHIA is not too large we could also note that the amplitude of the decrease for the studied ranges are equivalent between CMS result and ours. For SPDTracklets however, our data could be compatible with a flat behaviour as a function of centrality or decreasing which does not allow for a definite comparison.

ATLAS flow results show a flat dependency of tracklet v_2 with multiplicity. This is compatible with our measurement made using V0M as an estimator. However, the ATLAS result clashes with our

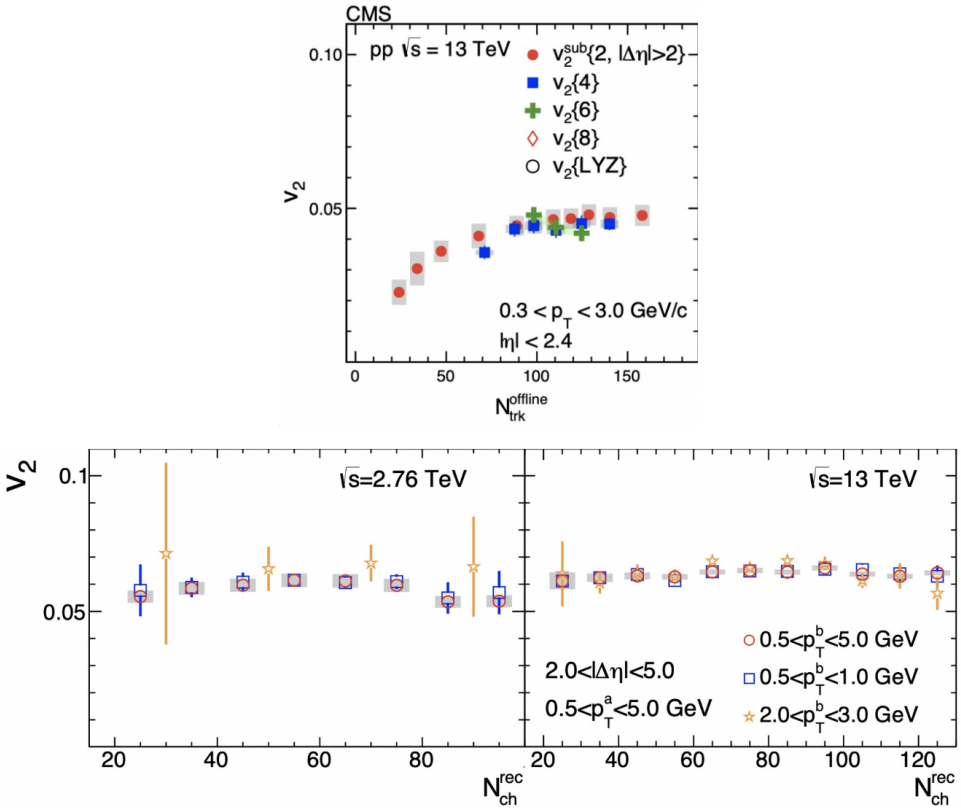

Figure 6.9: $v_{2,tracklet}$ as a function of multiplicity in ATLAS [107] and CMS [135] studies.

observations made using SPDTracklets, both in the behaviour and magnitude of the flow. Even though the strength of the statements is diluted by the large systematic uncertainties, the elliptic flow measured for light particles seems to increase with decreasing multiplicity, with central values from around 10% to as high as 15% which is twice as much as what was measured by ATLAS.

In my opinion, this discrepancy has only one origin: the bias coming from SPD-based estimators. As this analysis relies on correlations with tracklets from the SPD, using them as a centrality estimator will necessarily bias the measurements. One could imagine specific topologies of events like dijets which would produce many tracklets and tend to be considered central, due to the high SPD activity. This would create a deep difference between the non-flow in peripheral events, where dijet events are disfavoured, and the non-flow in central events. This could explain why the simple yield subtraction is not working well enough in PYTHIA simulations and why, in data, template fitting needs an F factor of 3 to fully suppress non-flow. Moreover, this bias could explain why the magnitude of the tracklet flow is not compatible with any existing result, because such effect is not present elsewhere.

However, because this bias affects the tracklets, it should impact the tracklet-tracklet correlations as well as the dimuon-tracklet correlations. So much so that, when factorizing to get to the J/ψ v_2, the bias would cancel out and the final J/ψ v_2 would remain unaffected, which is what we will indeed observe in the following section.

6.2 J/ψ elliptic flow

Using the results from tracklet elliptic flow and the dimuon-tracklet correlations, one can apply factorization to evaluate $v_{2,J/\psi}$ and its systematic uncertainties.

6.2.1 Behaviour with transverse momentum

Using the default parameters and procedures of the analysis to obtain the central values and statistical uncertainties on the flow measurement, one can obtain the V_2 of the J/ψ-tracklet pairs. By dividing the results from each estimator by the corresponding tracklet v_2 one can compute the J/ψ v_2 as a function of p_{T}, as shown in Figure 6.10, for V0M, SPDTrackelts, and SPDClusters, using most of the implemented extraction methods (the yield subtraction method and alternatives, each with or without the ZYAM hypothesis, and the template fit method with and without ZYAM hypothesis as well).

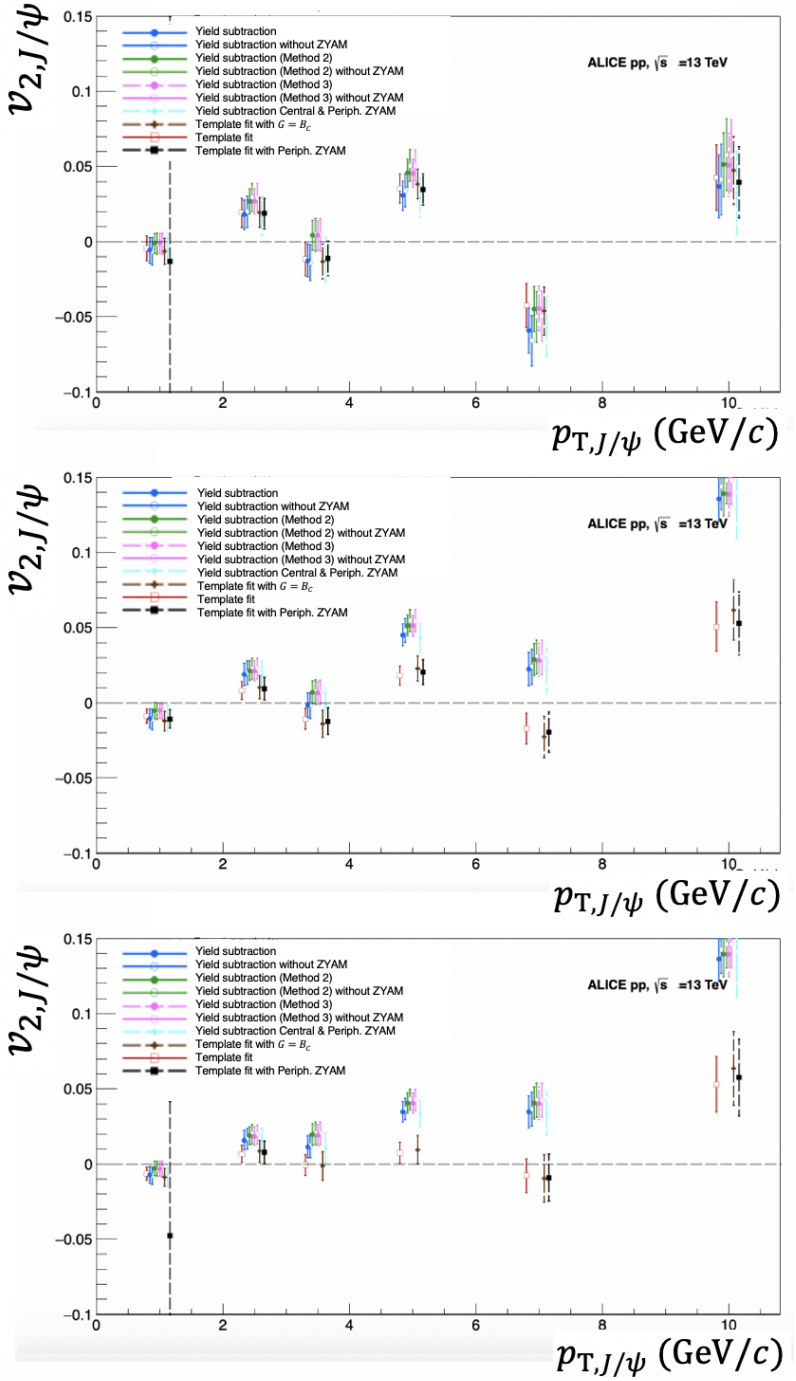

Figure 6.10: $v_{2,J/\psi}$ as a function of dimuon p_{T} using different extraction methods and different centrality estimators. Top: V0M, Middle: SPDTracklets, Bottom: SPDClusters.

Without having evaluated the systematic uncertainties we can already highlight some features of these results. Using V0M, the J/ψ elliptic flow oscillates around zero, and from the variation caused by the methods, one could expect to see systematic uncertainties at least as large as the statistical uncertainties which would make the flow compatible with zero. Still with V0M, we observe that the ZYAM hypothesis has a tendency to decrease the measured flow, which was already observed for tracklets. We also observe that template fit and yield subtraction give compatible results, as was the case for tracklet flow.

For SPDTracklets, the J/ψ elliptic flow also oscillates. But contrary to V0M, the yield subtraction method measures more flow than the template fit method, especially at high-p_{T} where non-flow should prevail. The template fit procedure gives compatible measurements of the J/ψ flow between V0M and SPDTracklets, whereas yield subtraction seems more impacted by non-flow as was the case for the tracklet flow.

Finally, for SPDClusters, the J/ψ results are compatible with those obtained with SPDTracklets, although they seem to be more stable, which may indicate more robustness from this estimator. Again, it seems that SPD-based estimators display a similar behaviour.

Systematic uncertainties evaluation

Systematic uncertainties are evaluated and presented in the same way as for tracklet-tracklet correlations. Plots showing the detailed effects can be found in Appendix E and a summary of the systematic uncertainties is found in Tables 6.4, 6.5 and 6.6 for V0M, SPDTrackelts and SPDClusters estimators, respectively.

In each table, we study the impact of selection cuts (like z_{vtx}, $\Delta\eta$), the impact of the event mixing (with the various pooling alternatives) and the impact of the extraction procedure per se (invariant mass fit, V_2 fit ranges and parametrization, non-flow subtraction method). The propagation of the total uncertainties on $v_{2,tracklet}$ (line "Propagation from tracklet v_2") is done and the line "Full Syst. Uncorrelated" gives the final systematic uncertainty on the J/ψ v_2. To that we add a limit on the sensitivity of the measurement, given by the tracklet flow measured by PYTHIA (on the line "PYTHIA tracklet v_2 (sensitivity limit)").

Discussion on the systematic uncertainties

The behaviour of the systematic uncertainties for V0M and SPDTrackelts is very similar. We observe a gradual increase of the magnitude of the systematic uncertainties with increasing transverse momentum, and also the fact that the uncertainties are mainly driven by the flow extraction process. The final result is highly sensitive to the parametrization of the V_2 fit, the extraction procedure and the centrality classes. However, it is not impacted by the invariant mass fit, which is something we hinted at from the previous chapter as the low number of mass bins in the analysis does not allow for a fine discrimination between dimuon invariant mass fitting templates. Indeed, only ten bins are used on the whole invariant mass range when extracting signal from background flow contributions. A slight change in the signal or background template shapes does not produce a significant change. The binning of the event mixing pools also has a non-negligible impact, especially concerning the dimuon mass binning. However, the systematic uncertainties from selection cuts are negligible in front of the others. Even the propagation of the global systematic effect coming from $v_{2,tracklet}$ uncertainties does not have that much of an impact in general as the systematic uncertainties on $V_{2,J/\psi-tracklet}$ are already quite large.

Unexpectedly, for SPDClusters, the hierarchy of the systematic uncertainties is different. While the ones associated to the event mixing and the extraction procedure keep the same magnitude, the ones associated to selection cuts, like z_{vtx} or $\Delta\eta$ range, become dominant. This behaviour is unexpected as it was assumed that SPDTracklets and SPDClusters being strongly correlated and linked to the same physical effect, they would give similar results.

Using these systematic uncertainties tables, one can plot the behaviour of inclusive J/ψ elliptic flow as a function of p_{T} for various centrality estimators, as shown in Figures 6.11, 6.12 and 6.13.

V0M	0-2 GeV/c		2-3 GeV/c		3-4 GeV/c		4-6 GeV/c		6-8 GeV/c		8-12 GeV/c	
Source	Yield sub.	Template fit	Yield sub.	Template fit	Yield sub.	Template fit	Yield sub.	Template fit	Yield sub.	Template fit	Yield sub.	Template fit
Default v_2 value	**-0,00584**	**-0,00441**	**0,01802**	**0,01912**	**-0,01266**	**-0,01151**	**0,03064**	**0,03532**	**-0,05892**	**-0,04245**	**0,03671**	**0,04257**
Statistical unc.	0,00842	0,00820	0,00965	0,00972	0,01082	0,01101	0,00967	0,00962	0,01503	0,01472	0,02098	0,02161
z_{vtx} cut	0,0014	0,0012	0,0006	0,0006	0,0019	0,0017	0,0010	0,0007	0,0042	0,0037	0,0008	0,0011
$\Delta\eta_{min}$	0,0012	0,0012	0,0014	0,0014	0,0015	0,0014	0,0003	0,0004	0,0006	0,0007	0,0030	0,0026
$\Delta\eta_{max}$	0,0021	0,0019	0,0025	0,0024	0,0008	0,0004	0,0005	0,0006	0,0013	0,0012	0,0063	0,0061
ME normalization	0,0000	0,0000	0,0000	0,0000	0,0000	0,0000	0,0000	0,0000	0,0000	0,0000	0,0000	0,0000
Summation method	0,0017	0,0016	0,0004	0,0003	0,0009	0,0009	0,0018	0,0016	0,0023	0,0013	0,0030	0,0042
Pooling with mass	0,0006	0,0002	0,0017	0,0013	0,0026	0,0036	0,0026	0,0018	0,0050	0,0069	0,0004	0,0015
Pooling with ϕ	0,0003	0,0002	0,0005	0,0006	0,0020	0,0022	0,0004	0,0002	0,0108	0,0095	0,0005	0,0004
Pooling with centrality	0,0004	0,0004	0,0005	0,0006	0,0011	0,0011	0,0003	0,0003	0,0021	0,0023	0,0046	0,0046
Invariant mass fit	0,0003	0,0003	0,0003	0,0002	0,0007	0,0007	0,0007	0,0005	0,0050	0,0034	0,0054	0,0036
Background V_2 shape	0,0034	0,0035	0,0015	0,0015	0,0026	0,0029	0,0012	0,0011	0,0045	0,0043	0,0022	0,0022
Range V_2 fit	0,0059	0,0061	0,0037	0,0039	0,0027	0,0021	0,0024	0,0025	0,0033	0,0018	0,0057	0,0048
Extraction method	0,0022	0,0006	0,0041	0,0027	0,0079	0,0074	0,0070	0,0092	0,0068	0,0046	0,0068	0,0104
Centrality choice	0,0043	0,0040	0,0026	0,0028	0,0094	0,0089	0,0029	0,0031	0,0079	0,0080	0,0184	0,0208
Syst. Uncorrelated	**0,0090**	**0,0087**	**0,0072**	**0,0066**	**0,0136**	**0,0131**	**0,0088**	**0,0104**	**0,0183**	**0,0167**	**0,0230**	**0,0258**
Syst. Uncorrelated (Percentage)	**154%**	**197%**	**40%**	**34%**	**107%**	**114%**	**29%**	**30%**	**31%**	**39%**	**63%**	**61%**
Propagation from tracklet v_2	5,94%	2,70%	5,94%	2,70%	5,94%	2,70%	5,94%	2,70%	5,94%	2,70%	5,94%	2,70%
Full Syst. Uncorrelated (Percentage)	**154%**	**197%**	**40%**	**34%**	**107%**	**114%**	**29%**	**30%**	**32%**	**39%**	**63%**	**61%**
Full Syst. Uncorrelated	**0,0090**	**0,0087**	**0,0073**	**0,0066**	**0,0136**	**0,0131**	**0,0089**	**0,0105**	**0,0187**	**0,0167**	**0,0232**	**0,0259**
PYTHIA tracklet v_2 (sensitivity limit)	0,0363	0,0373	0,0363	0,0373	0,0363	0,0373	0,0363	0,0373	0,0363	0,0373	0,0363	0,0373

Table 6.4: Table of absolute systematic uncertainties for the measurement of $v_{2,J/\psi}$ as a function of transverse momentum using V0M. A bar chart of these uncertainties can be found in Figure E.19.

SPDTracklets	0-2 GeV/c		2-3 GeV/c		3-4 GeV/c		4-6 GeV/c		6-8 GeV/c		8-12 GeV/c	
Source	Yield sub.	Template fit	Yield sub.	Template fit	Yield sub.	Template fit	Yield sub.	Template fit	Yield sub.	Template fit	Yield sub.	Template fit
Default v_2 value	**-0,01032**	**-0,00876**	**0,01880**	**0,00805**	**-0,00154**	**-0,01061**	**0,04516**	**0,01805**	**0,02240**	**-0,01715**	**0,13548**	**0,05059**
Statistical unc.	0,00644	0,00488	0,00744	0,00596	0,00825	0,00698	0,00728	0,00647	0,01110	0,01044	0,01487	0,01645
z_{vtx} cut	0,0011	0,0008	0,0008	0,0006	0,0017	0,0014	0,0017	0,0011	0,0035	0,0027	0,0017	0,0024
$\Delta\eta_{min}$	0,0000	0,0001	0,0002	0,0002	0,0007	0,0009	0,0006	0,0002	0,0006	0,0003	0,0003	0,0014
$\Delta\eta_{max}$	0,0004	0,0003	0,0006	0,0007	0,0004	0,0006	0,0024	0,0015	0,0008	0,0016	0,0022	0,0043
ME normalization	0,0000	0,0000	0,0000	0,0000	0,0000	0,0000	0,0000	0,0000	0,0000	0,0000	0,0000	0,0000
Summation method	0,0005	0,0004	0,0008	0,0005	0,0006	0,0006	0,0010	0,0006	0,0010	0,0004	0,0005	0,0011
Pooling with mass	0,0018	0,0014	0,0011	0,0008	0,0022	0,0012	0,0002	0,0001	0,0113	0,0111	0,0100	0,0161
Pooling with ϕ	0,0004	0,0004	0,0006	0,0005	0,0004	0,0005	0,0002	0,0004	0,0035	0,0041	0,0093	0,0119
Pooling with centrality	0,0012	0,0009	0,0007	0,0005	0,0006	0,0004	0,0004	0,0005	0,0029	0,0022	0,0024	0,0028
Invariant mass fit	0,0007	0,0003	0,0002	0,0001	0,0006	0,0003	0,0006	0,0003	0,0024	0,0010	0,0024	0,0019
Background V_2 shape	0,0024	0,0020	0,0011	0,0007	0,0021	0,0017	0,0018	0,0016	0,0015	0,0016	0,0038	0,0027
Range V_2 fit	0,0048	0,0038	0,0013	0,0010	0,0012	0,0004	0,0025	0,0021	0,0004	0,0001	0,0045	0,0040
Extraction method	0,0024	0,0021	0,0012	0,0019	0,0041	0,0032	0,0029	0,0036	0,0030	0,0024	0,0016	0,0052
Centrality choice	0,0049	0,0038	0,0016	0,0018	0,0089	0,0070	0,0019	0,0029	0,0077	0,0048	0,0065	0,0039
Syst. Uncorrelated	**0,0081**	**0,0064**	**0,0033**	**0,0033**	**0,0106**	**0,0082**	**0,0057**	**0,0057**	**0,0155**	**0,0137**	**0,0169**	**0,0225**
Syst. Uncorrelated (Percentage)	**78%**	**73%**	**17%**	**41%**	**686%**	**78%**	**13%**	**32%**	**69%**	**80%**	**12%**	**44%**
Propagation from tracklet v_2	7,97%	11,58%	7,97%	11,58%	7,97%	11,58%	7,97%	11,58%	7,97%	11,58%	7,97%	11,58%
Full Syst. Uncorrelated (Percentage)	**79%**	**74%**	**19%**	**42%**	**686%**	**78%**	**15%**	**34%**	**69%**	**81%**	**15%**	**46%**
Full Syst. Uncorrelated	**0,0081**	**0,0065**	**0,0036**	**0,0034**	**0,0106**	**0,0083**	**0,0067**	**0,0061**	**0,0156**	**0,0138**	**0,0201**	**0,0232**
PYTHIA tracklet v_2 (sensitivity limit)	0,0544	0,0653	0,0544	0,0653	0,0544	0,0653	0,0544	0,0653	0,0544	0,0653	0,0544	0,0653

Table 6.5: Table of absolute systematic uncertainties for the measurement of $v_{2,J/\psi}$ as a function of transverse momentum using SPDTracklets. A bar chart of these uncertainties can be found in Figure E.20.

SPDClusters	0-2 GeV/c		2-3 GeV/c		3-4 GeV/c		4-6 GeV/c		6-8 GeV/c		8-12 GeV/c	
Source	Yield sub.	Template fit	Yield sub.	Template fit	Yield sub.	Template fit	Yield sub.	Template fit	Yield sub.	Template fit	Yield sub.	Template fit
Default v_2 value	**-0,00726209**	**-0,00661702**	**0,0158289**	**0,00673282**	**0,011473**	**-0,000635283**	**0,0347869**	**0,00748165**	**0,0348071**	**-0,00775309**	**0,136301**	**0,0530079**
Statistical unc.	0,00544949	0,00435074	0,00650557	0,00562463	0,00741776	0,00697922	0,00679115	0,00686317	0,0107516	0,011278	0,0149132	0,0184729
z_{vtx} cut	0,0009	0,0010	0,0027	0,0027	0,0049	0,0033	0,0042	0,0064	0,0034	0,0009	0,0114	0,0085
$\Delta\eta_{min}$	0,0018	0,0016	0,0033	0,0034	0,0046	0,0031	0,0033	0,0061	0,0056	0,0006	0,0113	0,0072
$\Delta\eta_{max}$	0,0013	0,0012	0,0031	0,0032	0,0056	0,0042	0,0036	0,0058	0,0044	0,0005	0,0118	0,0089
ME normalization	0,0000	0,0000	0,0000	0,0000	0,0000	0,0000	0,0000	0,0000	0,0000	0,0000	0,0000	0,0000
Summation method	0,0009	0,0009	0,0027	0,0028	0,0056	0,0041	0,0033	0,0058	0,0044	0,0005	0,0106	0,0081
Pooling with mass	0,0042	0,0035	0,0075	0,0078	0,0103	0,0075	0,0079	0,0125	0,0271	0,0170	0,0436	0,0472
Pooling with ϕ	0,0038	0,0033	0,0062	0,0065	0,0117	0,0085	0,0079	0,0130	0,0141	0,0048	0,0284	0,0225
Pooling with centrality	0,0017	0,0016	0,0032	0,0032	0,0058	0,0041	0,0034	0,0060	0,0047	0,0010	0,0101	0,0065
Invariant mass fit	0,0002	0,0001	0,0003	0,0002	0,0005	0,0004	0,0006	0,0003	0,0021	0,0011	0,0017	0,0017
Background V_2 shape	0,0013	0,0010	0,0009	0,0005	0,0015	0,0015	0,0013	0,0011	0,0012	0,0015	0,0037	0,0019
Range V_2 fit	0,0028	0,0022	0,0013	0,0008	0,0006	0,0001	0,0049	0,0047	0,0004	0,0005	0,0026	0,0012
Extraction method	0,0043	0,0018	0,0031	0,0015	0,0081	0,0060	0,0060	0,0037	0,0058	0,0018	0,0034	0,0002
Centrality choice	0,0013	0,0013	0,0031	0,0027	0,0039	0,0029	0,0029	0,0052	0,0070	0,0035	0,0180	0,0122
Syst. Uncorrelated	**0,0084**	**0,0065**	**0,0127**	**0,0127**	**0,0216**	**0,0157**	**0,0161**	**0,0239**	**0,0336**	**0,0182**	**0,0606**	**0,0566**
Syst. Uncorrelated (Percentage)	**116%**	**99%**	**80%**	**188%**	**189%**	**2473%**	**46%**	**320%**	**96%**	**235%**	**44%**	**107%**
Propagation from tracklet v_2	5,58%	10,72%	5,58%	10,72%	5,58%	10,72%	5,58%	10,72%	5,58%	10,72%	5,58%	10,72%
Full Syst. Uncorrelated (Percentage)	**116%**	**99%**	**80%**	**188%**	**189%**	**2473%**	**47%**	**320%**	**97%**	**235%**	**45%**	**107%**
Full Syst. Uncorrelated	**0,0085**	**0,0066**	**0,0127**	**0,0127**	**0,0216**	**0,0157**	**0,0162**	**0,0239**	**0,0336**	**0,0183**	**0,0611**	**0,0569**
PYTHIA tracklet v_2 (sensitivity limit)	0,0502	0,0535	0,0502	0,0535	0,0502	0,0535	0,0502	0,0535	0,0502	0,0535	0,0502	0,0535

Table 6.6: Table of absolute systematic uncertainties for the measurement of $v_{2,J/\psi}$ as a function of transverse momentum using SPDClusters. A bar chart of these uncertainties can be found in Figure E.21.

Discussion on the behaviour of J/ψ flow with transverse momentum

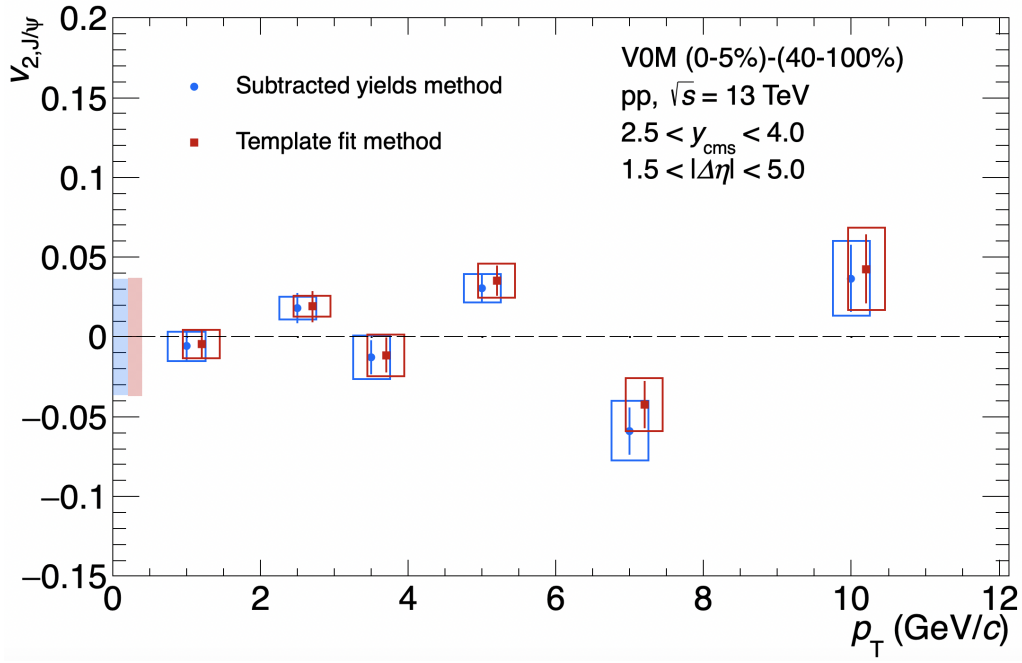

Figure 6.11: $v_{2,J/\psi}$ as a function of p_{T} in pp collisions at $\sqrt{s} = 13$ TeV, using V0M estimator. The uncorrelated systematics including the ones propagated from the tracklet v_2 measurement are represented by the empty boxes. The PYTHIA systematic uncertainty, seen as a limit on the sensitivity of the measurement, is represented as a filled box centered around zero.

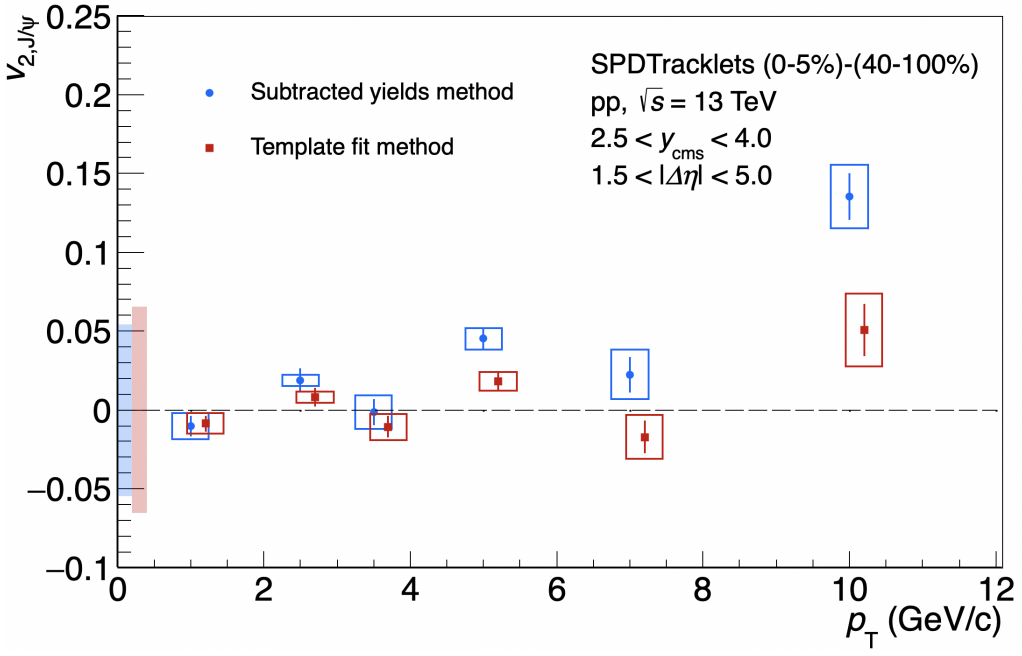

Figure 6.12: $v_{2,J/\psi}$ as a function of p_{T} in pp collisions at $\sqrt{s} = 13$ TeV, using SPDTracklets estimator. The uncorrelated systematics including the ones propagated from the tracklet v_2 measurement are represented by the empty boxes. The PYTHIA systematic uncertainty, seen as a limit on the sensitivity of the measurement, is represented as a filled box centered around zero.

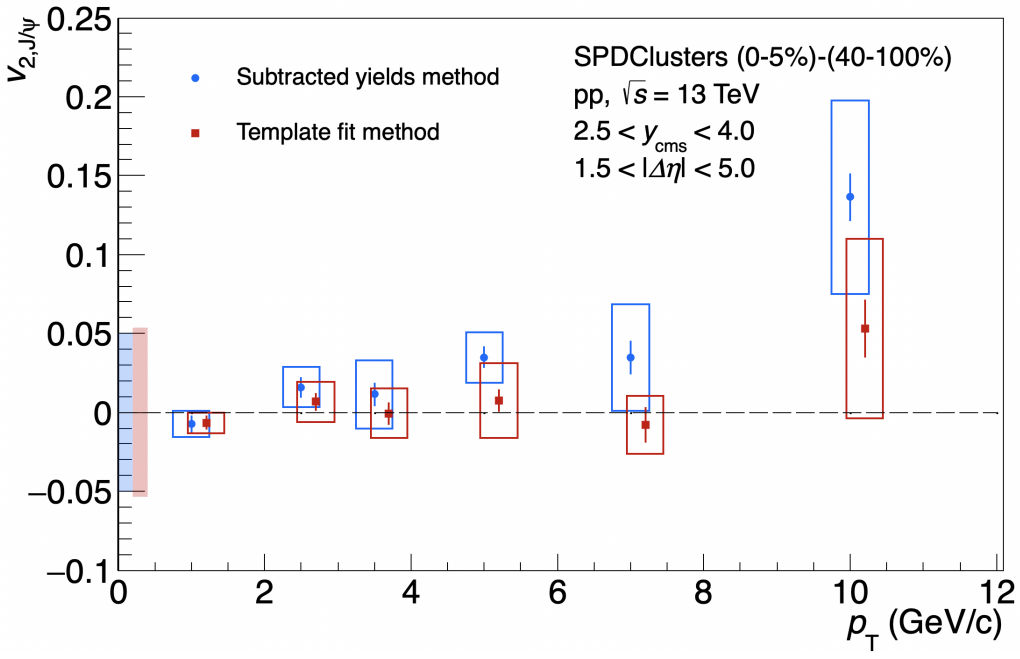

Figure 6.13: $v_{2,J/\psi}$ as a function of p_{T} in pp collisions at $\sqrt{s} = 13$ TeV, using SPDClusters estimator. The uncorrelated systematics including the ones propagated from the tracklet v_2 measurement are represented by the empty boxes. The PYTHIA systematic uncertainty, seen as a limit on the sensitivity of the measurement, is represented as a filled box centered around zero.

The result obtained using V0M shows an oscillation of $v_{2,J/\psi}$ around zero, with values compatible with zero within uncertainties (even more so considering all datapoints are within the sensitivity limit deduced from PYTHIA measurements - or close by), regardless of the extraction method. Compatible results are found for SPD-based estimators using the template fit method, which confirms the robustness of the template fitting procedure in extracting flow regardless of the centrality definition, as was hinted by the PYTHIA check. However, the yield subtraction method that was used by the ALICE Collaboration in the p–Pb J/ψ elliptic flow study [102] measures a larger flow with SPD-based estimators, especially at high-p_{T}, which may be an indication that non-flow is not fully suppressed, even more so than what was already evidenced by the PYTHIA check for tracklet flow.

The interpretation of these results is that J/ψ does not flow in pp collisions, or barely, within uncertainties and limits. This behaviour was to be expected from a final state effects point of view because it is not expected that a fireball could be produced in pp, so no heavy-flavour flow development is expected. If any, it should be in all cases lower than what is predicted in p–Pb [203].

The CMS collaboration, by studying the production of prompt and non-prompt D^0 meson [198], corroborated the possibility for charm to develop flow in pp to the level or less than light flavours. The result from this analysis agrees with this interpretation. In the coalescence picture, the flow of prompt J/ψ would be twice as much as the flow of individual charm quarks. If the prompt J/ψ flow were close to the inclusive case, our results would indicate that charm quark flow could be compatible with null or low values within uncertainties.

By integrating over the p_{T} range of 1 to 12 GeV/c, one can evaluate the compatibility of inclusive J/ψ v_2 with zero. The results and systematic uncertainties study are shown in Table 6.7 for V0M (left) and SPDTracklets (right).

For V0M, yield subtraction method gives: $v_{2,J/\psi} = 0.0215 \pm 0.0046_{(stat.)} \pm 0.0101_{(syst.)} \pm 0.0363_{(sensitivity.)}$ which is a 0.6σ deviation from 0, while template fit method gives: $v_{2,J/\psi} = 0.0171 \pm 0.0051(stat.) \pm 0.0076(syst.) \pm 0.0373_{(sensitivity.)}$ which is a 0.5σ deviation from 0.

For SPDTracklets, yield subtraction method gives: $v_{2,J/\psi} = 0.0286 \pm 0.0036_{(stat.)} \pm 0.0060_{(syst.)} \pm 0.0544_{(sensitivity.)}$ which is a 0.5σ deviation from 0, while template fit method gives: $v_{2,J/\psi} = 0.0086 \pm 0.0033(stat.) \pm 0.0047(syst.) \pm 0.0653_{(sensitivity.)}$ which is a 0.1σ deviation from 0. For all centrality estimators and non-flow suppression methods, we measure a large compatibility with 0 and with small

V0M	1-12 GeV/c		SPDTracklets	1-12 GeV/c	
Source	Yield sub.	Template fit	Source	Yield sub.	Template fit
Default v_2 value	**0,02152**	**0,01713**	Default v_2 value	**0,02861**	**0,00864**
Statistical unc.	0,00462	0,00509	Statistical unc.	0,00355	0,00331
z_{vtx} cut	0,0004	0,0003	z_{vtx} cut	0,0003	0,0002
η_{min}	0,0003	0,0003	η_{min}	0,0003	0,0001
$\Delta\eta_{max}$	0,0005	0,0004	$\Delta\eta_{max}$	0,0005	0,0001
ME normalization	0,0000	0,0000	ME normalization	0,0000	0,0000
Summation method	0,0014	0,0012	Summation method	0,0009	0,0005
Pooling with mass	0,0014	0,0014	Pooling with mass	0,0002	0,0002
Pooling with ϕ	0,0005	0,0005	Pooling with ϕ	0,0001	0,0002
Pooling with centrality	0,0005	0,0006	Pooling with centrality	0,0001	0,0001
Invariant mass fit	0,0005	0,0003	Invariant mass fit	0,0004	0,0001
Background V_2 shape	0,0011	0,0012	Background V_2 shape	0,0010	0,0010
Range V_2 fit	0,0032	0,0040	Range V_2 fit	0,0021	0,0023
Extraction method	0,0079	0,0030	Extraction method	0,0035	0,0030
Centrality choice	0,0046	0,0051	Centrality choice	0,0034	0,0023
Syst. Uncorrelated	**0,0100**	**0,0076**	**Syst. Uncorrelated**	**0,0056**	**0,0046**
Syst. Uncorrelated (Percentage)	**47%**	**44%**	**Syst. Uncorrelated (Percentage)**	**19%**	**53%**
Propagation from tracklet v_2	5,94%	2,70%	Propagation from tracklet v_2	7,97%	11,58%
Full Syst. Uncorrelated (Percentage)	**47%**	**44%**	**Full Syst. Uncorrelated (Percentage)**	**21%**	**55%**
Full Syst. Uncorrelated	**0,0101**	**0,0076**	**Full Syst. Uncorrelated**	**0,0060**	**0,0047**
PYTHIA tracklet v_2 (sensitivity limit)	0,0363	0,0373	PYTHIA tracklet v_2 (sensitivity limit)	0,0544	0,0653
Deviation (sigma)	**0,57**	**0,45**	**Deviation (sigma)**	**0,52**	**0,13**

Table 6.7: Table of absolute systematic uncertainties for the measurement of $v_{2,J/\psi}$ for a transverse momentum integrated between 1 and 12 GeV/c using V0M (left) or SPDTracklets (right).

values in general.

One can compare the pp result with existing ALICE analyses on $v_{2,J/\psi}$ in larger collision systems (p–Pb, Pb–p and Pb–Pb) [102, 100], shown in Figure 6.14. The flow in pp seems lower than in larger systems, although the significance of such comparison must be assessed. One way to better evaluate system size-dependent effects is by comparing the effects of systems' responses to initial anisotropies on the J/ψ. As was previously mentioned in Chapter 2, there is a linear relationship between the initial anisotropy ϵ_2 of the medium and the elliptic flow v_2: $v_{2,tracklets} = \kappa_{2,tracklets}\epsilon_2$ and $v_{2,J/\psi} = \kappa_{2,J/\psi}\epsilon_2$. By dividing the J/ψ flow by the tracklet flow, one has access to $\frac{\kappa_{2,J/\psi}}{\kappa_{2,tracklets}}$ which quantifies for each system how the flow development compares for the J/ψ and the tracklets. This observable is shown in Figure 6.15 for pp, p–Pb, Pb–p and Pb–Pb collisions.

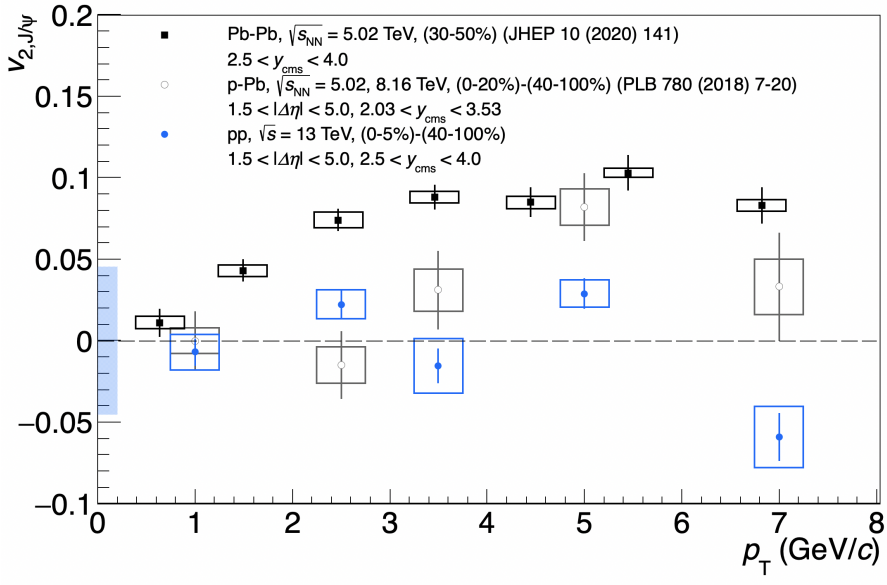

Figure 6.14: $v_{2,J/\psi}$ as a function of p_{T} for different system sizes.

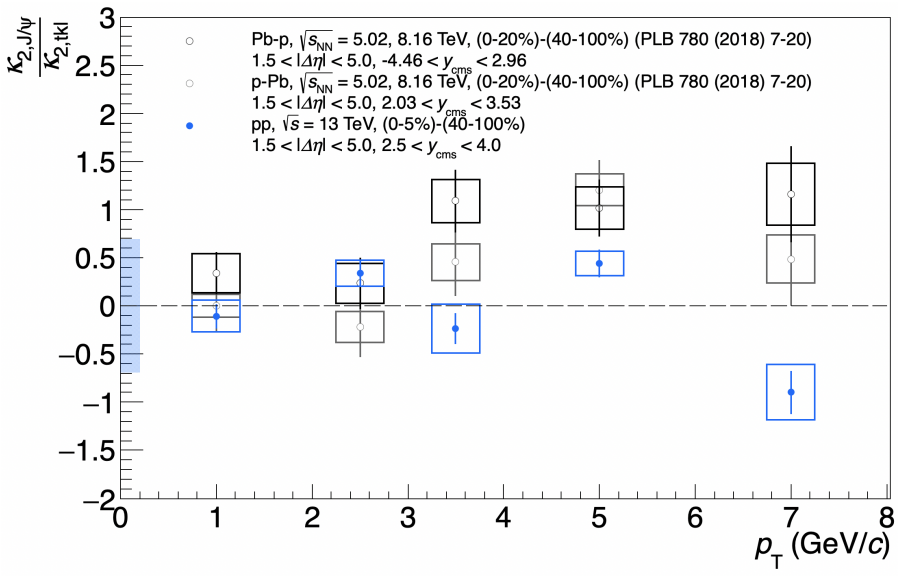

Figure 6.15: $v_{2,J/\psi}/v_{2,tracklet} = \kappa_{2,J/\psi}/\kappa_{2,tracklet}$ as a function of p_T for different system sizes.

In Figure 6.14, we see that the J/ψ seems to exhibit less flow in pp than in larger systems over the whole p_T range. Even more so considering that the data points represent the case where all non-flow was correctly subtracted. The PYTHIA uncertainty (represented by a filled box around zero) should bring the pp data points closer to zero which would reinforce our observations. The same can be said from Figure 6.15, where the $\kappa_{2,J/\psi}/\kappa_{2,tracklet}$ ratio is lower than unity and lower than in p–Pb and Pb–p systems, which indicates that J/ψ develops less flow than light particles, even more so in pp collisions than in p–Pb and Pb–p collisions.

One can assess the χ^2 between the different data points and compute the resulting significance between the different systems. The results for larger systems having been computed for $\Delta\Phi$ cuts of 5 mrad on the tracklets, the pp values used for the comparison have been computed too for a 5 mrad cut instead of the default 10 mrad. The systematic uncertainties have been scaled based on the change in v_2 so that they keep the same relative importance. Using the results from 6.15, over the studied p_T range, there is a 1.5σ difference between pp and p-Pb, and a 2.4σ difference between pp and Pb-p, and so a 2.4σ difference for pp versus the average of p-Pb and Pb-p. This is a notable deviation but not highly significant.

Also, apart from showing that results from different systems are different, such σ-deviations do not clearly state if J/ψ exhibits less flow in pp. In order to study this point, we must restrict the range from 3 to 6 GeV/c. This is the range in which flow was observed in p–Pb and Pb–p systems [102] so this is where we can say if pp collisions generate less flow than p–Pb and Pb–p systems or not. On this restricted range, we measure a 1.8σ difference between pp and p–Pb, and a 2.3σ difference between pp and Pb–p, and so a 2.5σ difference for pp versus the average of p–Pb and Pb–p. As a conclusion, inclusive J/ψ in pp collisions show less flow than in medium systems within at least 2.5σ.

We can also compare these results to existing ones from CMS on charged hadrons [135] and prompt D^0 hadrons [198], as shown in Figure 6.16. Because the extraction method, kinematic cuts and centrality classes are different between our analysis and CMS results, no definite conclusion can be confidently drawn. However, some hints of a mass hierarchy (and so flavour hierarchy too) can be seen between the three datasets, especially between 2 and 4 GeV/c where charged hadrons flow the most. In this range, light particles exhibit more flow than open-charm which in turn exhibits more flow than charmonium if we consider that it does develop a small amount of flow (which is possible within uncertainty). This would further confirm the existing mass-ordering at low-p_T in pp (see Chapter 2).

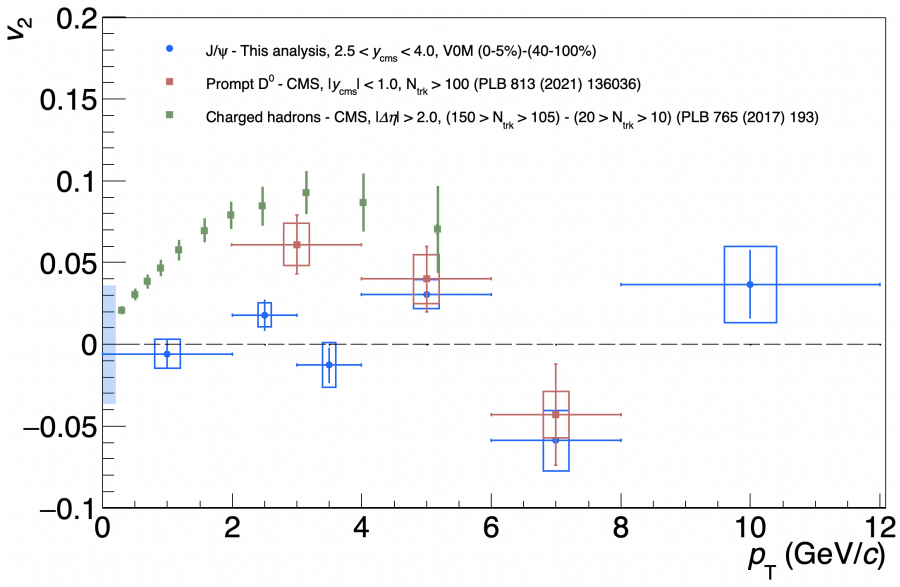

Figure 6.16: $v_{2,J/\psi}$ as a function of p_{T} for different particle species in pp collisions. In blue, J/ψ from this analysis. In red, prompt D^0 hadrons from Ref. [198]. In green, charged hadrons from Ref. [135].

6.2.2 Behaviour with centrality

Like for the tracklet flow, we can evaluate $v_{2,J/\psi}$ for different central classes to assess the behaviour of the elliptic flow with centrality.

Systematic uncertainties evaluation

Using the usual procedure, Tables 6.8 and 6.9 show the systematic uncertainties evaluation on $v_{2,J/\psi}$ as a function of centrality for V0M and SPDTracklets, respectively.

Discussion

In general, we see that the systematic uncertainties keep the same hierarchy regardless of centrality, except in some cases where the event mixing pooling can become dominant without any apparent reason. Again, the sources associated to the flow extraction procedure (choosing the V_2 parametrization and extraction method) cause the most effects, compared to cuts and selection criteria for example. Overall, there is a balance between the results of yield subtraction and template fit methods for every source.

From these tables we can plot the behaviour of the J/ψ v_2 as a function of centrality for V0M and SPDTracklets depending on the extraction method chosen, shown in Figure 6.17. In both cases, in an effort to mitigate the randomness of the pooling systematic uncertainty increases, the values have been smoothed from one centrality bin to another. This was done by averaging the value of the pooling uncertainty in a bin with its two neighbouring bins. In the case of the first and last bins the average was weighted (2/3 for the first or last bin, 1/3 for its neighbour).

V0M	0-1%		1-3%		3-5%		5-10%		10-15%		15-20%		20-30%	
Source	Yield sub.	Template fit	Yield sub.	Template fit	Yield sub.	Template fit	Yield sub.	Template fit	Yield sub.	Template fit	Yield sub.	Template fit	Yield sub.	Template fit
Default v_2 value	**0,01596**	**0,01143**	**0,01253**	**0,00467**	**0,04085**	**0,04030**	**0,02387**	**0,01954**	**0,01582**	**0,01001**	**0,03770**	**0,03448**	**0,00523**	**-0,00803**
Statistical unc.	0,00780	0,00829	0,00700	0,00783	0,00824	0,00875	0,00655	0,00746	0,00801	0,00946	0,00937	0,01174	0,00961	0,01320
z_{vtx} cut	0,0006	0,0005	0,0001	0,0001	0,0016	0,0016	0,0013	0,0010	0,0009	0,0010	0,0022	0,0030	0,0008	0,0011
$\Delta\eta_{min}$	0,0014	0,0016	0,0003	0,0005	0,0004	0,0003	0,0005	0,0003	0,0002	0,0004	0,0006	0,0011	0,0026	0,0035
$\Delta\eta_{max}$	0,0015	0,0015	0,0011	0,0013	0,0011	0,0011	0,0012	0,0011	0,0008	0,0012	0,0004	0,0001	0,0020	0,0022
ME normalization	0,0000	0,0000	0,0000	0,0000	0,0000	0,0000	0,0000	0,0000	0,0000	0,0000	0,0000	0,0000	0,0000	0,0000
Summation method	0,0011	0,0009	0,0021	0,0019	0,0011	0,0009	0,0004	0,0004	0,0005	0,0002	0,0006	0,0003	0,0011	0,0006
Pooling with mass	0,0012	0,0015	0,0000	0,0003	0,0062	0,0064	0,0013	0,0016	0,0017	0,0019	0,0004	0,0001	0,0009	0,0021
Pooling with ϕ	0,0003	0,0003	0,0001	0,0002	0,0012	0,0013	0,0002	0,0003	0,0002	0,0002	0,0013	0,0015	0,0009	0,0009
Pooling with centrality	0,0036	0,0061	0,0073	0,0123	0,0205	0,0234	0,0028	0,0028	0,0059	0,0063	0,0157	0,0189	0,0195	0,0240
Invariant mass fit	0,0008	0,0005	0,0005	0,0003	0,0003	0,0005	0,0004	0,0001	0,0005	0,0003	0,0003	0,0003	0,0006	0,0005
Background V_2 shape	0,0017	0,0017	0,0017	0,0019	0,0010	0,0007	0,0010	0,0009	0,0025	0,0028	0,0013	0,0014	0,15%	0,23%
Range V_2 fit	0,0054	0,0063	0,0033	0,0043	0,0002	0,0007	0,0017	0,0020	0,0023	0,0024	0,0012	0,0017	0,0017	0,0019
Extraction method	0,0103	0,0052	0,0085	0,0035	0,0068	0,0035	0,0087	0,0041	0,0095	0,0056	0,0096	0,0069	0,0084	0,0040
Syst. Uncorrelated	**0,0126**	**0,0108**	**0,0121**	**0,0138**	**0,0226**	**0,0247**	**0,0096**	**0,0059**	**0,0119**	**0,0095**	**0,0187**	**0,0205**	**0,0217**	**0,0250**
Syst. Uncorrelated (Percentage)	**79%**	**94%**	**96%**	**296%**	**55%**	**61%**	**40%**	**30%**	**75%**	**95%**	**50%**	**60%**	**415%**	**311%**
Propagation from tracklet v_2	3,94%	1,27%	4,53%	1,20%	5,02%	2,03%	5,92%	3,02%	6,24%	3,25%	5,18%	1,69%	7,00%	2,55%
Full Syst. Uncorrelated (Percentage)	**79%**	**94%**	**96%**	**296%**	**56%**	**61%**	**41%**	**30%**	**75%**	**95%**	**50%**	**60%**	**415%**	**311%**
Full Syst. Uncorrelated	**0,0127**	**0,0108**	**0,0121**	**0,0138**	**0,0227**	**0,0247**	**0,0097**	**0,0060**	**0,0119**	**0,0095**	**0,0188**	**0,0205**	**0,0217**	**0,0250**
PYTHIA tracklet v_2 (sensitivity limit)	0,0333	0,0323	0,0364	0,0378	0,0384	0,0406	0,0392	0,0409	0,0409	0,0456	0,0427	0,0510	0,0435	0,0563

Table 6.8: Table of absolute systematic uncertainties for the measurement of $v_{2,J/\psi}$ as a function of centrality using V0M. A bar chart of these uncertainties can be found in Figure E.22

SPDTracklets	0-1%		1-3%		3-5%		5-10%		10-15%		15-20%		20-30%	
Source	Yield sub.	Template fit	Yield sub.	Template fit	Yield sub.	Template fit	Yield sub.	Template fit	Yield sub.	Template fit	Yield sub.	Template fit	Yield sub.	Template fit
Default v_2 value	**0,02236**	**0,00425**	**0,03450**	**0,01300**	**0,02851**	**0,00767**	**0,04882**	**0,02202**	**0,02843**	**0,00406**	**0,03669**	**0,00806**	**0,03467**	**0,00398**
Statistical unc.	0,00594	0,00515	0,00554	0,00479	0,00658	0,00560	0,00513	0,00487	0,00628	0,00580	0,00762	0,00746	0,00716	0,00793
z_{vtx} cut	0,0005	0,0005	0,0005	0,0004	0,0006	0,0004	0,0008	0,0008	0,0008	0,0006	0,0008	0,0007	0,0009	0,0009
$\Delta\eta_{min}$	0,0004	0,0001	0,0004	0,0002	0,0008	0,0002	0,0014	0,0006	0,0004	0,0003	0,0010	0,0000	0,0014	0,0006
$\Delta\eta_{max}$	0,0005	0,0003	0,0002	0,0005	0,0010	0,0003	0,0014	0,0005	0,0009	0,0001	0,0009	0,0002	0,0016	0,0006
ME normalization	0,0000	0,0000	0,0000	0,0000	0,0000	0,0000	0,0000	0,0000	0,0000	0,0000	0,0000	0,0000	0,0000	0,0000
Summation method	0,0012	0,0006	0,0005	0,0002	0,0010	0,0006	0,0008	0,0004	0,0003	0,0005	0,0004	0,0003	0,0010	0,0005
Pooling with mass	0,0007	0,0006	0,0010	0,0008	0,0001	0,0001	0,0008	0,0007	0,0002	0,0003	0,0021	0,0017	0,15%	0,15%
Pooling with ϕ	0,0001	0,0000	0,0005	0,0005	0,0003	0,0002	0,0003	0,0003	0,0005	0,0004	0,0001	0,0002	0,0002194	0,00012015
Pooling with centrality	0,0091	0,0298	0,0001	0,0007	0,0065	0,0042	0,0138	0,0108	0,0070	0,0062	0,0002	0,0016	0,0027	0,0047
Invariant mass fit	0,0006	0,0003	0,0003	0,0001	0,0003	0,0001	0,0002	0,0003	0,0005	0,0002	0,0003	0,0001	0,0003	0,0001
Background V_2 shape	0,0018	0,0015	0,0016	0,0016	0,0017	0,0011	0,0003	0,0000	0,0024	0,0022	0,0009	0,0012	0,12%	0,07%
Range V_2 fit	0,0045	0,0041	0,0007	0,0012	0,0009	0,0014	0,0003	0,0006	0,0020	0,0020	0,0020	0,0025	0,0020	0,0015
Extraction method	0,0052	0,0066	0,0030	0,0026	0,0027	0,0005	0,0019	0,0018	0,0027	0,0012	0,0022	0,0018	0,0021	0,0021
Syst. Uncorrelated	**0,0117**	**0,0308**	**0,0037**	**0,0035**	**0,0074**	**0,0046**	**0,0141**	**0,0111**	**0,0082**	**0,0070**	**0,0041**	**0,0041**	**0,0051**	**0,0058**
Syst. Uncorrelated (Percentage)	**52%**	**725%**	**11%**	**27%**	**26%**	**60%**	**29%**	**50%**	**29%**	**173%**	**11%**	**51%**	**15%**	**145%**
Propagation from tracklet v_2	6,90%	8,76%	7,23%	9,84%	7,71%	10,81%	7,65%	12,29%	7,76%	13,91%	9,00%	15,45%	8,14%	15,85%
Full Syst. Uncorrelated (Percentage)	**53%**	**725%**	**13%**	**29%**	**27%**	**61%**	**30%**	**52%**	**30%**	**174%**	**14%**	**53%**	**17%**	**146%**
Full Syst. Uncorrelated	**0,0118**	**0,0308**	**0,0045**	**0,0038**	**0,0078**	**0,0047**	**0,0146**	**0,0114**	**0,0085**	**0,0070**	**0,0053**	**0,0043**	**0,0059**	**0,0058**
PYTHIA tracklet v_2 (sensitivity limit)	0,0539	0,0628	0,0548	0,0656	0,0544	0,0671	0,0555	0,0718	0,0597	0,0834	0,0616	0,0929	0,0656	0,1117

Table 6.9: Table of absolute systematic uncertainties for the measurement of $v_{2,J/\psi}$ as a function of centrality using SPDTracklets. A bar chart of these uncertainties can be found in Figure E.23

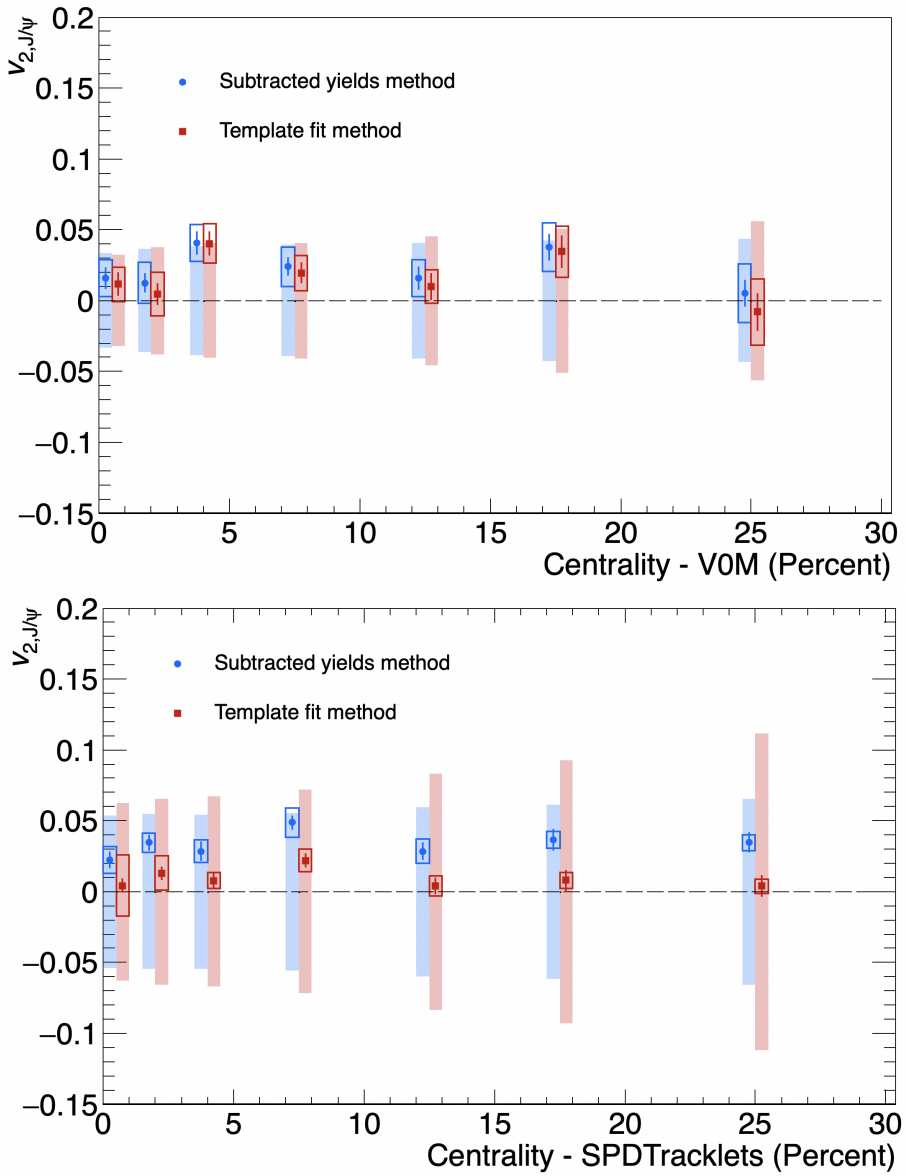

Figure 6.17: $v_{2,J/\psi}$ as a function of centrality estimated from (top) V0M (bottom) SPDTracklets, colours depend on the extraction method (Yield subtraction or Template fit). Data points are grouped around the middle point of the central class used. Uncorrelated systematics including the propagation of the ones from the tracklet v_2 measurement are represented using empty boxes. The PYTHIA systematic uncertainty, encoding the limit of the sensitivity of the measurement is represented as a filled box centered around zero.

In Figure 6.17, for both estimators and extraction methods, we observe no particular monotonous behaviour of the elliptic flow as a function of centrality. As was the case for the p_{T}-dependent results, for V0M, both yield subtraction and template fit give compatible results, which are compatible with a no/low flow scenario for the J/ψ. For SPDTracklets, template fit shows comparable results with V0M, but again, yield subtraction systematically measures a higher flow. In all cases, regardless of the centrality estimator or the extraction method, all results are compatible with zero as all are within the PYTHIA systematic uncertainty encoding the sensitivity limit of the measurements.

6.3 Light-flavour and heavy-flavour particle flow in pp collisions

Using the results produced by the V0M estimator which was used in previous similar analyses [102, 100], we measure a light particle elliptic flow of around 5 to 6%, although with large uncertainties. This result is compatible with previous studies which evidenced the flow of light particles in the smallest hadronic collision system in similar amplitudes.

Concerning inclusive J/ψ, the results as a function of p_{T} and centrality do not evidence any particular behaviour and elliptic flow values are compatible with a no flow or low flow scenario. This is what is expected from final state effect theories like the transport model which predict less flow as collision systems become smaller and less able to develop an expanding fireball [203]. Initial state predictions can on their side be extremely limited by the knowledge of quarkonium production mechanisms, which prevents theoretical predictions at intermediate and high p_{T} [249].

Comparing this analysis result on the J/ψ flow in pp to existing ones from CMS on the charged hadron and prompt D^0 flow (see Figure 6.16) we further hint at a possible mass-ordering of elliptic flow in pp, in the hypothesis where J/ψ does develop a low amount of flow. Consequently, heavy-flavour flow is lower than light-flavour flow.

From open-charm results [198], it appears that in pp collisions within the coalescence picture, charm could develop flow, which should be equal to or less than light flavours. This interpretation is not excluded by our results which, within uncertainty, tend to favour interpretations where charm quarks develop little to no flow.

6.4 Extraction methods and centrality estimators in flow analyses

What this analysis also highlights is the strong dependence of the results on the chosen non-flow subtraction method and the centrality estimator.

While inclusive J/ψ elliptic flow extraction using simple yield subtraction method seems to work rather well with V0M, it does not manage to be efficient with SPDTracklets. The inefficacy of this method becomes more obvious if we compare it to template fitting which shows a robustness, an equivalent efficiency, and compatible results between different centrality estimators.

Presumably, the inability of yield subtraction to work well with SPD-based estimators stems from biases in event selection and centrality classification created by the simultaneous use of tracklets from the SPD for both centrality estimation and physics correlations. The use of a mixed estimator using the information from both V0M and SPD to maximize the pseudorapidity coverage could potentially mitigate this effect. However, from the tracklet flow result, it seems that the mixed estimator results are mainly driven by V0M without being better.

This analysis is highly limited by the low number of candidates offered by charmonia. It prevents us from using more elaborate non-flow suppression methods like the "improved template fit" [137] which removes biases in the measurement of the flow as it assesses the residual flow in the peripheral class. Multi-particle cumulants (4-pairs, 6-pairs, etc.) would allow us to possibly suppress residual non-flow effects, but it would come at a cost, with much larger statistical uncertainties in the context of this analysis (more than 50% of relative uncertainty [127]).

Further LHC data taking would provide more candidates which would improve the results but mostly allow us to implement more sophisticated and robust non-flow suppression methods in small systems. The addition of the Muon Forward Tracker (MFT) would also allow us to distinguish prompt from non-prompt J/ψ. A measurement of the differentiated prompt and non-prompt J/ψ flow could allow the study of the flow of beauty and charm in small systems, in particular, prompt J/ψ would provide a pure charm measurement, which would strongly constrain the flow of individual charm quarks in pp collisions.

Conclusion

This thesis studied the elliptic flow of the J/ψ in pp collisions with ALICE. As is usual in small collision systems, the flow was studied using azimuthal correlations of J/ψ-hadron pairs. Over the transverse momentum and multiplicity ranges we studied, no significant J/ψ elliptic flow is observed. This measurement suffers from uncertainties driven by the extraction methods' inaccuracies in suppressing parasitic non-flow effects in small systems and the few number of heavy probes compared to light flavours. Nevertheless, we measure J/ψ elliptic flow coefficients significantly lower than in larger systems (Pb–Pb and p–Pb) and lower than lighter probes in pp, leading to hints of a mass-ordering (and flavour-ordering) of flow which is reminiscent of hydrodynamic observations in larger systems, assuming J/ψ does develop a small amount of flow in pp. No full theoretical explanations are available for this flow measurement in pp. However, flow is expected to be small from a transport model perspective, which is what we observe, while initial state predictions are too limited by our knowledge of quarkonium production mechanisms to be compared to our data.

During this analysis, we also noticed the importance of the centrality estimator. Multiple estimators were used, varying in acceptance. Estimators which are determining centrality in the same acceptance region as the particle correlations are particularly prone to non-flow effects and disagreements between extraction methods. The current interpretation is that the interplay between centrality determination and particle correlations within a similar acceptance region leads to biases which corrupt the description of non-flow and makes extraction methods less accurate. However, the template fit extraction method appears more robust, with results agreeing regardless of the centrality estimator. To avoid sensitivity to selection biases, this should be the favoured method in the future, as seems to be already the case for light flavours. More extensive sets of events acquired in Run 3 might also allow us to use the improved template fit, which will further improve the evaluation of non-flow and provide more accurate flow measurements. Moreover, adding the forward MFT will allow us to separate prompt from non-prompt J/ψ, providing a clean measurement of charm flow in pp. However, if issues still prevail concerning the accuracy of the non-flow suppression, new extraction methods might have to be devised.

On the detector side, the muon spectrometer was commissioned, and we implemented the Quality Control software to monitor the status of the muon spectrometer based on multiple physics observables. QC proved efficient in the commissioning itself, allowing us to study the detector noise and its mapping. It has also proven helpful since the start of Run 3 by providing live feedback on the occupancy and efficiency of the detectors. Invariant mass plots using the first Run 3 data have even shown the onset of a J/ψ peak. The software is continuously improved by adding new observables and more comprehensive layouts for shifters and experts.

The study of the clustering showed the importance of devising efficient algorithms to ensure accurate reconstruction in the muon spectrometer. This study led to the implementation of Monte Carlo simulations based on Test-Beam events, which manage to reproduce features of real events, like the various effects from the electronics (threshold and noise), and also the dependency of clustering resolution on pad size, position, charge, etc. Moreover, this study highlights a behaviour specific to the new readout electronic: an unexpected reduction of the charge spread. This effect is under investigation and will allow us to understand the electronics better. The Monte Carlo simulations, which we can improve further, may allow us to develop quicker and more accurate clustering algorithms, and will be used in future physics analyses, ultimately improving the accuracy of the muon physics analyses in ALICE.

Appendix A

Résumé en Français

Chapitre 1: Le plasma quarks-gluons, une introduction

La physique des particules permet d'étudier les composants fondamentaux de la matière et leurs interactions. Le Modèle Standard (voir Fig. 1.1) peut être vu comme un catalogue de ces particules qui forment la matière et portent les interactions fondamentales, ainsi que les équations qui régissent leur comportement. Néanmoins, le Modèle Standard, bien que prédictif, reste une théorie qui souffre de multiples limitations. Au sein de cette théorie, la QCD (chromodynamique quantique) décrit l'interaction forte qui permet la cohésion du noyau atomique. Les particules sensibles à l'interaction forte, les quarks et les gluons, portent une charge de couleur. Les gluons, médiateurs de l'interaction forte, portant une charge de couleur non nulle, la constante de couplage α_S de la QCD n'est pas constante. A faibles énergies, α_S est grande, à haute énergie, elle diminue. Ainsi, il existe en QCD un phénomène de confinement à basse énergie où les quarks sont confinés en hadrons neutres de couleur. Le déconfinement (appelé liberté asymptotique) ne se produit qu'à haute énergie.

Le plasma quarks-gluons (QGP) est un état de la matière déconfiné dans lequel les quarks et les gluons évoluent librement. C'est un état primordial de la matière qui constituait l'Univers quelques microsecondes après le Big Bang. Un moyen de reformer cet état de la matière est de réaliser des collisions d'ions lourds dans des accélérateurs de particules comme le LHC (Grand Collisionneur de Hadrons). Lorsque deux ions lourds entrent en collision, il peut se former du QGP qui va s'étendre suivant l'hydrodynamique et refroidir avant de se ré-hadroniser en repassant sous une température critique. Malheureusement, le QGP a une durée de vie très courte, de l'ordre de 10 fm$/c$. Il ne peut pas être directement observé et nous avons recours à de multiples sondes (différentes particules produites pendant la collision par exemple) qui peuvent être mesurées pour remonter aux propriétés du QGP.

Une de ces sondes est le quarkonium. C'est un état lié de deux quarks lourds $Q\bar{Q}$. Ses composants portant une charge de couleur, le quarkonium peut être influencé par le QGP qui est un milieu coloré. De plus, le quarkonium est composé de charges lourdes qui sont créées aux premiers instants de la collision et le temps de vie des quarkonia est suffisamment long pour qu'ils ne se désintègrent qu'après la disparition du QGP ce qui assure qu'ils sont sensibles à toute la vie du plasma quarks-gluons. Cette thèse se concentre sur le J/ψ qui est un charmonium, état lié d'un quark charmé et de son anti-quark. Le processus de formation des paires de quarks lourds peut être décrit par la QCD perturbative, puisqu'il s'agit d'un processus à haute énergie où la constante de couplage est faible. Par contre, le processus de formation d'un état lié n'est pas perturbatif, et différents modèles comme le modèle d'évaporation de couleur (CEM), le modèle de singlet de couleur (CSM) ou d'octet de couleur (CO) tentent de décrire ce processus. Quoiqu'il en soit, le quarkonia, une fois dans le QGP, peut voir ses propriétés modifiées par le milieu coloré. Le phénomène d'écrantage (analogue à celui des charges électriques) peut conduire, dans un milieu trop dense en charges colorées, à la fonte des états liés et donc à une diminution de la population des espèces de quarkonia qui est liée à la température du milieu. Différentes espèces de quarkonia ayant différentes énergies de liaison, leur fonte a lieu à différentes températures ce qui peut permettre de construire un thermomètre du QGP. Au contraire, les populations de quarkonia peuvent être augmentées grâce au phénomène de (re)génération, dans lequel des quarks lourds isolés, potentiellement venant de paires différentes, se rencontrent et se lient pour former un quarkonium. D'autres effets, nommés effets de la matière nucléaire froide, impactent également les propriétés des

quarkonia, bien qu'ils ne soient pas liés à la présence de QGP.

L'étude des quarkonia dans les collisions d'ions lourds repose sur la mesure de plusieurs de leurs propriétés. Par exemple, le facteur de modification nucléaire R_{AA} permet de mesurer la production relative de quarkonia en collisions d'ion lourds par rapport aux mesures faites en collisions proton-proton. Entre autres résultats, en comparant ce facteur pour ALICE et PHENIX où l'énergie est plus basse (5.02 TeV contre 0.2 TeV, au centre de masse) la régénération du J/ψ en collisions Pb–Pb a été observée.

Le flot elliptique est une observable liée aux effets collectifs. Lorsque deux ions lourds entrent en collision, la collision n'est pas parfaitement frontale. Il existe un paramètre d'impact non nul entre les deux noyaux qui fait que la région de collision est anisotrope. Elle a une forme d'amande. Or, si un QGP se forme, il cherche à s'étendre selon les lois de l'hydrodynamique et devenir une sphère. Pour passer de cette forme anisotrope d'amande à une forme de sphère, les particules du QGP subiront des forces de pressions anisotropes qui seront plus fortes dans le plan de la collision que dans le plan transverse. Cela entraine alors des anisotropies de quantité de mouvement entre les particules de l'état final. Le flot elliptique permet, à partir de la mesure de la distribution angulaire des particules de l'état final, de quantifier cette capacité du système à transformer cette anisotropie géométrique (la forme d'ellipse de l'amande) en anisotropie de quantité de mouvement. Dans les petits systèmes, où il y a peu de particules produites, le flot elliptique, noté v_2 est mesuré comme le coefficient du second ordre dans la décomposition de Fourier de la distribution azimutale des paires de particules, selon Eq. 2.7.

Comparer les résultats obtenus en mesurant ces observables à différents modèles tentant de prédire les modes de production et de destruction des quarkonia dans le QGP permet de discriminer entre ces théories et déterminer laquelle est la meilleure. Parmi les théories en jeu se trouvent, le modèle de transport, qui incorpore une dynamique permanente entre la suppression et la régénération des quarkonia dans le QGP; le modèle des comovers, qui ressemble au modèle de transport sauf que les interactions entre le milieu et les quarkonium sont décrites comme des interactions avec les particules qui entourent le quarkonia et se déplacent avec lui; le modèle d'hadronisation statistique qui suppose que toutes les particules fondent dans le QGP et ne sont formées qu'au freeze-out lorsque le QGP a assez refroidi. Les populations des différentes espèces sont alors calculées à partir de modèles de physique statistique.

Chapitre 2: Le flot anisotrope dans l'étude du QGP

Il existe différents types de flot. Le flot radial est le flot créé par les particules poussées uniformément loin du point d'interaction. Le flot longitudinal décrit le mouvement des particules le long du faisceau, et le flot anisotrope est généré par les non-uniformités dans le plan transverse. Pour mesurer le flot anisotrope, dont les coefficients sont notés v_n, plusieurs méthodes sont employées. Dans des collisions d'ions lourds, il y a assez de multiplicité, c'est-à-dire de particules produites, pour définir avec précision un plan de réaction et mesurer la distribution angulaire des particules de l'état final par rapport à ce plan. Dans les petits systèmes de collision, comme proton-proton, le faible nombre de particules produites pousse à constituer des paires de particules et à mesurer la distribution du $\Delta\phi$ de ces paires sur tous les évènements enregistrés. En toute rigueur, on mesure alors $v_n\{2\}$ qui est la rms de v_n. Des "paires" d'un plus grand nombre de particules peuvent être constituées, elles permettent notamment de supprimer certains effets parasites.

On pourrait alors croire qu'il suffit de mesurer des collisions, faire des paires de particules, mesurer la distribution azimutale $\Delta\phi$ de ces paires et calculer ses coefficients de Fourier. Le problème vient du fait que la distribution angulaire des particules n'est pas forcément liée aux effets collectifs. D'autres effets, appelés effets de non-flot peuvent changer la distribution. De plus, la contribution de ses effets varie comme l'inverse de la multiplicité. Ils prévalent donc en petits systèmes et doivent être identifiés et supprimés correctement. Quelques exemples de ces effets incluent les dijets qui sont une conséquence du confinement en QCD et sont des cônes collimatés dos-à-dos de particules. En associant des particules de cônes opposés on crée un surplus de corrélations en $\Delta\phi = \pi$ et en associant des particules du même cône, on crée un surplus en $\Delta\phi = 0$. Des corrélations de courte portée entre les bosons favorisent les corrélations à $\Delta\phi = 0$ et $\Delta\eta = 0$, où η est la pseudorapidité et décrit l'angle d'une particule par rapport au faisceau.

La suppression de la majeure partie des effets de non-flot comme les corrélations à courte portée passe par l'utilisation d'un gap en $\Delta\eta$ qui permet de supprimer toutes les paires dont la valeur en $\Delta\eta$ ne passe pas un seuil minimal. Reste alors la contribution résiduelle des dijets. Afin de la supprimer,

différentes collaborations du LHC ont utilisé différentes méthodes. ALICE considère que la contribution des dijets est indépendante de la multiplicité. Ainsi, en mesurant les distributions de paires pour des événements de haute et de basse multiplicité et en soustrayant ces deux distributions, on supprime les effets des dijets qui sont identiques dans les deux catégories d'événements. Ne restent alors que les effets collectifs (uniquements présents à haute multiplicité) qui sont alors mesurés. C'est la méthode de soustraction de yields. ATLAS considère que la contribution des dijets peut dépendre de la multiplicité. Donc, au lieu de soustraire une fois la distribution à basse multiplicité, on la soustrait F fois, avec F un paramètre libre de la procédure de fit. On mesure alors les effets collectifs dans la distribution soustraite. C'est la méthode dite de template fit.

Ces méthodes ont permis d'obtenir de multiples résultats sur le flot elliptique dans différents systèmes de collision. L'étude du flot elliptique a débuté dans les années 1990 en observant des collisions A–A. L'évolution du flot avec la centralité/multiplicité valide la description géométrique de l'origine du flot elliptique. L'évolution du flot avec le moment transverse des particules légères montre des comportements qui valident la description hydrodynamique du QGP (une hiérarchie de masse à bas p_T où, à p_T égal, une particule légère a un v_2 plus important), et l'idée d'une coalescence de quarks à partir d'un milieu déconfiné (à haut p_T où le flot des baryons est distinct de celui des mésons). Pour les saveurs lourdes, le flot du J/ψ a été mesuré comme étant positif sur la bande de p_T étudiée, les hadrons charmés ouverts montrent également du flot, les bottomonia par contre, non. Le modèle de transport est en très bon accord avec les résultats obtenus sur le J/ψ.

Plus récemment, les collisions de plus petits systèmes sont également étudiées. Cette initiative marque un changement dans la façon de concevoir les petits systèmes, qui n'étaient jusqu'alors que des références pour les collisions A–A créant du QGP. Ainsi, des études de collisions p–Au, d-Au, et He^3-Au à RHIC ont permis de mettre en évidence l'origine géométrique du flot. Les particules légères ont montré du flot elliptique dans les collisions p–A avec les mêmes hiérarchies de masse et de nombres de quarks qu'en collisions A–A, laissant supposer la formation d'un état déconfiné régi par l'hydrodynamique. Pour les saveurs lourdes en revanche, cette hiérarchie de masse n'est qu'approximative, après que différentes collaborations aient mesuré le flot du J/ψ, et du D^0 prompt (charme ouvert) et non-prompt (montrant de comportement de la beauté). De plus, le modèle de transport, reproduisant correctement les résultats du flot elliptique du J/ψ dans les collisions Pb–Pb ne parvient pas à reproduire ceux en p–Pb. Et aucune autre théorie ne le peut pour l'instant.

Dans les collisions proton-proton, du flot elliptique pour les particules légères a d'abord été identifié par CMS. ALICE a ensuite mesuré la dépendance en p_T de ce flot elliptique pour différentes espèces légères ce qui a mis à jour les mêmes hiérarchies que dans les systèmes plus larges, attribués à l'hydrodynamique et à un milieu déconfiné. Néanmoins, pour les saveurs lourdes, peu de résultats existent. En particulier, ATLAS a mesuré le flot elliptique de muons charmés ou de muons venant de la beauté, semblant indiquer que le charme était sensible aux effets collectifs mais pas la beauté. Mesurer le flot elliptique du J/ψ est alors une analyse cruciale puisqu'elle permettrait de déterminer si le charmonium flotte en collisions pp comme il le fait dans des systèmes plus grands. Aussi, cette analyse pourrait nous indiquer les origines du flot elliptique dans les systèmes plus grands, ce qui reste une question ouverte dans les collisions p–Pb.

Chapitre 3: Description de l'expérience ALICE

ALICE est une des quatre expériences principales du LHC, avec ATLAS, CMS et LHCb. Au CERN, à la frontière entre la France et la Suisse, un complexe d'accélérateurs accélère des particules et les injecte dans les annaux principaux du LHC (mesurant 27km de circonférence). Au niveau des expériences principales, les faisceaux (un allant dans le sens horaire et l'autre anti-horaire) peuvent entrer en collision.

Alors que des expériences comme CMS et ATLAS ont un spectre d'étude général, ALICE (A Large Ion Collider Experiment) se focalise sur l'étude du QGP. Pour cela elle est composée d'une multitude de sous-systèmes de détection, assemblés en une structure mesurant 16 mètres de haut, comme de large et 26 mètres de long. Les sous-systèmes sont séparés en deux catégories. Le "central barrel" à mi-rapidité autour du point d'interaction, et le spectromètre à muons vers l'avant.

Dans le central barrel, on retrouve des détecteurs comme l'ITS (Inner Tracking System) dont les deux couches internes forment le SPD (Silicon Pixel Detector) qui est formé de pixels en silicone permettant

une mesure des traces des particules produites à mi-rapidité avec un très faible budget matériel. Il est utilisé dans cette thèse pour identifier la position du point d'interaction ainsi que pour le comptage et la reconstruction des traces des particules légères (les tracklets). Dans le central barrel, on trouve également le V0 qui est placé de part et d'autre du SPD et est formé de scintillateurs qui permettent de mesurer l'énergie déposée par les particules produites vers l'avant et vers l'arrière. Il est utilisé pour le triggering des évènements ainsi que pour la détermination de la centralité, une quantité allant de 0% (central, la collision est frontale) à 100% (périphérique, les noyaux se recouvrent à peine) déterminée par un fit de la distribution d'énergie dans le V0.

Vers l'avant, le spectromètre à muons assure la reconstruction des traces des muons dans ses cinq stations de tracking. Un aimant permet la détermination du moment transverse des muons. Des absorbeurs protègent les chambres de tracking de particules parasites et des chambres de trigger (déclanchement) placées en aval permettent d'identifier les événements contenant au moins un muon.

Durant les trois dernières années, de 2018 à 2021, le LHC était arrêté et l'expérience ALICE a pu être améliorée. Les améliorations permettent à présent à ALICE durant le Run 3 d'enregistrer les événements en continu (au lieu de déclencher l'acquisition). Cela implique de repenser le software et d'adapter le hardware de l'expérience. Certains détecteurs ont alors aussi été améliorés, comme l'ITS dont chaque couche est à présent similaire aux couches du SPD, ou ajoutés, comme le MFT (Muon Forward Tracker) qui offre à présent des capacités de vertexing vers l'avant (ce qui permettra de séparer les contributions prompt et non-prompt des hadrons lourds produits vers l'avant). Concernant le spectromètre à muons, les systèmes de détections restent inchangés, seule l'électronique de front-end a été adaptée à la nouvelle acquisition.

Chapitre 4: Mise en service du spectromètre à muons

Comme présenté dans le chapitre précédent, le système de détection du spectromètre à muons reste inchangé entre le Run 2 et le Run 3. Néanmoins, l'électronique de front-end, qui sert à l'acquisition des données, a été améliorée. Cela peut avoir un impact sur les signaux laissés par les particules dans les chambres de tracking.

Les détecteurs du spectromètre à muons sont des MPWC (Multi-wire proportional chambers). Elles sont composées d'un volume de gaz enfermé entre deux cathodes segmentées en pads. Entre les cathodes se trouve un plan d'anodes sous forme de fils chargés à environ 1700V. Lorsqu'une particule chargée traverse le détecteur, elle ionise le gaz. Les électrons sont dirigés vers les anodes et les ions se déposent sur les pads des cathodes. Le dépôt de charges sur les pads suit une distribution de Mathieson-Gatti (qui ressemble à une loi gaussienne avec des queues de distribution plus larges). L'étendue de la distribution est régie par un paramètre: K_3. Il est déterminé par la géométrie du détecteur, et plus il est élevé, plus la distribution est étalée. La géométrie des slats de détecteurs impose alors un K_3 de 0.5. Une fois la charge déposée, chaque pad touché se voit associer un digit qui est une structure contenant la charge déposée, l'identifiant du pad, et le timestamp de l'impact. Les digits sont alors rassemblés par composantes connexes appelées preclusters qui s'étendent sur les deux cathodes. Les distributions de charge de chaque precluster est alors clusterisée, ce qui permet de déterminer la position de l'impact initial. Différentes méthodes de clustering sont étudiées, notamment les procédures consistant à fitter une distribution de charge théorique (en l'occurrence plutôt une distribution de Mathieson-Gatti) sur la distribution mesurée.

Cependant, la nouvelle électronique peut avoir un effet sur la distribution de charge mesurée à cause du bruit électronique, des seuils d'acquisition et d'autres processus de traitement du signal inhérents à l'électronique. Pour vérifier ces effets, des données ont été recueillies lors d'un Test Beam. Des particules chargées ont été envoyées sur des détecteurs équipés avec la nouvelle électronique, ainsi que sur un détecteur en silicone afin d'avoir une précision sur la position de l'impact à 10 µm près. Il faut alors, à partir de ces résultats, construire une simulation Monte Carlo qui reproduit le comportement de l'électronique et la reconstruction des impacts et détermination des positions des hits. L'intérêt est double. D'une part, on peut s'assurer que la précision sur la position des impacts est équivalente sinon meilleure que les 70 µm acquis durant le Run 2. D'autre part, cela permettra à la collaboration de posséder une simulation Monte Carlo du comportement des détecteurs du spectromètre qui pourra être utilisée dans les analyses futures et la détermination de l'efficacité des détecteurs.

Au cours des tests, il a été observé que la forme de la distribution théorique utilisée pour le clustering

a un immense impact sur la qualité de la reconstruction. Si les distributions théorique et expérimentale ne coïncident pas, la résolution est détériorée et des biais peuvent apparaître. Notamment, il a été observé dans les données Test Beam que les dépôts de charge seraient mieux décrits par une distribution de Mathieson-Gatti plus piquée avec $K_3 = 0.2$. Ce phénomène et lié à la nouvelle électronique et notre simulation devrait permettre de déterminer quel en est la cause précise. La simulation a alors été calibrée à partir des données Test Beam. D'une part, les charges des événements simulés suivent la même distribution de Landau, la géométrie du détecteur DE819 utilisé pour le Test Beam est reproduite, et la position des impacts suit la même distribution que celle du Test Beam. Concernant l'électronique, le bruit électronique est simulé par l'ajout d'un bruit gaussien de σ 1 ADC, les effets de seuils bas et hauts sur la charge de chaque pad est également simulée. Tous les paramètres possibles ont alors été calibrés à partir des mesures Test Beam.

Malgré cela, nous mesurons que l'étendue des dépôts de charge dans nos simulations est toujours trop large par rapport aux données Test Beam. Des analyses supplémentaires ont permis d'identifier que les données mesurées ne sont effectivement pas bien reproduites par une distribution de Mathieson à $K_3 = 0.5$ mais plutôt 0.2 et que ce paramètre semble dépendre de la charge déposée ce qui n'était pas inclus dans l'étude de Mathieson et Gatti. La raison de cet écart pourrait venir de la suppression de zéro, qui est un processus géré automatiquement par la nouvelle électronique, ce qui n'était pas le cas avant et dont l'impact doit être évalué par de futures études en laboratoire. Cependant, même si notre simulation ne parvient pas à reproduire cette réduction de l'étendue du dépôt de charge, simuler des évènements avec $K_3 = 0.2$ suffit à reproduire des résultats physiques obtenus à partir du Test Beam.

En particulier, nous avons également étudié l'évolution de la résolution (la précision de la détermination de la position des impacts) en fonction de plusieurs paramètres comme la largeur des pads, le bruit et les seuils de l'électronique, la position des impacts, et l'incertitude associée à la mesure de la charge de chaque pad. Des résultats cohérents avec la physique des détecteurs sont obtenus grâce à notre simulation, dont la résolution semble légèrement détériorée par rapport aux mesures Test Beam. Cependant, cette détérioration pourrait avoir comme origine l'incertitude associée à la mesure de la charge de chaque pad qui serait surestimée.

Maintenant que la nouvelle électronique a été caractérisée, il faut s'assurer du bon fonctionnement des détecteurs du spectromètre pendant la prise de données. Pour cela, un logiciel de contrôle qualité (QC) a été développé. Il permet d'observer les données acquises quel que soit leur état dans la chaine de traitement des données, depuis les données brutes des détecteurs jusqu'au traces de muon reconstruites. Périodiquement, le QC va analyser ces données, mesurer des observables définies en amont, et afficher l'état du détecteur selon si la valeur de l'observable est satisfaisante ou non pour un détecteur en fonctionnement normal. Les shifters et experts peuvent alors surveiller les histogrammes en sortie du QC qui décrivent le comportement et l'état de fonctionnement du spectromètre à muons et décider si le fonctionnement est normal ou nécessite une action.

Il existe plusieurs tâches de contrôle réalisées par le QC. Une tâche va utiliser les valeurs des piédestaux et le bruit mesuré sur chaque pad pour s'assurer que l'électronique est correctement connectée, que le mapping (qui encode la position géométrique de chaque pad) est correct, et qu'aucun pad n'est trop bruité ce qui perturberait la prise de données en inondant le flot des données d'acquisition. Une autre tâche se sert des digits reconstruits et mesure l'occupation de chaque pad ce qui permet d'identifier des zones mortes du détecteur par exemple. Une autre tâche va mesurer les erreurs d'acquisition relevée par l'électronique. Une autre se sert des préclusters pour déterminer la corrélation géométrique entre les deux cathodes d'un détecteur pour s'assurer que chacune voit correctement les impacts de particules. Chacune de ses tâches produit alors des histogrammes en sortie qui peuvent par exemple reproduire la géométrie du spectromètre afin de localiser des problèmes de fonctionnement.

En pratique, le QC a été utilisé lors de l'installation du spectromètre afin de s'assurer que le bruit et le mapping étaient conformes aux attentes. Typiquement, une source de bruit électronique venu de la commande de la ventilation de la caverne d'ALICE a été identifiée et corrigée. Pendant la prise de donnée du Run 3, le QC permet actuellement aux shifters de surveiller le bon fonctionnement du spectromètre et permet également de produire des premiers histogrammes de physique à partir des traces reconstruites.

Chapitre 5: Analyse du flot elliptique du J/ψ en collisions proton-proton à 13 TeV

Dans ce chapitre est présentée la toute première analyse du flot elliptique du J/ψ en collisions proton-proton. Les données Run 2 d'ALICE sont utilisées ce qui représente une luminosité totale de 24.38 ± 0.87 pb^{-1}. Deux types d'évènements sont traités. Les évènements Minimum Bias (qui requièrent une coïncidence de signaux dans les deux parties du V0), et les évènements CMUL qui sont des évènements Minimum Bias possédant une paire de muons de charge opposée avec un $p_T > 0.5$ GeV/c. Les évènements utilisés dans l'analyse doivent également passer une série de critères supplémentaires (suppression de pileup, reconstruction acceptable du point d'interaction, etc.) qui assure leur bonne qualité.

Dans cette analyse, la collectivité du J/ψ est évaluée en mesurant le flot des paires dimuon-tracklet et tracklet-tracklet, les tracklets étant reconstruites dans le SPD à mirapidité et les dimuons vers l'avant dans le spectromètre. Le flot elliptique de chaque type de paire est égal au produit des flots elliptiques de chaque composant de la paire. Ainsi, après avoir séparé les contributions du signal J/ψ des autres dimuons du background, on peut obtenir par factorisation le flot du J/ψ.

Afin de supprimer le non-flot, on l'a vu, il nous faut séparer les événements haute-multiplicité et basse-multiplicité. En collisions d'ions lourds il s'agit plutôt d'événements centraux et périphériques, respectivement. Cependant, la définition géométrique de la centralité ne fonctionne pas dans les collisions proton-proton. Un analogue, la multiplicité (nombre de particules produites lors de l'événement) est alors utilisée et les quantiles sont définis à partir de l'activité laissée dans différents détecteurs. Par exemple, dans cette thèse, la multiplicité a été estimée à partir de l'activité dans le V0 (V0M), du nombre de tracklets dans le SPD (SPDTracklets) ou encore par un mélange de ces deux informations, afin de voir si cet estimateur hybride serait plus robuste que les autres car ayant une meilleure couverture en pseudorapidité.

Une fois les classes de multiplicité définies, par défaut 0-5% pour des événements haute-multiplicité et 40-100% pour la basse-multiplicité, on peut alors mesurer les per-trigger yields: une quantité qui indique la distribution spatiale des tracklets autour d'un dimuon, obtenue à partir des comptes des $\Delta\phi$ et $\Delta\eta$ de chaque paire. Pour cela, chaque dimuon est appairé avec chaque tracklet de son événement. Aussi, pour évaluer les effets non-physiques des détecteurs, les dimuons sont appairés avec les tracklets d'autres événements similaires. Le rapport de ces deux distributions calculées sur la totalité des événements donne une distribution de yields idépendante des effets détecteurs.

Les dépendances en z_{vtx} et en $\Delta\eta$ sont ensuite supprimées par un jeu de projections et sommations. Deux étapes restent alors: extraire le J/ψ signal du background de dimuons, et soustraire les effets de non-flot. L'extraction du signal se fait en utilisant la forme de la masse invariante des dimuons afin d'extraire le template du signal et du background qui sont utilisés pour fitter les données de flot en fonction de la masse. La soustraction du non-flot se fait à partir des méthodes d'ALICE ou d'ATLAS comme présentées plus haut.

En répétant ce travail pour les paires tracklet-tracklet (rendu plus simple par l'absence de dépendances en masse ou en moment du dimuon par exemple), on obtient alors la valeur du flot du J/ψ que l'on recherche.

De nombreuses vérifications ont été faites pour s'assurer de la bonne implémentation de l'analyse. Elles concernent l'event mixing, la propagation d'erreurs, la factorisation des coefficients de flot, l'impact du trigger, l'accord entre l'analyse de la masse invariante vis-à-vis d'une analyse utilisant le même jeu de données. La plus importante de ces vérifications a permis de reproduire les résultats obtenus pour le flot elliptique du J/ψ dans les collisions p–Pb, ce qui assure que l'analyse est bien implémentée.

Cependant, cela ne nous assure pas que la procédure l'analyse (utilisée par ALICE en p–Pb) soit aussi valable en collisions pp, notamment parce que le non-flot est bien plus important en pp et qu'il faut s'assurer qu'il est complètement supprimé. Pour cela, nous avons mesuré les corrélations tracklet-tracklet dans des événements Monte Carlo générés par PYTHIA8. Dans PYTHIA8, le non-flot est simulé mais pas le vrai flot issu d'effets collectifs. Ainsi, on s'attend à mesurer un flot elliptique nul si tout le non-flot est correctement supprimé par notre procédure. Or, ce n'est pas le cas. On mesure un flot résiduel de 3 à 4% selon la méthode. Cette quantité est alors interprétée comme une limite sur la sensibilité de la mesure sur le flot du J/ψ. En d'autres termes, si le flot du J/ψ est inférieur à 4% nous ne pouvons pas savoir s'il y a effectivement du flot ou si la mesure vient du non-flot mal supprimé par la procédure d'analyse.

Ce chapitre présente également la méthode d'évaluation des incertitudes systématiques. Pour chaque source d'incertitude, des alternatives à la configuration par défaut de l'analyse sont implémentées. Par exemple, des coupures plus ou moins strictes, des méthodes d'analyse différentes, des classes de centralités ou des critères alternatifs. L'incertitude associée à chaque source est alors estimée comme la rms des valeurs obtenues par les analyses alternatives par rapport à l'analyse par défaut. Chaque incertitude est ensuite ajoutée de manière non-corrélée.

Chapitre 6: Résultats et analyse critique

Le flot des tracklets, nécessaire pour le calcul du flot du J/ψ a déjà été mesuré lors d'autres analyses. Quelle que soit la méthode de suppression de non-flot, en utilisant V0M comme estimateur de centralité, on obtient un flot de 6%, ce qui est attendu. Le facteur F du template fit d'ATLAS est proche de 1 ce qui explique le bon accord avec les méthodes de soustraction de yields (type ALICE). Cependant, en utilisant un estimateur de centralité basé sur le SPD, la méthode d'ATLAS montre un facteur F proche de 3, et donc un flot d'environ 10%.

Cet effet qui rend la mesure du template fit "non-physique" est à mon sens due au biais qu'il existe en utilisant le SPD à la fois comme estimateur de centralité et comme outil de mesure des tracklets pour les corrélations. Par exemple, les événements avec des jets produiront beaucoup d'activité dans le SPD donc seront rangés dans la catégorie haute-multiplicité. Ainsi, la description du non-flot entre événements haute et basse multiplicité est drastiquement différente, ce qui explique le besoin de soustraire presque 3 fois la distribution de yields basse multiplicité pour supprimer tout le non-flot. Cela n'étant pas possible avec la méthode de soustraction simple d'ALICE, on peut s'attendre à un surplus de non-flot dans la mesure finale.

L'utilisation d'un estimateur hybride ne rend pas les résultats meilleurs sur quelque plan que ce soit (incertitudes, biais). Les résultats qu'il permet d'obtenir sont proches des résultats obtenus avec le V0 seul.

La dépendance en centralité du flot des trackelts obtenue par l'estimateur V0M est compatible avec les comportements déjà observés par CMS et ATLAS. CMS, dont la méthode est proche d'ALICE mesure une baisse du flot à mesure que la multiplicité diminue, alors que ATLAS mesure un flot constant. Ces résultats sont reproduits (dans la limite des incertitudes dominées par la limite sur la sensibilité de la mesure estimée par PYTHIA8) par notre analyse. En revanche, il y a un net désaccord avec le résultat d'ATLAS en utilisant le SPD comme estimateur. C'est, a priori, une conséquence du biais de mesure discuté plus haut.

Enfin, à partir des corrélations dimuon-tracklet et des résultats sur le flot elliptique des particules légères, on peut obtenir le flot elliptique du J/ψ. En utilisant V0M comme estimateur de centralité, on n'observe aucune dépendance particulière du v_2 du J/ψ en fonction de p_T. Le flot est compatible avec zéro sur toute la plage de p_T de 0 à 12 GeV/c. La compatibilité est d'autant plus forte que la limite sur la sensibilité de la mesure est de 4%. On observe qu'avec V0M les résultats obtenus par la méthode de soustraction de yields d'ALICE et de template fit d'ATLAS sont compatibles. En utilisant SPDTracklets comme estimateur de centralité, on observe que les résultats de la méthode d'ATLAS restent inchangés, preuve de la solidité de la méthode par sa capacité à supprimer le non-flot (malgré le biais observé sur la mesure du flot des tracklets). Au contraire, le flot mesuré par la méthode d'ALICE est plus élevé, en particulier à haut p_T, ce qui semble indiquer qu'il existe une grande quantité de non-flot résiduel mal supprimé par la méthode. Ainsi, le choix de l'estimateur de centralité a un impact drastique sur la mesure finale. Face à cela, la méthode d'ATLAS semble plus robuste.

En intégrant entre 1 et 12 GeV/c, on peut calculer la compatibilité du flot du J/ψ avec zéro. Quel que soit l'estimateur de centralité ou la méthode de suppression du non-flot, le flot mesuré est en accord avec zéro à moins de 1σ, notamment lié à la limite sur la sensibilité de la mesure estimée par PYTHIA8.

En comparant ce résultat du flot elliptique du J/ψ en collisions pp à 13 TeV avec les résultats obtenus par ALICE en p–Pb et Pb–Pb, on observe que le flot est plus faible en collisions pp, en particulier entre 3 et 6 GeV/c, là où le flot était maximal dans les études menées dans des systèmes de collisions plus larges. Afin de comparer correctement le flot du J/ψ entre les différents systèmes, on normalise le flot elliptique du J/ψ par celui des tracklets. Cela permet donc de comparer comment le système répond aux anisotropies du J/ψ par rapport à celles des particules légères. De 3 à 6 GeV/c, on peut alors observer une baisse de la réponse en pp de 2.5σ par rapport aux systèmes p–Pb et Pb–p.

Au lieu de comparer le flot du J/ψ entre différents systèmes de collision, on peut se focaliser sur le système pp et comparer le flot de différentes espèces. En particulier, notre mesure peut être comparée aux mesures de flot elliptique de CMS pour le D^0 prompt (un quark charmé et un quark léger) et les hadrons chargés (dominés par les saveurs légères). Bien que les méthodes d'analyse soient différentes, comme le sont les couvertures en rapidité, une comparaison qualitative entre 2 et 4 GeV/c (là où le flot des hadrons chargés est maximal) on observe que les hadrons chargés développent plus de flot elliptique que le D^0 et que le J/ψ. Ainsi, dans l'hypothèse selon laquelle le J/ψ développerait un flot non-nul mais faible (ce qui est possible vu les incertitudes) on retrouverait une hiérarchie de masse, observée pour les particules légères en collisions pp et plus généralement valable en p–Pb et surtout en Pb–Pb. Elle est en général expliquée par l'hydrodynamique.

L'évolution du flot elliptique du J/ψ est aussi présentée en fonction de la centralité, sans montrer de dépendance particulière, puisque chaque point est compatible avec zéro, quel que soit la méthode de suppression de non-flot ou l'estimateur de centralité.

On observe donc que sur les plages de centralité et de moment transverse étudiées, le flot elliptique du J/ψ est compatible avec zéro, et plus largement avec les faibles valeurs de flot aux incertitudes près.

Appendix B

Dataset

In this appendix are given two tables. The first one details the dataset used for the analysis, with the periods, passes and run numbers. The second one gives the number of events kept in the analysis for each run group as a function of the various selection criteria.

Period	Pass and AOD	# runs	Runs
LHC16h	pass1, AOD234	72	255467, 255466, 255465, 255463, 255447, 255442, 255440, 255415, 255402, 255398, 255352, 255351, 255350, 255283, 255280, 255276, 255275, 255256, 255255, 255253, 255252, 255251, 255249, 255248, 255247, 255242, 255240, 255182, 255180, 255177, 255176, 255173, 255171, 255167, 255162, 255159, 255154, 255111, 255091, 255086, 255085, 255082, 255079, 255076, 255075, 255074, 255073, 255071, 255068, 255042, 255010, 255009, 255008, 254984, 254983, 254654, 254653, 254652, 254651, 254649, 254648, 254646, 254644, 254640, 254632, 254630, 254629, 254621, 254608, 254606, 254604, 254419
LHC16j	pass1, AOD234	49	256420, 256418, 256417, 256415, 256373, 256372, 256371, 256368, 256366, 256365, 256364, 256363, 256362, 256361, 256356, 256311, 256307, 256302, 256298, 256297, 256295, 256292, 256290, 256289, 256287, 256284, 256283, 256282, 256281, 256231, 256228, 256227, 256223, 256222, 256219, 256215, 256213, 256212, 256210, 256204, 256169, 256161, 256158, 256157, 256156, 256149, 256148, 256147, 256146
LHC16k	pass1, AOD	171	258537, 258499, 258498, 258477, 258456, 258454, 258452, 258426, 258399, 258393, 258391, 258388, 258387, 258359, 258336, 258332, 258307, 258306, 258303, 258302, 258301, 258299, 258280, 258278, 258274, 258273, 258271, 258270, 258258, 258257, 258256, 258204, 258203, 258202, 258197, 258178, 258117, 258114, 258113, 258109, 258108, 258107, 258063, 258062, 258060, 258059, 258049, 258048, 258045, 258042, 258041, 258039, 258019, 258017, 258014, 258012, 258008, 257989, 257986, 257979, 257963, 257960, 257958, 257957, 257939, 257937, 257936, 257932, 257912, 257901, 257893, 257892, 257737, 257735, 257734, 257733, 257727, 257725, 257724, 257697, 257694, 257688, 257687, 257685, 257684, 257682, 257644, 257642, 257636, 257635, 257632, 257630, 257606, 257605, 257604, 257601, 257595, 257594, 257592, 257590, 257588, 257587, 257566, 257565, 257564, 257563, 257562, 257561, 257560, 257541, 257540, 257531, 257530, 257492, 257491, 257490, 257488, 257487, 257474, 257468, 257457, 257433, 257364, 257358, 257330, 257322, 257320, 257318, 257260, 257224, 257095, 257092, 257086, 257084, 257083, 257082, 257080, 257077, 257071, 257026, 257021, 257012, 257011, 256944, 256942, 256941, 256697, 256695, 256694, 256691, 256684, 256681, 256677, 256676, 256658, 256620, 256619, 256591, 256567, 256565, 256564, 256561, 256560, 256557, 256556, 256554, 256552, 256512, 256510, 256506, 256504
LHC16o	pass1, AOD234	101	264035, 264033, 263985, 263984, 263981, 263979, 263978, 263977, 263923, 263920, 263917, 263916, 263905, 263866, 263863, 263861, 263830, 263829, 263824, 263823, 263813, 263810, 263803, 263793, 263792, 263790, 263787, 263786, 263785, 263784, 263744, 263743, 263741, 263739, 263738, 263737, 263691, 263690, 263689, 263682, 263662, 263657, 263654, 263653, 263652, 263647, 263529, 263497, 263496, 263490, 263487, 263332, 262858, 262855, 262853, 262849, 262847, 262844, 262842, 262841, 262778, 262777, 262776, 262768, 262760, 262727, 262725, 262723, 262719, 262717, 262713, 262705, 262635, 262632, 262628, 262594, 262593, 262583, 262578, 262574, 262572, 262571, 262570, 262569, 262568, 262567, 262563, 262537, 262533, 262532, 262528, 262492, 262487, 262451, 262430, 262428, 262424, 262423, 262422, 262419, 262418
LHC16p	pass1, AOD234	38	264347, 264346, 264345, 264341, 264336, 264312, 264305, 264281, 264279, 264277, 264273, 264267, 264266, 264265, 264264, 264262, 264261, 264260, 264259, 264238, 264233, 264232, 264198, 264197, 264194, 264188, 264168, 264164, 264138, 264137, 264129, 264110, 264109, 264086, 264085, 264082, 264078, 264076
LHC17h	muon_calo_pass2, AOD	103	273103, 273101, 273100, 273099, 273077, 273010, 273009, 272985, 272983, 272976, 272949, 272947, 272939, 272935, 272934, 272933, 272932, 272905, 272903, 272880, 272873, 272871, 272870, 272836, 272835, 272834, 272833, 272829, 272828, 272784, 272783, 272782, 272762, 272760, 272749, 272747, 272746, 272692, 272691, 272620, 272619, 272608, 272607, 272585, 272577, 272575, 272574, 272521, 272469, 272468, 272466, 272463, 272462, 272461, 272414, 272413, 272411, 272400, 272394, 272360, 272359, 272335, 272194, 272156, 272155, 272154, 272153, 272152, 272151, 272123, 272101, 272100, 272076, 272075, 272042, 272041, 272040, 272039, 272038, 272036, 272034, 272030, 272029, 272025, 272020, 271970, 271969, 271962, 271955, 271953, 271946, 271925, 271921, 271915, 271912, 271886, 271879, 271878, 271874, 271873, 271871, 271870, 271868
LHC17i	muon_calo_pass1, AOD	56	274442, 274390, 274387, 274385, 274364, 274363, 274360, 274357, 274355, 274329, 274283, 274281, 274280, 274278, 274276, 274271, 274270, 274269, 274268, 274266, 274264, 274263, 274259, 274232, 274212, 274148, 274147, 274125, 274094, 274092, 274064, 274063, 274058, 273986, 273985, 273946, 273942, 273918, 273889, 273887, 273886, 273885, 273825, 273824, 273719, 273711, 273709, 273695, 273690, 273689, 273687, 273654, 273653, 273593, 273592, 273591

LHC17k	muon_calo_pass2, AOD	100	276508, 276507, 276506, 276500, 276462, 276461, 276439, 276438, 276437, 276435, 276434, 276432, 276429, 276351, 276348, 276302, 276297, 276294, 276292, 276291, 276290, 276259, 276230, 276205, 276178, 276177, 276170, 276169, 276166, 276145, 276141, 276140, 276108, 276105, 276104, 276102, 276099, 276098, 275664, 275661, 275657, 275650, 275648, 275624, 275559, 275558, 275515, 275472, 275471, 275467, 275459, 275457, 275453, 275452, 275448, 275406, 275404, 275401, 275369, 275361, 275360, 275357, 275332, 275328, 275283, 275247, 275246, 275245, 275188, 275177, 275175, 275174, 275173, 275151, 275150, 275149, 275076, 275075, 275073, 275070, 275068, 275067, 274979, 274978, 274886, 274884, 274883, 274882, 274822, 274817, 274815, 274811, 274807, 274806, 274803, 274802, 274801, 274743, 274736, 274708
LHC17l	pass1, AOD234	118	278216, 278215, 278191, 278189, 278167, 278166, 278165, 278164, 278163, 278130, 278127, 278126, 278123, 278122, 278121, 277996, 277991, 277989, 277988, 277987, 277952, 277930, 277907, 277904, 277903, 277901, 277900, 277899, 277898, 277897, 277876, 277870, 277848, 277847, 277842, 277841, 277836, 277834, 277801, 277800, 277799, 277795, 277794, 277749, 277747, 277746, 277725, 277577, 277576, 277575, 277574, 277537, 277536, 277531, 277530, 277479, 277478, 277476, 277473, 277472, 277470, 277418, 277417, 277389, 277386, 277384, 277383, 277360, 277314, 277312, 277310, 277293, 277262, 277256, 277197, 277196, 277194, 277193, 277189, 277188, 277184, 277183, 277182, 277181, 277180, 277155, 277121, 277117, 277091, 277087, 277082, 277079, 277076, 277073, 277037, 277017, 277016, 277015, 276972, 276971, 276970, 276969, 276920, 276917, 276916, 276762, 276675, 276674, 276672, 276671, 276670, 276669, 276644, 276608, 276557, 276553, 276552, 276551
LHC17m	muon_calo_pass1, AOD	117	280140, 280135, 280134, 280131, 280126, 280118, 280114, 280111, 280108, 280066, 280052, 280051, 280049, 279955, 279954, 279952, 279893, 279890, 279886, 279884, 279880, 279879, 279855, 279854, 279853, 279830, 279827, 279826, 279773, 279749, 279747, 279719, 279718, 279715, 279689, 279688, 279684, 279683, 279682, 279679, 279677, 279676, 279642, 279641, 279600, 279598, 279597, 279583, 279565, 279564, 279563, 279562, 279561, 279560, 279559, 279488, 279487, 279483, 279441, 279439, 279435, 279410, 279391, 279355, 279354, 279349, 279348, 279344, 279342, 279312, 279310, 279309, 279274, 279273, 279270, 279268, 279267, 279265, 279264, 279242, 279238, 279235, 279234, 279208, 279207, 279201, 279199, 279157, 279155, 279130, 279125, 279123, 279122, 279117, 279106, 279075, 279074, 279073, 279068, 279044, 279043, 279041, 279038, 279037, 279036, 279008, 279007, 279005, 278999, 278964, 278963, 278959, 278941, 278939, 278936, 278915, 278914
LHC17o	muon_calo_pass1, AOD203	170	281961, 281956, 281953, 281946, 281940, 281939, 281931, 281928, 281918, 281916, 281915, 281894, 281893, 281892, 281755, 281754, 281753, 281751, 281750, 281741, 281713, 281709, 281707, 281706, 281705, 281672, 281667, 281664, 281658, 281655, 281654, 281651, 281645, 281642, 281640, 281635, 281634, 281633, 281592, 281583, 281581, 281580, 281574, 281569, 281568, 281563, 281562, 281557, 281511, 281509, 281477, 281475, 281450, 281449, 281446, 281444, 281441, 281415, 281321, 281301, 281277, 281275, 281244, 281243, 281242, 281241, 281240, 281213, 281212, 281191, 281190, 281181, 281180, 281179, 281081, 281080, 281079, 281062, 281061, 281060, 281036, 281035, 281033, 281032, 280998, 280997, 280996, 280994, 280990, 280947, 280943, 280940, 280936, 280897, 280890, 280881, 280880, 280856, 280848, 280847, 280845, 280844, 280842, 280793, 280792, 280786, 280768, 280767, 280766, 280765, 280764, 280763, 280761, 280756, 280755, 280754, 280753, 280706, 280705, 280681, 280679, 280676, 280671, 280650, 280648, 280647, 280645, 280639, 280637, 280634, 280613, 280583, 280581, 280576, 280575, 280574, 280551, 280550, 280547, 280546, 280519, 280518, 280448, 280447, 280446, 280445, 280443, 280419, 280418, 280415, 280413, 280412, 280406, 280405, 280403, 280375, 280374, 280352, 280351, 280350, 280349, 280348, 280312, 280310, 280290, 280286, 280285, 280284, 280283, 280282
LHC17r	muon_calo_pass1, AOD	32	282704, 282703, 282702, 282700, 282677, 282676, 282673, 282671, 282670, 282668, 282667, 282666, 282653, 282651, 282629, 282622, 282620, 282618, 282615, 282609, 282608, 282607, 282606, 282580, 282579, 282575, 282573, 282546, 282545, 282544, 282528, 282504
LHC18c	muon_calo_pass1, AOD	48	285958, 285957, 285946, 285917, 285893, 285892, 285869, 285851, 285830, 285812, 285811, 285810, 285806, 285805, 285804, 285781, 285778, 285777, 285756, 285755, 285754, 285753, 285752, 285751, 285722, 285698, 285697, 285664, 285663, 285662, 285659, 285643, 285642, 285641, 285640, 285639, 285603, 285602, 285601, 285599, 285578, 285577, 285576, 285575, 285557, 285515, 285497, 285496
LHC18d	muon_calo_pass1, AOD	45	286350, 286349, 286348, 286345, 286340, 286337, 286336, 286314, 286313, 286312, 286311, 286310, 286309, 286308, 286289, 286288, 286287, 286284, 286282, 286261, 286258, 286257, 286254, 286230, 286229, 286203, 286202, 286201, 286199, 286198, 286159, 286130, 286129, 286127, 286124, 286064, 286028, 286027, 286026, 286025, 286018, 286014, 285980, 285979, 285978
LHC18e	muon_calo_pass1, AOD	44	286350, 286349, 286348, 286345, 286340, 286337, 286336, 286314, 286313, 286312, 286311, 286310, 286309, 286308, 286289, 286288, 286287, 286284, 286282, 286261, 286258, 286257, 286254, 286230, 286229, 286203, 286202, 286201, 286199, 286198, 286159, 286130, 286129, 286127, 286124, 286064, 286028, 286027, 286026, 286025, 286018, 286014, 285980, 285979, 285978
LHC18f	muon_calo_pass1, AOD	68	287977, 287975, 287941, 287923, 287784, 287783, 287658, 287657, 287656, 287654, 287578, 287576, 287575, 287573, 287524, 287521, 287520, 287518, 287517, 287516, 287513, 287486, 287484, 287481, 287480, 287451, 287413, 287389, 287388, 287387, 287385, 287381, 287380, 287360, 287358, 287356, 287355, 287353, 287349, 287347, 287346, 287344, 287343, 287325, 287324, 287323, 287283, 287254, 287251, 287250, 287249, 287248, 287209, 287208, 287204, 287203, 287202, 287201, 287155, 287137, 287077, 287072, 287071, 287066, 287064, 287063, 287021, 287000
LHC18l	muon_calo_pass1, AOD	85	289971, 289966, 289943, 289941, 289940, 289935, 289931, 289928, 289888, 289884, 289880, 289857, 289856, 289855, 289852, 289849, 289830, 289816, 289815, 289814, 289811, 289808, 289775, 289757, 289731, 289729, 289724, 289723, 289721, 289666, 289664, 289660, 289659, 289658, 289657, 289654, 289632, 289626, 289625, 289582, 289581, 289579, 289577, 289576, 289574, 289547, 289494, 289493, 289468, 289466, 289465, 289463, 289462, 289444, 289426, 289373, 289370, 289369, 289368, 289367, 289366, 289365, 289363, 289356, 289355, 289354, 289353, 289309, 289308, 289306, 289303, 289300, 289280, 289278, 289277, 289276, 289275, 289254, 289253, 289249, 289247, 289243, 289242, 289241, 289240
LHC18m	muon_calo_pass1, AOD	187	292397, 292298, 292274, 292273, 292270, 292269, 292265, 292242, 292241, 292240, 292192, 292168, 292167, 292166, 292164, 292163, 292162, 292161, 292160, 292140, 292115, 292114, 292109, 292108, 292107, 292106, 292081, 292080, 292077, 292075, 292062, 292061, 292060, 292040, 292012, 291982, 291976, 291953, 291948, 291945, 291944, 291943, 291942, 291803, 291796, 291795, 291769, 291760, 291756, 291755, 291729, 291706, 291698, 291697, 291694, 291692, 291690, 291665, 291661, 291657, 291626, 291625, 291624, 291622, 291618, 291615, 291614, 291590, 291485, 291484, 291482, 291481, 291457, 291456, 291453, 291451, 291447, 291446, 291420, 291419, 291417, 291416, 291402, 291400, 291399, 291397, 291375, 291373, 291363, 291362, 291361, 291360, 291286, 291285, 291284, 291283, 291282, 291265, 291263, 291110, 291100, 291066, 291065, 291041, 291037, 291035, 291006, 291005, 291004, 291003, 291002, 290980, 290979, 290976, 290975, 290948, 290944, 290943, 290935, 290932, 290895, 290894, 290892, 290862, 290860, 290853, 290848, 290790, 290787, 290776, 290774, 290769, 290766, 290764, 290742, 290721, 290699, 290696, 290692, 290687, 290665, 290660, 290658, 290645, 290632, 290627, 290615, 290614, 290613, 290612, 290590, 290553, 290550, 290549, 290544, 290540, 290539, 290538, 290501, 290499, 290469, 290467, 290459, 290458, 290456, 290428, 290427, 290425, 290423, 290421, 290420, 290418, 290411, 290404, 290401, 290375, 290374, 290350, 290327, 290324, 290323, 290300, 290297, 290293, 290254, 290223, 290222

LHC18o	muon_calo_pass1, AOD	39	293898, 293896, 293893, 293891, 293886, 293856, 293831, 293830, 293829, 293809, 293807, 293806, 293805, 293802, 293799, 293776, 293774, 293773, 293741, 293740, 293698, 293696, 293695, 293692, 293691, 293588, 293587, 293497, 293496, 293494, 293475, 293474, 293424, 293413, 293392, 293391, 293388, 293386, 293368
LHC18p	muon_calo_pass1, AOD	78	294925, 294916, 294884, 294883, 294880, 294877, 294875, 294852, 294818, 294817, 294816, 294815, 294813, 294809, 294775, 294774, 294772, 294769, 294749, 294747, 294743, 294742, 294741, 294722, 294721, 294718, 294716, 294715, 294710, 294703, 294653, 294636, 294634, 294633, 294632, 294593, 294591, 294590, 294588, 294587, 294586, 294563, 294558, 294556, 294553, 294531, 294530, 294529, 294527, 294526, 294525, 294524, 294503, 294502, 294310, 294308, 294307, 294305, 294242, 294241, 294212, 294210, 294208, 294205, 294201, 294200, 294199, 294156, 294155, 294154, 294152, 294131, 294128, 294013, 294012, 294011, 294010, 294009

Table B1: Dataset used for the analysis

Group	Period	Pass	AOD type	**#Pass Phy&TrigSel**	#Pileup	#No contributor	#Bad σ_z	#Bad z_{vtx}	#No Tkl within $\|\eta\| < 1$	**#Valid CMUL7**
1	*16h*	*pass1*	*AOD234*	***13982849***	*59579*	*69245*	*40902*	*445397*	*206563*	***13306996***
	16j	*pass1*	*AOD234*	***11486273***	*43757*	*55035*	*31931*	*268408*	*162157*	***11035798***
	16k	*pass1*	*AOD*	***106858532***	*235930*	*514082*	*305056*	*2740867*	*1542048*	***102590137***
	16o	*pass1*	*AOD234*	***19314753***	*50558*	*79959*	*42357*	*540457*	*226331*	***18516110***
	16p	*pass1*	*AOD234*	***7522689***	*17476*	*31794*	*16301*	*249202*	*88512*	***7175289***
	17i	*muon_calo_pass1*	*AOD*	***11743712***	*37988*	*50733*	*25096*	*302318*	*134746*	***11273251***
	17k	*muon_calo_pass2*	*AOD*	***28687838***	*96955*	*122202*	*61348*	*609031*	*327845*	***27663344***
	17l	*pass1*	*AOD234*	***2061776***	*7980*	*8677*	*4599*	*43641*	*23562*	***1987219***
All Group 1				**201658422**	550223	931727	527590	5199321	2711764	**193548144**
2	17h	muon_calo_pass2	AOD	**8750269**	27587	37404	18757	223058	100633	**8402198**
3	17h	muon_calo_pass2	AOD	**14957275**	54819	63729	32116	342990	171562	**14394161**
4	*17k*	*muon_calo_pass2*	*AOD*	***2295280***	*7533*	*10323*	*5531*	*58278*	*28682*	***2201983***
	18l	*muon_calo_pass1*	*AOD*	***25777736***	*57372*	*116185*	*62714*	*508097*	*321020*	***24901400***
	18m	*muon_calo_pass1*	*AOD*	***5920676***	*16045*	*26789*	*15188*	*156889*	*77065*	***5676558***
	18o	*muon_calo_pass2*	*AOD*	***15004942***	*55258*	*68394*	*38595*	*433389*	*195898*	***14334235***
	18p	*muon_calo_pass2*	*AOD*	***32014466***	*112755*	*145071*	*81686*	*841343*	*416059*	***30673869***
All Group 4				**81013100**	248963	366762	203714	1997996	1038724	**77788045**
5	*17l*	*pass1*	*AOD234*	***36047394***	*152704*	*159538*	*82556*	*688023*	*433239*	***34784553***
	17m	*muon_calo_pass1*	*AOD*	***43645928***	*196028*	*194709*	*101015*	*952664*	*530324*	***41983332***
	17o	*muon_calo_pass1*	*AOD203*	***79003485***	*326539*	*455359*	*219833*	*2072850*	*1206009*	***75438170***
	17r	*muon_calo_pass1*	*AOD*	***16627131***	*59627*	*93686*	*45175*	*478998*	*248322*	***15849093***
	18c	*muon_calo_pass1*	*AOD*	***9803090***	*21591*	*44123*	*19705*	*200879*	*111136*	***9469450***
	18d	*muon_calo_pass1*	*AOD*	***12905055***	*33804*	*55847*	*29580*	*275217*	*153650*	***12447749***
	18e	*muon_calo_pass1*	*AOD*	***16860588***	*39574*	*72775*	*38385*	*400046*	*199785*	***16228163***
	18f	*muon_calo_pass1*	*AOD*	***23058269***	*48506*	*100125*	*51846*	*597790*	*275256*	***22147112***
All Group 5				**237950940**	878373	1176162	588095	5666467	3157721	**228347622**
6	18m	muon_calo_pass1	AOD	**9014378**	26601	43930	25065	286722	126202	**8584444**
7	18m	muon_calo_pass1	AOD	**1799596**	5416	8963	5152	59273	26453	**1710711**
8	18m	muon_calo_pass1	AOD	**3046975**	8869	15426	9001	97970	44676	**2898949**
9	18m	muon_calo_pass1	AOD	**4316611**	11714	21156	12283	122470	61816	**4125084**
10	18m	muon_calo_pass1	AOD	**8404510**	24681	43066	25768	287625	127065	**7975941**
11	18m	muon_calo_pass1	AOD	**5444103**	15720	25926	15130	150729	74970	**5207719**
12	18m	muon_calo_pass1	AOD	**18294611**	52813	85912	49427	463184	248670	**17547676**
Total				**594650790**	1905779	2820163	1512098	14897805	7890256	**570530694**

Table B2: Impact of selection criteria on event statistics

Appendix C

Invariant mass fit

C.1 Fit functions

Here is a list of the functions used for the invariant mass fits.

C.1.1 Double Crystal Ball

This function requires a normalisation factor N, 2 Gaussian parameters for the core (mean and width), and 4 tail parameters $(\alpha_1, n_1, \alpha_2, n_2)$.

$$CB2(x) = N \begin{cases} exp(\frac{-(x-\bar{x})^2}{2\sigma^2}) \text{ for } \frac{(x-\bar{x})}{\sigma} \in [-\alpha_1, \alpha_2] \\ A(B - \frac{(x-\bar{x})}{\sigma})^{-n_1} \text{ for } \frac{(x-\bar{x})}{\sigma} \leq -\alpha_1 \\ C(D + \frac{(x-\bar{x})}{\sigma})^{-n_2} \text{ for } \frac{(x-\bar{x})}{\sigma} \geq -\alpha_2 \end{cases} \tag{C.1}$$

with

$$\begin{aligned} A &= (\frac{n_1}{|\alpha_1|})^{n_1} exp(-\frac{|\alpha_1|^2}{2}), \\ B &= \frac{n_1}{|\alpha_1|} - |\alpha_1|, \\ C &= (\frac{n_2}{|\alpha_2|})^{n_2} exp(-\frac{|\alpha_2|^2}{2}), \\ D &= \frac{n_2}{|\alpha_2|} - |\alpha_2| \end{aligned} \tag{C.2}$$

The tail parameters are fixed to either Run2 or MC extracted values, as used in the pp analysis

Tail parameter	Run 2	MC
α_L	0.883	0.993
α_R	1.832	2.182
n_L	9.940	2.9075
n_R	15.323	3.122

Figure C.1: Extracted tails parameters for CB2 signal function from Run2 or from Monte-Carlo (taken from Ref. [246])

```
Double_t JPsiCrystalBallExtended(Double_t *x,Double_t *par)
{
```

```
        Double_t sum = 0;

        Double_t t = (x[0]-par[1])/par[2];
        if (par[3] < 0) t = -t;

        Double_t absAlpha = fabs((Double_t)par[3]);
        Double_t absAlpha2 = fabs((Double_t)par[5]);


        if (t <= -absAlpha) //left tail
        {
                Double_t a =  TMath::Power(par[4]/absAlpha,par[4])*
                exp(-0.5*absAlpha*absAlpha);
                Double_t b = par[4]/absAlpha - absAlpha;

                sum += (par[0])*(a/TMath::Power(b - t, par[4]));
        } else if (t > -absAlpha && t < absAlpha2) // gaussian core
        {
                sum += (par[0])*(exp(-0.5*t*t));
        } else if (t >= absAlpha2) //right
        {
                Double_t c =  TMath::Power(par[6]/absAlpha2,par[6])*
                exp(-0.5*absAlpha2*absAlpha2);
                Double_t d = par[6]/absAlpha2 - absAlpha2;

                sum += (par[0])*(c/TMath::Power(d + t, par[6]));
        } else
        sum += 0;

        return sum ;
}

Double_t Psi2SCrystalBallExtended(Double_t *x,Double_t *par)
{
Double_t sum = 0;

Double_t t = (x[0]-(par[1]+mDiff))/(par[2]*par[8]);
if (par[3] < 0) t = -t;

Double_t absAlpha = fabs((Double_t)par[3]);
Double_t absAlpha2 = fabs((Double_t)par[5]);

if (t < -absAlpha) //left tail
{
Double_t a =  TMath::Power(par[4]/absAlpha,par[4])*
exp(-0.5*absAlpha*absAlpha);
Double_t b = par[4]/absAlpha - absAlpha;

sum += (par[7])*(a/TMath::Power(b - t, par[4]));
}
else if (t >= -absAlpha && t < absAlpha2) // gaussian core
{
sum += (par[7])*(exp(-0.5*t*t));
}
else if (t >= absAlpha2) //right tail
```

```
{
Double_t c =  TMath::Power(par[6]/absAlpha2,par[6])*
exp(-0.5*absAlpha2*absAlpha2);
Double_t d = par[6]/absAlpha2 - absAlpha2;

sum += (par[7])*(c/TMath::Power(d + t, par[6]));
} else
sum += 0;

return sum ;

}
```

C.1.2 NA60

This function requires a normalisation factor N, 2 Gaussian parameters for the core (mean and width), and 8 tail parameters ($\alpha^L, p_1^L, p_2^L, p_3^L, \alpha^R, p_1^R, p_2^R, p_3^R$).

$$NA60(x) = N \times exp(-0.5(\frac{t}{t_0})^2) \tag{C.3}$$

with

$$t = \frac{x - \bar{x}}{\sigma} \tag{C.4}$$

and

$$\begin{cases} t_0 = 1 + p_1^L(\alpha^L - t)^{p_2^L - p_3^L\sqrt{\alpha^L - t}} \text{ for } t < \alpha^L \\ t_0 = 1 \text{ for } \alpha^L < t < \alpha^R \\ t_0 = 1 + p_1^R(t - \alpha^R)^{p_2^R - p_3^R\sqrt{t - \alpha^R}} \text{ for } t > \alpha^R \end{cases} \tag{C.5}$$

The tail parameters are fixed to MC extracted values, as used in the pp analysis

Tail parameter	MC
α_L	-0.4061
p_L^1	0.2302
p_L^2	1.2048
p_L^3	0.0390
α_R	2.0627
p_R^1	0.1836
p_R^2	1.2989
p_3^3	0.0643

Figure C.2: Extracted tails parameters for NA60 signal function from Monte-Carlo (taken from Ref. [246])

```
Double_t JPsiNA60(Double_t *x,Double_t *par)
{

        Double_t sum = 0;

        Double_t t0 = 1;

        Double_t t = (x[0]-par[1])/par[2];

        if (t < par[3]) //left tail
        {
                t0 = 1+pow(par[4]*(par[3]-t),par[5]-(par[6]*sqrt(par[3]-t)));

                sum += par[0]*exp(-0.5*pow(t/t0,2));
        }
        else if (t > par[7]) //right
        {
                t0 = 1+pow(par[8]*(t-par[7]),par[9]-(par[10]*sqrt(t-par[7])));

                sum += par[0]*exp(-0.5*pow(t/t0,2));
        }
        else{
                t0 = 1;

                sum += par[0]*exp(-0.5*pow(t/t0,2));
        }

        return sum ;
}

Double_t Psi2SNA60(Double_t *x,Double_t *par)
{

        Double_t sum = 0;

        Double_t t0 = 1;

        Double_t t = (x[0]-(par[1]+mDiff))/(par[2]*par[12]);

        if (t < par[3]) //left tail
        {
                t0 = 1+pow(par[4]*(par[3]-t),par[5]-(par[6]*sqrt(par[3]-t)));

                sum += par[11]*exp(-0.5*pow(t/t0,2));
        }
        else if (t > par[7]) //right
        {
                t0 = 1+pow(par[8]*(t-par[7]),par[9]-(par[10]*sqrt(t-par[7])));

                sum += par[11]*exp(-0.5*pow(t/t0,2));
        }
        else{
                t0 = 1;

                sum += par[11]*exp(-0.5*pow(t/t0,2));
        }
```

```
        return sum ;
}
```

C.1.3 Double Exponential

The double exponential function used in this analysis has 3 parameters.

$$ExpBkg(x) = e^{x\alpha_1} + Ne^{x\alpha_2} \tag{C.6}$$

```
Double_t ExpBkg(Double_t *x, Double_t *par)

{ return exp(x[0]*par[1]*(-1)) + par[2]*(exp(x[0]*par[3]*(-1))); }
```

C.1.4 Pol1/Pol2

The ratio of polynomials has 4 parameters.

$$Pol1Pol2(x) = N\frac{1 + a_1 x}{1 + b_1 x + b_2 x^2} \tag{C.7}$$

```
Double_t Pol1Pol2(Double_t *x, Double_t *par)

{ return par[0]*(((1+par[1]*x[0]))/(1+par[2]*x[0] +
par[3]*(x[0]*x[0]))); }
```

C.1.5 Variable Width Gaussian

The variable width gaussian has 4 parameters. The width is defined as

$$\sigma(x) = \alpha + \beta(\frac{x - \bar{x}}{x}) \tag{C.8}$$

and

$$VWG(x) = Ne^{\frac{-(x-\bar{x})^2}{2\sigma(x)^2}} \tag{C.9}$$

```
Double_t VWGaussian(Double_t *x, Double_t *par)

{ double sigma = par[2] + par[3]*((x[0]-par[1])/par[1]);
return par[0]*exp(-1.0*pow(x[0]-par[1],2)/(2*pow(sigma,2))); }
```

C.1.6 Chebychev Polynomials

Chebychev polynomials are a set of real polynomials $T_n(x)$ defined over $[-1, +1]$. They form an orthogonal basis with respect to the inner product. They are defined recursively as

$$\begin{cases} T_0(x) = 1 \\ T_1(x) = x \\ T_n(x) = 2xT_{n-1}(x) - T_{n-2}(x), \text{ for } n \geqslant 2 \end{cases} \tag{C.10}$$

```
Double_t Tchebychev(Double_t *x,Double_t *par)

{    Double_t xx = (x[0]-par[5])/(par[6]-par[5]);

Double_t poly = SmolTcheby(xx,par, 0);
for(int index=1; index<5;index++){
poly += par[index]*SmolTcheby(xx,par, index);
}
poly *= par[0];
return poly;
}

Double_t SmolTcheby(Double_t x,Double_t *par, int n)

{ if(n==0){
return 1;
}
if(n==1){
return x;
}
if(n>=2){
return 2*x*SmolTcheby(x, par, n-1) - SmolTcheby(x, par, n-2);
}
}
```

C.2 Cross-check of invariant mass fits

In this section are shown three comparative figures. They compare the invariant mass fit from this analysis and from Ref. [246], using the same parametrization.

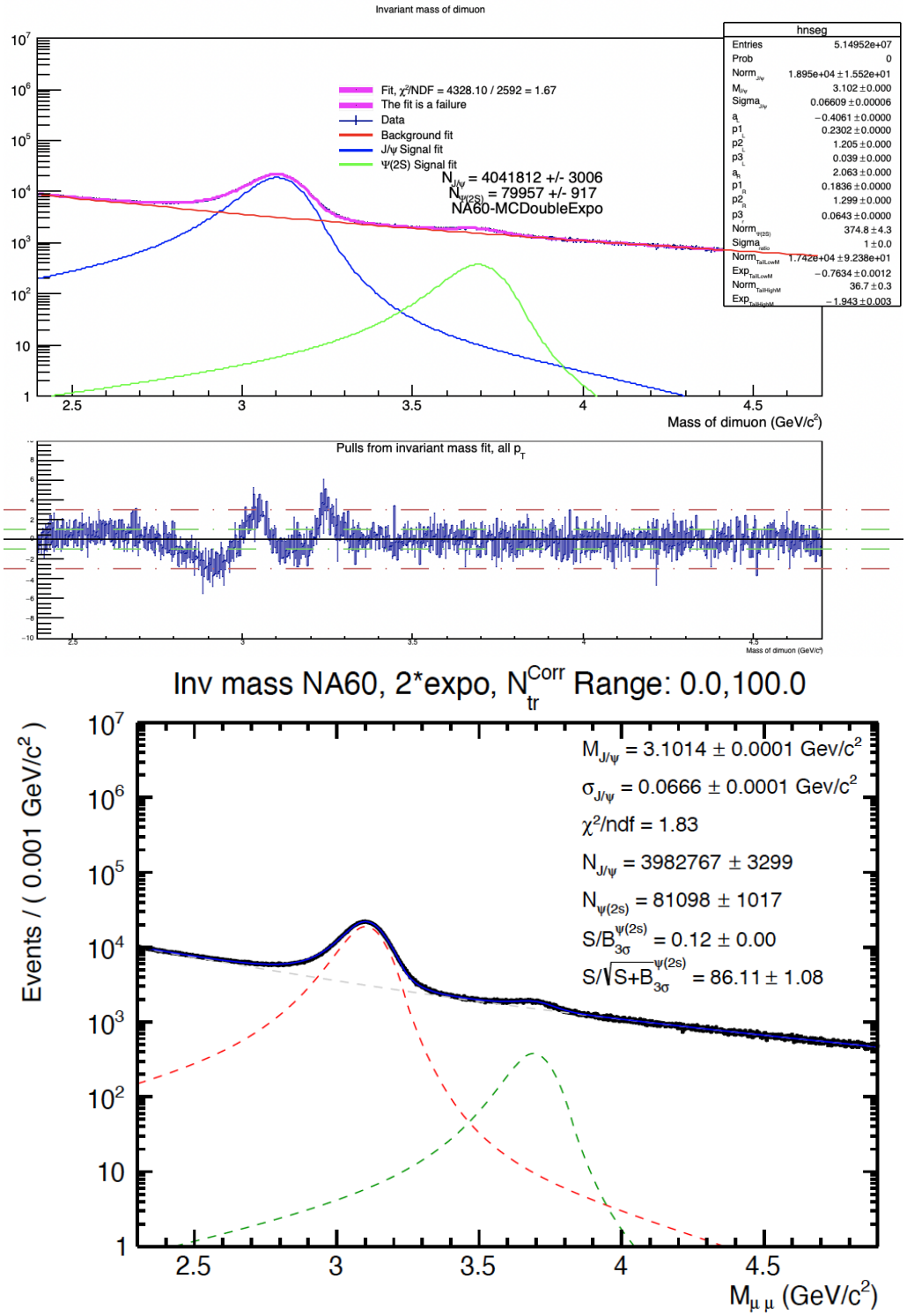

Figure C.3: Example of invariant mass fit using the same functions and fit parameters, Top: This analysis, Bottom: Ref. [246]

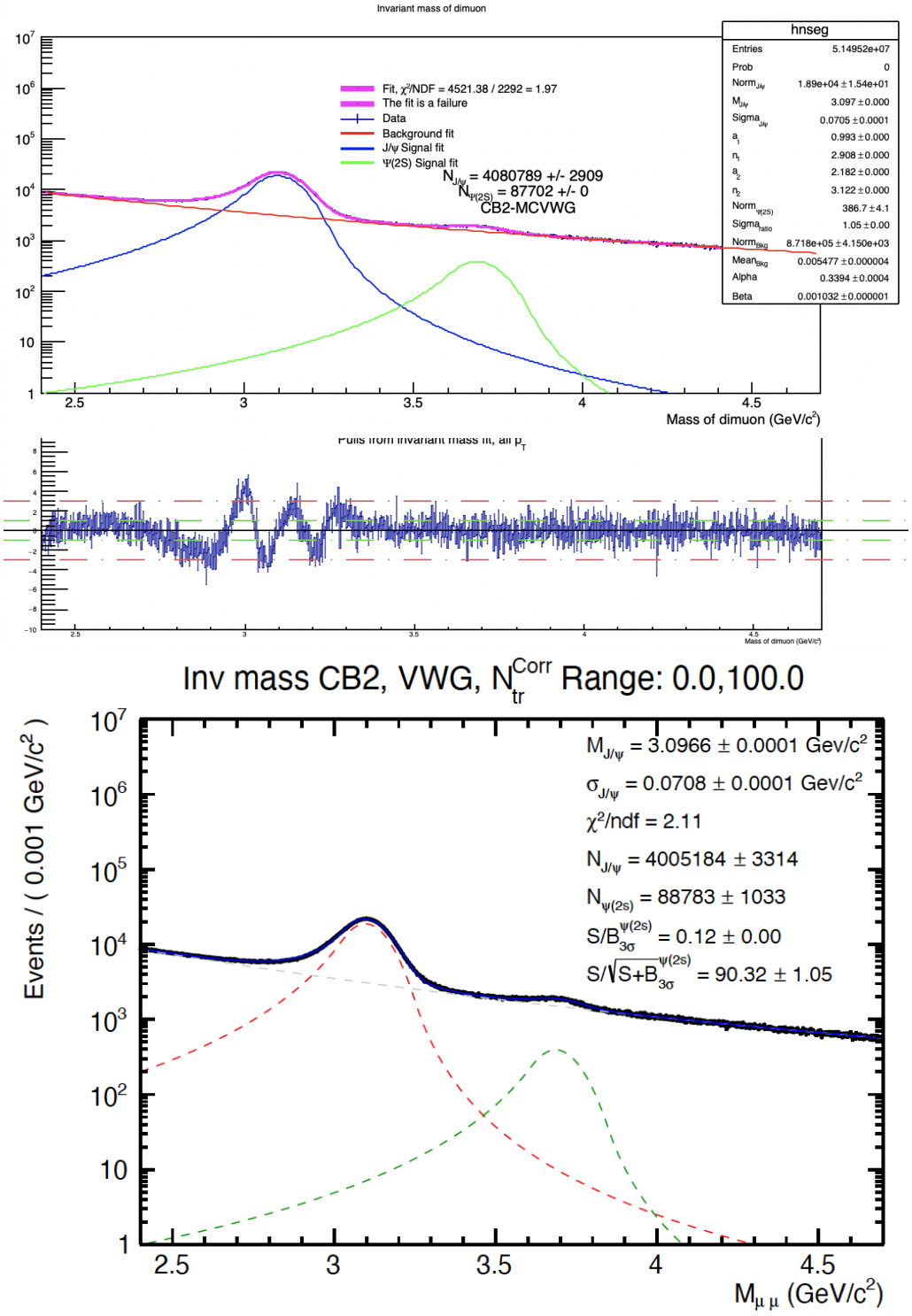

Figure C.4: Example of invariant mass fit using the same functions and fit parameters, Top: This analysis, Bottom: Ref. [246]

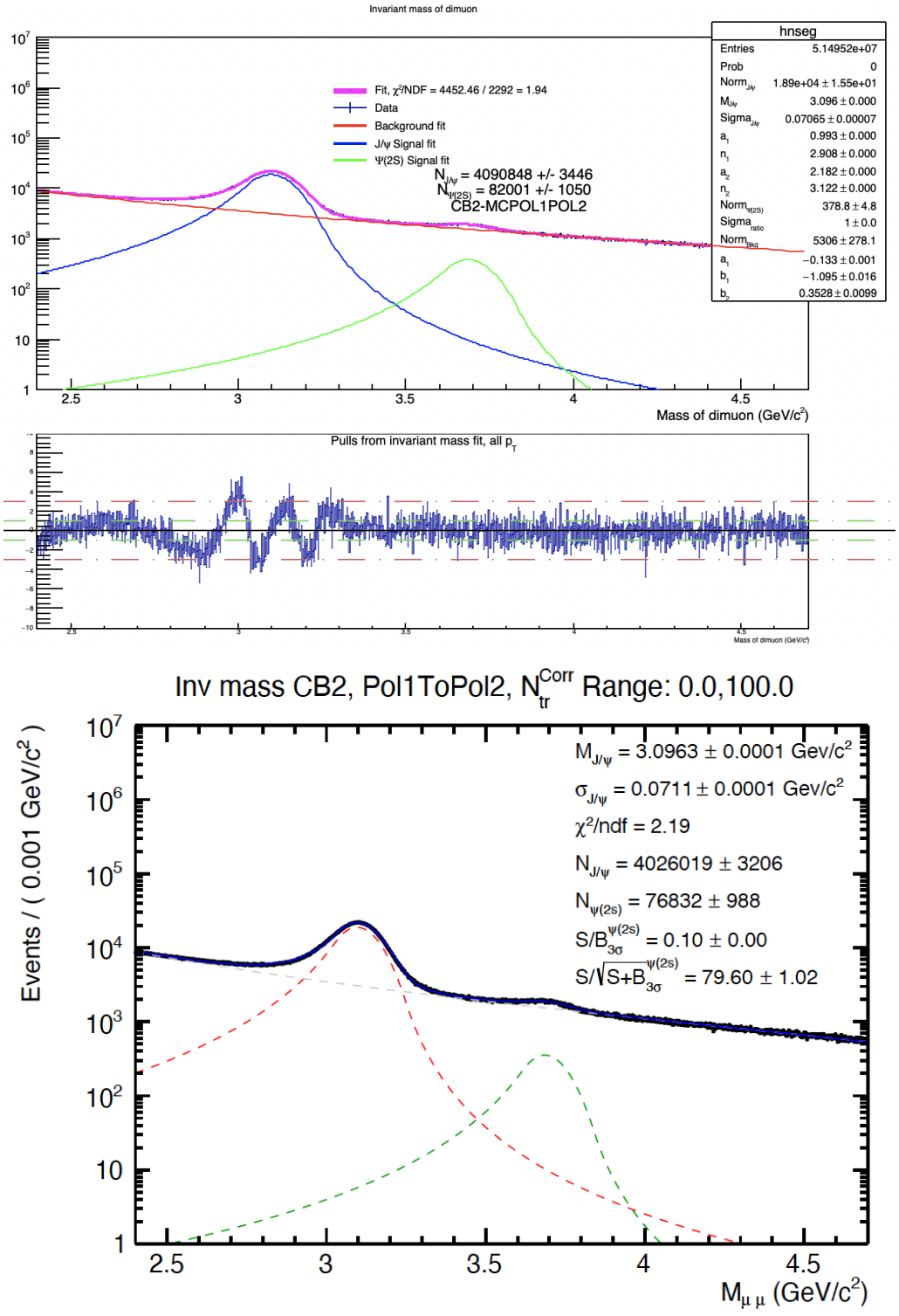

Figure C.5: Example of invariant mass fit using the same functions and fit parameters, Top: This analysis, Bottom: Ref. [246]

Appendix D

Tracklet flow systematics

In this appendix are shown figures showcasing the variations of tracklet v_2 following a change from default configuration to an alternative, for all studied systematic effects. We also show bar graphs giving a visual representation of the relative impact of each systematic uncertainty on the total systematic uncertainty on tracklet v_2 (from tables in Chapter 6) using various methods, centrality classes, and centrality estimators.

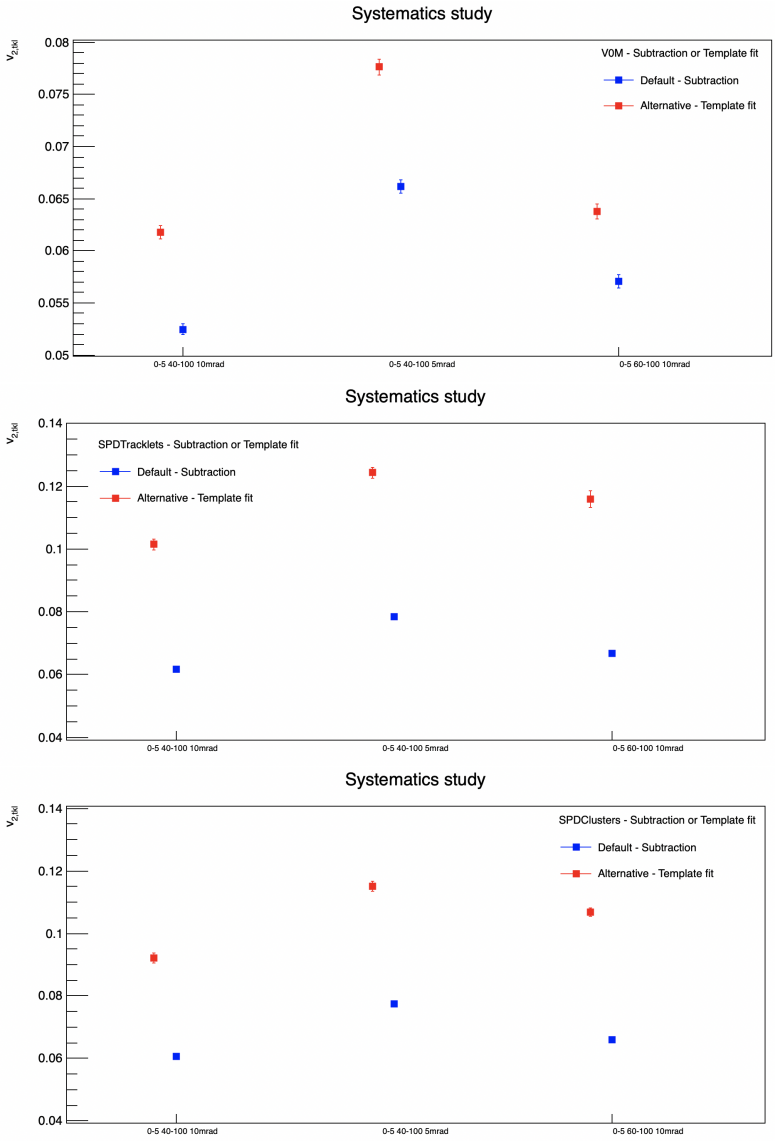

Figure D.1: Plot of the systematic variations on tracklet elliptic flow - Comparison template fit to yield subtraction. Top: V0M, Middle: SPDTracklets, Bottom: SPDClusters

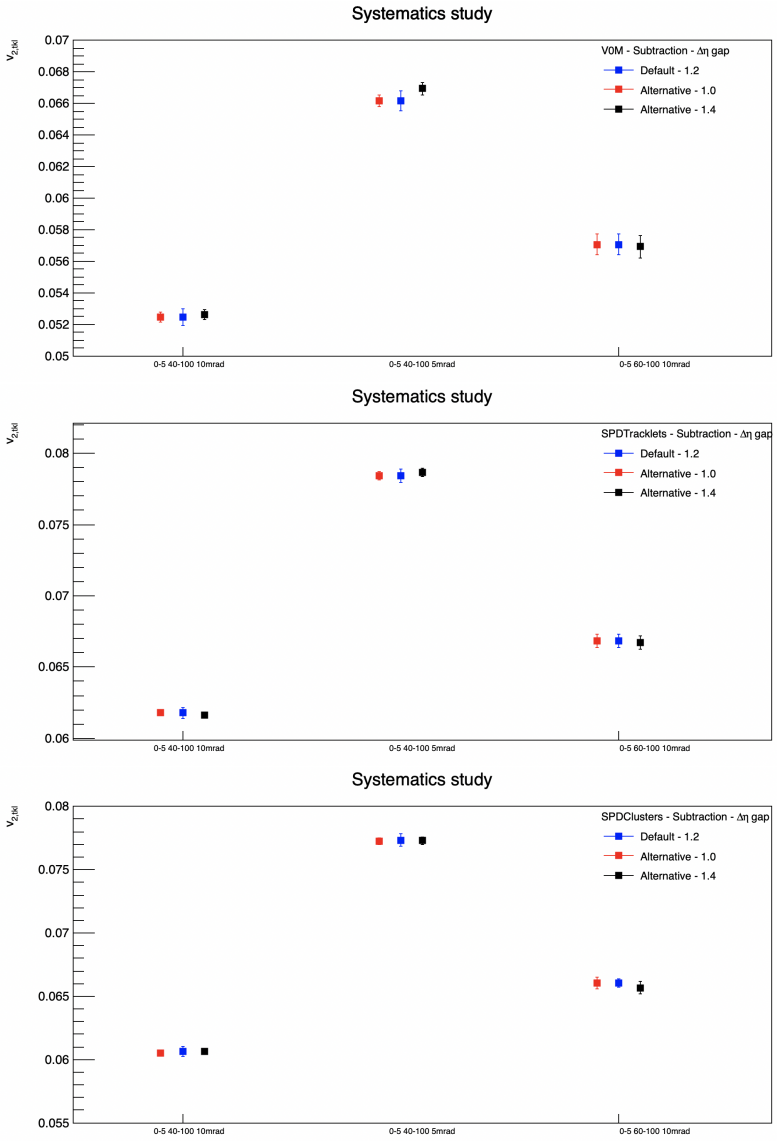

Figure D.2: Plot of the systematic variations on tracklet elliptic flow - Variation of the η-gap. Top: V0M, Middle: SPDTracklets, Bottom: SPDClusters

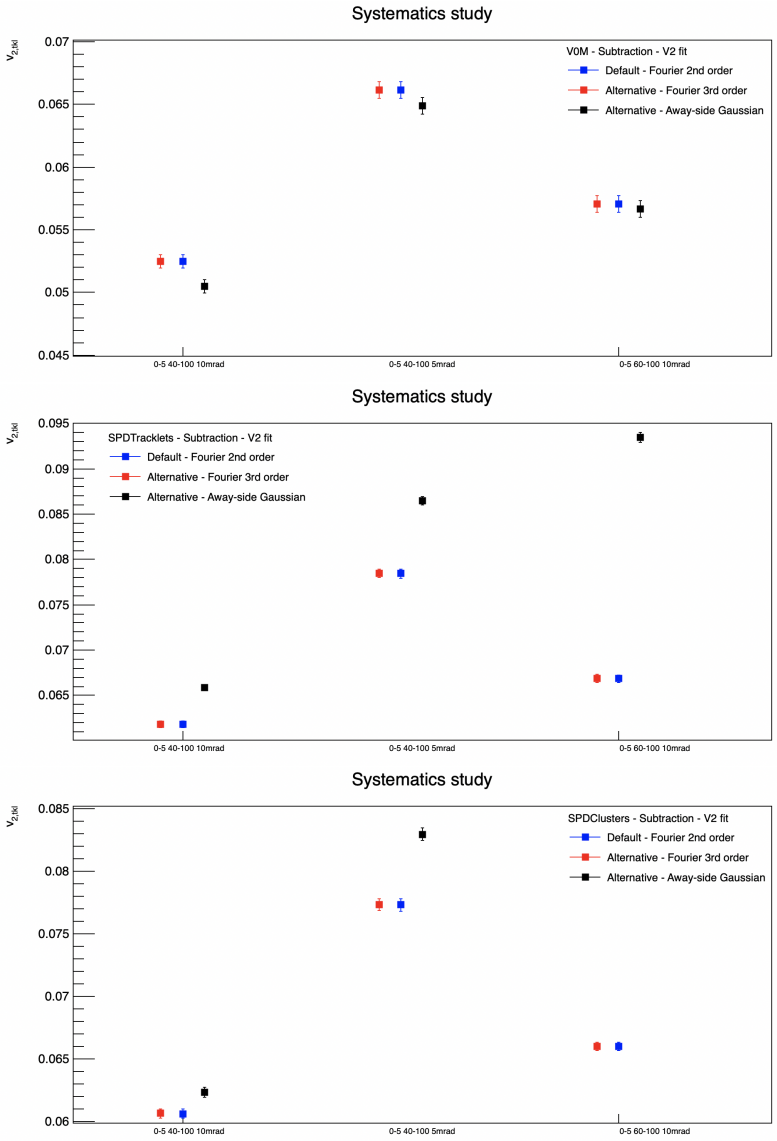

Figure D.3: Plot of the systematic variations on tracklet elliptic flow - Variation of the fit method. Top: V0M, Middle: SPDTracklets, Bottom: SPDClusters

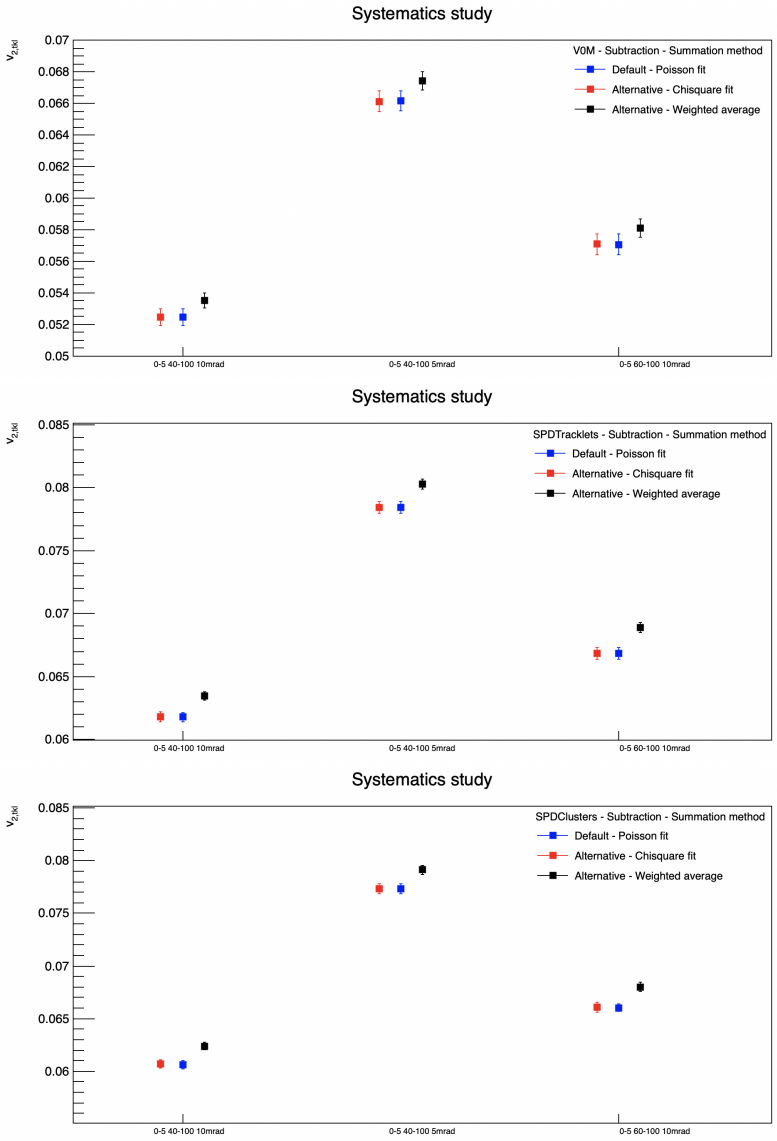

Figure D.4: Plot of the systematic variations on tracklet elliptic flow - Variation of the summation on z_{vtx}. Top: V0M, Middle: SPDTracklets, Bottom: SPDClusters

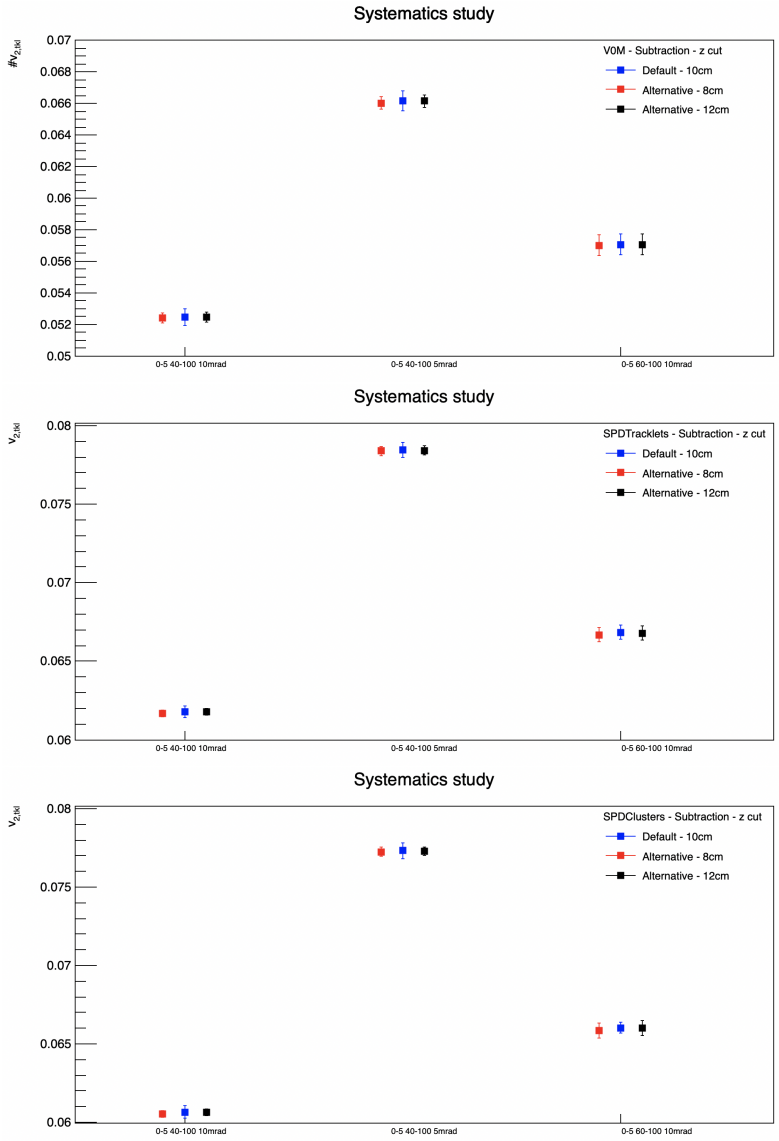

Figure D.5: Plot of the systematic variations on tracklet elliptic flow - Variation of the z_{vtx} cut. Top: V0M, Middle: SPDTracklets, Bottom: SPDClusters

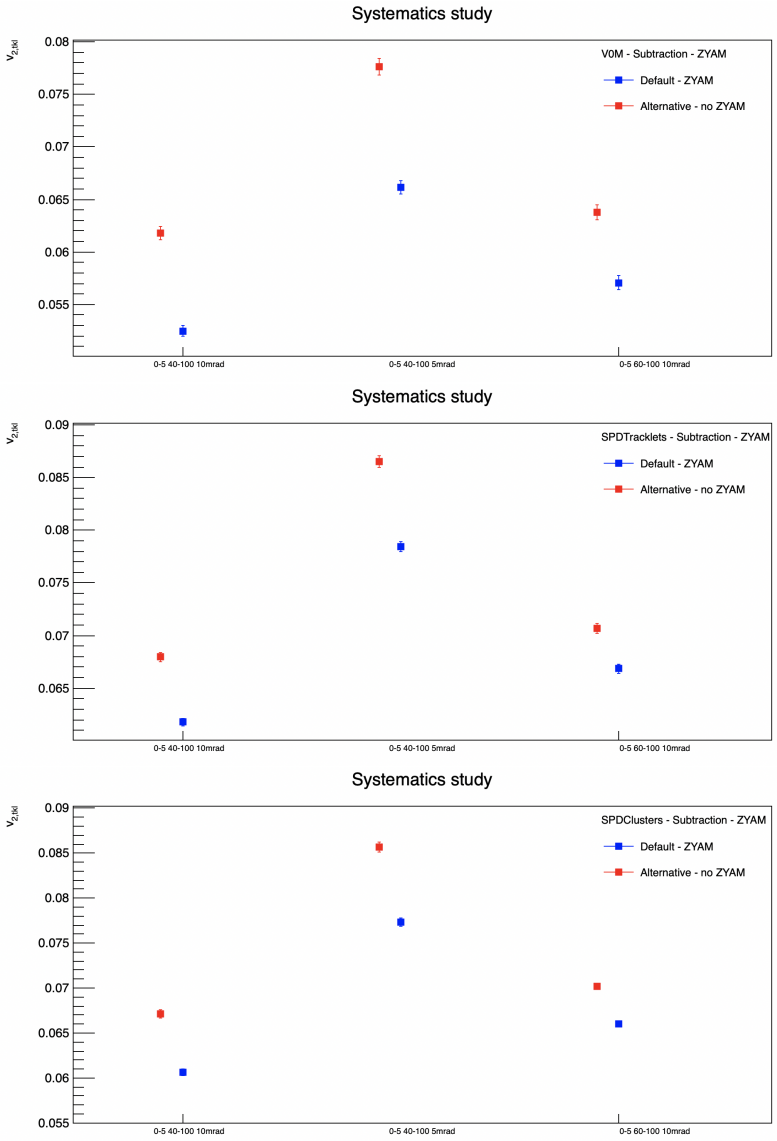

Figure D.6: Plot of the systematic variations on tracklet elliptic flow - Variation of the ZYAM hypothesis. Top: V0M, Middle: SPDTracklets, Bottom: SPDClusters

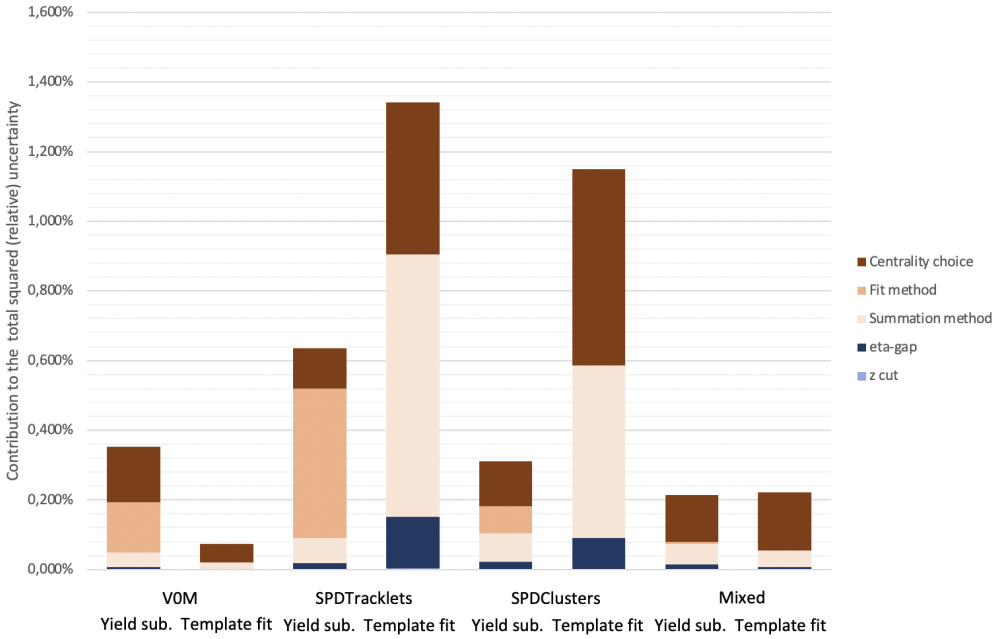

Figure D.7: Bar graph of the contribution of each uncertainty source to the squared total (relative) uncertainty on tracklet v_2 for various estimators and extraction methods.

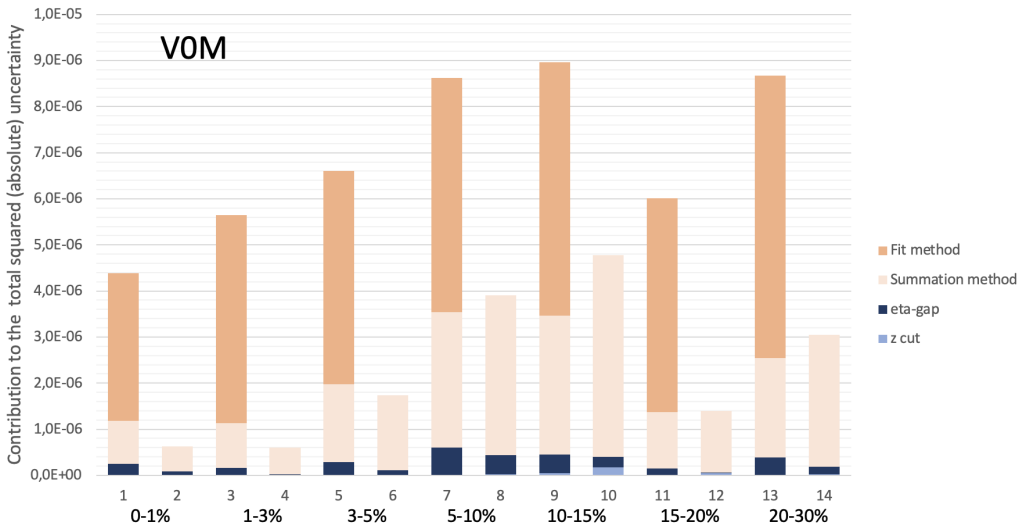

Figure D.8: Bar graph of the contribution of each uncertainty source to the squared total (absolute) uncertainty on tracklet v_2 for V0M and extraction methods as a function of the central class.

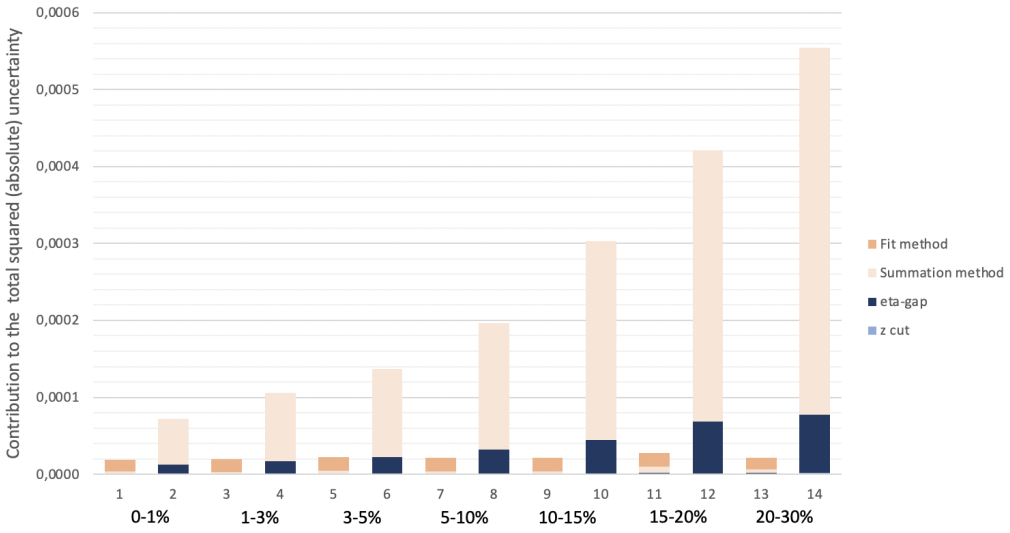

Figure D.9: Bar graph of the contribution of each uncertainty source to the squared total (absolute) uncertainty on tracklet v_2 for SPDTracklets and extraction methods as a function of the central class.

Appendix E

J/ψ flow systematics

In this appendix are shown figures showcasing the variations of J/ψ v_2 following a change from default configuration to an alternative, for all studied systematic effects. We also show bar graphs giving a visual representation of the relative impact of each systematic uncertainty on the total systematic uncertainty on tracklet v_2 (from tables in 6) using various methods, centrality classes, and centrality estimators.

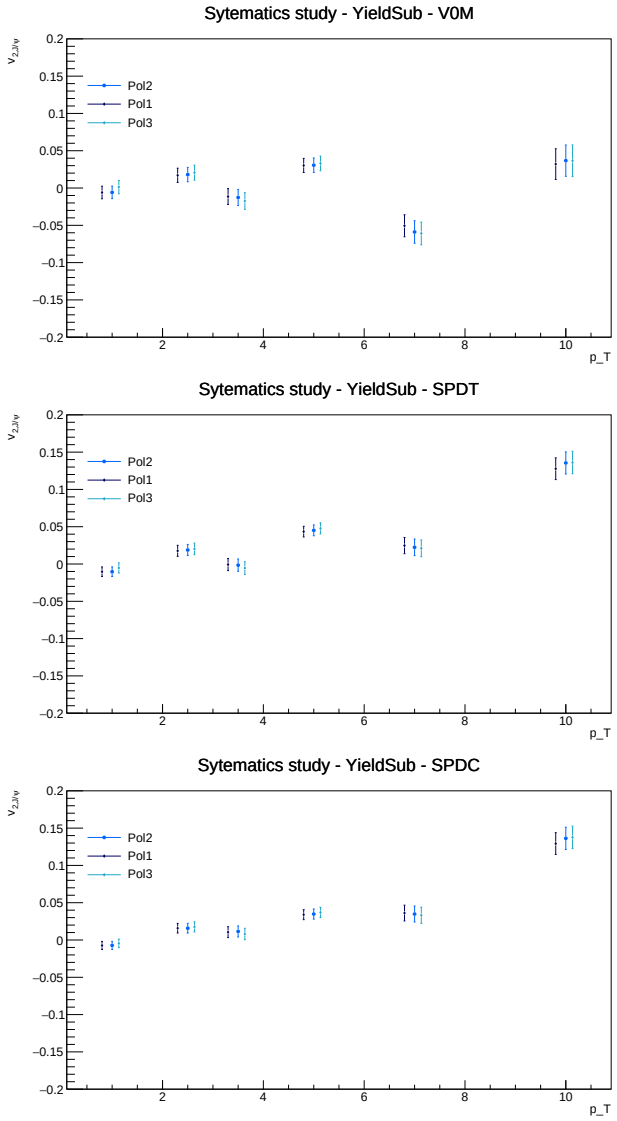

Figure E.1: Plot of the systematic variations on J/ψ elliptic flow from Yield subtraction - Comparison of background shape for V_2 fit. Top: V0M, Middle: SPDTracklets, Bottom: SPDClusters

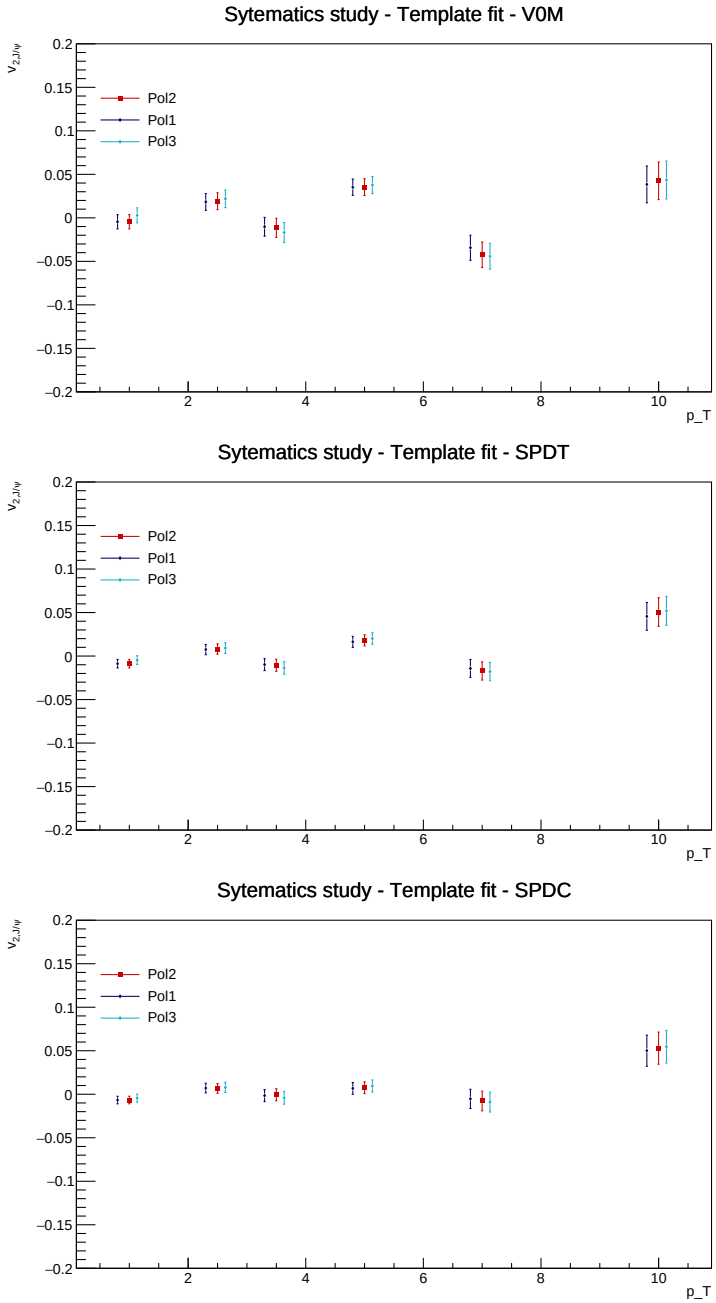

Figure E.2: Plot of the systematic variations on J/ψ elliptic flow from Template fit - Comparison of background shape for V_2 fit. Top: V0M, Middle: SPDTracklets, Bottom: SPDClusters

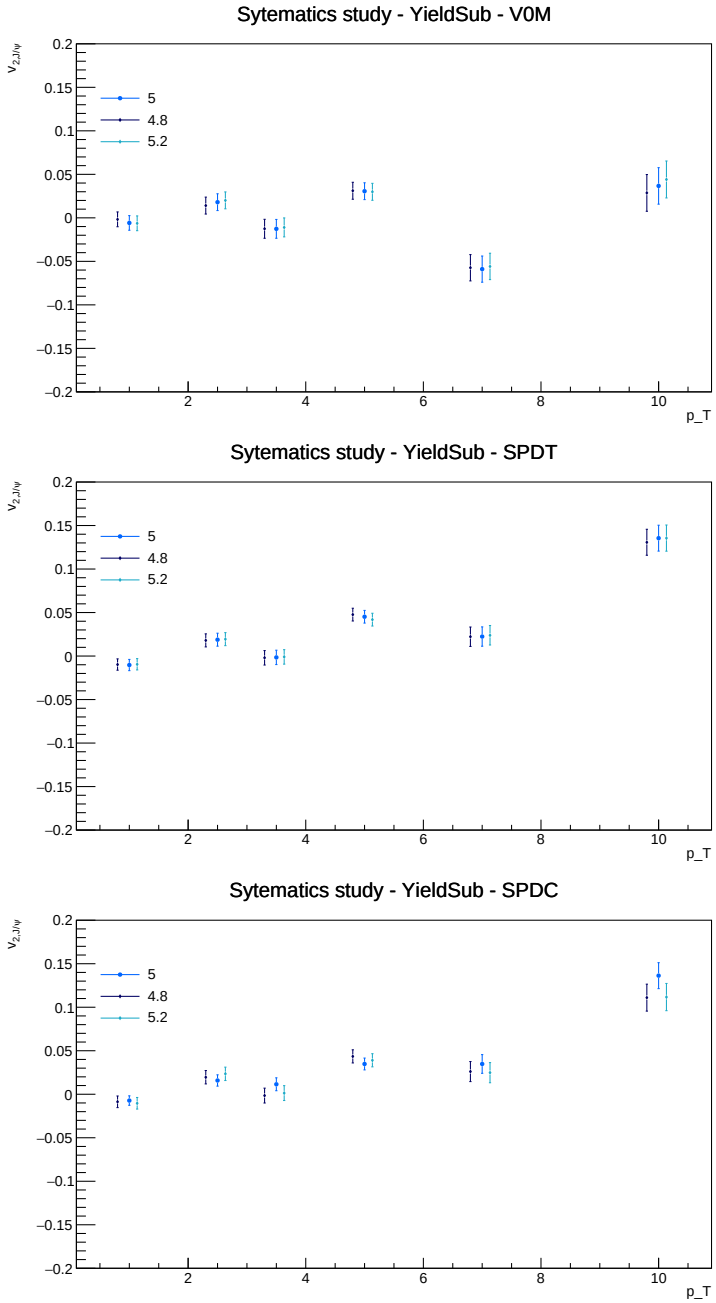

Figure E.3: Plot of the systematic variations on J/ψ elliptic flow from Yield subtraction - Comparison of $\Delta\eta$ maximum value. Top: V0M, Middle: SPDTracklets, Bottom: SPDClusters

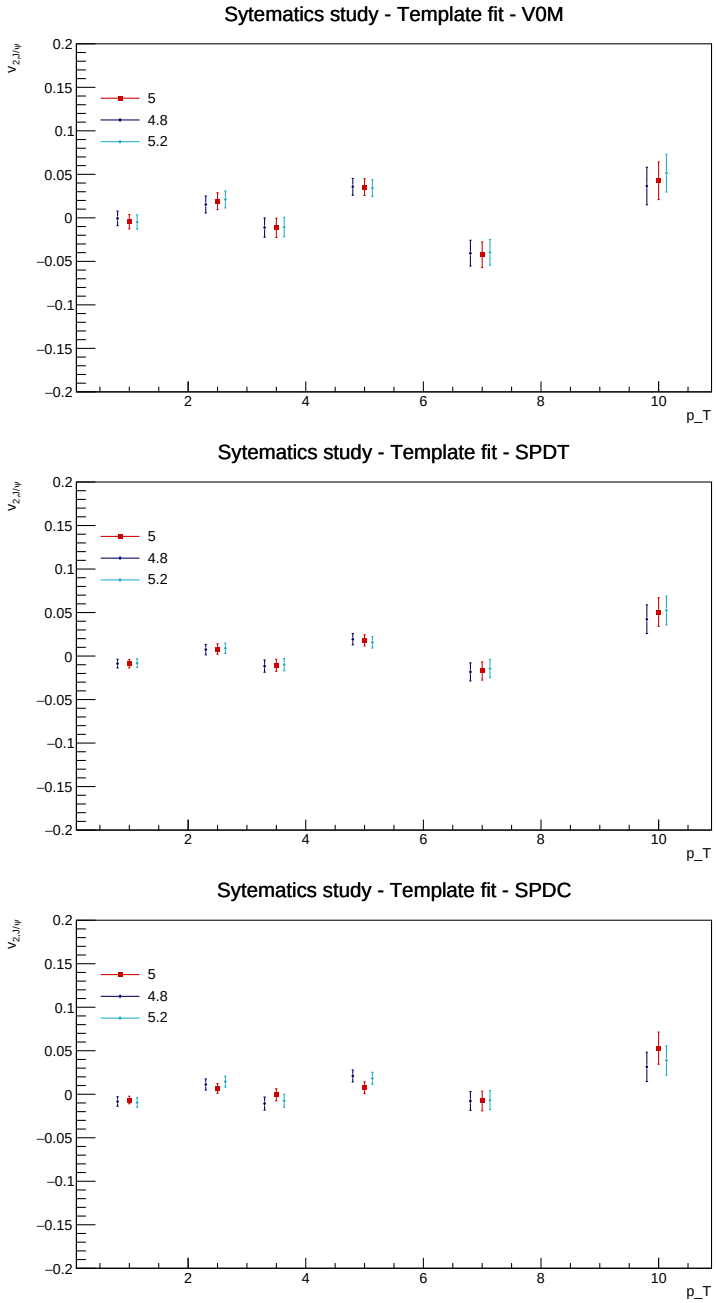

Figure E.4: Plot of the systematic variations on J/ψ elliptic flow from Template fit - Comparison of $\Delta\eta$ maximum value. Top: V0M, Middle: SPDTracklets, Bottom: SPDClusters

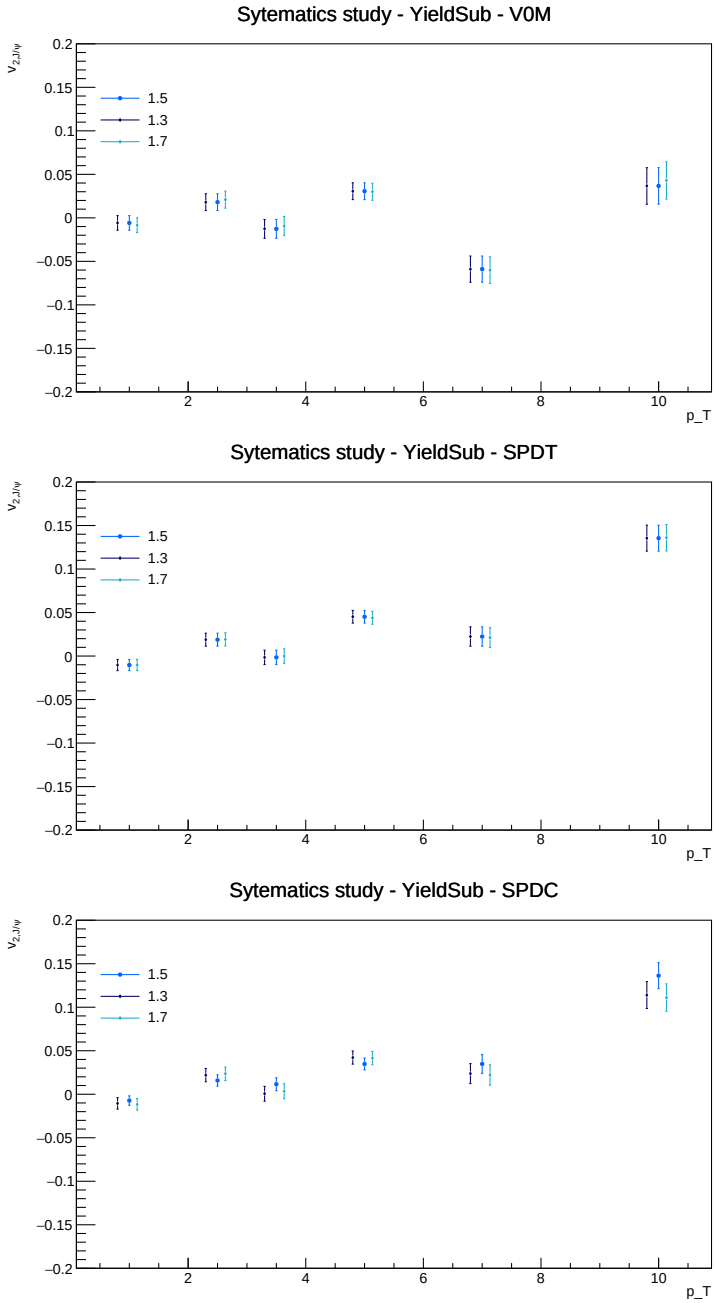

Figure E.5: Plot of the systematic variations on J/ψ elliptic flow from Yield subtraction - Comparison of $\Delta\eta$ minimum value. Top: V0M, Middle: SPDTracklets, Bottom: SPDClusters

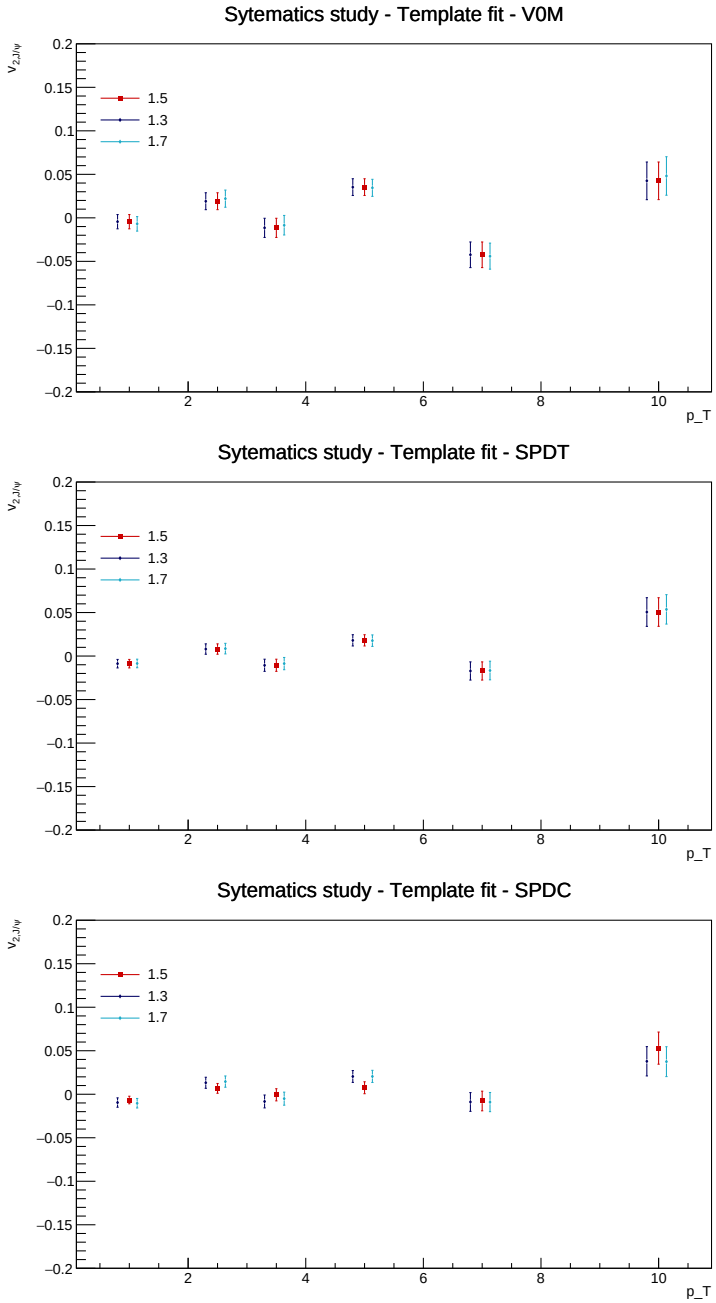

Figure E.6: Plot of the systematic variations on J/ψ elliptic flow from Template fit - Comparison of $\Delta\eta$ minimum value. Top: V0M, Middle: SPDTracklets, Bottom: SPDClusters

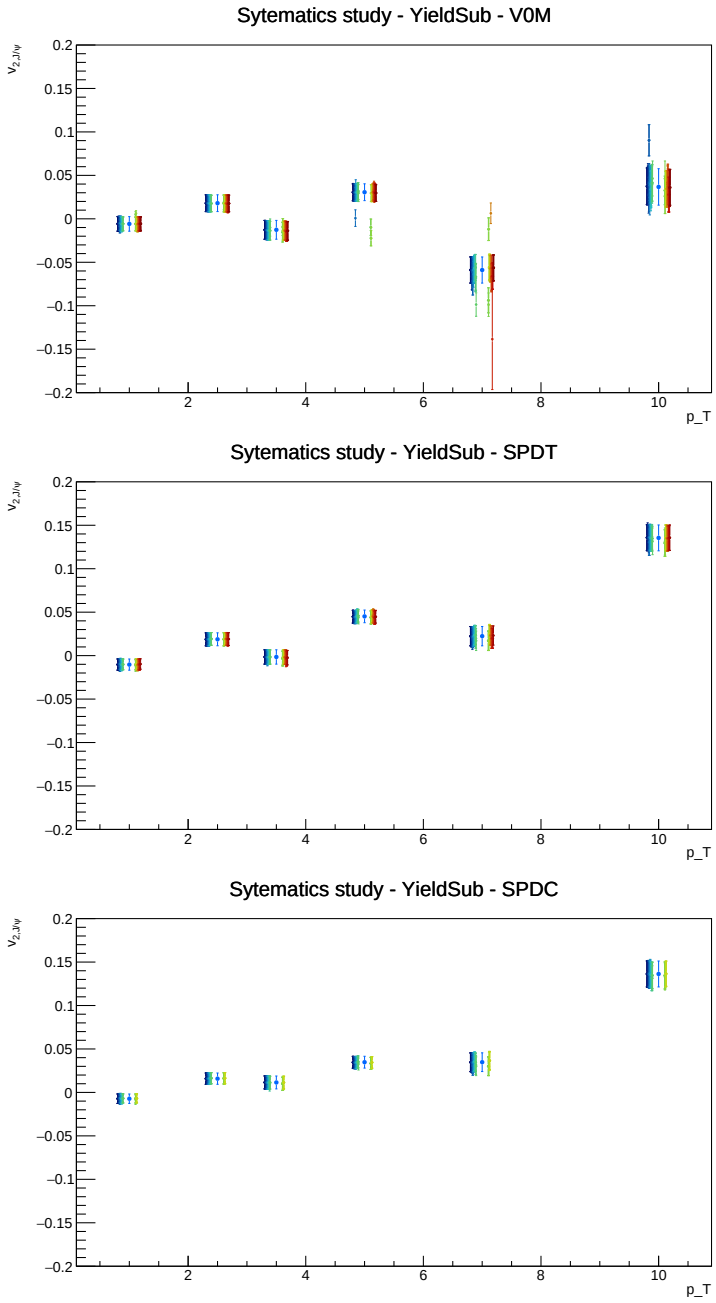

Figure E.7: Plot of the systematic variations on J/ψ elliptic flow from Yield subtraction - Comparison of invariant mass fit. Top: V0M, Middle: SPDTracklets, Bottom: SPDClusters

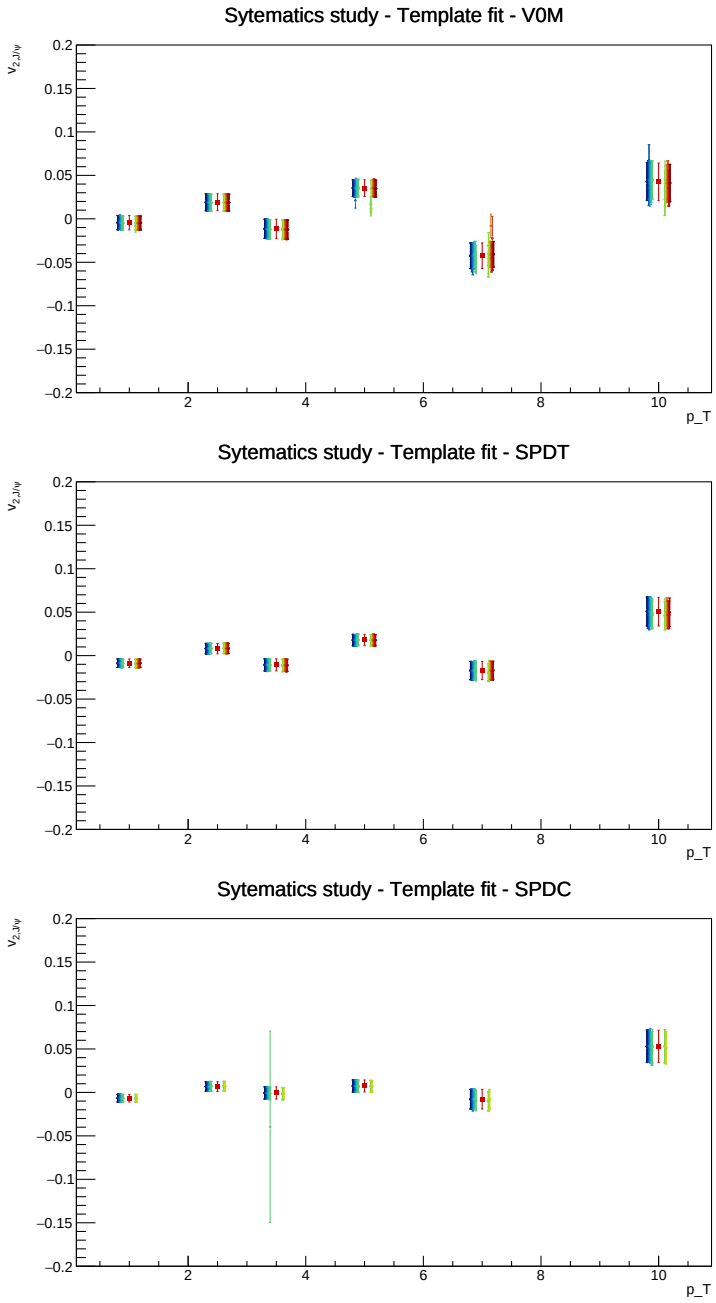

Figure E.8: Plot of the systematic variations on J/ψ elliptic flow from Template fit - Comparison of invariant mass fit. Top: V0M, Middle: SPDTracklets, Bottom: SPDClusters

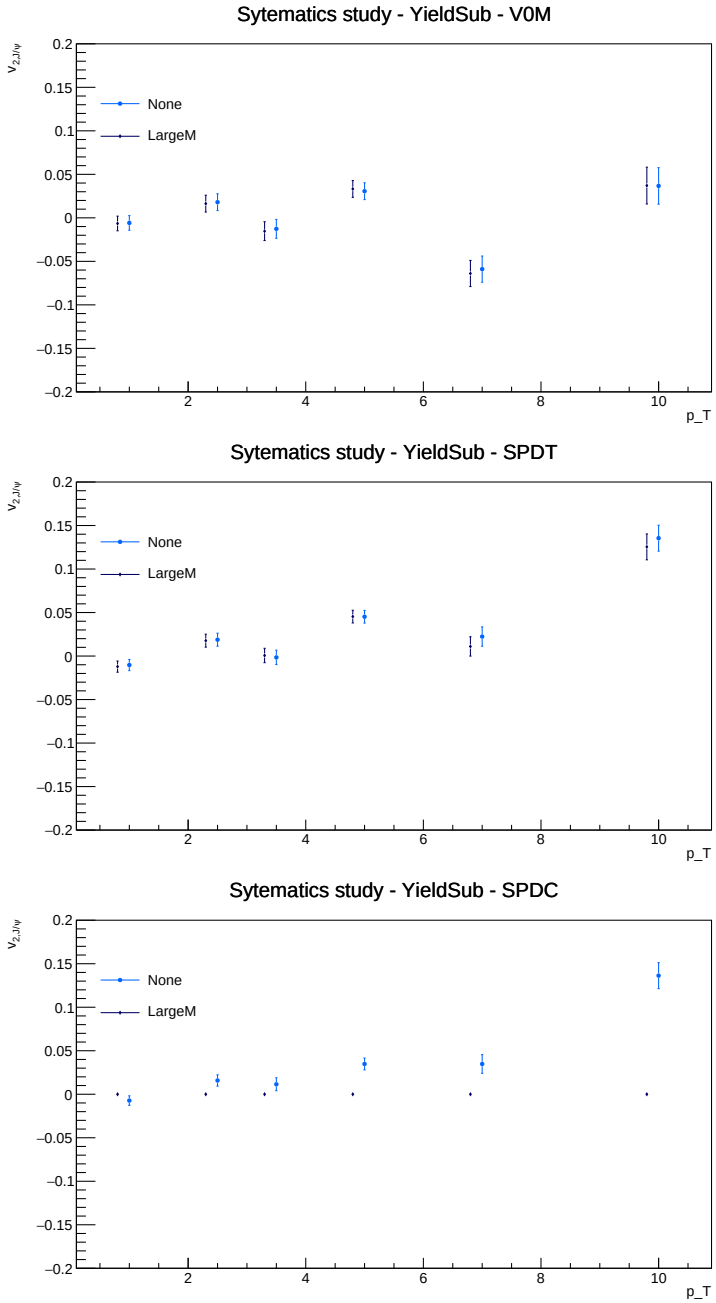

Figure E.9: Plot of the systematic variations on J/ψ elliptic flow from Yield subtraction - Comparison of pooling with dimuon mass. Top: V0M, Middle: SPDTracklets, Bottom: SPDClusters

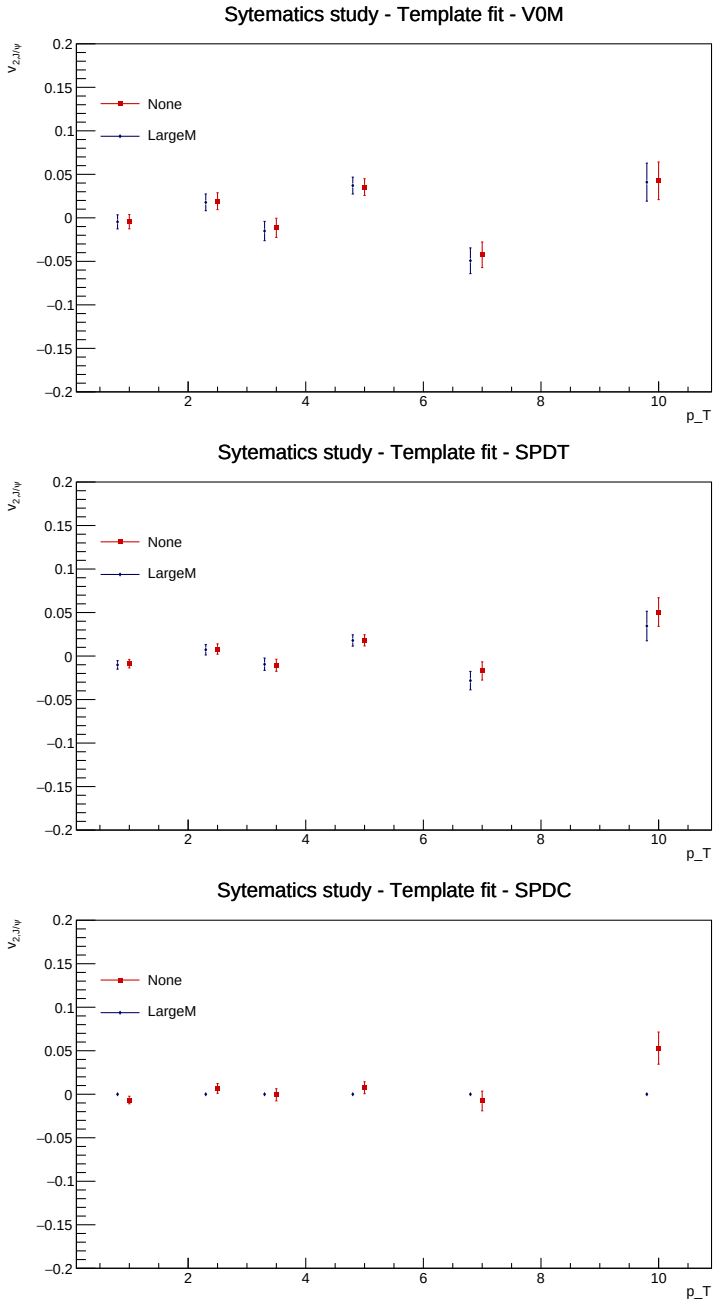

Figure E.10: Plot of the systematic variations on J/ψ elliptic flow from Template fit - Comparison of pooling with dimuon mass. Top: V0M, Middle: SPDTracklets, Bottom: SPDClusters

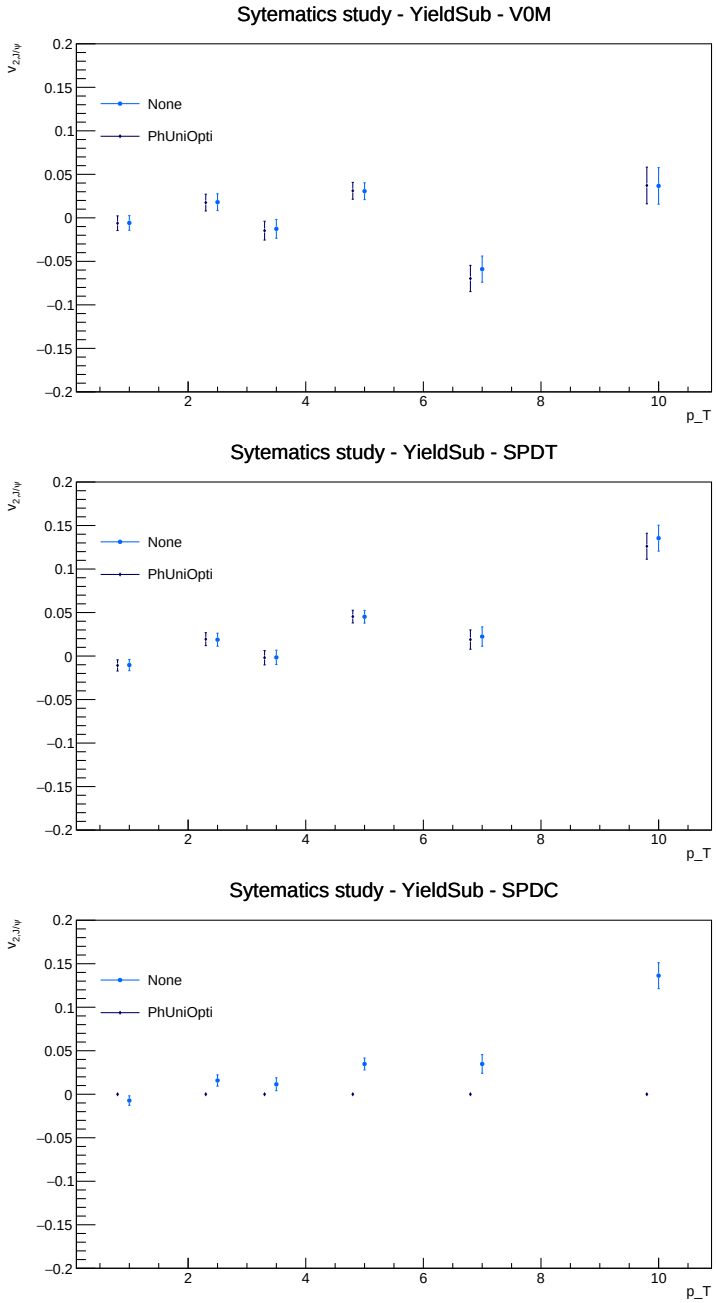

Figure E.11: Plot of the systematic variations on J/ψ elliptic flow from Yield subtraction - Comparison of pooling with dimuon phi. Top: V0M, Middle: SPDTracklets, Bottom: SPDClusters

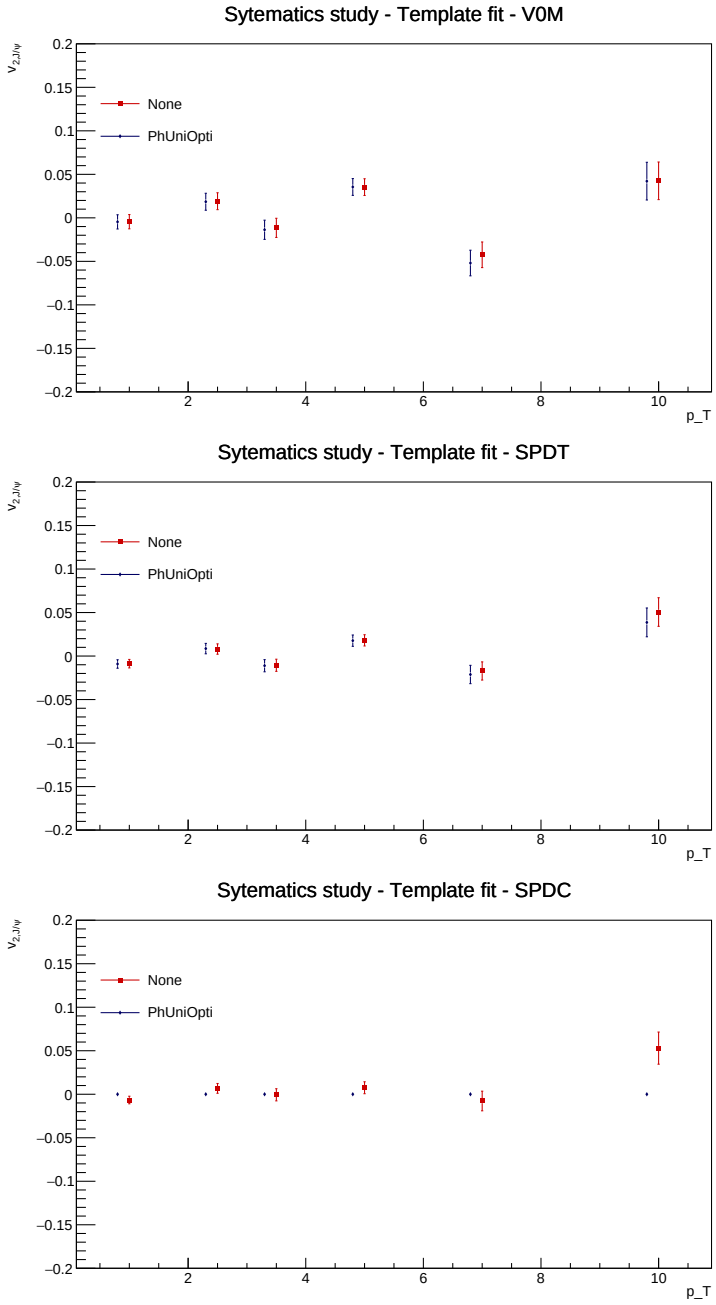

Figure E.12: Plot of the systematic variations on J/ψ elliptic flow from Template fit - Comparison of pooling with dimuon phi. Top: V0M, Middle: SPDTracklets, Bottom: SPDClusters

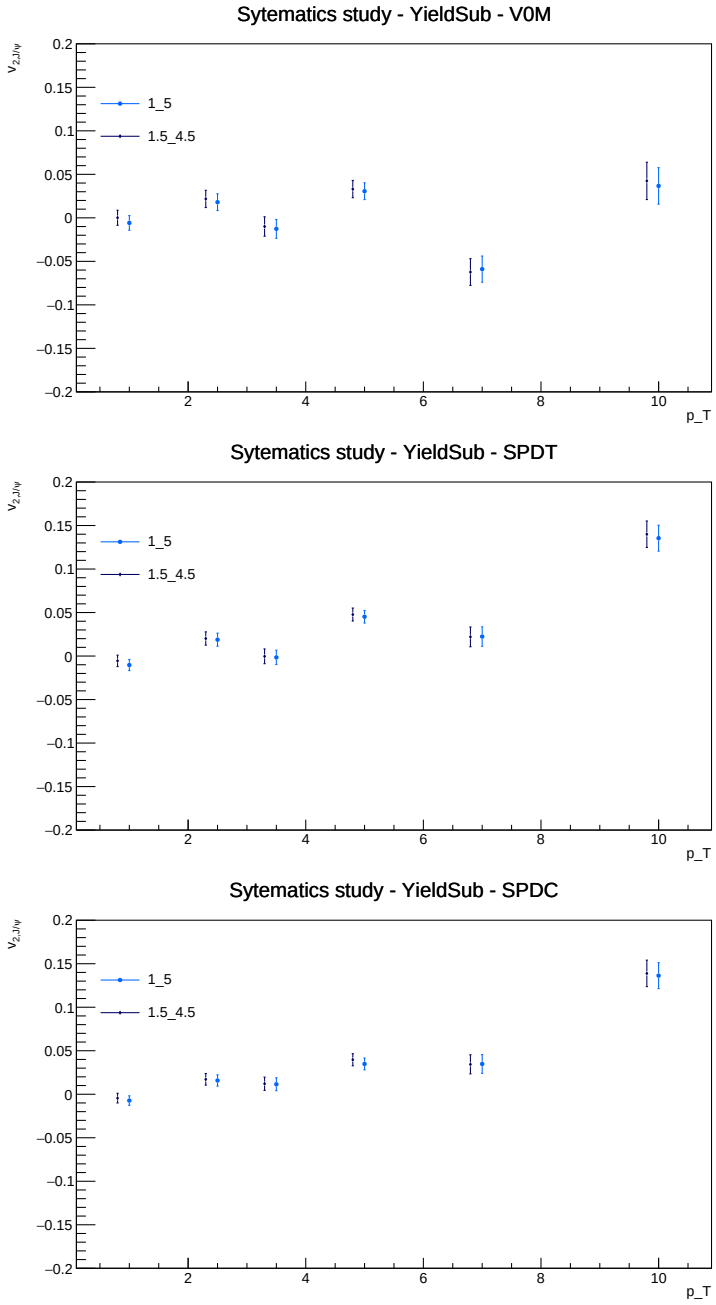

Figure E.13: Plot of the systematic variations on J/ψ elliptic flow from Yield subtraction - Comparison of V_2 fit range. Top: V0M, Middle: SPDTracklets, Bottom: SPDClusters

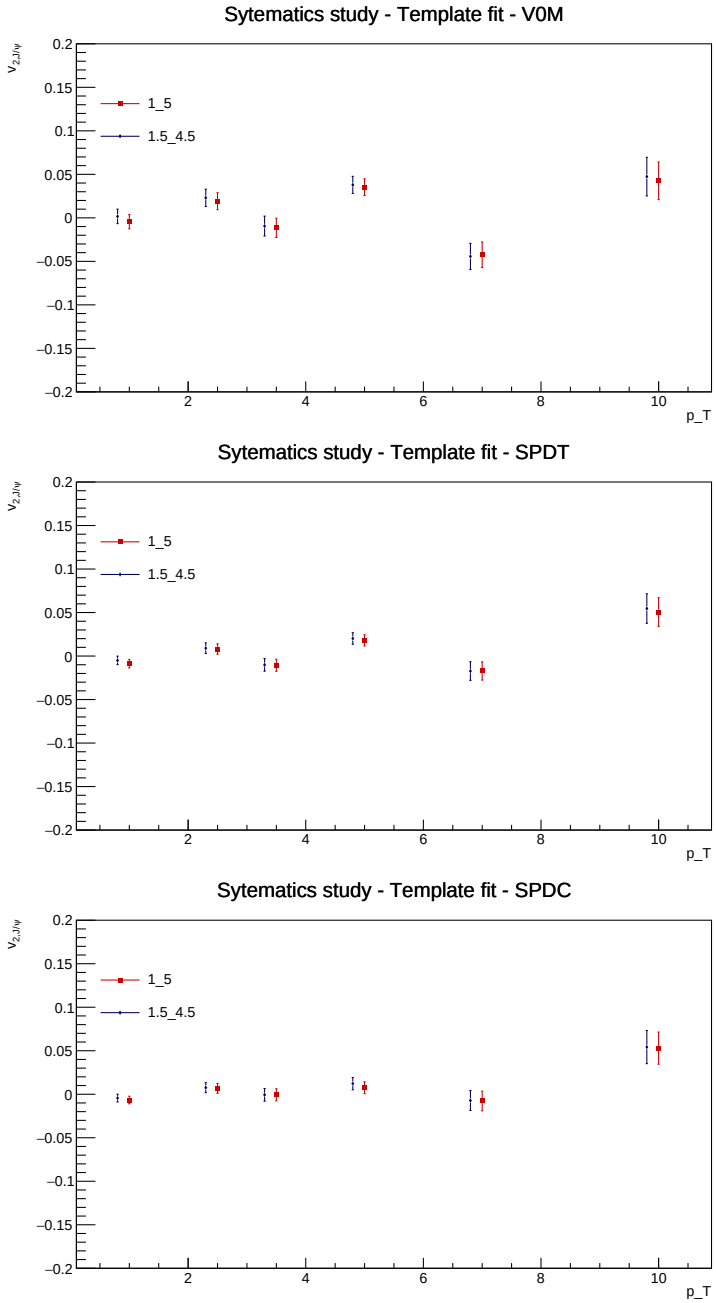

Figure E.14: Plot of the systematic variations on J/ψ elliptic flow from Template fit - Comparison of V_2 fit range. Top: V0M, Middle: SPDTracklets, Bottom: SPDClusters

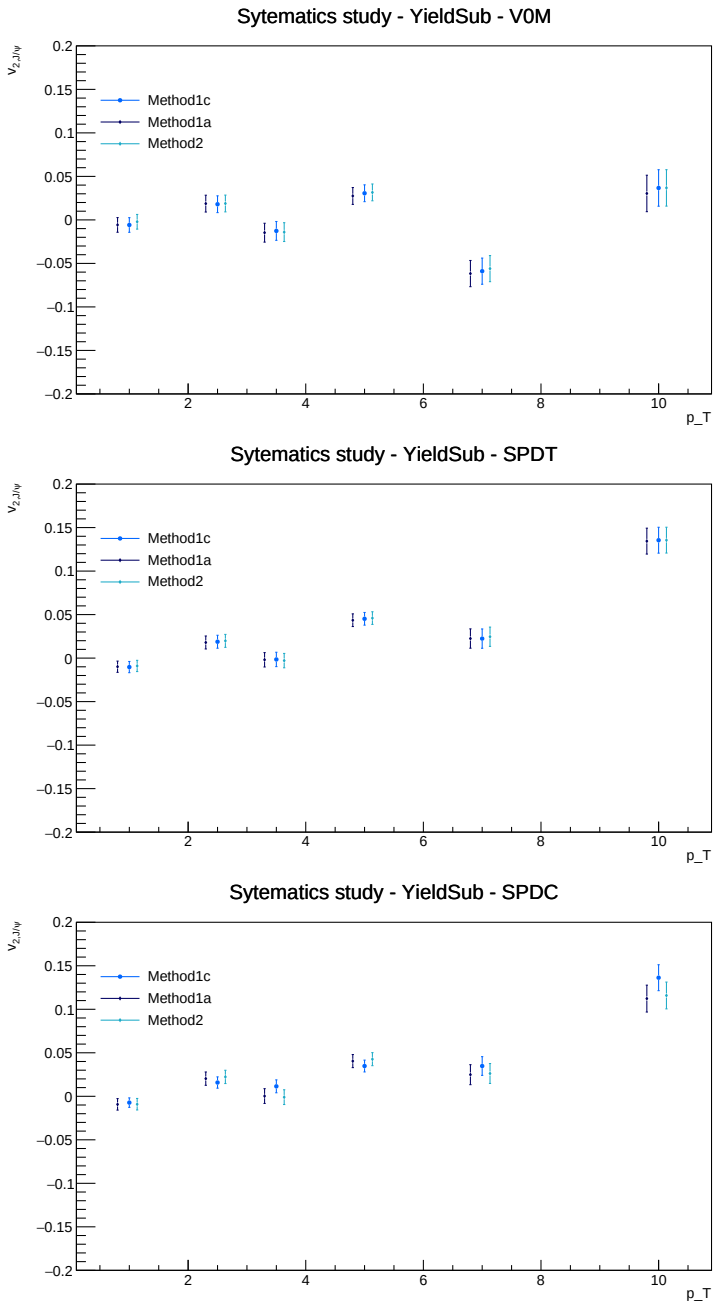

Figure E.15: Plot of the systematic variations on J/ψ elliptic flow from Yield subtraction - Comparison of methods of z_{vtx} summation (1a: Chisquare, 1c: Poisson, 2: weighted average). Top: V0M, Middle: SPDTracklets, Bottom: SPDClusters

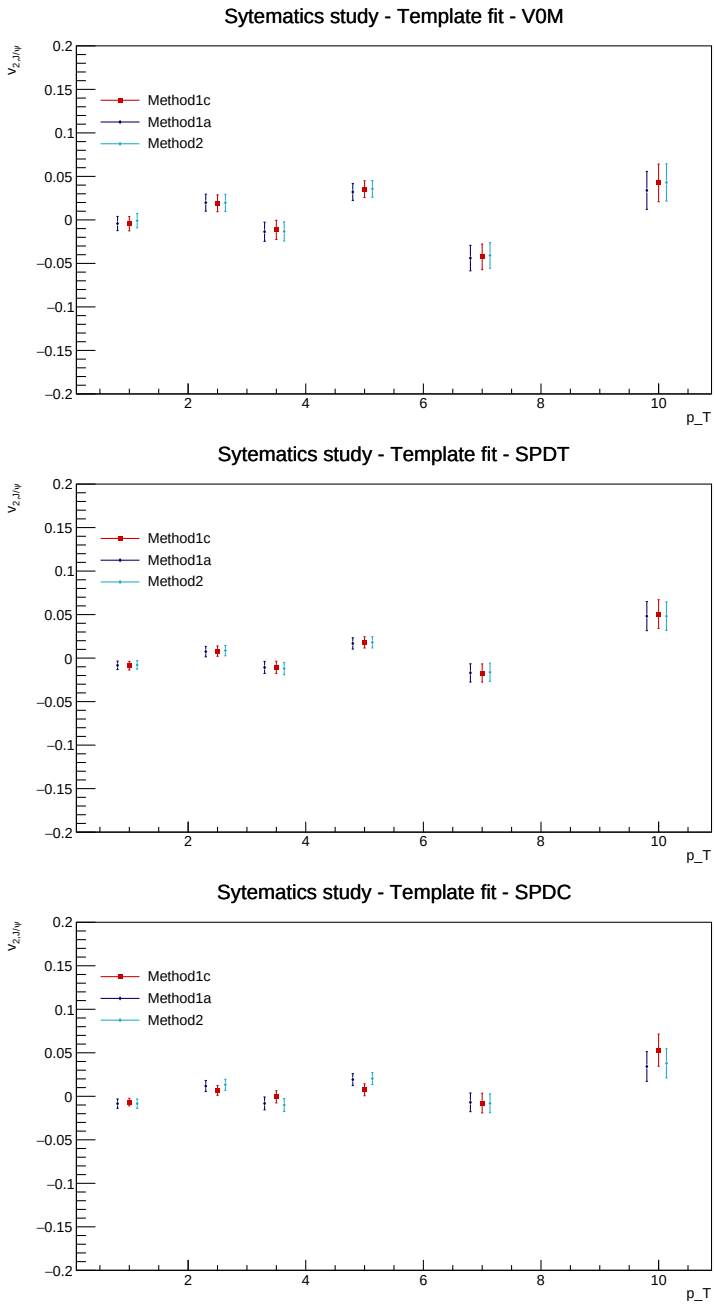

Figure E.16: Plot of the systematic variations on J/ψ elliptic flow from Template fit - Comparison of methods of z_{vtx} summation (1a: Chisquare, 1c: Poisson, 2: weighted average). Top: V0M, Middle: SPDTracklets, Bottom: SPDClusters

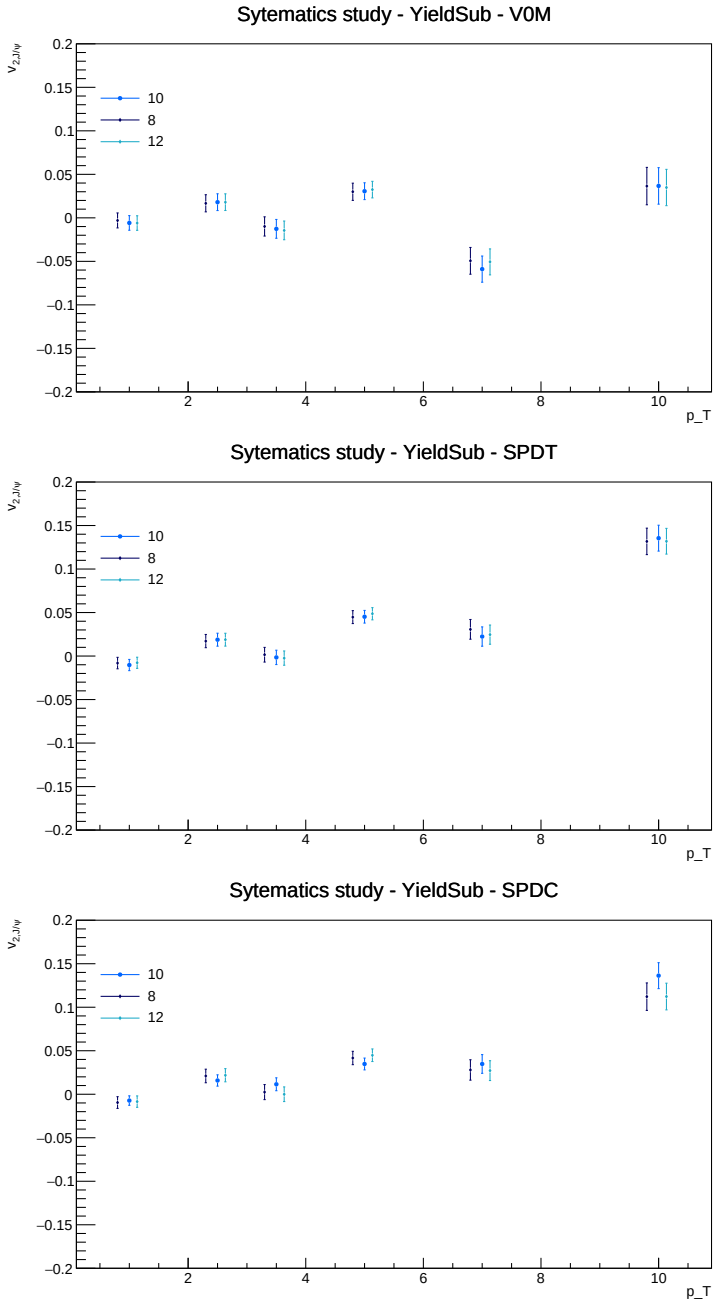

Figure E.17: Plot of the systematic variations on J/ψ elliptic flow from Yield subtraction - Comparison of z_{vtx} cut. Top: V0M, Middle: SPDTracklets, Bottom: SPDClusters

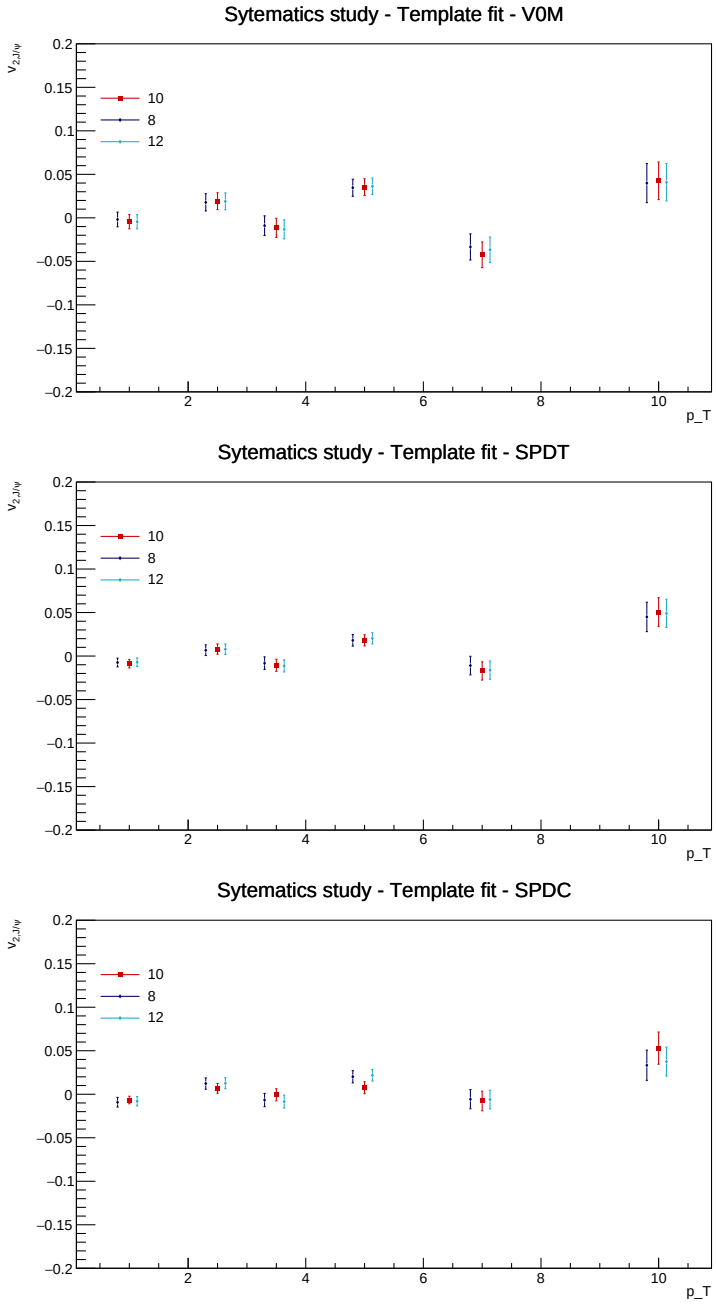

Figure E.18: Plot of the systematic variations on J/ψ elliptic flow from Template fit - Comparison of z_{vtx} cut. Top: V0M, Middle: SPDTracklets, Bottom: SPDClusters

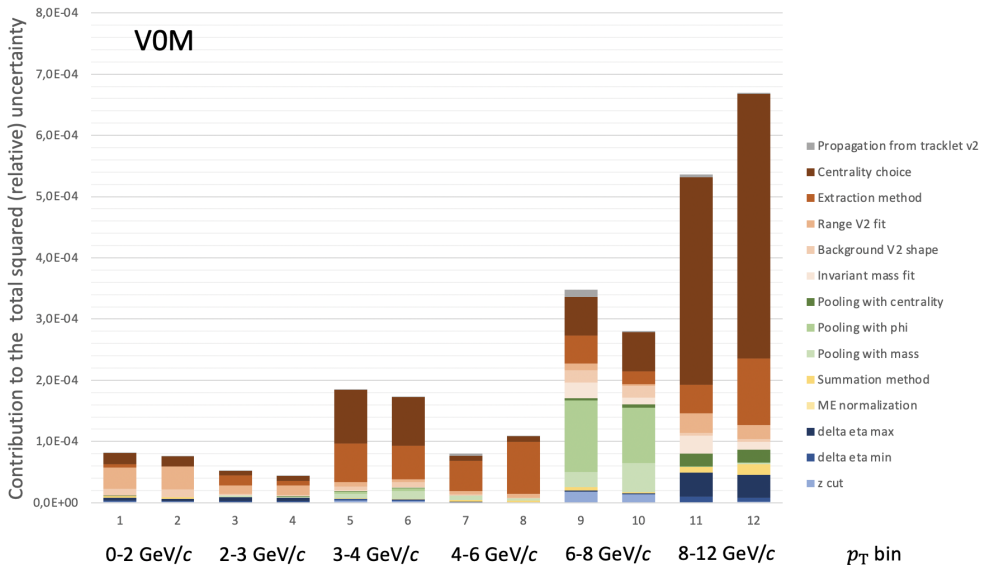

Figure E.19: Bar graph of the contribution of each uncertainty source to the squared total (absolute) uncertainty on J/ψ v_2 for V0M and extraction methods as a function of the transverse momentum. Uncertainties linked to extraction steps are in orange, pooling in green, yields definition in yellow, and selection cuts in blue.

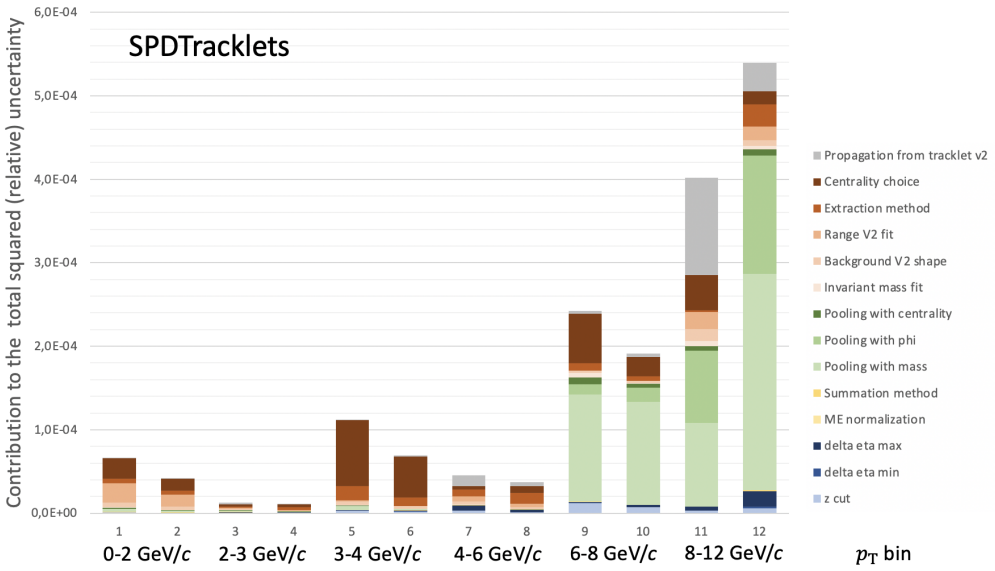

Figure E.20: Bar graph of the contribution of each uncertainty source to the squared total (absolute) uncertainty on J/ψ v_2 for V0M and extraction methods as a function of the transverse momentum. Uncertainties linked to extraction steps are in orange, pooling in green, yields definition in yellow, and selection cuts in blue.

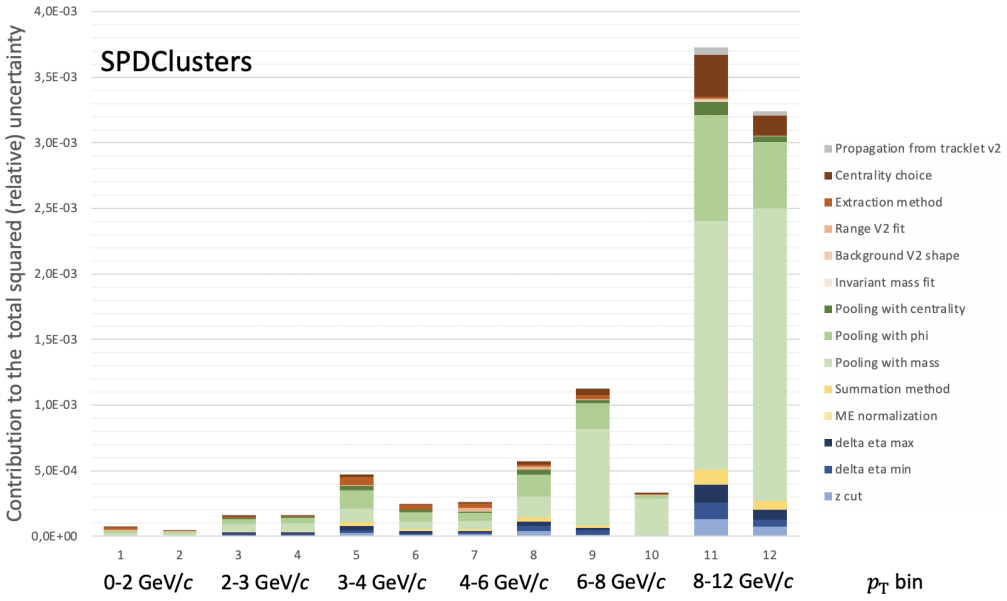

Figure E.21: Bar graph of the contribution of each uncertainty source to the squared total (absolute) uncertainty on J/ψ v_2 for V0M and extraction methods as a function of the transverse momentum. Uncertainties linked to extraction steps are in orange, pooling in green, yields definition in yellow, and selection cuts in blue.

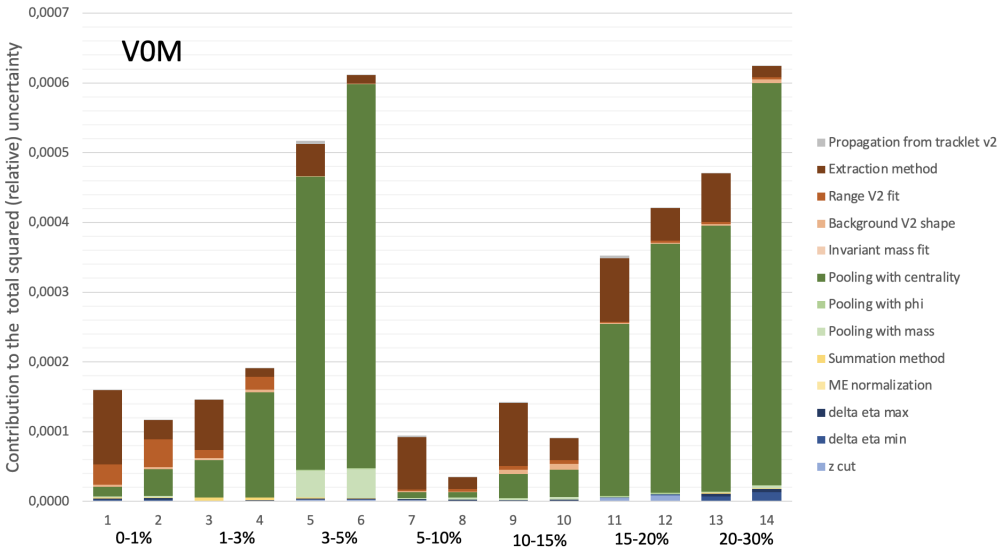

Figure E.22: Bar graph of the contribution of each uncertainty source to the squared total (absolute) uncertainty on J/ψ v_2 for V0M and extraction methods as a function of the central class. Uncertainties linked to extraction steps are in orange, pooling in green, yields definition in yellow, and selection cuts in blue.

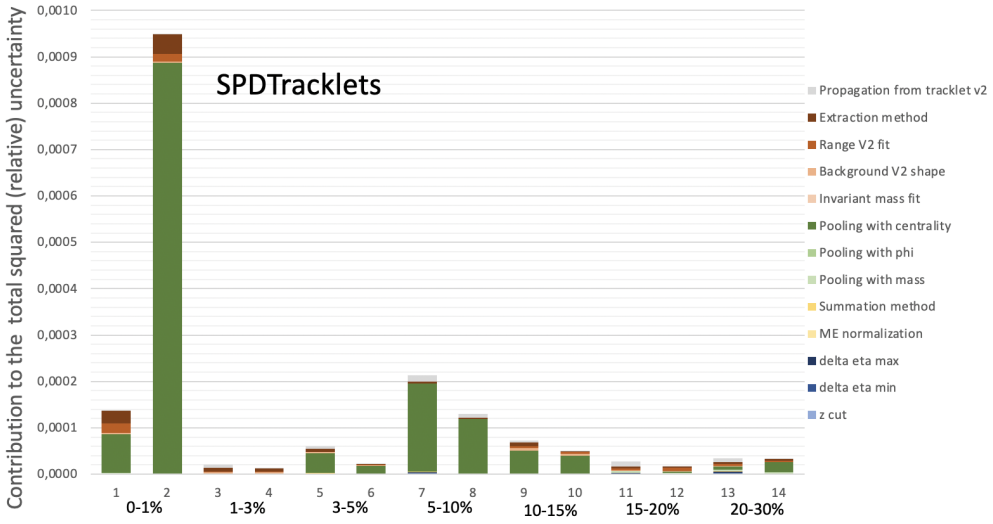

Figure E.23: Bar graph of the contribution of each uncertainty source to the squared total (absolute) uncertainty on J/ψ v_2 for V0M and extraction methods as a function of the central class. Uncertainties linked to extraction steps are in orange, pooling in green, yields definition in yellow, and selection cuts in blue.

List of Figures

List of Tables

Bibliography

[1] R. J. Quirk, "The "appendix probi" as a compendium of popular latin: Description and bibliography," *The Classical World*, vol. 98, no. 4, pp. 397–409, 2005.

[2] MissMJ and Cush for Wikimedia Commons, "Standard model of elementary particles," 2019.

[3] G. Aad *et al.*, "Observation of a new particle in the search for the Standard Model Higgs boson with the ATLAS detector at the LHC," *Phys. Lett. B*, vol. 716, pp. 1–29, 2012.

[4] S. Chatrchyan *et al.*, "Observation of a New Boson at a Mass of 125 GeV with the CMS Experiment at the LHC," *Phys. Lett. B*, vol. 716, pp. 30–61, 2012.

[5] P. W. Higgs, "Broken Symmetries and the Masses of Gauge Bosons," *Phys. Rev. Lett.*, vol. 13, pp. 508–509, 1964.

[6] C. Bambi and A. Dolgov, *Introduction to Particle Cosmology: The Standard Model of Cosmology and its Open Problems*. Springer Berlin, Heidelberg, 2016.

[7] G. Bertone and D. Hooper, "History of dark matter," *Rev. Mod. Phys.*, vol. 90, no. 4, p. 045002, 2018.

[8] G. Arcadi, M. Dutra, P. Ghosh, M. Lindner, Y. Mambrini, M. Pierre, S. Profumo, and F. S. Queiroz, "The waning of the WIMP? A review of models, searches, and constraints," *Eur. Phys. J. C*, vol. 78, no. 3, p. 203, 2018.

[9] P. A. Zyla *et al.*, "Review of Particle Physics - 89. Supersymmetry Part I - Theory," *PTEP*, vol. 2020, no. 8, p. 083C01, 2020.

[10] W. Adam and I. Vivarelli, "Status of searches for electroweak-scale supersymmetry after LHC Run 2," *Int. J. Mod. Phys. A*, vol. 37, no. 02, p. 2130022, 2022.

[11] P. A. Zyla *et al.*, "Review of Particle Physics - 89. Supersymmetry Part II - Experiment," *PTEP*, vol. 2020, no. 8, p. 083C01, 2020.

[12] R. Aaij *et al.*, "Test of lepton universality in beauty-quark decays," *Nature Phys.*, vol. 18, no. 3, pp. 277–282, 2022.

[13] A. M. Sirunyan *et al.*, "Search for singly and pair-produced leptoquarks coupling to third-generation fermions in proton-proton collisions at s=13 TeV," *Phys. Lett. B*, vol. 819, p. 136446, 2021.

[14] A. Bettini, *Introduction to Elementary Particle Physics*. Cambridge University Press, 2 ed., 2014.

[15] M. Thomson, *Modern Particle Physics*. Cambridge University Press, 2013.

[16] F. Halzen and A. D. Martin, *QUARKS AND LEPTONS: AN INTRODUCTORY COURSE IN MODERN PARTICLE PHYSICS*. 1984.

[17] R. K. Ellis, W. J. Stirling, and B. R. Webber, *QCD and Collider Physics*. Cambridge Monographs on Particle Physics, Nuclear Physics and Cosmology, Cambridge University Press, 1996.

[18] R. Aaij *et al.*, "Observation of $J/\psi p$ Resonances Consistent with Pentaquark States in $\Lambda_b^0 \to J/\psi K^- p$ Decays," *Phys. Rev. Lett.*, vol. 115, p. 072001, 2015.

[19] H. Sazdjian, "Introduction to chiral symmetry in QCD," *EPJ Web Conf.*, vol. 137, p. 02001, 2017.

[20] V. Friese, "Computational Challenges for the CBM Experiment," in *Mathematical Modeling and Computational Science*, (Berlin, Heidelberg), pp. 17–27, Springer Berlin Heidelberg, 01 2012.

[21] A. Andronic, P. Braun-Munzinger, K. Redlich, and J. Stachel, "Decoding the phase structure of QCD via particle production at high energy," *Nature*, vol. 561, no. 7723, pp. 321–330, 2018.

[22] G. Martinez, "Advances in Quark Gluon Plasma," 4 2013, arXiv:1304.1452.

[23] M. L. Miller, K. Reygers, S. J. Sanders, and P. Steinberg, "Glauber modeling in high-energy nuclear collisions," *Annual Review of Nuclear and Particle Science*, vol. 57, no. 1, pp. 205–243, 2007.

[24] J. D. Bjorken, "Highly relativistic nucleus-nucleus collisions: The central rapidity region," *Phys. Rev. D*, vol. 27, pp. 140–151, Jan 1983.

[25] B. Betz, "Jet Propagation and Mach-Cone Formation in (3+1)-dimensional Ideal Hydrodynamics," Master's thesis, 10 2009, arXiv:0910.4114.

[26] F. Gelis, E. Iancu, J. Jalilian-Marian, and R. Venugopalan, "The Color Glass Condensate," *Ann. Rev. Nucl. Part. Sci.*, vol. 60, pp. 463–489, 2010.

[27] F. Gelis, "Some Aspects of the Theory of Heavy Ion Collisions," *Rept. Prog. Phys.*, vol. 84, no. 5, p. 056301, 2021.

[28] S. Acharya *et al.*, "Anisotropic flow of identified particles in Pb-Pb collisions at $\sqrt{s}_{\rm NN} = 5.02$ TeV," *JHEP*, vol. 09, p. 006, 2018.

[29] Y. Akiba *et al.*, "The Hot QCD White Paper: Exploring the Phases of QCD at RHIC and the LHC," 2 2015, arXiv:1502.02730.

[30] J. Adam *et al.*, "Centrality dependence of the pseudorapidity density distribution for charged particles in Pb-Pb collisions at $\sqrt{s_{\rm NN}} = 5.02$ TeV," *Phys. Lett. B*, vol. 772, pp. 567–577, 2017.

[31] J. Rafelski, "Formation and Observables of the Quark-Gluon Plasma," *Phys. Rept.*, vol. 88, p. 331, 1982.

[32] J. Rafelski and B. Müller, "Strangeness production in the quark-gluon plasma," *Phys. Rev. Lett.*, vol. 56, pp. 2334–2334, May 1986.

[33] P. Koch, B. Muller, and J. Rafelski, "Strangeness in Relativistic Heavy Ion Collisions," *Phys. Rept.*, vol. 142, pp. 167–262, 1986.

[34] B. Müller, "Diagnosing the Quark-Gluon Plasma," 6 2021, arXiv:2106.11923.

[35] B. Muller, "Physics and signatures of the quark - gluon plasma," *Rept. Prog. Phys.*, vol. 58, pp. 611–636, 1995.

[36] P. Zyla *et al.*, "Review of Particle Physics," *PTEP*, vol. 2020, no. 8, p. 083C01, 2020. and 2021 update.

[37] T. Song, C. M. Ko, and S. H. Lee, "Quarkonium formation time in relativistic heavy-ion collisions," *Phys. Rev. C*, vol. 91, no. 4, p. 044909, 2015.

[38] S. Jacobs, M. G. Olsson, and C. Suchyta, III, "Comparing the Schrodinger and Spinless Salpeter Equations for Heavy Quark Bound States," *Phys. Rev. D*, vol. 33, p. 3338, 1986. [Erratum: Phys.Rev.D 34, 3536 (1986)].

[39] E. Eichten, K. Gottfried, T. Kinoshita, K. Lane, and T.-M. Yan, "Charmonium: The model," in *Quarkonia* (W. BUCHMÜLLER, ed.), vol. 9 of *Current Physics–Sources and Comments*, pp. 48–75, Elsevier, 1992.

[40] E. Eichten, K. Gottfried, T. Kinoshita, K. D. Lane, and T. M. Yan, "Charmonium: Comparison with experiment," *Phys. Rev. D*, vol. 21, pp. 203–233, Jan 1980.

[41] J.-P. Lansberg, "New Observables in Inclusive Production of Quarkonia," *Phys. Rept.*, vol. 889, pp. 1–106, 2020.

[42] H. Fritzsch, "Producing heavy quark flavors in hadronic collisions—' a test of quantum chromodynamics," *Physics Letters B*, vol. 67, no. 2, pp. 217–221, 1977.

[43] F. Halzen, "Cvc for gluons and hadroproduction of quark flavours," *Physics Letters B*, vol. 69, no. 1, pp. 105–108, 1977.

[44] J. F. Amundson, O. J. P. Eboli, E. M. Gregores, and F. Halzen, "Colorless states in perturbative QCD: Charmonium and rapidity gaps," *Phys. Lett. B*, vol. 372, pp. 127–132, 1996.

[45] M. B. Einhorn and S. D. Ellis, "Hadronic production of the new resonances: Probing gluon distributions," *Phys. Rev. D*, vol. 12, pp. 2007–2014, Oct 1975.

[46] C. Chao-Hsi, "Hadronic production of j/ψ associated with a gluon," *Nuclear Physics B*, vol. 172, pp. 425–434, 1980.

[47] W. Caswell and G. Lepage, "Effective lagrangians for bound state problems in qed, qcd, and other field theories," *Physics Letters B*, vol. 167, no. 4, pp. 437–442, 1986.

[48] G. T. Bodwin, E. Braaten, and G. P. Lepage, "Rigorous QCD analysis of inclusive annihilation and production of heavy quarkonium," *Phys. Rev. D*, vol. 51, pp. 1125–1171, 1995. [Erratum: Phys.Rev.D 55, 5853 (1997)].

[49] P. Debye and E. Hückel, "Zur theorie der elektrolyte. i. gefrierpunktserniedrigung und verwandte erscheinungen," *Physikalische Zeitschrift*, vol. 24, no. 185, p. 305, 1923.

[50] T. Matsui and H. Satz, "j/ψ suppression by quark-gluon plasma formation," *Physics Letters B*, vol. 178, no. 4, pp. 416–422, 1986.

[51] F. Karsch, M. T. Mehr, and H. Satz, "Color Screening and Deconfinement for Bound States of Heavy Quarks," *Z. Phys. C*, vol. 37, p. 617, 1988.

[52] F. Karsch, D. Kharzeev, and H. Satz, "Sequential charmonium dissociation," *Physics Letters B*, vol. 637, no. 1, pp. 75–80, 2006.

[53] H. Satz, "Colour deconfinement and quarkonium binding," *J. Phys. G*, vol. 32, p. R25, 2006.

[54] A. Rothkopf, "Heavy Quarkonium in Extreme Conditions," *Phys. Rept.*, vol. 858, pp. 1–117, 2020.

[55] M. A. Escobedo, F. Giannuzzi, M. Mannarelli, and J. Soto, "Heavy Quarkonium moving in a Quark-Gluon Plasma," *Phys. Rev. D*, vol. 87, no. 11, p. 114005, 2013.

[56] H. Satz, "Colour deconfinement and quarkonium binding," *Journal of Physics G: Nuclear and Particle Physics*, vol. 32, pp. R25–R69, feb 2006.

[57] P. Braun-Munzinger and J. Stachel, "(Non)thermal aspects of charmonium production and a new look at J / psi suppression," *Phys. Lett. B*, vol. 490, pp. 196–202, 2000.

[58] R. L. Thews, M. Schroedter, and J. Rafelski, "Enhanced J/ψ production in deconfined quark matter," *Phys. Rev. C*, vol. 63, p. 054905, 2001.

[59] P. Braun-Munzinger and J. Stachel, "The quest for the quark–gluon plasma," *Nature*, vol. 448, pp. 302–309, 2007.

[60] A. Andronic *et al.*, "Heavy-flavour and quarkonium production in the LHC era: from proton–proton to heavy-ion collisions," *Eur. Phys. J. C*, vol. 76, no. 3, p. 107, 2016.

[61] R. Vogt, "Cold Nuclear Matter Effects on J/ψ and Υ Production at the LHC," *Phys. Rev. C*, vol. 81, p. 044903, 2010.

[62] N. Armesto, "Nuclear shadowing," *J. Phys. G*, vol. 32, pp. R367–R394, 2006.

[63] H. Fujii and K. Watanabe, "Heavy quark pair production in high energy pA collisions: Quarkonium," *Nucl. Phys. A*, vol. 915, pp. 1–23, 2013.

[64] J. J. Aubert *et al.*, "The ratio of the nucleon structure functions $F2_n$ for iron and deuterium," *Phys. Lett. B*, vol. 123, pp. 275–278, 1983.

[65] Diaconu, Cristinel and Sauvan, Emmanuel, "Hera: a super-microscope for the proton at the energy frontier," *Europhysics News*, vol. 40, no. 5, pp. 21–25, 2009.

[66] D. Kharzeev and H. Satz, "Charmonium composition and nuclear suppression," *Phys. Lett. B*, vol. 366, pp. 316–322, 1996.

[67] F. Arleo, S. Peigne, and T. Sami, "Revisiting scaling properties of medium-induced gluon radiation," *Phys. Rev. D*, vol. 83, p. 114036, 2011.

[68] B. Jacak, "d+au at phenix: Insights on the cronin effect, shadowing and saturation," *Annals of Physics*, vol. 352, pp. 3–10, 2015. Special Issue Honoring Prof. Wit Busza.

[69] A. Capella, A. Kaidalov, A. Kouider Akil, and C. Gerschel, "j/ψ and ψ' suppression in heavy ion collisions," *Physics Letters B*, vol. 393, no. 3, pp. 431–436, 1997.

[70] E. G. Ferreiro, "Charmonium dissociation and recombination at LHC: Revisiting comovers," *Phys. Lett. B*, vol. 731, pp. 57–63, 2014.

[71] S. Ragoni, "UPC: a powerful tool for J/ψ photoproduction analysis in ALICE," *PoS*, vol. LHCP2020, p. 255, 2021.

[72] J. G. Contreras and J. D. Tapia Takaki, "Ultra-peripheral heavy-ion collisions at the LHC," *Int. J. Mod. Phys. A*, vol. 30, p. 1542012. 19 p, 2015.

[73] ALICE Collaboration, "Photoproduction of low-p_{T} J/ψ from peripheral to central Pb$-$Pb collisions at 5.02 TeV," 4 2022, arXiv:2204.10684.

[74] J. Adam *et al.*, "J/ψ suppression at forward rapidity in Pb-Pb collisions at $\sqrt{\mathbf{s}_{\mathrm{NN}}} = \mathbf{5.02}$ TeV," *Phys. Lett. B*, vol. 766, pp. 212–224, 2017.

[75] A. Andronic, P. Braun-Munzinger, K. Redlich, and J. Stachel, "The statistical model in Pb-Pb collisions at the LHC," *Nucl. Phys. A*, vol. 904-905, pp. 535c–538c, 2013.

[76] X. Zhao and R. Rapp, "Medium Modifications and Production of Charmonia at LHC," *Nucl. Phys. A*, vol. 859, pp. 114–125, 2011.

[77] K. Zhou, N. Xu, Z. Xu, and P. Zhuang, "Medium effects on charmonium production at ultrarelativistic energies available at the CERN Large Hadron Collider," *Phys. Rev. C*, vol. 89, no. 5, p. 054911, 2014.

[78] X. Du and R. Rapp, "Sequential Regeneration of Charmonia in Heavy-Ion Collisions," *Nucl. Phys. A*, vol. 943, pp. 147–158, 2015.

[79] E. G. Ferreiro, "Excited charmonium suppression in proton–nucleus collisions as a consequence of comovers," *Phys. Lett. B*, vol. 749, pp. 98–103, 2015.

[80] S. Acharya *et al.*, "Studies of J/ψ production at forward rapidity in Pb-Pb collisions at $\sqrt{s_{\mathrm{NN}}} =$ 5.02 TeV," *JHEP*, vol. 02, p. 041, 2020.

[81] A. M. Sirunyan *et al.*, "Measurement of prompt and nonprompt charmonium suppression in PbPb collisions at 5.02 TeV," *Eur. Phys. J. C*, vol. 78, no. 6, p. 509, 2018.

[82] ATLAS Collaboration, "Production of $\Upsilon(\mathrm{nS})$ mesons in Pb+Pb and pp collisions at 5.02 TeV," 5 2022, arXiv:2205.03042.

[83] CMS Collaboration, "Observation of the $\Upsilon\mathrm{(3S)}$ meson and sequential suppression of Υ states in PbPb collisions at $\sqrt{\mathrm{s_{NN}}} = 5.02$ TeV," tech. rep., CERN, Geneva, 2022.

[84] S. Acharya *et al.*, "Υ production and nuclear modification at forward rapidity in Pb–Pb collisions at sNN=5.02TeV," *Phys. Lett. B*, vol. 822, p. 136579, 2021.

[85] M. B. Gay Ducati and S. Martins, "Heavy meson photoproduction in peripheral AA collisions," *Phys. Rev. D*, vol. 97, no. 11, p. 116013, 2018.

[86] J. Cepila, J. G. Contreras, and M. Krelina, "Coherent and incoherent J/ψ photonuclear production in an energy-dependent hot-spot model," *Phys. Rev. C*, vol. 97, no. 2, p. 024901, 2018.

[87] M. Kłusek-Gawenda and A. Szczurek, "Photoproduction of J/ψ mesons in peripheral and semi-central heavy ion collisions," *Phys. Rev. C*, vol. 93, no. 4, p. 044912, 2016.

[88] M. Kłusek-Gawenda, R. Rapp, W. Schäfer, and A. Szczurek, "Dilepton Radiation in Heavy-Ion Collisions at Small Transverse Momentum," *Phys. Lett. B*, vol. 790, pp. 339–344, 2019.

[89] P. Faccioli, C. Lourenco, J. Seixas, and H. K. Wohri, "Towards the experimental clarification of quarkonium polarization," *Eur. Phys. J. C*, vol. 69, pp. 657–673, 2010.

[90] M. Butenschoen and B. A. Kniehl, "J/psi polarization at Tevatron and LHC: Nonrelativistic-QCD factorization at the crossroads," *Phys. Rev. Lett.*, vol. 108, p. 172002, 2012.

[91] B. Abelev *et al.*, "J/ψ polarization in pp collisions at $\sqrt{s} = 7$ TeV," *Phys. Rev. Lett.*, vol. 108, p. 082001, 2012.

[92] S. Acharya *et al.*, "Measurement of the inclusive J/ ψ polarization at forward rapidity in pp collisions at $\sqrt{\mathrm{s}} = 8$ TeV," *Eur. Phys. J. C*, vol. 78, no. 7, p. 562, 2018.

[93] R. Aaij *et al.*, "Measurement of J/ψ polarization in pp collisions at $\sqrt{s} = 7$ TeV," *Eur. Phys. J. C*, vol. 73, no. 11, p. 2631, 2013.

[94] R. Aaij *et al.*, "Measurement of the Υ polarizations in pp collisions at $\sqrt{s} = 7$ and 8 TeV," *JHEP*, vol. 12, p. 110, 2017.

[95] S. Chatrchyan *et al.*, "Measurement of the Prompt J/ψ and ψ(2S) Polarizations in pp Collisions at $\sqrt{s} = 7$ TeV," *Phys. Lett. B*, vol. 727, pp. 381–402, 2013.

[96] V. Khachatryan *et al.*, "$\Upsilon(\mathrm{nS})$ polarizations versus particle multiplicity in pp collisions at $\sqrt{s} =$ 7 TeV," *Phys. Lett. B*, vol. 761, pp. 31–52, 2016.

[97] S. Acharya *et al.*, "First measurement of quarkonium polarization in nuclear collisions at the LHC," *Phys. Lett. B*, vol. 815, p. 136146, 2021.

[98] S. Acharya *et al.*, "Evidence of Spin-Orbital Angular Momentum Interactions in Relativistic Heavy-Ion Collisions," *Phys. Rev. Lett.*, vol. 125, no. 1, p. 012301, 2020.

[99] R. Pasechnik and M. Šumbera, "Phenomenological review on quark–gluon plasma: Concepts vs. observations," *Universe*, vol. 3, no. 1, 2017.

[100] S. Acharya *et al.*, "J/ψ elliptic and triangular flow in Pb-Pb collisions at $\sqrt{s_{\mathrm{NN}}} = 5.02$ TeV," *JHEP*, vol. 10, p. 141, 2020.

[101] M. He, H. van Hees, and R. Rapp, "Heavy-Quark Diffusion in the Quark-Gluon Plasma," 4 2022, arXiv:2204.09299.

[102] S. Acharya *et al.*, "Search for collectivity with azimuthal J/ψ-hadron correlations in high multiplicity p-Pb collisions at $\sqrt{s_{\rm NN}}$ = 5.02 and 8.16 TeV," *Phys. Lett. B*, vol. 780, pp. 7–20, 2018.

[103] S. Chatrchyan *et al.*, "Observation of Long-Range Near-Side Angular Correlations in Proton-Lead Collisions at the LHC," *Phys. Lett. B*, vol. 718, pp. 795–814, 2013.

[104] G. Aad *et al.*, "Observation of Associated Near-Side and Away-Side Long-Range Correlations in $\sqrt{s_{NN}}$=5.02 TeV Proton-Lead Collisions with the ATLAS Detector," *Phys. Rev. Lett.*, vol. 110, no. 18, p. 182302, 2013.

[105] V. Khachatryan *et al.*, "Measurement of long-range near-side two-particle angular correlations in pp collisions at $\sqrt{s}$ =13 TeV," *Phys. Rev. Lett.*, vol. 116, no. 17, p. 172302, 2016.

[106] V. Khachatryan *et al.*, "Observation of Long-Range Near-Side Angular Correlations in Proton-Proton Collisions at the LHC," *JHEP*, vol. 09, p. 091, 2010.

[107] G. Aad *et al.*, "Observation of Long-Range Elliptic Azimuthal Anisotropies in $\sqrt{s}$ =13 and 2.76 TeV pp Collisions with the ATLAS Detector," *Phys. Rev. Lett.*, vol. 116, no. 17, p. 172301, 2016.

[108] G. Aad *et al.*, "Measurement of azimuthal anisotropy of muons from charm and bottom hadrons in pp collisions at $\sqrt{s} = 13$ TeV with the ATLAS detector," *Phys. Rev. Lett.*, vol. 124, no. 8, p. 082301, 2020.

[109] X. Du and R. Rapp, "In-Medium Charmonium Production in Proton-Nucleus Collisions," *JHEP*, vol. 03, p. 015, 2019.

[110] R. Snellings, "Elliptic Flow: A Brief Review," *New J. Phys.*, vol. 13, p. 055008, 2011.

[111] S. A. Voloshin, A. M. Poskanzer, and R. Snellings, "Collective phenomena in non-central nuclear collisions," *Landolt-Bornstein*, vol. 23, pp. 293–333, 2010.

[112] N. Herrmann, J. P. Wessels, and T. Wienold, "Collective flow in heavy-ion collisions," *Annual Review of Nuclear and Particle Science*, vol. 49, no. 1, pp. 581–632, 1999.

[113] J.-Y. Ollitrault, "Anisotropy as a signature of transverse collective flow," *Phys. Rev. D*, vol. 46, pp. 229–245, Jul 1992.

[114] U. Heinz and R. Snellings, "Collective flow and viscosity in relativistic heavy-ion collisions," *Ann. Rev. Nucl. Part. Sci.*, vol. 63, pp. 123–151, 2013.

[115] H. Song, Y. Zhou, and K. Gajdosova, "Collective flow and hydrodynamics in large and small systems at the LHC," *Nucl. Sci. Tech.*, vol. 28, no. 7, p. 99, 2017.

[116] C. Gale, S. Jeon, and B. Schenke, "Hydrodynamic Modeling of Heavy-Ion Collisions," *Int. J. Mod. Phys. A*, vol. 28, p. 1340011, 2013.

[117] R. D. Weller and P. Romatschke, "One fluid to rule them all: viscous hydrodynamic description of event-by-event central p+p, p+Pb and Pb+Pb collisions at $\sqrt{s} = 5.02$ TeV," *Phys. Lett. B*, vol. 774, pp. 351–356, 2017.

[118] W. Zhao, Y. Zhou, H. Xu, W. Deng, and H. Song, "Hydrodynamic collectivity in proton–proton collisions at 13 TeV," *Phys. Lett. B*, vol. 780, pp. 495–500, 2018.

[119] S. A. Bass *et al.*, "Microscopic models for ultrarelativistic heavy ion collisions," *Prog. Part. Nucl. Phys.*, vol. 41, pp. 255–369, 1998.

[120] A. Bzdak and G.-L. Ma, "Elliptic and triangular flow in p+Pb and peripheral Pb+Pb collisions from parton scatterings," *Phys. Rev. Lett.*, vol. 113, no. 25, p. 252301, 2014.

[121] K. Dusling, M. Mace, and R. Venugopalan, "Multiparticle collectivity from initial state correlations in high energy proton-nucleus collisions," *Phys. Rev. Lett.*, vol. 120, no. 4, p. 042002, 2018.

[122] S. Voloshin and Y. Zhang, "Flow study in relativistic nuclear collisions by Fourier expansion of Azimuthal particle distributions," *Z. Phys. C*, vol. 70, pp. 665–672, 1996.

[123] A. M. Poskanzer and S. A. Voloshin, "Methods for analyzing anisotropic flow in relativistic nuclear collisions," *Phys. Rev. C*, vol. 58, pp. 1671–1678, 1998.

[124] J. Barrette *et al.*, "Energy and charged particle flow in a 10.8-A/GeV/c Au + Au collisions," *Phys. Rev. C*, vol. 55, pp. 1420–1430, 1997. [Erratum: Phys.Rev.C 56, 2336–2336 (1997)].

[125] S. Wang, Y. Z. Jiang, Y. M. Liu, D. Keane, D. Beavis, S. Y. Chu, S. Y. Fung, M. Vient, C. Hartnack, and H. Stoecker, "Measurement of collective flow in heavy ion collisions using particle pair correlations," *Phys. Rev. C*, vol. 44, pp. 1091–1095, 1991.

[126] N. Borghini, P. M. Dinh, and J.-Y. Ollitrault, "A New method for measuring azimuthal distributions in nucleus-nucleus collisions," *Phys. Rev. C*, vol. 63, p. 054906, 2001.

[127] N. Borghini, P. M. Dinh, and J.-Y. Ollitrault, "Flow analysis from multiparticle azimuthal correlations," *Phys. Rev. C*, vol. 64, p. 054901, 2001.

[128] N. Borghini, P. M. Dinh, and J.-Y. Ollitrault, "Flow analysis from cumulants: A Practical guide," in *International Workshop on the Physics of the Quark Gluon Plasma*, 10 2001, arXiv:nucl-ex/0110016.

[129] A. Bilandzic, R. Snellings, and S. Voloshin, "Flow analysis with cumulants: Direct calculations," *Phys. Rev. C*, vol. 83, p. 044913, 2011.

[130] N. Borghini, P. M. Dinh, and J.-Y. Ollitrault, "Are flow measurements at SPS reliable?," *Phys. Rev. C*, vol. 62, p. 034902, 2000.

[131] P. M. Dinh, N. Borghini, and J.-Y. Ollitrault, "Effects of HBT correlations on flow measurements," *Phys. Lett. B*, vol. 477, pp. 51–58, 2000.

[132] M. A. Lisa, S. Pratt, R. Soltz, and U. Wiedemann, "Femtoscopy in relativistic heavy ion collisions," *Ann. Rev. Nucl. Part. Sci.*, vol. 55, pp. 357–402, 2005.

[133] P. Danielewicz, H. Ströbele, G. Odyniec, D. Bangert, R. Bock, R. Brockmann, J. W. Harris, H. G. Pugh, W. Rauch, R. E. Renfordt, A. Sandoval, D. Schall, L. S. Schroeder, and R. Stock, "Collective motion in nucleus-nucleus collisions at 800 mev/nucleon," *Phys. Rev. C*, vol. 38, pp. 120–134, Jul 1988.

[134] S. H. Lim, Q. Hu, R. Belmont, K. K. Hill, J. L. Nagle, and D. V. Perepelitsa, "Examination of flow and nonflow factorization methods in small collision systems," *Phys. Rev. C*, vol. 100, no. 2, p. 024908, 2019.

[135] V. Khachatryan *et al.*, "Evidence for collectivity in pp collisions at the LHC," *Phys. Lett. B*, vol. 765, pp. 193–220, 2017.

[136] M. Aaboud *et al.*, "Measurements of long-range azimuthal anisotropies and associated Fourier coefficients for pp collisions at $\sqrt{s} = 5.02$ and 13 TeV and p+Pb collisions at $\sqrt{s_{\mathrm{NN}}} = 5.02$ TeV with the ATLAS detector," *Phys. Rev. C*, vol. 96, no. 2, p. 024908, 2017.

[137] M. Aaboud *et al.*, "Correlated long-range mixed-harmonic fluctuations measured in pp, p+Pb and low-multiplicity Pb+Pb collisions with the ATLAS detector," *Phys. Lett. B*, vol. 789, pp. 444–471, 2019.

[138] J. Barrette *et al.*, "Observation of anisotropic event shapes and transverse flow in Au + Au collisions at AGS energy," *Phys. Rev. Lett.*, vol. 73, pp. 2532–2535, 1994.

[139] C. Alt *et al.*, "Directed and elliptic flow of charged pions and protons in Pb + Pb collisions at 40-A-GeV and 158-A-GeV," *Phys. Rev. C*, vol. 68, p. 034903, 2003.

[140] K. H. Ackermann *et al.*, "Elliptic flow in Au + Au collisions at (S(NN))**(1/2) = 130 GeV," *Phys. Rev. Lett.*, vol. 86, pp. 402–407, 2001.

[141] J. Adam *et al.*, "Anisotropic flow of charged particles in Pb-Pb collisions at $\sqrt{s_{\mathrm{NN}}} = 5.02$ TeV," *Phys. Rev. Lett.*, vol. 116, no. 13, p. 132302, 2016.

[142] J. Noronha-Hostler, M. Luzum, and J.-Y. Ollitrault, "Hydrodynamic predictions for 5.02 TeV Pb-Pb collisions," *Phys. Rev. C*, vol. 93, no. 3, p. 034912, 2016.

[143] H. Niemi, K. J. Eskola, R. Paatelainen, and K. Tuominen, "Predictions for 5.023 TeV Pb + Pb collisions at the CERN Large Hadron Collider," *Phys. Rev. C*, vol. 93, no. 1, p. 014912, 2016.

[144] S. Acharya *et al.*, "Investigations of Anisotropic Flow Using Multiparticle Azimuthal Correlations in pp, p-Pb, Xe-Xe, and Pb-Pb Collisions at the LHC," *Phys. Rev. Lett.*, vol. 123, no. 14, p. 142301, 2019.

[145] T. Sjöstrand, S. Ask, J. R. Christiansen, R. Corke, N. Desai, P. Ilten, S. Mrenna, S. Prestel, C. O. Rasmussen, and P. Z. Skands, "An introduction to PYTHIA 8.2," *Comput. Phys. Commun.*, vol. 191, pp. 159–177, 2015.

[146] H. Mäntysaari, B. Schenke, C. Shen, and P. Tribedy, "Imprints of fluctuating proton shapes on flow in proton-lead collisions at the LHC," *Phys. Lett. B*, vol. 772, pp. 681–686, 2017.

[147] B. Schenke, P. Tribedy, and R. Venugopalan, "Multiplicity distributions in p+p, p+A and A+A collisions from Yang-Mills dynamics," *Phys. Rev. C*, vol. 89, no. 2, p. 024901, 2014.

[148] K. Aamodt *et al.*, "Elliptic flow of charged particles in Pb-Pb collisions at 2.76 TeV," *Phys. Rev. Lett.*, vol. 105, p. 252302, 2010.

[149] P. Huovinen, P. F. Kolb, U. W. Heinz, P. V. Ruuskanen, and S. A. Voloshin, "Radial and elliptic flow at RHIC: Further predictions," *Phys. Lett. B*, vol. 503, pp. 58–64, 2001.

[150] N. Borghini and J.-Y. Ollitrault, "Momentum spectra, anisotropic flow, and ideal fluids," *Phys. Lett. B*, vol. 642, pp. 227–231, 2006.

[151] J. Barrette *et al.*, "Directed flow of light nuclei in Au + Au collisions at AGS energies," *Phys. Rev. C*, vol. 59, pp. 884–888, 1999.

[152] J. Adam *et al.*, "Higher harmonic flow coefficients of identified hadrons in Pb-Pb collisions at $\sqrt{s_{\rm NN}} = 2.76$ TeV," *JHEP*, vol. 09, p. 164, 2016.

[153] D. Molnar and S. A. Voloshin, "Elliptic flow at large transverse momenta from quark coalescence," *Phys. Rev. Lett.*, vol. 91, p. 092301, 2003.

[154] R. J. Fries, V. Greco, and P. Sorensen, "Coalescence Models For Hadron Formation From Quark Gluon Plasma," *Ann. Rev. Nucl. Part. Sci.*, vol. 58, pp. 177–205, 2008.

[155] S. Afanasiev *et al.*, "Elliptic flow for phi mesons and (anti)deuterons in Au + Au collisions at $\sqrt{s_{NN}} = 200$ GeV," *Phys. Rev. Lett.*, vol. 99, p. 052301, 2007.

[156] L. Adamczyk *et al.*, "Centrality dependence of identified particle elliptic flow in relativistic heavy ion collisions at $\sqrt{s_{NN}}$=7.7–62.4 GeV," *Phys. Rev. C*, vol. 93, no. 1, p. 014907, 2016.

[157] S. Chatrchyan *et al.*, "Study of high-pT charged particle suppression in PbPb compared to pp collisions at $\sqrt{s_{NN}} = 2.76$ TeV," *Eur. Phys. J. C*, vol. 72, p. 1945, 2012.

[158] N. Armesto, A. Dainese, C. A. Salgado, and U. A. Wiedemann, "Testing the color charge and mass dependence of parton energy loss with heavy-to-light ratios at RHIC and CERN LHC," *Phys. Rev. D*, vol. 71, p. 054027, 2005.

[159] J. Adams *et al.*, "Azimuthal anisotropy at RHIC: The First and fourth harmonics," *Phys. Rev. Lett.*, vol. 92, p. 062301, 2004. [Erratum: Phys.Rev.Lett. 127, 069901 (2021)].

[160] G. Aad *et al.*, "Measurement of the azimuthal anisotropy for charged particle production in $\sqrt{s_{NN}} = 2.76$ TeV lead-lead collisions with the ATLAS detector," *Phys. Rev. C*, vol. 86, p. 014907, 2012.

[161] S. Acharya *et al.*, "Energy dependence and fluctuations of anisotropic flow in Pb-Pb collisions at $\sqrt{s_{\rm NN}} = 5.02$ and 2.76 TeV," *JHEP*, vol. 07, p. 103, 2018.

[162] H. Niemi, G. S. Denicol, H. Holopainen, and P. Huovinen, "Event-by-event distributions of azimuthal asymmetries in ultrarelativistic heavy-ion collisions," *Phys. Rev. C*, vol. 87, no. 5, p. 054901, 2013.

[163] L. Yan and J.-Y. Ollitrault, "$\nu_4, \nu_5, \nu_6, \nu_7$: nonlinear hydrodynamic response versus LHC data," *Phys. Lett. B*, vol. 744, pp. 82–87, 2015.

[164] G. Aad *et al.*, "Measurement of the correlation between flow harmonics of different order in lead-lead collisions at $\sqrt{s_{NN}}$=2.76 TeV with the ATLAS detector," *Phys. Rev. C*, vol. 92, no. 3, p. 034903, 2015.

[165] B. B. Back *et al.*, "Energy dependence of elliptic flow over a large pseudorapidity range in Au+Au collisions at RHIC," *Phys. Rev. Lett.*, vol. 94, p. 122303, 2005.

[166] T. Hirano, "Relativistic Hydrodynamics at RHIC and LHC," *Prog. Theor. Phys. Suppl.*, vol. 168, pp. 347–354, 2007.

[167] L. Adamczyk *et al.*, "Measurement of J/ψ Azimuthal Anisotropy in Au+Au Collisions at $\sqrt{s_{NN}}$ = 200 GeV," *Phys. Rev. Lett.*, vol. 111, no. 5, p. 052301, 2013.

[168] CMS Collaboration, "Measurements of the azimuthal anisotropy of charmonia in PbPb collisions at $\sqrt{\mathrm{s_{NN}}} = 5.02$ TeV," tech. rep., CERN, Geneva, 2022.

[169] A. M. Sirunyan *et al.*, "Measurement of the azimuthal anisotropy of $\Upsilon(1S)$ and $\Upsilon(2S)$ mesons in PbPb collisions at sNN=5.02TeV," *Phys. Lett. B*, vol. 819, p. 136385, 2021.

[170] S. Acharya *et al.*, "Measurement of $\Upsilon(1\mathrm{S})$ elliptic flow at forward rapidity in Pb-Pb collisions at $\sqrt{s_{\mathrm{NN}}} = 5.02$ TeV," *Phys. Rev. Lett.*, vol. 123, no. 19, p. 192301, 2019.

[171] A. M. Sirunyan *et al.*, "Measurement of prompt D^0 meson azimuthal anisotropy in Pb-Pb collisions at $\sqrt{s_{NN}}$ = 5.02 TeV," *Phys. Rev. Lett.*, vol. 120, no. 20, p. 202301, 2018.

[172] Z.-w. Lin and D. Molnar, "Quark coalescence and elliptic flow of charm hadrons," *Phys. Rev. C*, vol. 68, p. 044901, 2003.

[173] M. Aaboud *et al.*, "Prompt and non-prompt J/ψ elliptic flow in Pb+Pb collisions at $\sqrt{s_{\mathrm{NN}}} = 5.02$ Tev with the ATLAS detector," *Eur. Phys. J. C*, vol. 78, no. 9, p. 784, 2018.

[174] CMS Collaboration, "Azimuthal anisotropy of nonprompt D^0 mesons in PbPb collisions at $\sqrt{s_{\mathrm{NN}}} = 5.02$ TeV," tech. rep., CERN, Geneva, 2022.

[175] B. Abelev *et al.*, "Long-range angular correlations on the near and away side in p-Pb collisions at $\sqrt{s_{NN}} = 5.02$ TeV," *Phys. Lett. B*, vol. 719, pp. 29–41, 2013.

[176] R. Aaij *et al.*, "Measurements of long-range near-side angular correlations in $\sqrt{s_{\mathrm{NN}}} = 5$TeV proton-lead collisions in the forward region," *Phys. Lett. B*, vol. 762, pp. 473–483, 2016.

[177] K. Dusling and R. Venugopalan, "Comparison of the color glass condensate to dihadron correlations in proton-proton and proton-nucleus collisions," *Phys. Rev. D*, vol. 87, no. 9, p. 094034, 2013.

[178] K. Dusling and R. Venugopalan, "Explanation of systematics of CMS p+Pb high multiplicity di-hadron data at $\sqrt{s}_{\mathrm{NN}} = 5.02$ TeV," *Phys. Rev. D*, vol. 87, no. 5, p. 054014, 2013.

[179] P. Bozek, "Collective flow in p-Pb and d-Pd collisions at TeV energies," *Phys. Rev. C*, vol. 85, p. 014911, 2012.

[180] A. Adare *et al.*, "Quadrupole Anisotropy in Dihadron Azimuthal Correlations in Central d+Au Collisions at $\sqrt{s_{NN}}$=200 GeV," *Phys. Rev. Lett.*, vol. 111, no. 21, p. 212301, 2013.

[181] L. Adamczyk *et al.*, "Long-range pseudorapidity dihadron correlations in d+Au collisions at $\sqrt{s_{\mathrm{NN}}} = 200$ GeV," *Phys. Lett. B*, vol. 747, pp. 265–271, 2015.

[182] C. Aidala *et al.*, "Creation of quark–gluon plasma droplets with three distinct geometries," *Nature Phys.*, vol. 15, no. 3, pp. 214–220, 2019.

[183] U. A. Acharya *et al.*, "Kinematic dependence of azimuthal anisotropies in $p + Au$, $d + Au$, and ${}^3He + Au$ at $\sqrt{s}_{NN} = 200$ GeV," *Phys. Rev. C*, vol. 105, no. 2, p. 024901, 2022.

[184] A. M. Sirunyan *et al.*, "Multiparticle correlation studies in pPb collisions at $\sqrt{s_{\mathrm{NN}}} = 8.16$ TeV," *Phys. Rev. C*, vol. 101, no. 1, p. 014912, 2020.

[185] B. B. Abelev *et al.*, "Multiparticle azimuthal correlations in p -Pb and Pb-Pb collisions at the CERN Large Hadron Collider," *Phys. Rev. C*, vol. 90, no. 5, p. 054901, 2014.

[186] V. Khachatryan *et al.*, "Evidence for Collective Multiparticle Correlations in p-Pb Collisions," *Phys. Rev. Lett.*, vol. 115, no. 1, p. 012301, 2015.

[187] M. Aaboud *et al.*, "Measurement of multi-particle azimuthal correlations in pp, p+Pb and low-multiplicity Pb+Pb collisions with the ATLAS detector," *Eur. Phys. J. C*, vol. 77, no. 6, p. 428, 2017.

[188] Z. Moravcova, "Observation of partonic flow in small collision systems with ALICE at the LHC." Quark Matter 2022.

[189] B. B. Abelev *et al.*, "Long-range angular correlations of π, K and p in p-Pb collisions at $\sqrt{s_{\mathrm{NN}}}$ = 5.02 TeV," *Phys. Lett. B*, vol. 726, pp. 164–177, 2013.

[190] V. Khachatryan *et al.*, "Long-range two-particle correlations of strange hadrons with charged particles in pPb and PbPb collisions at LHC energies," *Phys. Lett. B*, vol. 742, pp. 200–224, 2015.

[191] A. M. Sirunyan *et al.*, "Correlations of azimuthal anisotropy Fourier harmonics with subevent cumulants in pPb collisions at $\sqrt{s_{NN}}$ =8.16TeV," *Phys. Rev. C*, vol. 103, no. 1, p. 014902, 2021.

[192] A. M. Sirunyan *et al.*, "Elliptic flow of charm and strange hadrons in high-multiplicity pPb collisions at $\sqrt{s_{\mathrm{NN}}} = 8.16$ TeV," *Phys. Rev. Lett.*, vol. 121, no. 8, p. 082301, 2018.

[193] S. Acharya *et al.*, "Azimuthal Anisotropy of Heavy-Flavor Decay Electrons in p-Pb Collisions at $\sqrt{s_{\mathrm{NN}}} = 5.02$ TeV," *Phys. Rev. Lett.*, vol. 122, no. 7, p. 072301, 2019.

[194] A. M. Sirunyan *et al.*, "Observation of prompt J/ψ meson elliptic flow in high-multiplicity pPb collisions at $\sqrt{s_{\mathrm{NN}}} = 8.16$ TeV," *Phys. Lett. B*, vol. 791, pp. 172–194, 2019.

[195] C. Zhang, C. Marquet, G.-Y. Qin, S.-Y. Wei, and B.-W. Xiao, "Elliptic flow of heavy quarkonia in pa collisions," *Phys. Rev. Lett.*, vol. 122, p. 172302, May 2019.

[196] C. Zhang, C. Marquet, G.-Y. Qin, Y. Shi, L. Wang, S.-Y. Wei, and B.-W. Xiao, "Collectivity of heavy mesons in proton-nucleus collisions," *Phys. Rev. D*, vol. 102, no. 3, p. 034010, 2020.

[197] B. Schenke, S. Schlichting, and R. Venugopalan, "Azimuthal anisotropies in p+Pb collisions from classical Yang–Mills dynamics," *Phys. Lett. B*, vol. 747, pp. 76–82, 2015.

[198] A. M. Sirunyan *et al.*, "Studies of charm and beauty hadron long-range correlations in pp and pPb collisions at LHC energies," *Phys. Lett. B*, vol. 813, p. 136036, 2021.

[199] CMS Collaboration, "Azimuthal anisotropy of $\Upsilon(1S)$ mesons in pPb collisions at $\sqrt{s_{\mathrm{NN}}} = 8.16\ \mathrm{TeV}$," 2022, https://cds.cern.ch/record/2806156.

[200] E. Avsar, C. Flensburg, Y. Hatta, J.-Y. Ollitrault, and T. Ueda, "Eccentricity and elliptic flow in proton–proton collisions from parton evolution," *Phys. Lett. B*, vol. 702, pp. 394–397, 2011.

[201] J. D. Bjorken, S. J. Brodsky, and A. Scharff Goldhaber, "Possible multiparticle ridge-like correlations in very high multiplicity proton-proton collisions," *Phys. Lett. B*, vol. 726, pp. 344–346, 2013.

[202] B. Schenke, S. Schlichting, P. Tribedy, and R. Venugopalan, "Mass ordering of spectra from fragmentation of saturated gluon states in high multiplicity proton-proton collisions," *Phys. Rev. Lett.*, vol. 117, no. 16, p. 162301, 2016.

[203] R. Rapp. personal communication (June, 26 2022).

[204] L. Evans and P. Bryant, "LHC machine," *Journal of Instrumentation*, vol. 3, pp. S08001–S08001, aug 2008.

[205] CERN Press Office, "First beam in the LHC - accelerating science. Premier faisceau dans le LHC - accélérateur de science," p. 1.5 p, 2008. Issued on 8 August 2008.

[206] M. Bajko *et al.*, "Report of the Task Force on the Incident of 19th September 2008 at the LHC," tech. rep., CERN, Geneva, Mar 2009.

[207] L. Arnaudon, R. W. Assmann, A. Blondel, B. Dehning, G. E. Fischer, P. Grosse-Wiesmann, A. Hofmann, R. Jacobsen, J.-P. Koutchouk, J. Miles, R. Olsen, M. Placidi, R. Schmidt, and J. Wenninger, "Effects of terrestrial tides on the LEP beam energy," *Nucl. Instrum. Methods Phys. Res., A*, vol. 357, pp. 249–252. 8 p, Mar 1994.

[208] E. Bravin, G. Brun, B. Dehning, A. Drees, P. Galbraith, M. A. Geitz, K. N. Henrichsen, M. Koratzinos, and G. Mugnai, "The Influence of Train Leakage Currents on the LEP Dipole Field," *Nucl. Instrum. Methods Phys. Res., A*, vol. 417, pp. 9–15. 9 p, Sep 1997.

[209] N. Besson and PHENIICS Doctoral School, "Week 5 of "Des particules aux étoiles" [MOOC]." https://www.fun-mooc.fr/fr/cours/des-particules-aux-etoiles/, 2016.

[210] R. Steerenberg and HCPSS2020, "Course on Accelerator Physics for CERN-Fermilab Summer School HCPSS2020." https://indico.fnal.gov/event/43762/, August 2020.

[211] Anaïs Schaeffer for CERN, "LS2 Report: Beams circulate in the PS Booster. Nouvelles du LS2 : des faisceaux circulent dans le Booster du PS," 2021. Issued on 21 January 2021.

[212] O. Brüning and L. Rossi, "The High-Luminosity Large Hadron Collider," *Nature Reviews Physics*, vol. 1, pp. 241–243, Apr. 2019.

[213] C. Fabjan and J. Schukraft, "The story of ALICE: Building the dedicated heavy ion detector at LHC," p. 19.

[214] "Letter of Intent for A Large Ion Collider Experiment [ALICE]," tech. rep., CERN, Geneva, 1993.

[215] European organization for nuclear research, *ALICE: technical proposal for A Large Ion Collider Experiment at the CERN LHC.* Geneva: CERN, 1995. OCLC: 860433775.

[216] "The ALICE experiment at the CERN LHC," p. 259, 2008.

[217] ALICE Collaboration, "Performance of the ALICE Experiment at the CERN LHC," *International Journal of Modern Physics A*, vol. 29, p. 1430044, Sept. 2014. arXiv: 1402.4476.

[218] *ALICE Inner Tracking System (ITS): Technical Design Report*. Technical design report. ALICE, Geneva: CERN, 1999.

[219] G. Dellacasa *et al.*, "ALICE: Technical design report of the time projection chamber," 1 2000.

[220] P. Cortese *et al.*, "ALICE technical design report on forward detectors: FMD, T0 and V0," 9 2004.

[221] "ALICE technical design report of the dimuon forward spectrometer," 8 1999.

[222] "ALICE dimuon forward spectrometer: addendum to the Technical Design Report," 2000.

[223] *The forward muon spectrometer of ALICE: addendum to the technical proposal for a Large Ion Collider experiment at the CERN LHC*. LHC technical proposal, Geneva: CERN, 1996.

[224] "AliRoot source code." https://github.com/alisw/AliRoot.

[225] R. Brun *et al.*, "root-project/root: v6.18/02," Aug. 2019.

[226] C. Bierlich *et al.*, "A comprehensive guide to the physics and usage of PYTHIA 8.3," 3 2022.

[227] M. Gyulassy and X.-N. Wang, "HIJING 1.0: A Monte Carlo program for parton and particle production in high-energy hadronic and nuclear collisions," *Comput. Phys. Commun.*, vol. 83, p. 307, 1994.

[228] "Upgrade of the ALICE Readout & Trigger System," 2013.

[229] B. Abelev *et al.*, "Upgrade of the ALICE Experiment: Letter Of Intent," *J. Phys. G*, vol. 41, p. 087001, 2014.

[230] "Addendum of the Letter of Intent for the upgrade of the ALICE experiment : The Muon Forward Tracker," tech. rep., CERN, Geneva, Aug 2013. Final submission of the presetn LoI addendum is scheduled for September 7th.

[231] B. Abelev *et al.*, "Technical Design Report for the Upgrade of the ALICE Inner Tracking System," *J. Phys. G*, vol. 41, p. 087002, 2014.

[232] F. Reidt, "Upgrade of the ALICE ITS detector," *Nucl. Instrum. Meth. A*, vol. 1032, p. 166632, 2022.

[233] G. Aglieri Rinella, "The ALPIDE pixel sensor chip for the upgrade of the ALICE Inner Tracking System," *Nucl. Instrum. Meth. A*, vol. 845, pp. 583–587, 2017.

[234] A. Maevskaya, "ALICE FIT Data Processing and Performance during LHC Run 3," *Phys. At. Nucl.*, vol. 84, no. 4, pp. 579–584, 2021.

[235] "Technical Design Report for the Muon Forward Tracker," tech. rep., Jan 2015.

[236] P. Moreira, J. Christiansen, K. Wyllie, P. Moreira, S. Baron, S. Bonacini, J. Christiansen, P. Farthouat, S. Feger, R. Francisco, T. Grassi, P. Gui, M. Hansen, K. Kloukinas, P. Leitao, A. Marchioro, M. Marin, D. Porret, J. Silva, F. Tavernier, J. Troska, F. Vasey, and K. Wyllie, *GBTX manual; V0.18 draft*. Jul 2021.

[237] "VTRx project webpage." https://espace.cern.ch/project-versatile-link/public/default.aspx.

[238] P. Buncic, M. Krzewicki, and P. Vande Vyvre, "Technical Design Report for the Upgrade of the Online-Offline Computing System," 4 2015.

[239] Alkin, Anton, Eulisse, Giulio, Grosse-Oetringhaus, Jan Fiete, Hristov, Peter, and Kabus, Maja, "Alice run 3 analysis framework," *EPJ Web Conf.*, vol. 251, p. 03063, 2021.

[240] L. Musa, "Letter of Intent for an ALICE ITS Upgrade in LS3," tech. rep., CERN, Geneva, Dec 2019.

[241] "Letter of Intent: A Forward Calorimeter (FoCal) in the ALICE experiment," 6 2020.

[242] ALICE Collaboration, "Letter of intent for ALICE 3: A next generation heavy-ion experiment at the LHC," tech. rep., CERN, Geneva, Mar 2022.

[243] J. Gordon and E. Mathieson, "Cathode charge distributions in multiwire chambers: I. measurement and theory," *Nuclear Instruments and Methods in Physics Research Section A: Accelerators, Spectrometers, Detectors and Associated Equipment*, vol. 227, no. 2, pp. 267–276, 1984.

[244] F. James and M. Roos, "Minuit - a system for function minimization and analysis of the parameter errors and correlations," *Computer Physics Communications*, vol. 10, no. 6, pp. 343–367, 1975.

[245] E. Mathieson, "Cathode charge distributions in multiwire chambers: 4. Empirical formula for small anode-cathode separation," *Nuclear Instruments and Methods in Physics Research Section A: Accelerators, Spectrometers, Detectors and Associated Equipment*, vol. 270, pp. 602–603, July 1988.

[246] ALICE Collaboration, "Measurement of ψ(2S) production as a function of charged-particle pseudorapidity density in pp collisions at $\sqrt{s} = 13$ TeV and p-Pb collisions at $\sqrt{s_{\rm NN}} = 8.16$ TeV with ALICE at the LHC," 4 2022, arXiv:2204.10253.

[247] ALICE Collaboration, "System-size dependence of the charged-particle pseudorapidity density at $\sqrt{s_{\rm NN}} = 5.02$ TeV for pp, p-Pb, and Pb-Pb collisions," 4 2022, arXiv:2204.10210.

[248] J. Adam *et al.*, "Forward-central two-particle correlations in p-Pb collisions at $\sqrt{s_{\rm NN}} = 5.02$ TeV," *Phys. Lett. B*, vol. 753, pp. 126–139, 2016.

[249] C. Marquet. personal communication (May, 11 2022).